ABSTRACT

CHENG, LIPING. Mathematical Modeling of Laminar and Turbulent Single-phase and Two-phase Flows in Straight and Helical Ducts (Under the direction of Dr. Andrey V. Kuznetsov)

The purpose of this research is to investigate numerically the dynamics and heat transfer of laminar or turbulent flows in different media and complicated geometries, including the flow in a composite domain whose central portion is occupied by a clear fluid (turbulent flow) and whose peripheral portion is occupied by a fluid saturated porous medium (laminar flow); a laminar flow of a non-Newtonian fluid in a helical pipe; a laminar flow in a helical pipe filled with a fluid saturated porous medium; a two-phase laminar flow (non-Newtonian carrying fluid and solid particles) in a helical pipe. To model forced convection in a composite porous/fluid domain, the Brinkma-Forchheimer-extended Darcy equation is utilized for the porous region and a two-layer algebraic turbulence model is utilized for the flow in the central region. The effects of turbulence on velocity and temperature distributions as well as on the Nusselt number are analyzed. To investigate a fully developed laminar flow of a non-Newtonian fluid in a helical pipe, an orthogonal helical coordinate system is utilized and the Navier-Stokes and energy equations for the non-Newtonian fluid in this coordinate system are derived. The effects of the curvature and torsion of a helical pipe, the Dean number and Germano number on the velocities, secondary flow and heat transfer are presented. A full momentum equation for the flow in porous media that accounts for the Brinkman and Forchheimer extensions of the Darcy law as well as for the flow inertia is adopted to study the fully developed laminar flow in a helical pipe filled with a fluid saturated porous medium. The effects of the geometry of the helical pipe and the physical properties of the

porous medium are investigated. Accounting for the flow inertia is shown to be important for predicting the secondary flow in a helical pipe. For 3D modeling of two-phase laminar flow in a helical pipe, the Eulerian approach is utilized for fluid flow and the Lagrangian approach is utilized for tracking particles. The interaction between the solid particles and the fluid that carries them is accounted for by a source term in the momentum equation for the fluid. The influence of inter-particle and particle-wall collisions is also taken into account.

MATHEMATICAL MODELING OF LAMINAR AND TURBULENT SINGLE-PHASE AND TWO-PHASE FLOWS IN STRAIGHT AND HELICAL DUCTS

by

LIPING CHENG

A dissertation submitted to the Graduate Faculty of
North Carolina State University
in partial fulfillment of the
requirement for the Degree of
Doctor of Philosophy

MECHANICAL ENGINEERING

Raleigh

2004

APPROVED BY:

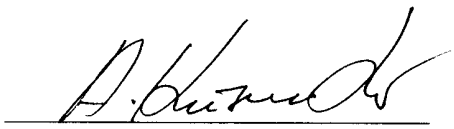

ANDREY V. KUZNETSOV
Chair of Advisory Committee

K. P. SANDEEP

WILLIAM L. ROBERTS

KEVIN M. LYONS

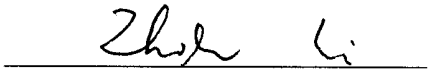

ZHILIN LI

献 给 我 至 爱 的 亲 人

To my family with love

BIOGRAPHY

Liping Cheng was born in Jinhua, Zhejiang, People's Republic of China on August 5, 1975. She was admitted to Tsinghua University, Beijing, China in 1993 and received her Bachelor of Engineering degree in Heating, Ventilating and Air-conditioning from the Department of Thermal Engineering in 1998. In the same year, she joined Institute of Nuclear Energy Technology, Tsinghua University, and graduated in 2001 with Master of Engineering degree. In the summer of 2001, she was admitted to North Carolina State University, Raleigh, NC, to pursue her PhD degree in the Department of Mechanical and Aerospace Engineering.

ACKNOWLEDGEMENTS

First and foremost I want to thank my advisor, Dr. Andrey V. Kuznetsov for his continuous support and guidance during my studies at NC State University. His enthusiasm in research and encouragement has been the driving force for the successful completion of my research and dissertation.

I gratefully acknowledge the support of this work by a USDA grant and Prof. K. P. Sandeep, for suggesting the project in the first place, and for critical advice and help for my research. My thanks would extend to the other committee members, Dr. Zhilin Li, Dr. William L. Roberts, and Dr. Kevin M. Lyons, for their valuable suggestion and comments for my dissertation.

This major undertaking has received the generous support from department staff and all former and current officemates, Dr. Ming Xiong, Dr. Qun Wan, Dr. Deming Mao, Patirop Chitrphiromsri, Peng Geng, etc. Their assistance, suggestions, encouragement and friendship are very important to me.

I would like to especially thank my family for their unconditional love and inspiration. I so appreciate their encouragement and patience. This study would not have been possible without the assistance and dedication of a great many people.

TABLE OF CONTENTS

LIST OF TABLES

LIST OF FIGURES

1 INTRODUCTION

In mechanical engineering applications, many different media or complicated geometries are utilized for fluid flow. In this dissertation, investigation is conducted on the dynamics and heat transfer in the following processes: the flow in a composite channel or duct whose central portion is occupied by a clear fluid and whose peripheral portion is occupied by a fluid saturated porous medium; a laminar flow of a non-Newtonian fluid in a helical pipe; a laminar flow in a helical pipe filled with a fluid saturated porous medium; a two-phase laminar flow in a helical pipe.

1.1 TURBULENCE EFFECTS ON FORCED CONVECTION IN COMPOSITE POROUS/FLUID DOMAIN

The interaction of turbulent flow in a homogeneous fluid region with flow in a porous region in a composite porous/fluid domain is of great practical interest. This problem is important in modeling solidification of binary alloys with electromagnetic stirring [1], investigation of turbulent flow near porous obstacles [2] for applications including microelectronic cooling [3], and studying the contaminant transport by air flow through forests and crops. Results of Antohe and Lage [4] and Prakash et al. [5, 6] indicate that the effect of the porous medium is to dampen turbulence. This occurs because of the friction between the fluid and the porous matrix. Also, porous matrix imposes heavy restrictions on the size of turbulent eddies in the porous region. Therefore, if permeability of the porous medium is sufficiently small, even if the flow in the clear fluid region is turbulent, the flow in the porous region may still remain laminar.

Despite considerable interest in modeling of macroscopic turbulence in homogeneous porous media ([4]-[12]), the number of papers addressing turbulent flow in composite porous/fluid domains is very limited. This dissertation concentrates on the problem of forced convection in a composite circular tube or a parallel plate channel, with its central part filled with a homogeneous fluid and its peripheral part filled with a fluid saturated porous medium. The effect of turbulence in the central region on heat transfer from the wall to the fluid is analyzed for two types of boundary conditions at the tube wall, constant heat flux and constant wall temperature.

1.2 LAMINAR FLOW OF A NON-NEWTONIAN FLUID IN A HELICAL PIPE

A secondary flow is induced in a plane perpendicular to the main flow when a fluid passes through a curved helically coiled pipe. The secondary flow helps to achieve better heat and mass transfer; this is one of the reasons why helically coiled pipes are applied in many branches of industry and the research on the flow dynamics of liquids in helical pipes attracts lots of attention. The first theoretical study was done by Dean [13] for fully developed laminar flow. He introduced a dimensionless parameter, later called the Dean number, to characterize the magnitude and the shape of the secondary motion. Germano [14, 15] introduced a helical orthogonal coordinate system and derived the Navier-Stokes equations in this coordinate system to study the effect of torsion on the secondary flow. Numerical studies have been conducted later on to examine the effects of torsion and curvature on the fluid flow in helical pipes ([16-21]). However, all of these works studied Newtonian fluids. Many industrial applications deal with non-Newtonian fluids, especially in aseptic processing of foods such as milk, soups, sauces, fruit juices, and other beverages. Sandeep [22] and

Sandeep et al. [23] pioneered in modeling flows of non-Newtonian fluids in helical pipes using the Ostwald-de Waele model (Bird et al., [24]). However, since a Cartesian coordinate system was used, the effects of the curvature and torsion on the secondary flow in the plane normal to the main flow could not be studied in sufficient details. In this dissertation Germano's orthogonal helical coordinate system is adopted for a fully developed laminar flow of a non-Newtonian fluid in a helical pipe and the governing equations in this coordinate system are derived. To solve the heat transfer problem, a thermal energy equation is derived and solved for the case of a constant wall heat flux. The effects of the Dean number, Germano number, and Prandtl number with a fixed Reynolds number on the hydrodynamics and heat transfer in non-Newtonian fluid flow in helical pipes are investigated.

1.3 LAMINAR FLOW IN A HELICAL PIPE FILLED WITH A FLUID SATURATED POROUS MEDIUM

Porous media are widely used in engineering applications, to study migration of moisture in fibrous insulation, grain storage, transport in contaminated soils, underground disposal of nuclear wastes, transport in drying processes, etc. Nield and Bejan [25] summarized the state-of-the-art on this topic. Another quickly developing research field related to porous media is concerned with biomedical applications. In a clotted artery, the lesions or "plaques" within the artery wall consist of localized deposits of fat compounds (lipids) surrounded by cells recruited from the blood stream and scar tissue; this acts as a porous medium that may diminish or completely eliminate the blood flow. The coronary arteries surrounding the heart are curved and at least segments of them can be modeled as helical.

Nothing has been published on flows in helical pipes filled with a fluid saturated porous medium. To fill the gap in the literature, an investigation on the laminar flow in a helical pipe filled with a porous medium is conducted. The Brinkman-Forchheimer-extended Darcy equation with inertia terms is solved numerically in an orthogonal helical coordinate system. The effects of the Darcy number, the Forchheimer coefficient, the curvature and torsion of the helical pipe on the axial flow velocity and secondary flow are investigated numerically.

1.4 TWO-PHASE LAMINAR FLOW IN A HELICAL PIPE

Governing equations for a two-phase 3D helical pipe flow of a non-Newtonian fluid with large particles are derived in an orthogonal helical coordinate system. The Lagrangian approach is utilized to model solid particle trajectories. The interaction between solid particles and fluid that carries them is accounted for by a source term in the momentum equation for the fluid. The force-coupling method (Maxey et al. [26]; Maxey and Patel [27]) is adopted, in which the momentum source term is no longer a Dirac delta function but is spread on the numerical mesh by using a finite-sized envelop with a spherical Gaussian distribution. The influences of inter-particle and particle-wall collisions are also taken into account.

1.5 INTRODUCTION OF PARTS AND CHAPTERS

This dissertation includes four parts and nine chapters. Part One, which includes Chapters 2 and 3, investigates the interaction of turbulent flow in a homogeneous fluid region with flow in a porous region in a composite porous/fluid domain when the flow in the porous region of

the domain is assumed to be laminar and the flow in the clear fluid region of the domain is assumed to be turbulent. Part Two is composed of Chapters 4 and 5 and investigates laminar flow and heat transfer of a non-Newtonian fluid in a helical pipe. The momentum and energy equations are derived and solved in an orthogonal helical coordinate system. The Ostwald-de Waele model is utilized to consider the effective viscosity of a non-Newtonian fluid. Part Three, which includes Chapters 6 and 7, describes the modeling of the laminar flow and heat transfer in a helical pipe filled with a fluid saturated porous medium. A full momentum equation for the flow in porous media, which accounts for the Brinkman and Forchheimer extensions of the Darcy law as well as for the flow inertia, is utilized. Part Four consists of Chapter 8, which describes mathematical 3D modeling of two-phase (non-Newtonian fluid and solid particles) in a helical pipe. The Eulerian/Lagrangian approach is applied and a Force Coupling method by Maxey is adopted to consider the back influence of the particles on the carrying fluid.

Chapter 2 (published as ref. [28]) studies a composite parallel-plate channel whose central portion is occupied by a clear fluid and whose peripheral portion is occupied by a fluid saturated porous medium. The laminar flow in the porous region of the channel is governed by the Brinkma-Forchheimer-extended Darcy equation, while the turbulent flow in the clear fluid region of the channel is modeled using the two-layer algebraic turbulence model suggested by Cebeci and Smith (Cebeci and Smith [29], Wilcox [30]). The validity of this laminar/turbulent assumption is validated by estimating the Reynolds numbers in the clear fluid and porous regions of the channel.

Chapter 3 (published as ref. [31]) investigates a similar problem to that in Chapter 2 except that the object is now a circular tube, the center of which is filled with a homogeneous fluid

and the neighboring porous region is adjacent to the tube wall. Two kinds of thermal boundary conditions (isoflux wall and isothermal wall) are investigated. The effects of turbulence in the central region on velocity and temperature distributions as well as on the Nusselt number are analyzed by comparing turbulent model predictions with predictions of the model that assumes laminar flow in both homogeneous fluid and porous flow domains.

When a fluid passes through a curved helically coiled pipe, the centrifugal force causes an increased axial velocity near the pipe outer wall and decreased axial velocity near the pipe inner wall and in the mean time, a secondary flow is generated. Chapter 4 (published as ref. [32]) investigates this phenomenon by a numerical study of a fully developed laminar flow of a non-Newtonian fluid in a helical pipe based on an orthogonal helical coordinate system suggested by Germano [13, 14]. The SIMPLE algorithm with a staggered grid is adopted to solve the governing equations. The effects of the pressure gradient, the curvature, and the torsion on the fully developed laminar flow in helical pipes are investigated. The comparison of flow dynamics between Newtonian and non-Newtonian fluids is presented.

To show the effect of helical pipe on heat transfer, in Chapter 5 (published as ref. [33]), both the Navier-Stokes and energy equations are derived and solved in the same orthogonal helical coordinate system as the one in Chapter 4. The effects of the Dean number, Germano number, and Prandtl number with a fixed Reynolds number on the hydrodynamics and heat transfer in non-Newtonian fluid flow in helical pipes are investigated for the case of a constant wall temperature boundary condition.

Chapter 6 (published as ref. [34, 35]) investigates laminar flow in a helical pipe filled with a porous medium, which is relevant to a number of engineering and biological applications,

such as the flow in a helical segment of a clotted human coronary artery. Since the secondary flow in a helical pipe becomes significant at a relatively large flow velocity, it is insufficient to describe the drag that the porous medium imposes on a fluid by using just one linear (Darcy) term; at larger filtration velocities the surface drag due to friction becomes comparable with the form drag due to solid obstacles (Nield and Bejan [25]). Since the form drag due to solid obstacles is proportional to the square of the filtration velocity, to account for this effect an additional quadratic drag term is introduced into the momentum equation, which is called the Forchheimer term. In this chapter, the most general form of a momentum equation for porous media, the Brinkman-Forchheimer-extended Darcy equation with inertia terms, is utilized; this equation is solved numerically in the same orthogonal helical coordinate system as described in the previous chapters. The geometry of a helical pipe is characterized by the curvature and torsion. In this study, the effects of the Darcy number, the Forchheimer coefficient, the curvature and torsion of the helical pipe on the axial flow velocity and secondary flow are investigated numerically.

Chapter 7 (submitted as ref. [36, 37]) is to carry out a heat transfer investigation for the flow in a helical pipe filled with a fluid saturated porous medium. In addition to the full momentum equation for porous media that accounts for the Brinkman and Forchheimer extensions of the Darcy law as well as for the flow inertia described in Chapter 6, an energy equation is also derived and solved. The effects of the Darcy number, the Forchheimer coefficient as well as the Dean and Germano numbers on the axial flow velocity, secondary flow, temperature distribution, and the Nusselt number are investigated.

Chapter 8 (submitted as ref. [38]) simulates a two-phase 3D flow of a non-Newtonian fluid in a helical pipe with large particles. The governing equations for the fluid flow in an

orthogonal helical coordinate system are derived. The influence of the particles on the fluid is described by adding a source term to the momentum equation for the fluid flow. The particle-particle and particle-wall interactions are taken into account. It is shown that the particles have a significant effect on the flow field. The effects of mean flow velocity and the initial radial positions of particles on the residence time distribution (RTD) of the particles are analyzed.

REFERENCES

1. Prescott, P.J. and Incropera, F.P. (1995) The effect of turbulence on solidification of a binary metal alloy with electromagnetic stirring. *ASME Journal of Heat Transfer,* 117: 716-724

2. Wang, H. and Takle, E.S. (1995) Boundary-layer flow and turbulence near porous obstacles. *Boundary Layer Meteorology,* 74: 73-88

3. Kim, S.Y., Koo, J-M and Kuznetsov, AV (2001) Effect of anisotropy in permeability and effective thermal conductivity on thermal performance of an aluminum foam heat sink. *Numerical Heat Transfer* A, 40: 21-36

4. Antohe, B.V. and Lage, J.L. (1997) A general two-equation macroscopic model for incompressible flow in porous media, *International Journal of Heat and Mass Transfer,* 40: 3013-3024.

5. Nakayama A. and Kuwahara F. (1999)A macroscopic turbulence model for flow in a porous medium, *ASME Journal of Fluids Engineering,* 121: 427-433.

6. Kuwahara, F., Kameyama Y., Yamashita S. and Nakayama A. (1998) Numerical modeling of turbulent flow in porous media using a spatially periodic array, *Journal of Porous Media,* 1: 47-55.

7. Pedras, MHJ and de Lemos, MJS (2001) Macroscopic turbulence modeling for incompressible flow through undeformable porous media. *International Journal of Heat and Mass Transfer,* 44: 1081-1093.

8. Pedras, MHJ and de Lemos, MJS (2001) Simulation of turbulent flow in porous media using a spatially periodic array and a low Re two-equation closure. *Numerical Heat Transfer*, Part A, 39: 35-59.

9. Pedras, MHJ and de Lemos, MJS (2000) On the definition of turbulent kinetic energy for flow in porous media. *International Communications in Heat and Mass Transfer,* 27: 211-220.

10. Kuwahara, F., Kameyama, Y., Yamashita, S. and Nakayama, A (1998) Numerical modeling of turbulent flow in porous media using a spatially periodic array. *Journal of Porous Media,* 1: 47-55.

11. Nield, D.A. (1997) Turbulence model for flow through porous media – Comments. *International Journal of Heat and Mass Transfer,* 40: 2499-2499

12. Masuoka, T. and Takatsu, Y. (1996) Turbulence model for flow through porous media. *International Journal of Heat and Mass Transfer*, 39: 2803-2809.

13. Dean, W.R. (1927) Note on the motion of fluid in a curved pipe, *Philosophical Magazine,* 4 (7): 208-223.

14. Germano M. (1982) On the effect of torsion on a helical pipe flow, *J. Fluid Mech.*, 125: 1-8.

15. Germano M. (1989) The Dean equations extended to a helical pipe flow, *J. Fluid Mech.,* 203: 289-305.

16. Yang G., Dong Z. F. and Ebadian M. A. (1995) Laminar forced convection in a helicoidal pipe with finite pitch, *Int. J. Heat Mass Transfer,* 38: 853-862.

17. Hüttl, T. J. (1997) Navier Stokes solutions of laminar flows based on orthogonal helical coordinates, *Numerical Methods in Laminar and Turbulent Flow* ,10: 191-202.

18. Hüttl, T. J. (2000) Influence of curvature and torsion on turbulent flow in curved and helically coiled pipes, *Int. J. Heat and Fluid Flow*, 21: 345-353.

19. Pharoah, J.G., Litster, S. and Djilali, N. (2003) Mass transfer enhancement in membrane separation –rotating vs. helical modules", *CFD 2003*, Vancouver, May: 28-30.

20. Zheng, B., Lin, C.X. and Ebadian, M.A. (2000) Combined laminar forced convection and thermal radiation in a helical pipe, *Int. J. Heat and Mass Transfer*, 43: 1067-1078.

21. Lin, C.X., Zhang, P., and Ebadian, M.A. (1997) Laminar forced convection in the entrance region of helical pipes, *Int. J. Heat Mass Transfer*, 40: 3293-3304.

22. Sandeep, K.P. (1996): *Computational and experimental studies on the fluid dynamics and heat transfer aspects in conventional and helical holding tubes for aseptic food processing.* PhD Thesis, Pennsylvania State University, State College, Pennsylvania.

23. Sandeep, K.P., Zuritz C.A. and Puri V.M. (2000): Modeling non-Newtonian two-phase flow in conventional and helical-holding tubes. *Int. J. Food Science and Technology*, 35: 511-522.

24. Bird, R.B., Stewart W.E. and Lightfoot, E.N. (2002) *Transport Phenomena*, 2nd ed. -New York: John Wiley and Sons.

25. Nield, D.A., Bejan A.(1999) *Convection in Porous Media*, 2nd ed., Springer, New York.

26. Maxey, M.R., Patel, B.K., Chang, E.J., and Wang, P. (1997) Simulation of dispersed turbulent multiphase flow, *Fluid Dyn. Res.*, 20: 143-156.

27. Maxey, M.R. and Patel, B.K (2001) Localized force representations for particles sedimenting in stokes flow, *Int. J. Multiphase Flow*, 27: 1603-1626.

28. Kuznetsov, A. V., Cheng, L. and Xiong, M. (2002) Effects of thermal dispersion and turbulence on forced convection in a composite parallel-plate channel: Investigation of constant wall heat flux and constant wall temperature cases, *Numerical Heat Transfer A*, 42: 365-383.

29. Cebeci, T. and Smith, A.M.O. (1974) *Analysis of Turbulent Boundary Layers*, *Ser. in Appl. Math & Mech.*, Vol. XV, Academic Press, New York.

30. Wilcox, D.C. (1994) *Turbulence Modeling for CFD*, DCW Industries, La Canada, CA.

31. Kuznetsov, A.V., Cheng, L. and Xiong, M. (2003) Investigation of turbulence effects on forced convection in a composite porous/fluid duct: Constant wall flux and constant wall temperature cases, *Heat and Mass transfer,* 39: 613-623.

32. Cheng, L. and Kuznetsov, A.V. (2004) Investigation of a laminar flow of a non-Newtonian fluid in a helical pipe, *International Journal of Applied Mechanics and Engineering* (in press).

33. Cheng, L. and Kuznetsov, A.V. (2004) Heat transfer in a laminar flow of a non-Newtonian fluid in a helical pipe, *International Journal of Transport Phenomena* (in press).

34. Cheng, L. and Kuznetsov, A.V. (2004) Numerical investigation of laminar flow in a helical pipe filled with a fluid saturated porous medium: the sensitivity of secondary flow to parameter variations, *Proceedings of 2004 ASME International Mechanical Engineering Congress*, Anaheim, California, November 13-19, ASME paper IMECE2004-60499, pp. 1-6.

35. Cheng, L. and Kuznetsov, A.V. (2004) Investigation of laminar flow in a helical pipe filled with a fluid saturated porous medium, *European Journal of Mechanics B/Fluids* (in press).

36. Cheng, L. and Kuznetsov, A.V. (2004) Heat transfer in a laminar flow in a helical pipe filled with a fluid saturated porous medium, *International Journal of Thermal Sciences* (submitted).

37. Cheng, L. and Kuznetsov, A.V. (2005) Numerical investigation of heat transfer in a laminar flow in a helical pipe filled with a fluid saturated porous medium: the sensitivity to parameter variations, *Proceedings of 4th International Conference on Computational Heat and Mass Transfer*, Paris-Cachan, May 17-20, 2005 (accepted).

38. Cheng, L. and Kuznetsov, A.V. and Sandeep, K.P. (2004) Mathematical modeling of two-phase non-Newtonian flow in a helical pipe, *International Journal for Numerical Methods in Fluids* (submitted).

PART ONE:

TURBULENCE EFFECTS ON COMPOSITE POROUS/FLUID DOMAIN

2 EFFECTS OF THERMAL DISPERSION AND TURBULENCE ON FORCED CONVECTION IN A COMPOSITE PARALLEL-PLATE CHANNEL: INVESTIGATION OF CONSTANT WALL HEAT FLUX AND CONSTANT WALL TEMPERATURE CASES

ABSTRACT

In this chapter, a composite parallel-plate channel whose central portion is occupied by a clear fluid and whose peripheral portion is occupied by a fluid saturated porous medium is considered. The flow in the porous region of the channel is assumed to be laminar, governed by the Brinkma-Forchheimer-extended Darcy equation, while the flow in the clear fluid region of the channel is assumed to be turbulent. The validity of this laminar/turbulent assumption is validated by estimating Reynolds numbers in the clear fluid and porous regions of the channel. Although the flow in the porous region remains laminar, it is still fast enough for the quadratic drag (Forchheimer) effects to be important. In this situation, hydrodynamic mixing of the interstitial fluid at the pore scale becomes important, and may cause significant thermal dispersion. It is shown that thermal dispersion may result in some counter-intuitive effects, such as the increase of the Nusselt number when the width of the clear fluid region in the center of the channel is decreased.

Nomenclature

a_f fluid thermal diffusivity, m^2/s

a_T eddy diffusivity of heat, m^2/s

A^+ Van Driest coefficient, defined in equation (2.9)

c_F Forchheimer coefficient

C dimensionless experimental constant in the correlation for thermal dispersion

d_p average diameter of porous particle, m

Da Darcy number

F_{Kleb} Klebanoff intermittency function, defined in equation (2.7)

h heat transfer coefficient, W/m^2K

k_{eff} effective thermal conductivity of the porous medium, W/mK

k_f fluid thermal conductivity, W/mK

k_m stagnant thermal conductivity of the porous medium, W/mK

Nu Nusselt number, $h2R/k_f$

p pressure, Pa

Pr Prandtl number, ν_f/a_f

Pr_t turbulent Prandtl number, ν_T/a_T

q''_W wall heat flux, W/m^2

r transverse coordinate, m

r^+ dimensionless transverse coordinate, $u_\tau r/\nu_f$

R half parallel plates separation distance, m

R^+ dimensionless half parallel plates separation distance, $u_\tau R/\nu_f$

$Re_{2\xi R}$ Reynolds number based on the width of the clear fluid region and the mean velocity in this region

Re_K Reynolds number for the flow in the porous region based on $K^{1/2}$

Re_p Reynolds number based on the average particle diameter and the friction velocity at the porous/fluid interface, $u_\tau d_p / \nu_f$

T temperature, K

T_m mean flow temperature, K

T_W wall temperature, K

u longitudinal velocity, m/s

u^+ dimensionless velocity, u / u_τ

u_τ friction velocity at the porous/fluid interface, $(\tau_i / \rho_f)^{1/2}$, m/s

U_m^+ dimensionless mean flow velocity in the channel

y^+ dimensionless distance from the porous/fluid interface, $\xi R^+ - r^+$

y_m^+ the smallest dimensionless distance from the interface for which $\mu_{T_i} = \mu_{T_o}$

Greek symbols

α_T closure coefficient in Cebeci-Smith model, defined in equation (2.9)

β dimensionless adjustable coefficient in the matching condition for the shear stress at the porous/fluid interface

θ dimensionless temperature for the constant wall heat flux case,

$(1/\mathrm{Nu})(T - T_W)/(T_m - T_W)$

κ von Karman constant, defined in equation (2.9)

μ_{eff} effective viscosity of porous medium, kg/ms

μ_f fluid viscosity, kg/ms

μ_T eddy viscosity, kg/ms

μ_T^+ dimensionless eddy viscosity, μ_T/μ_f

μ_{T_i} dimensionless eddy viscosity in the inner layer

μ_{T_o} dimensionless eddy viscosity in the outer layer

ν_f fluid kinematic viscosity, m^2/s

ν_T eddy diffusivity of momentum, m^2/s

ξ dimensionless position of the interface

ρ_f fluid density, kg/m^3

τ_i shear stress at the porous/fluid interface, N/m^2

ϕ dimensionless temperature for the constant wall temperature case,

$(T - T_W)/(T_m - T_W)$

2.1 INTRODUCTION

Modeling of turbulent flows in porous media has been addressed in numerous publications (Pedras and de Lemos [1-3], Antohe and Lage [4], Nakayama and Kuwahara [5], Kuwahara et al. [6], Nield [7], and Masuka and Takatsu [8]). In a domain completely filled with a fluid saturated porous medium the flow may become turbulent, once the appropriately defined Reynolds number (for example, Re_K , which is based on the square root of permeability as the length scale) becomes larger than its critical value. However, in composite porous/fluid domains the situation may be different. Results of Antohe and Lage [4] and Prakash et al. [9, 10] indicate that the effect of the porous medium is to dampen turbulence. This occurs because of the friction between the fluid and the porous matrix. Also, porous matrix imposes heavy restrictions on the size of turbulent eddies in the porous region. Therefore, if permeability of the porous medium is sufficiently small, even if the flow in the clear fluid region is turbulent, the flow in the porous region may still remain laminar. Later in this chapter, this hypothesis will be verified by computing Reynolds numbers for the clear fluid and porous regions and comparing them with their critical values.

Even if the flow in the porous region remains laminar, the filtration velocity may still be large enough for the quadratic drag (Forchheimer) effect to be important. Therefore, momentum transport in the porous region is described utilizing the Brinkman-Forchheimer-extended Darcy equation (the utilization of the Brinkman extension is important to retain the continuity of the filtration velocity at the porous/fluid interface and to impose the no-slip boundary condition at the solid wall). If filtration velocity is large enough for the Forchheimer term to be important in the momentum equation, the energy equation must account for the additional heat transfer in the porous medium due to the hydrodynamic

mixing of the interstitial fluid at the pore scale. This effect is called thermal dispersion (Nield and Bejan [11]).

Thermal dispersion results in apparent increase of thermal conductivity of the porous medium. Amiri and Vafai [12, 13] suggested accounting for thermal dispersion by assuming that the effective thermal conductivity consists of the stagnant and the dispersion conductivity. Strictly speaking, for a two-dimensional flow in an isotropic porous medium, it is necessary to consider effects of thermal dispersion on heat transfer in both longitudinal and transverse directions. However, Plumb [14] assumed that the longitudinal thermal dispersion coefficient was negligible and the transverse coefficient was proportional to the streamwise velocity component. According to Amiri and Vafai [12, 13] who constructed their correlation based on experimental findings of Wakao and Kaguei [15], the effective thermal conductivity in the transverse direction, k_{eff}, can be expressed as:

$$k_{eff} = k_m + C k_f \, Pr \frac{\rho_f u d_p}{\mu_f} \qquad (2.1)$$

where the stagnant thermal conductivity of the porous matrix, k_m, can be approximated by the following equation:

$$k_m = \varepsilon k_f + (1-\varepsilon) k_s \qquad (2.2)$$

In equations (2.1) and (2.2) C is the dimensionless experimental constant, which according to Wakao and Kaguei [15] equals to 0.1 for the transverse dispersion; d_p is the average diameter of a porous particle; k_f is the thermal conductivity of the fluid phase; k_s is the thermal conductivity of the solid phase; Pr is the Prandtl number, $\mu_f c_f / k_f$; c_f is the specific

heat of the fluid; u is the filtration velocity; ε is the porosity; μ_f is the dynamic viscosity of the fluid; and ρ_f is the density of the fluid.

It should be noted that despite considerable number of publications addressing forced convection in composite channels (Poulikakos and Kazmierczak [16], Vafai and Thiyagaraja [17], Kuznetsov [18], and many others), previous work in this area addressed only the laminar flow case. This chapter investigates the interaction between turbulent flow in the clear fluid region of the channel and laminar non-Darcian flow in the porous region. Special consideration is given to the effect of thermal dispersion in the porous medium. It is shown that although the flow in the porous region remains laminar, thermal dispersion may have a dramatic impact on heat transfer in the channel.

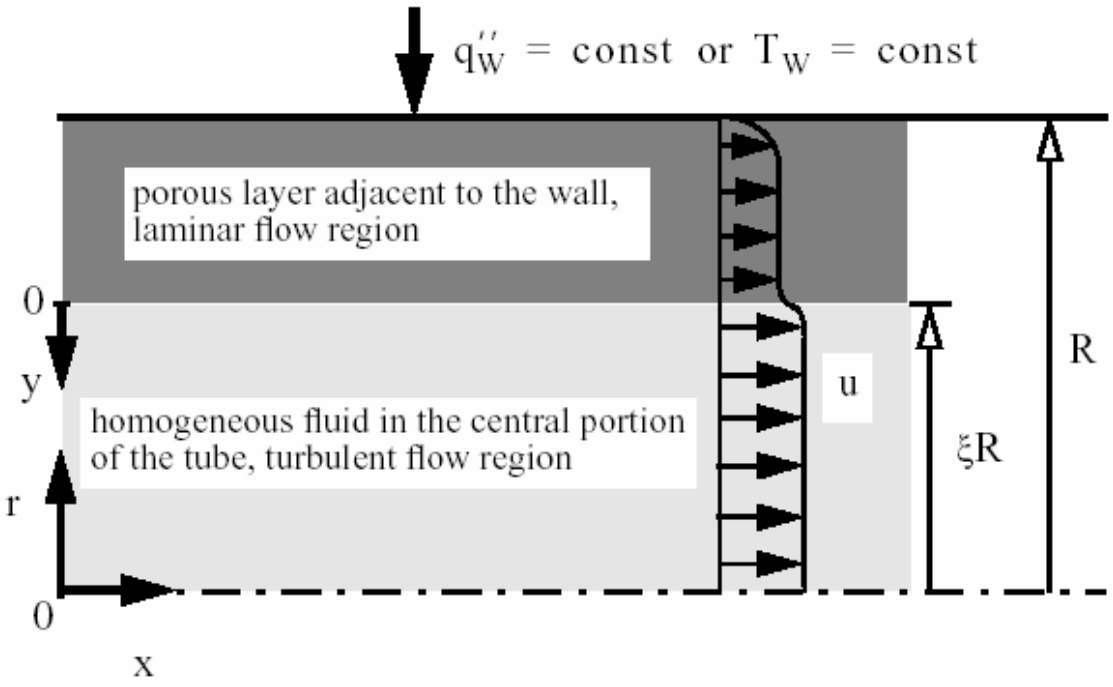

Figure 2.1 Schematic diagram of the composite parallel-plate channel

Figure 2.1 displays a schematic diagram of the problem considered in this chapter. Homogeneous fluid occupies the central portion of the parallel plate channel, $0 \le r \le \xi R$. The peripheral part of the channel, $\xi R \le r \le R$, is occupied by an isotropic fluid saturated porous medium of uniform porosity. Two cases of thermal boundary condition are considered: a constant wall heat flux, q''_W, and a constant wall temperature, T_W. The flow is assumed hydrodynamically and thermally fully developed.

2.2 MOMENTUM TRANSPORT IN THE CHANNEL

The flow domain is divided into two regions, the clear fluid region, where the flow is turbulent, and the porous region, where the flow is laminar. For the clear fluid region, the two-layer algebraic turbulence model suggested by Cebeci and Smith (Cebeci and Smith [19], Wilcox [20]) is utilized. According to this model, the velocity distribution in the clear fluid region, $0 \le r \le \xi R$, is computed from the following equation:

$$\frac{du^+}{dy^+} = \frac{1}{1+\mu_T^+}\left(1-\frac{y^+}{\xi R^+}\right) \qquad (2.3)$$

where u^+ is the dimensionless velocity, u/u_τ; u is the longitudinal velocity; u_τ is the friction velocity at the porous/fluid interface, $\sqrt{\tau_i/\rho_f}$; τ_i is the shear stress at the porous/fluid interface (at $r = \xi R$); R^+ is the dimensionless half separation distance between the parallel plates, $u_\tau R/\nu_f$; R is the half separation distance between the parallel plates; ν_f is the fluid kinematic viscosity; y^+ is the dimensionless distance from the porous/fluid interface, $\xi R^+ - r^+$; r^+ is the dimensionless transverse coordinate, $u_\tau r/\nu_f$; r is the

transverse coordinate; μ_T^+ is the dimensionless eddy viscosity, μ_T / μ_f; and μ_T is the eddy viscosity.

According to the Cebeci-Smith model [19, 20], the turbulent flow domain is divided into two layers, the inner layer ($0 \le y^+ \le y_m^+$) and the outer layer ($y^+ > y_m^+$), and dimensionless eddy viscosity is computed as:

$$\mu_T^+ = \begin{cases} \mu_{T_i}^+ & \text{for } y^+ \le y_m^+ \\ \mu_{T_o}^+ & \text{for } y^+ > y_m^+ \end{cases} \qquad (2.4)$$

where y_m^+ is the smallest value for which $\mu_{T_i} = \mu_{T_o}$. The value of dimensionless eddy viscosity in the inner layer, $\mu_{T_i}^+$, is computed according to the following equation:

$$\mu_{Ti}^+ = \left(\kappa y^+\right)^2 \left[1 - \exp\left(-y^+ / A^+\right)\right]^2 \left|du^+ / dy^+\right| \qquad (2.5)$$

and the value of dimensionless eddy viscosity in the outer layer, $\mu_{T_o}^+$, is computed as:

$$\mu_{To}^+ = \alpha_T U_c^+ \delta_v^+ F_{Kleb} \qquad (2.6)$$

where U_c^+ is the dimensionless centerline velocity, $\left(u\big|_{r=0}\right) / u_\tau$; F_{Kleb} is the Klebanoff intermittency function:

$$F_{Kleb} = \left[1 + 5.5\left[y^+ / \left(\xi R^+\right)\right]^6\right]^{-1} \qquad (2.7)$$

and δ_v^+ is the dimensionless velocity thickness:

$$\delta_v^+ = \int_0^{\xi R^+} \left(1 - u^+ / U_c^+\right) dy^+ \qquad (2.8)$$

The closure coefficients for the Cebeci-Smith model are:

$$\kappa = 0.40,\ \alpha_T = 0.0168,\ A^+ = 26 \qquad (2.9)$$

In the traditional formulation of the Cebeci-Smith model, the value of the Van Driest's coefficient, A^+, is corrected to account for the effect of pressure gradient [20]. However, because it is assumed that the flow occurs under favorable pressure gradient, dp/dx<0, this correction to the value of A^+ is not utilized here.

In the porous region, $\xi R^+ \le r^+ \le R^+$, the Brinkman-Forchheimer extension of the Darcy law (Nield and Bejan, [11]) is utilized. Utilizing the dimensionless variables defined above, this equation can be presented as:

$$\frac{1}{\xi R^+} + \left(\frac{\mu_{eff}}{\mu_f}\right)\frac{d^2u^+}{\left(dr^+\right)^2} - \frac{u^+}{Da\left(R^+\right)^2} - \frac{c_F}{Da^{1/2}R^+}\left(u^+\right)^2 = 0 \qquad (2.10)$$

where c_F is the Forchheimer coefficient; Da is the Darcy number, K/R^2; and μ_{eff} is the effective viscosity in the porous region.

At the walls of the channel the no-slip boundary condition is utilized:

$$u^+\Big|_{r^+=R^+} = 0 \qquad (2.11)$$

From the definition of u^+ and r^+ it follows that at the porous/fluid interface:

$$\left.\frac{\partial u^+}{\partial r^+}\right|_{r^+=\xi R^+-0} = -1 \qquad (2.12)$$

To match the laminar velocity in the porous region with the turbulent velocity in the clear fluid region at the porous/fluid interface the boundary conditions suggested by Ochoa-Tapia and Whitaker [21, 22] are utilized:

$$u^+\Big|_{r^+=R^++0} = u^+\Big|_{r^+=R^+-0} = u_i^+, \quad \left(\frac{\mu_{eff}}{\mu_f}\right)\left.\frac{\partial u^+}{\partial r^+}\right|_{r^+=\xi R^++0} - \left.\frac{\partial u^+}{\partial r^+}\right|_{r^+=\xi R^+-0} = \frac{\beta u_i^+}{Da^{1/2}R^+} \qquad (2.13a,b)$$

where u_i^+ is the dimensionless velocity at the porous/fluid interface, u_i / u_τ; and β is the dimensionless adjustable coefficient. Equation (2.13b) represents the jump in the shear stress condition derived in [21, 22]. In refs. [21, 22] a laminar flow in both clear fluid and porous regions was assumed. However, according to the Cebeci-Smith model (equation (2.3)) the dimensionless eddy viscosity, μ_T^+, is equal to zero at the porous/fluid interface. Therefore, equations (2.13a,b) are still valid.

The major assumption made in this research is that the flow in the clear fluid region is turbulent while the flow in the porous region is laminar. To prove that this assumption is valid it is necessary to estimate Reynolds numbers in the clear fluid and porous regions and compare them with their critical values.

The Reynolds number based on the width of the clear fluid region, $2\xi R$, and the mean velocity in this region, $(U_m)_{hom\,fl}$, is defined as:

$$Re_{2\xi R} = (U_m)_{hom\,fl} 2\xi R / \nu_f = U_m^+ 2\xi R^+ \qquad (2.14)$$

where $(U_m^+)_{hom\,fl}$ is the dimensionless mean velocity in the clear fluid region, $(U_m)_{hom\,fl} / u_\tau$:

$$(U_m^+)_{hom\,fl} = \frac{1}{\xi R^+} \int_0^{\xi R^+} u^+ dr^+ \qquad (2.15)$$

For the flow in a channel, the critical Reynolds number is 4×10^3.

For the porous region, the Reynolds number based on $K^{1/2}$ is defined as:

$$Re_K = v_{fil} K^{1/2} / \nu_f \qquad (2.16)$$

where K is the permeability of the porous medium.

For small values of the Darcy number, the velocity profile in the porous region consists of three regions [23], two boundary layers (one adjacent to the solid wall and the other adjacent to the porous/fluid interface) and the constant velocity region between them. In this constant velocity region second term in equation (2.10) is negligible, and velocity can be obtained by solving a simple quadratic equation as:

$$u^{+}_{bulk} = -\frac{1}{2c_F Da^{1/2} R^{+}} + \left[\left(\frac{1}{2c_F Da^{1/2} R^{+}} \right)^2 + \frac{Da^{1/2}}{c_F \xi} \right]^{1/2} \qquad (2.17)$$

Estimating filtration velocity, v_{fil}, in the bulk of the fluid region as $v_{fil} = u_\tau u^{+}_{bulk}$, equation (2.16) can be recast as:

$$Re_K = R^{+} Da^{1/2} \left\{ -\frac{1}{2c_F Da^{1/2} R^{+}} + \left[\left(\frac{1}{2c_F Da^{1/2} R^{+}} \right)^2 + \frac{Da^{1/2}}{c_F \xi} \right]^{1/2} \right\} \qquad (2.18)$$

According to Bear [24], most experiments indicate that actual turbulence in porous media occurs at values of the Reynolds number at least one order of magnitude higher than the Reynolds number at which deviation from the Darcy law is observed due to the Forchheimer (quadratic drag) effects. According to Nield and Bejan [11], transition from Darcy to Forchheimer flow regime occurs when Re_K is larger than 10. This means that the turbulent flow regime may occur in porous media if Re_K is larger than 100.

Computational results for $c_F = 0.55$, $R^{+} = 10^3$, $\beta = 0$, $\mu_{eff} / \mu_f = 1$, and $\xi = 0.6$ are given in Table 2.1. It can be seen that for all values of the Darcy number utilized in computations the value of $Re_{2\xi R}$ is much larger than the critical Reynolds number of 4×10^3. This indicates that the flow in the clear fluid region is turbulent. At the same time, Re_K is much smaller

than 100. This means that assumption that flow in the clear fluid region is turbulent and in the porous region is laminar is a reasonable one.

Table 2.1 Reynolds numbers in the clear fluid and porous regions of the channel.

Da	$Re_{2\xi R}$	Re_K
0.0001	8,874.128	1.715
0.001	9,652.916	12.965
0.01	10,788.735	76.946

2.3 HEAT TRANSFER IN THE CHANNEL

2.3.1 CONSTANT WALL HEAT FLUX

The energy equation for the clear fluid region, $0 \le r^+ \le \xi R^+$, is based on the constant turbulent Prandtl number model:

$$\frac{d}{dr^+}\left[\left(1+\mu_T^+\frac{Pr}{Pr_t}\right)\frac{d\theta}{dr^+}\right] = -\frac{1}{2\left(R^+\right)^2}\frac{u^+}{U_m^+} \qquad (2.19)$$

where a_f is the fluid thermal diffusivity, Pt_t is the turbulent Prandtl number, ν_T / a_T; a_T is the eddy diffusivity of heat; and U_m^+ is the mean fluid velocity in the channel:

$$U_m^+ = \frac{1}{R^+}\int_0^{R^+} u^+ dr^+ \qquad (2.20)$$

In Eq. (2.19), θ is the dimensionless temperature, which is defined as:

$$\theta = (1/Nu)(T - T_W)/(T_m - T_W) \qquad (2.21)$$

where T is the temperature, T_W is the wall temperature (at $r^+ = R^+$), T_m is the mean temperature in the channel:

$$T_m = \frac{1}{RU_m}\int_0^R uTdr \qquad (2.22)$$

and Nu is the Nusselt number:

$$Nu = h2R/k_f = 2Rq''/\left[k_f\left(T_W - T_m\right)\right] \qquad (2.23)$$

where h is the heat transfer coefficient.

Utilizing equation (2.1) for effective thermal conductivity of the porous medium in the transverse direction, the energy equation for the porous region, $\xi R^+ \le r^+ \le R^+$, can be presented as:

$$\frac{d}{dr^+}\left[\left(\frac{k_m}{k_f} + C\,Pr\,Re_p\,u^+\right)\frac{d\theta}{dr^+}\right] = -\frac{1}{2\left(R^+\right)^2}\frac{u^+}{U_m^+} \qquad (2.24)$$

where k_m is the stagnant thermal conductivity of the porous medium (when $u^+ = 0$) and

$Re_p = \dfrac{u_\tau d_p}{\nu_f}$ is the Reynolds number based on the average particle diameter and the friction velocity at the porous/fluid interface.

In equation (2.24), following Kaviany [25], Nakayama et al. [26], Cheng et al. [27], Vafai and Kim [28], and Nield et al. [29], the longitudinal heat conduction is neglected. This assumption can be rigorously justified for large Peclet numbers (Bejan [30]). Also, energy equation (2.24) accounts for transverse thermal dispersion, while longitudinal thermal dispersion term is neglected. This is consistent with the neglect of longitudinal conduction. If $\partial^2\theta/\partial x^2$ is negligible in comparison with $\partial^2\theta/\partial r^2$, then the contribution from longitudinal dispersion will automatically be negligible too, since it is multiplied by a negligible term.

Energy equations (2.19) and (2.24) must be solved subject to the following boundary conditions:

$$\theta\big|_{r^+=R^+} = 0\,,\ \left.\frac{\partial\theta}{\partial r^+}\right|_{r^+=0} = 0 \qquad (2.25a,b)$$

plus the continuity of the temperature and heat flux through the porous/fluid interface:

$$\theta\big|_{r^+=\xi R^+-0} = \theta\big|_{r^+=\xi R^+ +0}\,,\qquad \left.\frac{\partial\theta}{\partial r^+}\right|_{r^+=\xi R^+-0} = \frac{k_{eff}}{k_f}\left.\frac{\partial\theta}{\partial r^+}\right|_{r^+=\xi R^+ +0} \qquad (2.26a,b)$$

Finally, the Nusselt number is computed utilizing the compatibility condition (Bejan [31]), as:

$$Nu = U_m^+ R^+ \Big/ \left[\int_0^{R^+} u^+\,\theta\,dr^+\right] \qquad (2.27)$$

2.3.2 CONSTANT WALL TEMPERATURE

In this case the dimensionless temperature is redefined as:

$$\phi = \frac{T - T_W}{T_m - T_W} \qquad (2.28)$$

The dimensionless energy equation in the porous region ($\xi R^+ \le r^+ \le R^+$) is:

$$\frac{d}{dr^+}\left[\left(\frac{k_m}{k_f} + C\,Pr\,Re_p\,u^+\right)\frac{d\theta}{dr^+}\right] = -\frac{1}{2\left(R^+\right)^2}\,Nu\,\phi\,\frac{u^+}{U_m^+} \qquad (2.29)$$

The dimensionless energy equation in the clear fluid region ($0 \le r^+ \le \xi R^+$) is:

$$\frac{d}{dr^+}\left[\left(1 + \mu_T^+\,\frac{Pr}{Pr_t}\right)\frac{d\phi}{dr^+}\right] = -\frac{1}{2\left(R^+\right)^2}\,Nu\,\phi\,\frac{u^+}{U_m^+} \qquad (2.30)$$

Equations (2.29) and (2.30) must be solved subject to boundary conditions (24a, b) and (25a, b). Finally, Nusselt number can be found from the following compatibility condition:

$$\mathrm{Nu} = -2\frac{k_m}{k_f} R^+ \left.\frac{d\phi}{dr^+}\right|_{r^+=R^+} \qquad (2.31)$$

2.4 RESULTS AND DISCUSSION

Values of all parameters utilized in computations are shown directly on the figures. Unless it is specifically indicated on the figure, all computations are performed utilizing the turbulent flow model for the clear fluid region. Figure 2.2(a) displays the effect of the adjustable coefficient, β, in the matching condition for the shear stress at the porous/fluid interface (given by equation (2.11b)) on velocity profiles in the channel for two different values of the Darcy number, 10^{-2} and 10^{-3}. For all velocity profiles displayed in this figure, the Forchheimer term is accounted for ($c_F = 0.55$). According to estimations of Ochoa-Tapia and Whitaker (1995a, 1995b), β may change from minus unity to plus unity. The case of $\beta = 0$ corresponds to direct matching of the shear stress at the porous/fluid interface, while non-zero value of β implies that there is a jump in the shear stress at the interface. Compared to the case of the laminar flow in both porous and clear fluid regions, which was considered in Kuznetsov [32], the effect of β displayed in Fig. 2.2(a) is less heavy. Changing Darcy number has more heavy impact on the velocity profile than changing β. The flow structure in the porous region is also clearly seen. There are two momentum boundary layers in this region, one at the solid wall and another at the porous/fluid interface. Between the boundary layers the flow velocity remains constant, determined by the Darcy-Forchheimer equation.

Figures 2.2(b) and 2.2(c) display temperature distributions for the constant wall heat flux and constant wall temperature cases, respectively. Variation of β has almost no effect on the

temperature profiles, therefore only profiles that correspond to $\beta = 0$ are displayed. Computations are performed both accounting for the Forchheimer quadratic drag ($c_F = 0.55$) and neglecting it ($c_F = 0$). The kink at the porous/fluid interface occurs because of the thermal dispersion in the porous medium. Transverse thermal dispersion in the porous region is accounted for by increasing effective thermal conductivity in the transverse direction. This results in a large thermal conductivity in the transverse direction at the porous side of the interface. At the fluid side of the interface, turbulent effects are negligible, and the effective thermal conductivity is equal to the molecular thermal conductivity of the fluid. This explains the large kink on the temperature profile at the porous/fluid interface.

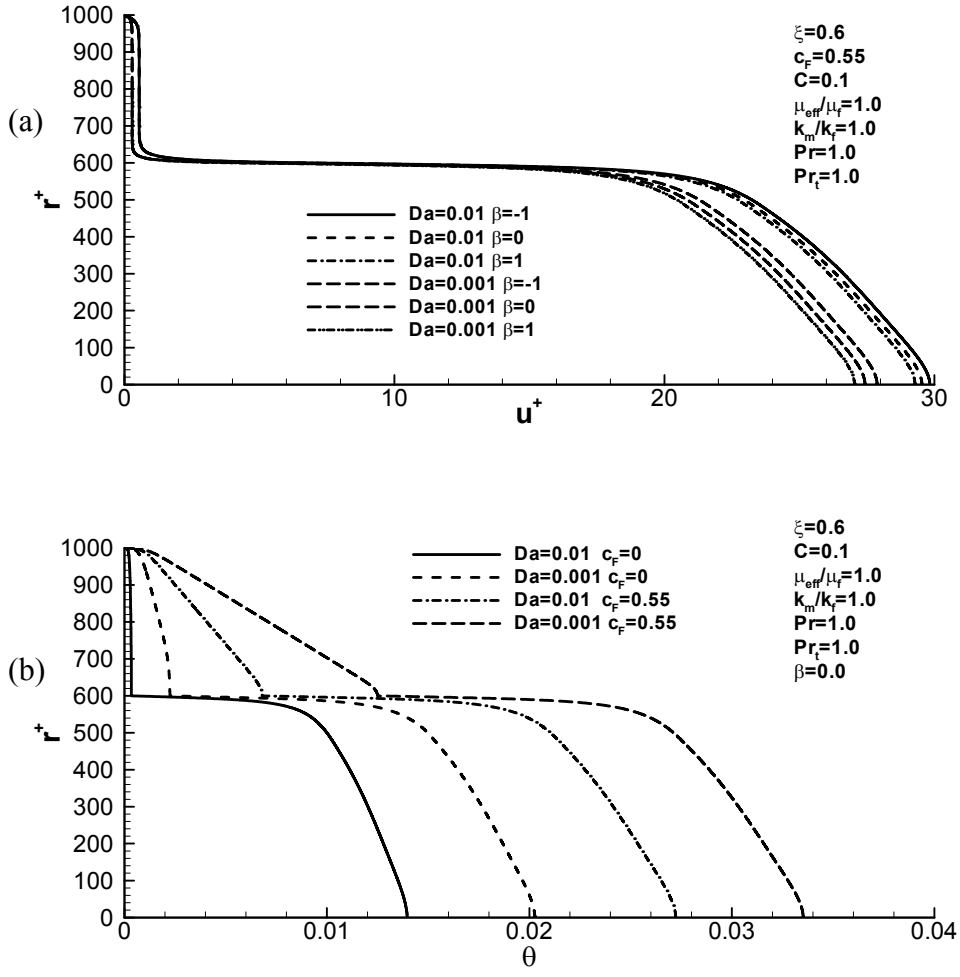

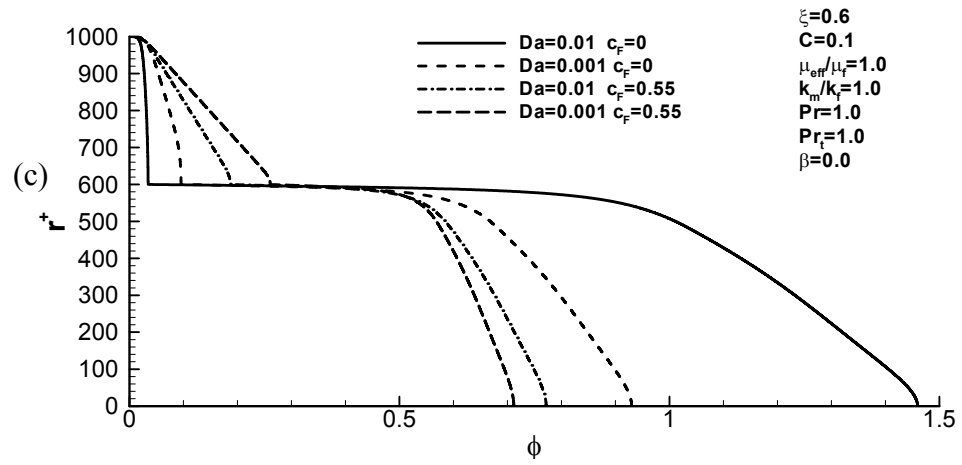

Figure 2.2 Dimensionless velocity (a) and dimensionless temperature profiles for the isoflux (b) and isothermal (c) wall cases

The effect of thermal dispersion is illuminated in Figures 2.3(a) and 2.3(b), which display profiles of the dimensionless temperature for the isoflux and isothermal wall boundary conditions, respectively. Computations are performed accounting for thermal dispersion ($C = 0.1$) and neglecting it ($C = 0$). Temperature profiles computed neglecting thermal dispersion do not have a kink at the interface. This is because computations are performed assuming that the stagnant thermal conductivity of the porous medium is equal to the fluid thermal conductivity.

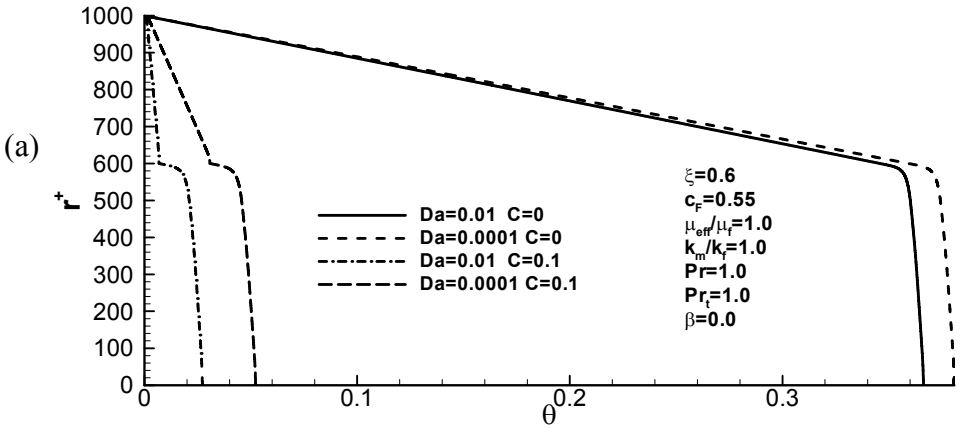

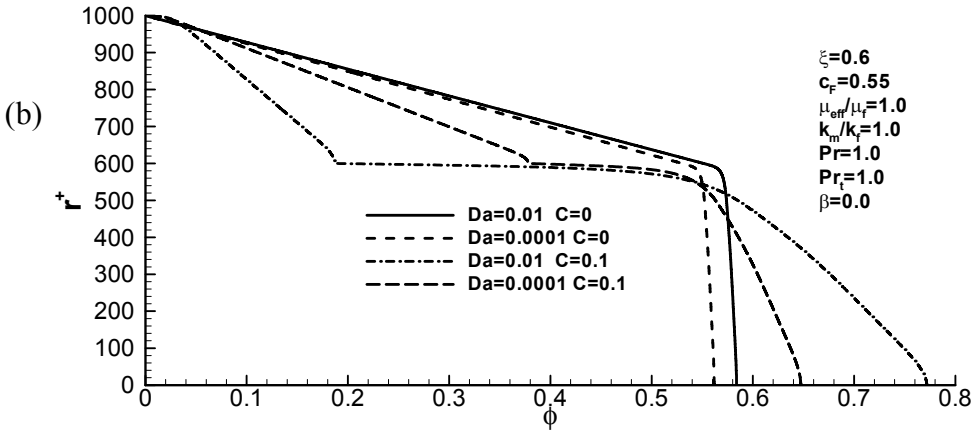

Figure 2.3 Effect of thermal dispersion on the dimensionless temperature distributions: isoflux (a) and isothermal (b) wall cases

Figures 2.4-2.6 are computed for the constant wall heat flux. Figure 2.4(a) displays the effect of the position of the fluid/porous interface on the Nusselt number. $\xi = 0$ corresponds to the channel fully occupied by the porous medium while $\xi = 1$ corresponds to the channel fully occupied by the clear fluid. At small values of ξ the behavior of the Nusselt number is quite unexpected. When ξ is smaller than 0.05 Fig. 2.4(a) shows a dramatic increase of the Nusselt number when the size of the clear fluid region in the center of the channel becomes smaller. To explain this unexpected effect, Fig. 2.5 displays velocity profiles in the channel (Fig. 2.5(a)) and the dimensionless effective thermal conductivity (Fig. 2.5(b)) computed for $\xi = 0$ and $\xi = 0.05$. Dimensionless effective thermal conductivity in the porous region is given by $k_m / k_f + C \, Pr \, Re_p \, u^+$ (cf. Eq. (2.24)) while in the clear fluid region it is given by $1 + \mu_T^+ \, Pr / Pr_t$ (cf. Eq. (2.19)). As long as the clear fluid region exists in the center of the channel ($\xi = 0.05$), fluid tends to flow through this opening instead of going through the porous layers adjacent to the walls. However, once this opening is completely closed ($\xi = 0$), the fluid is forced to go through the porous layers. Closing the clear fluid region

thus results in a dramatic increase of filtration velocity in the porous medium. According to Eq. (2.1), the increase of effective thermal conductivity due to thermal dispersion is proportional to the filtration velocity. As shown in Fig. 2.5(b), the dramatic increase of filtration velocity results in a dramatic increase of effective thermal conductivity of the porous medium, which leads to the dramatic increase in the Nusselt number.

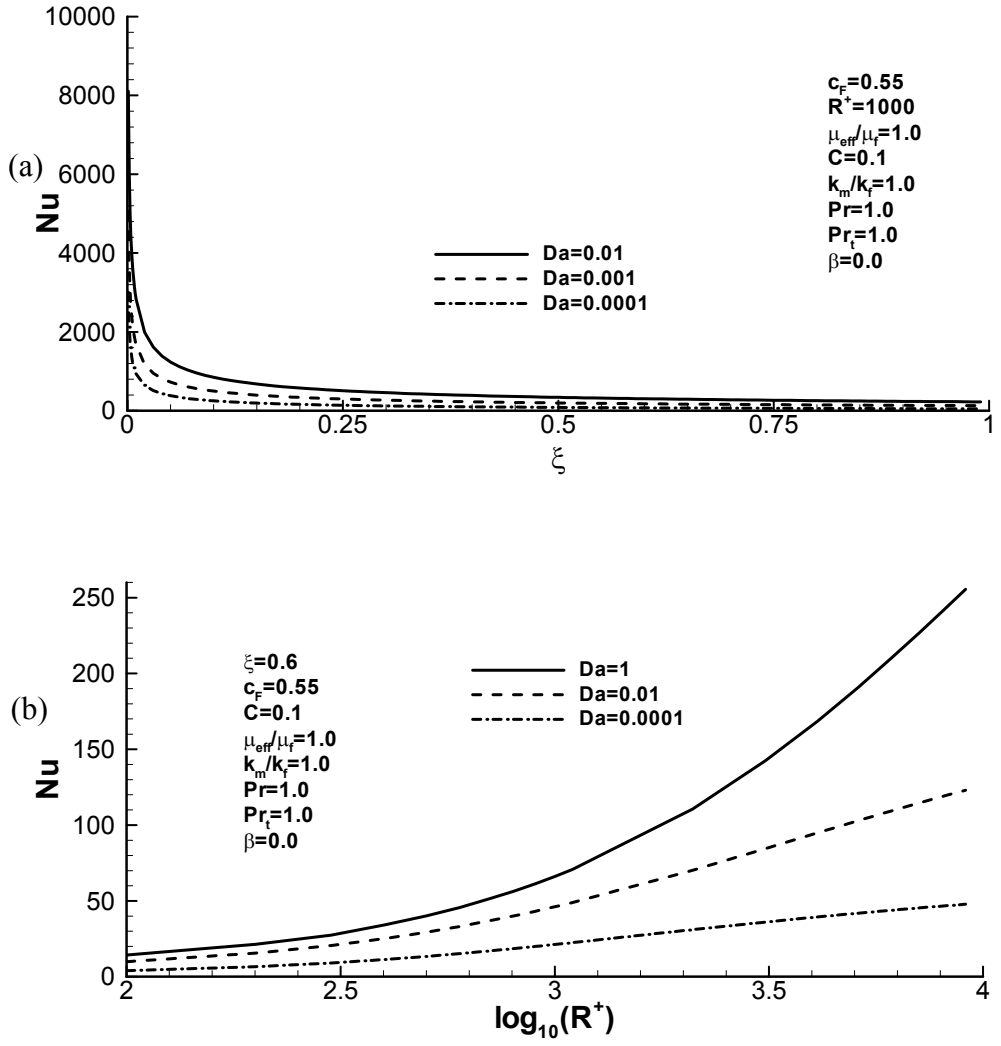

Figure 2.4 Dependence of the Nusselt number on the dimensionless position of the interface (a) and the dimensionless half width of the channel (b) for the isoflux wall case

Figure 2.4(b) displays the dependence of the Nusselt number on the dimensionless half width of the channel, R^+. R^+ can also be interpreted as the Reynolds number based on the friction velocity at the porous/fluid interface and half width of the channel. Increase of R^+ results in an increase of the Nusselt number, as expected. This increase is faster for larger value of the Darcy number.

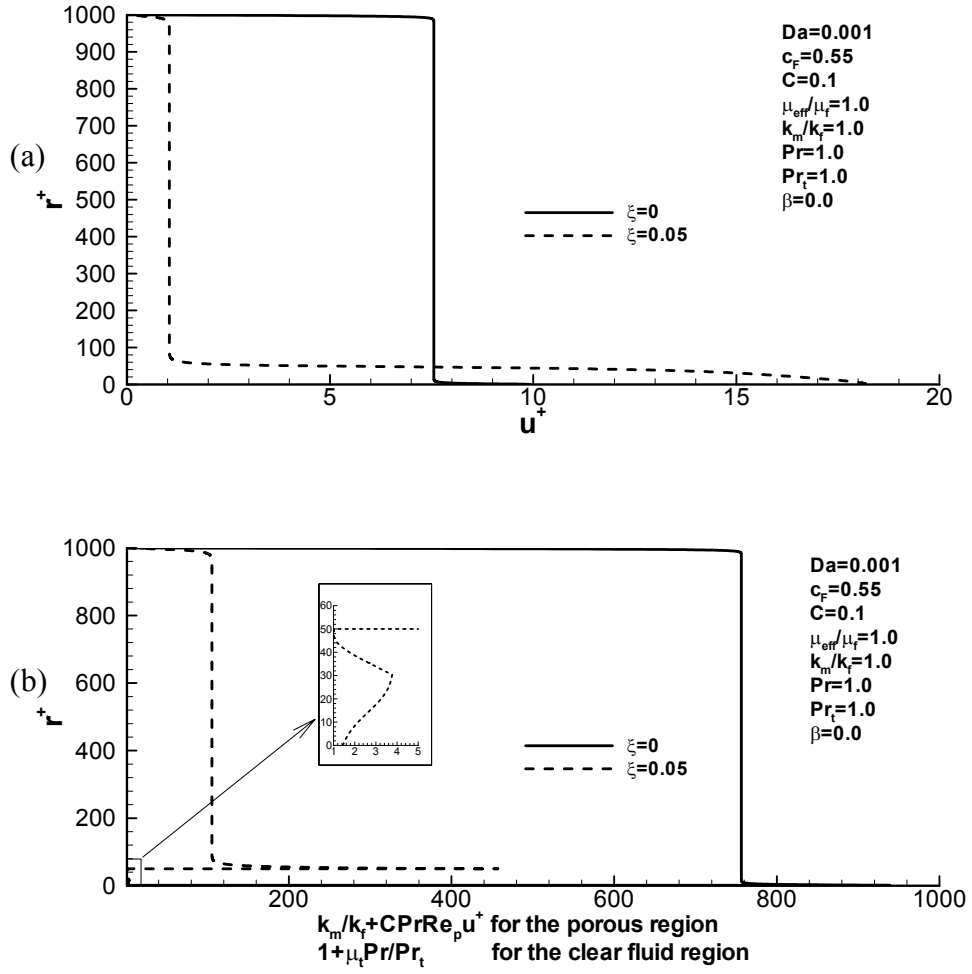

Figure 2.5 Distributions of the dimensionless velocity (a) and the dimensionless effective thermal conductivity (b) for the completely porous channel ($\xi = 0$) and for the channel with a small clear fluid opening in the center ($\xi = 0.05$)

Figure 2.6(a) displays the dependence of the Nusselt number on the Darcy number. To show the effect of turbulence in the clear fluid region, computations are performed utilizing both

turbulent and laminar flow models in the clear fluid region (computations corresponding to the laminar model are performed by setting the eddy viscosity in the clear fluid region, μ_T, to zero). For the turbulent flow case, increase of the Darcy number results in increase of the Nusselt number, while for the laminar flow case, the Nusselt number remains almost constant. As expected, laminar flow model heavily underpredicts values of the Nusselt number. Computations displayed in Fig. 2.6(a) are performed for two cases, accounting for the Forchheimer term in the momentum equation for the porous region and neglecting it. The effect of the Forchheimer quadratic drag is to decrease the Nusselt number. This is because quadratic drag decreases filtration velocity in the porous layer and thus decreases its effective thermal conductivity (cf. Eq. (2.1)). Variation of c_F has more effect on the Nusselt number when the turbulent flow model in the clear fluid region is utilized than it does when the laminar flow model in this region is utilized.

(a)

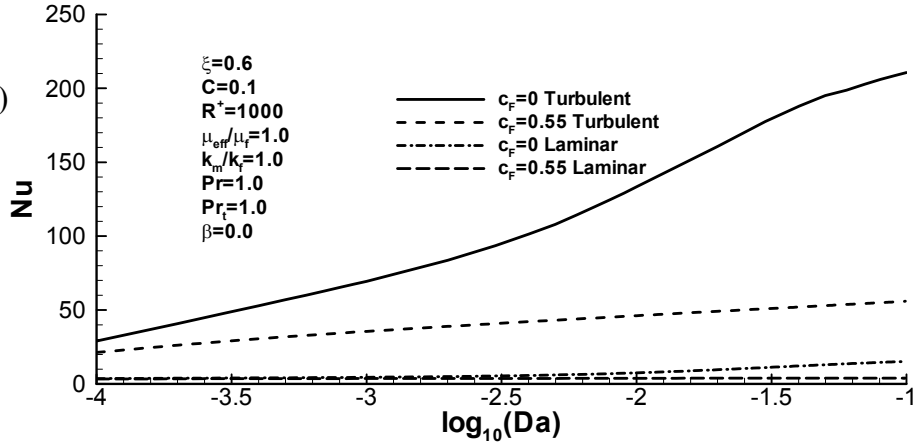

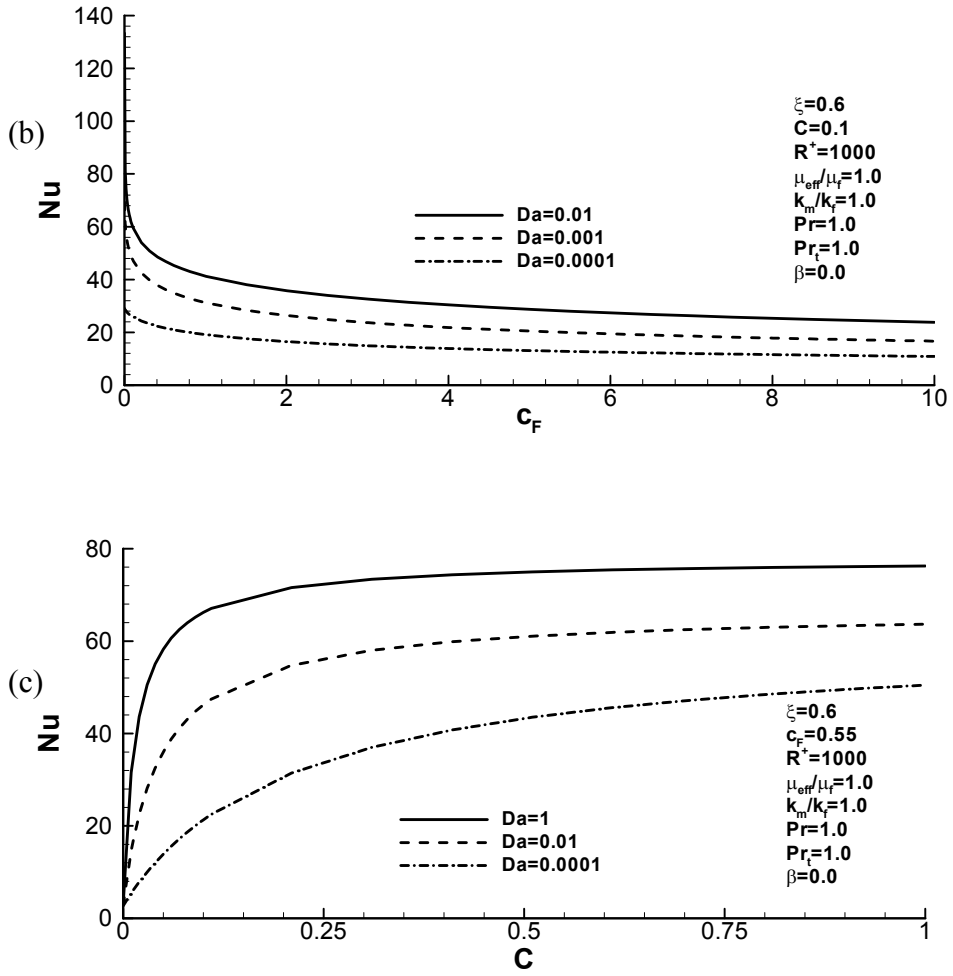

Figure 2.6 Dependence of the Nusselt number on the Darcy number (a), the Forchheimer coefficient (b), and the dimensionless experimental constant in the correlation for thermal dispersion (c) for the isoflux wall case

Figure 2.6(b) displays the dependence of the Nusselt number on the Forchheimer coefficient. The increase of the Forchheimer coefficient increases quadratic drag and therefore decreases filtration velocity. This results in a decrease of the Nusselt number.

Figure 2.6(c) displays the dependence of the Nusselt number on the dimensionless experimental constant in the correlation for thermal dispersion, C. Increase of C increases effective thermal conductivity of the porous medium and therefore increases Nusselt number.

Figures 2.7 and 2.8 are computed for the constant wall temperature. Figures 2.7(a, b) display the dependences of the Nusselt number on the dimensionless position of the porous/fluid interface, ξ, and on the dimensionless half thickness of the channel, R^+, respectively. These dependences are similar to those for the constant wall heat flux case displayed in Figs. 2.4(a, b). The major difference is that the values of the Nusselt number are slightly smaller than those for the isoflux case for the same parameter values.

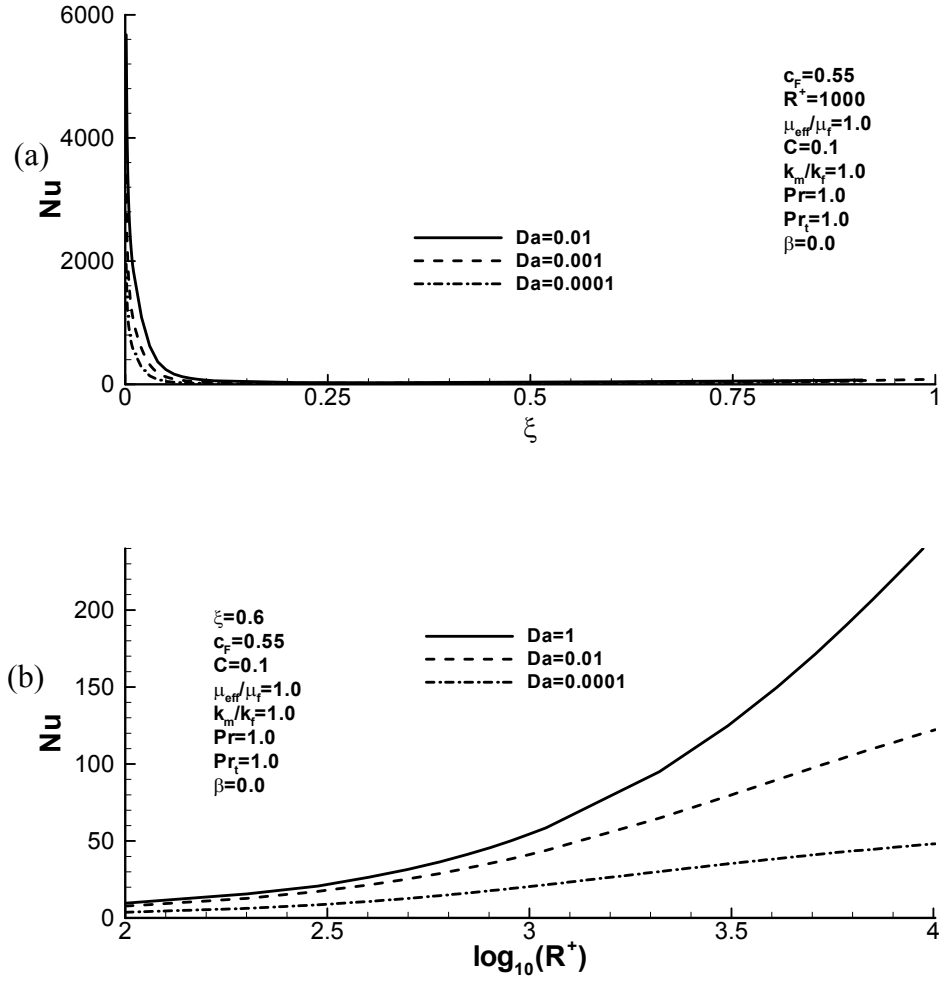

Figure 2.7 Dependence of the Nusselt number on the dimensionless position of the interface (a) and the dimensionless half width of the channel (b) for the isothermal wall case

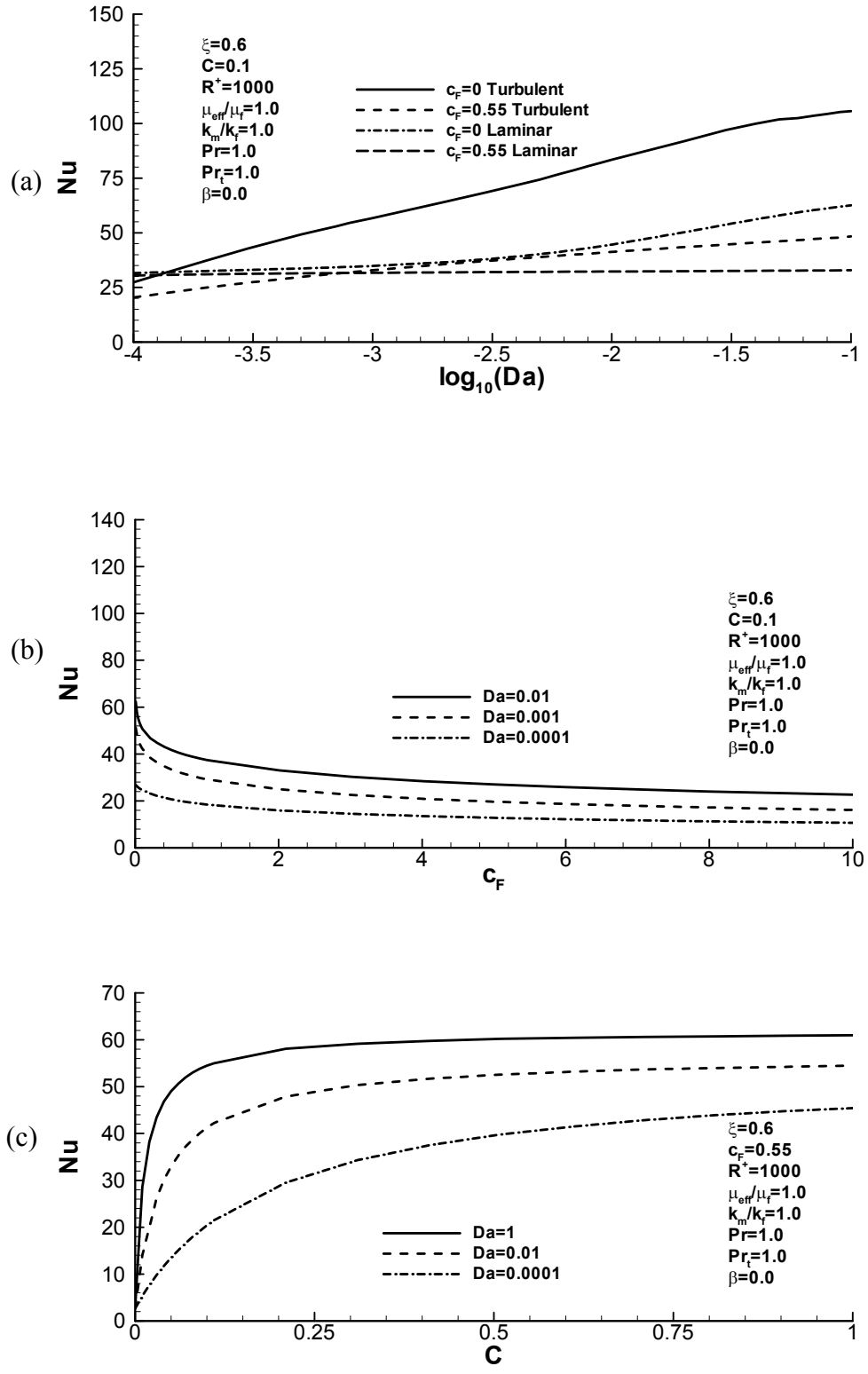

Figure 2.8 Dependence of the Nusselt number on the Darcy number (a), the Forchheimer coefficient (b), and the dimensionless experimental constant in the correlation for thermal dispersion (c) for the isothermal wall case

Figures 2.8(a, b, c) display the dependences of the Nusselt number on the Darcy number, Da, the Forchheimer coefficient, c_F , and the dimensionless experimental constant in the correlation for thermal dispersion, C, respectively. These dependencies are similar to the corresponding dependencies for the constant wall heat flux case displayed in Figs. 2.6(a, b, c). Again, the major difference is that that the Nusselt number is slightly smaller than the corresponding values for the constant wall heat flux case.

2.5 CONCLUSIONS

This chapter investigates the effects of thermal dispersion on forced convection heat transfer in a composite channel partly filled with a fluid saturated porous medium. Flow in the central portion of the channel occupied by the clear fluid is turbulent, while it remains laminar in two porous layers adjacent to the walls of the channel. Probably the most important conclusion of this chapter is the behavior of the Nusselt number when the width of the clear fluid region in the center of the channel is decreased. The model predicts that decreasing the size of the clear fluid opening increases the Nusselt number. This counter-intuitive result is explained by the effect of thermal dispersion. Closing the clear fluid region forces more fluid to flow through porous layers adjacent to the walls of the channel. This increases filtration velocity. According to the model utilized in this research, the increase of transverse thermal conductivity due to thermal dispersion is proportional to the filtration velocity. Therefore, closing the clear fluid region causes the increase of effective thermal conductivity of the porous medium, which increases the Nusselt number.

REFERENCES

1. Pedras, M.H.J. and de Lemos, M.J.S. (2001) Macroscopic turbulence modeling for incompressible flow through undeformable porous media, *International Journal of Heat and Mass Transfer*, 44: 1081-1093.

2. Pedras, M.H.J. and de Lemos, M.J.S.(2001) Simulation of turbulent flow in porous media using a spatially periodic array and a low Re two-equation closure, *Numerical Heat Transfer, Part A*, 39: 35-59.

3. Pedras, M.H.J. and de Lemos, M.J.S. (2000) On the definition of turbulent kinetic energy for flow in porous media., *International Communications in Heat and Mass Transfer*, 27: 211-220.

4. Antohe, B.V. and Lage, J.L.(1997) A general two-equation macroscopic model for incompressible flow in porous media, *International Journal of Heat and Mass Transfer*, 40: 3013-3024.

5. Nakayama, A. and Kuwahara, F.(1999) A macroscopic turbulence model for flow in a porous medium, *ASME Journal of Fluids Engineering*, 121: 427-433.

6. Kuwahara, F., Kameyama, Y., Yamashita, S. and Nakayama, A.(1998) Numerical modeling of turbulent flow in porous media using a spatially periodic array, *Journal of Porous Media*, 1: 47-55.

7. Nield, D.A.(1997) Turbulence model for flow through porous media – Comments, *International Journal of Heat and Mass Transfer*, 40: 2499-2499.

8. Masuoka, T. and Takatsu, Y. (1996) Turbulence model for flow through porous media, *International Journal of Heat and Mass Transfer*, 39: 2803-2809.

9. Prakash, M., Turan, O.F., Li, Y.G., Mahoney, J. and Thorpe, G.R. (2001) Impinging round jet studies in a cylindrical enclosure with and without a porous layer: Part I – Flow visualizations and simulations, *Chemical Engineering Science*, 56: 3855-3878.

10. Prakash, M., Turan, O.F., Li, Y.G., Mahoney, J., and Thorpe, G.R.(2001) Impinging round jet studies in a cylindrical enclosure with and without a porous layer: Part II – LDV measurements and simulations, *Chemical Engineering Science*, 56: 3879-3892.

11. Nield, D.A. and Bejan, A. (1999) *Convection in Porous Media*, 2nd ed., Springer, New York.

12. Amiri, A. and Vafai, K. (1998) Transient analysis of incompressible flow through a packed bed, *Int. J. Heat Mass Transfer*, 41: 4259-4279.

13. Amiri, A. and Vafai, K. (1994) Analysis of dispersion effects and non-thermal equilibrium, non-Darcian, variable porosity incompressible flow through porous media, *Int. J. Heat Mass Transfer*, 37: 939-954.

14. Plumb, O.A. (1983) The effect of thermal dispersion on heat transfer in packed bed boundary layers, *Proceedings of ASME JSME Thermal Engineering Joint Conference*, 2: 17-22.

15. Wakao, N. and Kaguei, S. (1982) *Heat and Mass Transfer in Packed Beds*, Gordon and Breach, New York.

16. Poulikakos, D. and Kazmierczak, M. (1987) Forced convection in a duct partially filled with a porous material, *ASME Journal of Heat Transfer*, 109: 563-662.

17. Vafai, K. and Thiyagaraja, R. (1987) Analysis of flow and heat transfer at the interface region of a porous medium, *International Journal of Heat and Mass Transfer*, 30: 1391-1405.

18. Kuznetsov, A.V. (2000) Analytical studies of forced convection in partly porous configurations, *Handbook of Porous Media*, edited by K. Vafai, Marcel Dekker, New York, pp. 269-312.

19. Cebeci, T. and Smith, A.M.O. (1974) *Analysis of Turbulent Boundary Layers*, Ser. in Appl. Math & Mech., Vol. XV, Academic Press, New York.

20. Wilcox, D.C. (1994) *Turbulence Modeling for CFD*, DCW Industries, La Canada, CA.

21. Ochoa-Tapia, J.A. and Whitaker, S. (1995) Momentum transfer at the boundary between a porous medium and a homogeneous fluid - I. Theoretical development, *International Journal of Heat and Mass Transfer*, 38: 2635-2646.

22. Ochoa-Tapia, J.A. and Whitaker, S. (1995) Momentum transfer at the boundary between a porous medium and a homogeneous fluid - II. Comparison with experiment, *International Journal of Heat and Mass Transfer*, 38: 2647-2655.

23. Kuznetsov, A.V. (1998) Analytical study of fluid flow and heat transfer during forced convection in a composite channel partly filled with a Brinkman-Forchheimer porous medium, *Flow, Turbulence and Combustion*, 60: 173-192.

24. Bear, J. (1988) *Dynamics of Fluids in Porous Media*, Elsevier, New York, 1972 [corrected reprint, Dover, New York.

25. Kaviany, M. (1985) Laminar flow through a porous channel bounded by isothermal parallel plates, *International Journal of Heat and Mass Transfer*, 28: 851-858,.

26. Nakayama, A., Koyama, H. and F. Kuwahara (1988) An analysis on forced convection in a channel filled with a Brinkman-Darcy porous medium: Exact and approximate solutions, *Wärme- und Stoffübertragung*, 23: 291-295.

27. Cheng, P., Hsu, C.T. and Chowdhury, A. (1988) Forced convection in the entrance region of a packed channel with asymmetric heating, *ASME Journal of Heat Transfer*, 110: 946-954.

28. Vafai, K. and Kim, S.J. (1989) Forced convection in a channel filled with a porous medium: An exact solution, *ASME Journal of Heat Transfer*, 111: 1103-1106.

29. Nield, D.A., Junqueira, S.L.M. and Lage, J.L. (1996) Forced convection in a fluid saturated porous medium channel with isothermal or isoflux boundaries, *Journal of Fluid Mechanics*, 322: 201-214.

30. Bejan, A. (1995) *Convection Heat Transfer*, 2nd ed., Wiley, New York.

31. Bejan, A. (1993) *Heat Transfer*, Wiley, New York.

32. Kuznetsov, A.V. (1996) Analytical investigation of the fluid flow in the interface region between a porous medium and a clear fluid in channels partially filled with a porous medium, *Applied Scientific Research*, 56: 53-67.

3 INVESTIGATION OF TURBULENCE EFFECTS ON FORCED CONVECTION IN A COMPOSITE POROUS/FLUID DUCT: CONSTANT WALL FLUX AND CONSTANT WALL TEMPERATURE CASES

ABSTRACT

Forced convection heat transfer in composite porous/fluid domains is of great practical and theoretical significance. However, research in this area traditionally addressed only the laminar flow case in both homogeneous fluid and porous regions of the domain. This chapter investigates the interaction between turbulent flow in the center of a circular tube filled with a homogeneous fluid and laminar flow in the porous layer adjacent to the tube wall. A two-layer algebraic turbulence model suggested by Cebeci and Smith is utilized for the flow in the central region of the tube. The effects of turbulence in the central region on velocity and temperature distributions as well as on the Nusselt number are analyzed.

List of symbols

a_f fluid thermal diffusivity, m^2/s

a_T eddy diffusivity of heat, m^2/s

A^+ Van Driest coefficient, defined in equation (3.7)

c_F Forchheimer coefficient

Da Darcy number

F_{Kleb} Klebanoff intermittency function, defined in equation (3.5)

h heat transfer coefficient, W/m^2K

k_f fluid thermal conductivity, W/mK

k_{eff} effective thermal conductivity of porous medium, W/mK

Nu Nusselt number, $h2R/k_f$

p pressure, Pa

Pr Prandtl number, ν_f / a_f

Pr_t turbulent Prandtl number, ν_T / a_T

q''_W wall heat flux, W/m^2

r radial coordinate, m

r^+ dimensionless radial coordinate, $u_\tau r/\nu_f$

R duct radius, m

R^+ dimensionless radius of the duct, $u_\tau R/\nu_f$

$Re_{2\xi R}$ Reynolds number based on the diameter of the homogeneous fluid region and the mean velocity in this region

T temperature, K

T_m mean flow temperature, K

T_W wall temperature, K

u longitudinal velocity, m/s

u^+ dimensionless velocity, u/u_τ

u_τ friction velocity at the porous/fluid interface, $(\tau_i / \rho_f)^{1/2}$, m/s

U_m^+ dimensionless mean flow velocity in the duct

y^+ dimensionless distance from the porous/fluid interface, $\xi R^+ - r^+$

y_m^+ the smallest dimensionless distance from the interface for which $\mu_{T_i} = \mu_{T_o}$

Greek symbols

α_T closure coefficient in the Cebeci-Smith model, defined in equation (3.7)

β dimensionless adjustable coefficient in the matching condition for the shear stress at the porous/fluid interface

θ dimensionless temperature for the constant wall heat flux case, $(1/Nu)(T - T_W)/(T_m - T_W)$

κ von Karman constant, defined in equation (3.7)

μ_{eff} effective viscosity of porous medium, kg/ms

μ_f fluid viscosity, kg/ms

μ_T eddy viscosity, kg/ms

μ_T^+ dimensionless eddy viscosity, μ_T / μ_f

μ_{T_i} dimensionless eddy viscosity in the inner layer

μ_{T_o} dimensionless eddy viscosity in the outer layer

ν_f fluid kinematic viscosity, m^2/s

ν_T eddy diffusivity of momentum, m^2/s

ξ dimensionless position of the interface

ρ_f fluid density, kg/m^3

τ_i shear stress at the porous/fluid interface, N/m^2

ϕ dimensionless temperature for the constant wall temperature case,

$(T - T_W)/(T_m - T_W)$

3.1 INTRODUCTION

Interaction of turbulent flow in a homogeneous fluid region with flow in a porous region in a composite porous/fluid domain is of great practical interest. This problem is important in modeling solidification of binary alloys with electromagnetic stirring [1], investigation of turbulent flow near porous obstacles [2] for applications including microelectronic cooling [3], and studying the contaminant transport by air flow through forests and crops. Recent theoretical and experimental investigation by Prakash et al. [4, 5] addressed turbulent flow generated by a round water jet that impinges on a porous foam. It is established that the flow field in the fluid layer is affected by the flow in the porous medium, especially when permeability of the porous medium is high.

Despite considerable interest towards modeling of macroscopic turbulence in homogeneous porous media (Pedras and de Lemos [6-8], Antohe and Lage [9], Nakayama and Kuwahara [10], Kuwahara et al. [11], Nield [12], and Masuka and Takatsu [13]), the number of papers addressing turbulent flow in composite porous/fluid domains is very limited. Interaction

between turbulent flow in a homogeneous fluid region and laminar flow in a porous medium is a problem that is of practical interest. This chapter concentrates on the problem of forced convection in a composite circular tube, with its central part filled with a homogeneous fluid and its peripheral part filled with a fluid saturated porous medium. The effect of turbulence in the central region of the tube on heat transfer from the wall of the tube to the fluid is analyzed for two types of boundary conditions at the tube wall, constant heat flux, and constant wall temperature.

It should be noted that despite a considerable number of publications addressing forced convection in composite channels (Poulikakos and Kazmierczak [14], Vafai and Thiyagaraja [15], Kuznetsov [16], and many others), all the previous work in this area addressed only the laminar flow case. The main objective of this chapter is to investigate how turbulence in the homogeneous flow region affects the Nusselt number.

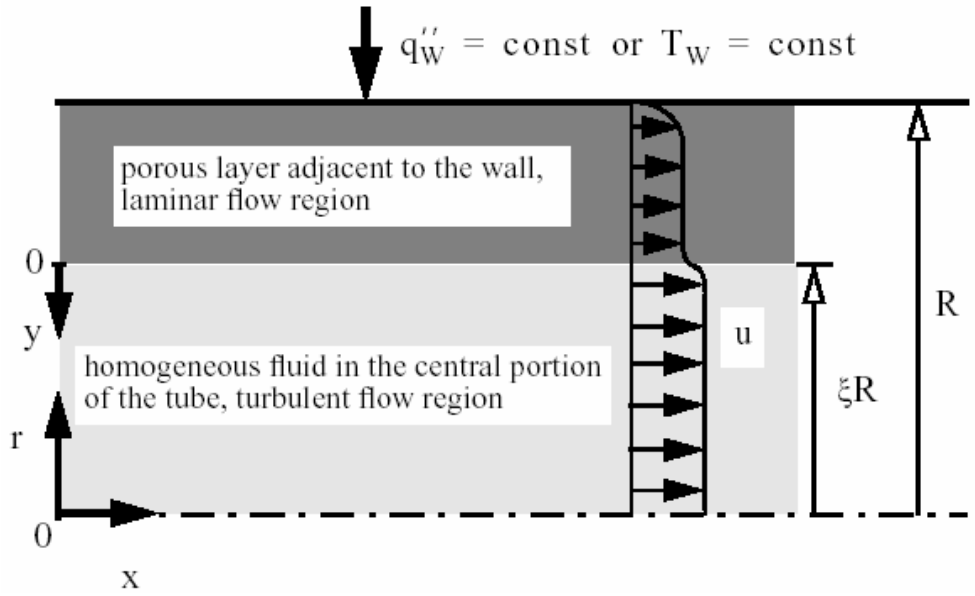

Figure 3.1 Schematic diagram of the problem

3.2 PROBLEM DESCRIPTION

A schematic diagram of the problem considered in this research is displayed in Figure 3.1. The central portion of the circular tube, $0 \le r \le \xi R$, is occupied by a homogeneous fluid while its peripheral part, $\xi R \le r \le R$, is occupied by an isotropic porous medium of uniform porosity. The wall of the tube is subjected to either a constant heat flux, q''_W, or a constant wall temperature, T_W. The flow is assumed to be hydrodynamically and thermally fully developed. The investigation carried out in this chapter is based on the assumption that the flow in the homogeneous fluid region is turbulent while the flow in the porous layer adjacent to the wall is laminar. From a physical standpoint, this is a good assumption if permeability of the porous layer is small. Indeed, previous results of turbulence modeling [4, 9] indicated that porous medium dampens turbulence. Therefore, if permeability of a porous medium is sufficiently small, then true turbulence, in which there is a cascade of energy from large eddies to smaller eddies, cannot develop in the porous region.

3.3 HYDRODYNAMIC PROBLEM IN THE COMPOSITE CHANNEL

As mentioned above, the flow domain is divided into two regions, the homogeneous fluid region, where the flow is turbulent, and the porous region, where the flow is laminar. The momentum equation for the homogeneous fluid region is based on a two-layer algebraic turbulence model suggested by Cebeci and Smith (Cebeci and Smith [17], Wilcox [18]). According to this model, the velocity distribution in the homogeneous fluid region, $0 \le r \le \xi R$, is computed from the following equation:

$$\frac{du^+}{dy^+} = \frac{1}{1+\mu_T^+}\left(1-\frac{y^+}{\xi R^+}\right) \qquad (3.1)$$

where u^+ is the dimensionless velocity, u/u_τ; u is the longitudinal velocity; u_τ is the friction velocity at the porous/fluid interface, $\sqrt{\tau_i/\rho_f}$; τ_i is the shear stress at the porous/fluid interface (at $r = \xi R$); ρ_f is the fluid density; R^+ is the dimensionless radius of the tube, $u_\tau R/\nu_f$; R is the tube radius; ν_f is the fluid kinematic viscosity; y^+ is the dimensionless distance from the porous/fluid interface, $\xi R^+ - r^+$; r^+ is the dimensionless radius, $u_\tau r/\nu_f$; r is the radial coordinate; μ_T^+ is the dimensionless eddy viscosity, μ_T/μ_f; μ_T is the eddy viscosity; and μ_f is the fluid viscosity.

According to the Cebeci-Smith model [17, 18], the turbulent flow domain is divided into two layers, the inner layer ($0 \le y^+ \le y_m^+$) and the outer layer ($y^+ > y_m^+$). The dimensionless eddy viscosity is then computed as:

$$\mu_T^+ = \begin{cases} \mu_{T_i}^+ & \text{for } y^+ \le y_m^+ \\ \mu_{T_o}^+ & \text{for } y^+ > y_m^+ \end{cases} \qquad (3.2)$$

where y_m^+ is the smallest value for which $\mu_{T_i} = \mu_{T_o}$. The value of the dimensionless eddy viscosity in the inner layer, $\mu_{T_i}^+$, is computed according to the following equation:

$$\mu_{Ti}^+ = \left(\kappa y^+\right)^2\left[1-\exp\left(-y^+/A^+\right)\right]^2\left|du^+/dy^+\right| \qquad (3.3)$$

and the value of the dimensionless eddy viscosity in the outer layer, $\mu_{T_o}^+$, is computed as:

$$\mu_{To}^+ = \alpha_T U_c^+ \delta_v^+ F_{Kleb} \qquad (3.4)$$

where U_c^+ is the dimensionless centerline velocity, $\left(u\big|_{r=0}\right)/u_\tau$; F_{Kleb} is the Klebanoff intermittency function:

$$F_{Kleb} = \left[1 + 5.5\left[y^+ / \left(\xi R^+\right)\right]^6\right]^{-1} \qquad (3.5)$$

and δ_v^+ is the dimensionless velocity thickness:

$$\delta_v^+ = \int_0^{\xi R^+} \left(1 - u^+ / U_c^+\right) dy^+ \qquad (3.6)$$

The closure coefficients for the Cebeci-Smith model are:

$$\kappa = 0.40, \quad \alpha_T = 0.0168, \quad A^+ = 26 \qquad (3.7)$$

The traditional formulation of the Cebeci-Smith model includes a correction to the value of the Van Driest's coefficient, A^+, to account for the effect of pressure gradient [18]. This correction is omitted here because the flow occurs under a favorable pressure gradient, dp/dx<0.

For the porous region ($\xi R^+ \le r^+ \le R^+$), the Brinkman-Forchheimer extension of the Darcy law (Nield and Bejan, [19]) is utilized. Even if in the bulk of the porous layer the filtration velocity is small, it may still be large at the interface; therefore accounting for the Forchheimer term is important. The Brinkman term is included to allow for the continuity of filtration velocity through the porous/fluid interface and also to allow utilizing the no-slip boundary condition at the tube wall (the utilization of the Darcy-Forcheimer equation would require a slip at the solid wall). In dimensionless variables the Brinkman-Forchheimer-extended Darcy equation can be presented as:

$$\frac{2}{\xi R^+} + \left(\frac{\mu_{eff}}{\mu_f}\right)\frac{1}{r^+}\frac{d}{dr^+}\left(r^+\frac{du^+}{dr^+}\right) - \frac{u^+}{Da\left(R^+\right)^2} - \frac{c_F}{Da^{1/2}R^+}\left(u^+\right)^2 = 0 \qquad (3.8)$$

where c_F is the Forchheimer coefficient; Da is the Darcy number, K/R^2; and μ_{eff} is the effective viscosity in the porous region.

At the wall of the tube the no-slip boundary condition is utilized:

$$u^+\Big|_{r^+=R^+} = 0 \qquad (3.9)$$

From the definition of u^+ and r^+ it follows that at the porous/fluid interface:

$$\left.\frac{\partial u^+}{\partial r^+}\right|_{r^+=\xi R^+-0} = -1 \qquad (3.10)$$

To match the velocity in the porous region with the velocity in the homogeneous fluid region at the porous/fluid interface, the boundary conditions suggested by Ochoa-Tapia and Whitaker [20, 21] are utilized:

$$u^+\Big|_{r^+=R^++0} = u^+\Big|_{r^+=R^+-0} = u_i^+, \quad \left(\frac{\mu_{eff}}{\mu_f}\right)\left.\frac{\partial u^+}{\partial r^+}\right|_{r^+=\xi R^++0} - \left.\frac{\partial u^+}{\partial r^+}\right|_{r^+=\xi R^+-0} = \frac{\beta u_i^+}{Da^{1/2}R^+} \qquad (3.11a,b)$$

where u_i^+ is the dimensionless velocity at the porous/fluid interface, u_i / u_τ; and β is the dimensionless adjustable coefficient. Equation (3.11b) represents the jump in the shear stress condition derived in [20, 21]. It should be noted that refs. [20, 21] assumed laminar flow in both homogeneous fluid and porous regions. However, according to the Cebeci-Smith model (equation (3.3)), the dimensionless eddy viscosity, μ_T^+, equals zero at the porous/fluid interface. Thus it is assumed that equations (3.11a,b) are still valid for the flow situation considered in this chapter.

A major assumption made in this research is that the flow in the homogeneous fluid region is turbulent while the flow in the porous region is laminar. To estimate the validity of this assumption, Reynolds numbers must be estimated in these regions and compared with their critical values.

The Reynolds number based on the diameter of the homogeneous fluid region, $2\xi R$, and the mean velocity in this region, $(U_m)_{hom\,fl}$, is defined as:

$$Re_{2\xi R} = (U_m)_{hom\,fl} 2\xi R / \nu_f = (U_m^+)_{hom\,fl} 2\xi R^+ \qquad (3.12)$$

where $(U_m^+)_{hom\,fl}$ is the dimensionless mean velocity in the homogeneous fluid region, $(U_m)_{hom\,fl} / u_\tau$:

$$(U_m^+)_{hom\,fl} = \frac{2}{(\xi R^+)^2} \int_0^{\xi R^+} u^+ r^+ dr^+ \qquad (3.13)$$

For the flow in a pipe, the critical Reynolds number is 4×10^3.

For the porous region, the Reynolds number based on $K^{1/2}$ is defined as:

$$Re_K = v_{fil} K^{1/2} / \nu_f \qquad (3.14)$$

where K is the permeability of the porous medium.

For small values of the Darcy number, the velocity profile in the porous region consists of three regions [22], two boundary layers (one adjacent to the solid wall and the other adjacent to the porous/fluid interface) and the constant velocity region between them. In this constant velocity region second term in equation (3.8) is negligible and velocity can be obtained by solving a simple quadratic equation as:

$$u_{bulk}^+ = -\frac{1}{2c_F Da^{1/2} R^+} + \left[\left(\frac{1}{2c_F Da^{1/2} R^+} \right)^2 + \frac{2Da^{1/2}}{c_F \xi} \right]^{1/2} \qquad (3.15)$$

Estimating filtration velocity, v_{fil}, in the bulk of the fluid region as $v_{fil} = u_\tau u_{bulk}^+$, equation (3.14) can be recast as:

$$\mathrm{Re_K} = \mathrm{R^+ Da^{1/2}} \left\{ -\frac{1}{2\mathrm{c_F Da^{1/2} R^+}} + \left[\left(\frac{1}{2\mathrm{c_F Da^{1/2} R^+}} \right)^2 + \frac{2\mathrm{Da^{1/2}}}{\mathrm{c_F}\xi} \right]^{1/2} \right\} \qquad (3.16)$$

According to Bear [23], most experiments indicate that actual turbulence in porous media occurs at values of Reynolds number at least one order of magnitude higher than the Reynolds number at which deviation from the Darcy law is observed due to the Forchheimer (quadratic drag) effects. According to Nield and Bejan [19], transition from Darcy to Forchheimer flow regime occurs when $\mathrm{Re_K}$ is larger than 10. This means that the turbulent flow regime may occur in porous media if $\mathrm{Re_K}$ is larger than 100.

Computations show that for $\mathrm{R^+} = 1000$, $\mathrm{Da} = 10^{-4}$, and $\xi = 0.6$ the value of $\mathrm{Re}_{2\xi\mathrm{R}}$ is 8.928×10^3, which is larger than the critical Reynolds number of 4×10^3. This indicates that the flow in the homogeneous fluid region is turbulent. For the same parameter values, $\mathrm{Re_K}$ is equal to 1.715, which is much smaller than 100. This means that the flow in the porous region is laminar.

3.4 HEAT TRANSFER PROBLEM: CONSTANT WALL HEAT FLUX CASE

The energy equation for the homogeneous fluid region, $0 \le \mathrm{r^+} \le \xi \mathrm{R^+}$, is based on the constant turbulent Prandtl number model:

$$\frac{1}{\mathrm{r^+}} \frac{\mathrm{d}}{\mathrm{dr^+}} \left[\left(1 + \mu_{\mathrm{T}}^+ \frac{\mathrm{Pr}}{\mathrm{Pr_t}} \right) \mathrm{r^+} \frac{\mathrm{d}\theta}{\mathrm{dr^+}} \right] = -\frac{1}{\left(\mathrm{R^+}\right)^2} \frac{\mathrm{u^+}}{\mathrm{U_m^+}} \qquad (3.17)$$

where Pr is the Prandtl number, $\nu_{\mathrm{f}} / a_{\mathrm{f}}$; a_{f} is the fluid thermal diffusivity, Pr_t is the turbulent Prandtl number, $\nu_{\mathrm{T}} / a_{\mathrm{T}}$; a_{T} is the eddy diffusivity of heat; and $\mathrm{U_m^+}$ is the mean fluid velocity in the tube:

$$U_m^+ = \frac{2}{\left(R^+\right)^2}\int_0^{R^+} u^+ r^+ dr^+ \qquad (3.18)$$

In Eq. (3.17), θ is the dimensionless temperature, which is defined as:

$$\theta = \left(1/Nu\right)\left(T - T_W\right)/\left(T_m - T_W\right) \qquad (3.19)$$

where T is the temperature, T_W is the wall temperature (at $r^+ = R^+$), T_m is the mean temperature in the tube:

$$T_m = \frac{2}{R^2 U_m}\int_0^R uTrdr \qquad (3.20)$$

and Nu is the Nusselt number:

$$Nu = h2R/k_f = 2Rq''/\left[k_f\left(T_W - T_m\right)\right] \qquad (3.21)$$

where k_f is the fluid thermal conductivity and h is the heat transfer coefficient.

The energy equation for the porous region, $\xi R^+ \le r^+ \le R^+$, is:

$$\frac{k_{eff}}{k_f}\frac{1}{r^+}\frac{d}{dr^+}\left[r^+\frac{d\theta}{dr^+}\right] = -\frac{1}{\left(R^+\right)^2}\frac{u^+}{U_m^+} \qquad (3.22)$$

where k_{eff} is the effective thermal conductivity of the porous medium.

Energy equations (3.17) and (3.22) must be solved subject to the following boundary conditions:

$$\theta\big|_{r^+=R^+} = 0\,,\ \left.\frac{\partial\theta}{\partial r^+}\right|_{r^+=0} = 0 \qquad (3.23a,b)$$

plus the continuity of the temperature and heat flux through the porous/fluid interface:

$$\theta\big|_{r^+=\xi R^+-0} = \theta\big|_{r^+=\xi R^+ +0}\,,\qquad \left.\frac{\partial\theta}{\partial r^+}\right|_{r^+=\xi R^+-0} = \frac{k_{eff}}{k_f}\left.\frac{\partial\theta}{\partial r^+}\right|_{r^+=\xi R^+ +0} \qquad (3.24a,b)$$

Finally, the Nusselt number is computed utilizing the compatibility condition (Bejan [24]), as:

$$Nu = U_m^+ \left(R^+\right)^2 \Big/ \left[2\int_0^{R^+} u^+ \theta r^+ dr^+ \right] \qquad (3.25)$$

3.5 HEAT TRANSFER PROBLEM: CONSTANT WALL TEMPERATURE CASE

In this case the dimensionless temperature is redefined as:

$$\phi = \frac{T - T_W}{T_m - T_W} \qquad (3.26)$$

The dimensionless energy equation in the porous region ($\xi R^+ \le r^+ \le R^+$) is:

$$\frac{k_{eff}}{k_f} \frac{1}{r^+} \frac{d}{dr^+} \left[r^+ \frac{d\phi}{dr^+} \right] = -\frac{1}{\left(R^+\right)^2} Nu\, \phi \frac{u^+}{U_m^+} \qquad (3.27)$$

The dimensionless energy equation in the homogeneous fluid region ($0 \le r^+ \le \xi R^+$) is:

$$\frac{1}{r^+} \frac{d}{dr^+} \left[\left(1 + \mu_T^+ \frac{Pr}{Pr_t} \right) r^+ \frac{d\phi}{dr^+} \right] = -\frac{1}{\left(R^+\right)^2} Nu\, \phi \frac{u^+}{U_m^+} \qquad (3.28)$$

Equations (3.27) and (3.28) must be solved subject to boundary conditions (23a,b) and (24a,b). Finally, the Nusselt number can be found from the following compatibility condition:

$$Nu = -2 \frac{k_{eff}}{k_f} R^+ \left. \frac{d\phi}{dr^+} \right|_{r^+ = R^+} \qquad (3.29)$$

3.6 RESULTS AND DISCUSSION

Computations are performed utilizing the following parameter values: $\mathrm{Pr} = 1$, $\mathrm{Pr_t} = 1$, $\mu_{\mathrm{eff}} / \mu_{\mathrm{f}} = 1$, $\mathrm{k_{eff}} / \mathrm{k_f} = 1$, and $\beta = 0$ (the last condition implies direct matching of the shear stress at the porous/fluid interface). Values of other parameters utilized in computations are directly shown in the figures. Figure 3.2(a) depicts dimensionless velocity profiles for different values of the Darcy number and the Forchheimer coefficient. It shows that the velocity increases with the increase of the Darcy number. This is because a larger Darcy number corresponds to a larger permeability and thus results in a larger filtration velocity. This increase is especially heavy when the Forchheimer coefficient is equal to zero. It also shows that the Forchheimer coefficient has larger effect on the velocity distribution for a larger value of the Darcy number. When the Darcy number equals 10^{-4}, the velocity in the porous region is very small. Two non-overlapped boundary layers can be observed in the porous region when the Forchheimer coefficient is equal to zero or 0.55, one at the fixed wall and another at the porous/fluid interface. However, when the Darcy number is equal to 10^{-2} and the Forchheimer coefficient is equal to zero, the two boundary layers overlap and the velocity increases rapidly with the increase of the distance from the wall of the tube.

Figures 3.2(b) and 3.2(c) depict corresponding dimensionless temperature profiles for the cases of constant heat flux and constant wall temperature, respectively. Because thermophysical properties are independent of the temperature, the velocity distribution is independent of thermal boundary conditions (cf. Fig. 3.2(a)). Comparing Figs. 3.2(b) and 3.2(c), it can be seen that the boundary condition for the temperature does not have much

effect on the shape of the dimensionless temperature distribution. However, the magnitude of the dimensionless temperature variation is significantly different, which can

be explained by different definitions of the dimensionless temperatures used for the isoflux and isothermal cases (given by equations (3.19) and (3.26), respectively).

The results shown in Figs. 3.2(a)-(c) are computed by assuming turbulent flow in the homogeneous fluid region. To better understand the effect of turbulence in the central portion of the channel on the velocity and temperature distributions, computations are performed assuming laminar flow in the homogeneous fluid region. This is done by setting the eddy viscosity, μ_T , to zero. It is important to note that the real flow is turbulent, and the comparisons with computations carried out utilizing the laminar flow model are performed only to emphasize the effects of turbulence. Corresponding dimensionless velocity and temperature distributions are displayed in Figs. 3.3(a)-(c). Comparing these figures with Figs. 3.2(a)-(c), it can be seen that for the case of laminar flow model in the homogeneous fluid region, the velocity in this region is much larger than for the turbulent flow model. This is because in the real (turbulent) flow case the interaction between turbulent eddies will increase apparent viscosity, thus decreasing velocity in the central portion of the tube and making the velocity profile flatter.

Figure 3.4(a) depicts the dependence of the Nusselt number on the dimensionless thickness of the homogeneous fluid region. When ξ equals unity, there is no porous layer and the tube is completely occupied by a homogeneous fluid. When ξ equals zero, there is no homogeneous fluid region and the tube is completely occupied by a fluid saturated porous medium. An unexpected result shown in Fig. 3.4(a) is that for $\xi = 0$ (completely porous

channel) the Nusselt number is practically independent of the Darcy number. An explanation of this unexpected result is given in Figs. 3.5(a) and 3.5(b). As follows from Fig. 3.5(a), for the channel fully occupied by the porous medium, the momentum boundary layer at the channel wall is very thin, and velocity profiles almost correspond to the slug flow. (It should be noted that this conclusion is valid only for the relatively large Reynolds number case investigated in this chapter.) The dimensionless temperature distribution (Fig. 3.5(b)) is also practically independent of the Darcy number. As a result, the Nusselt number, computed according to equation (3.25), exhibits almost no dependence on the Darcy number for the case of completely porous channel.

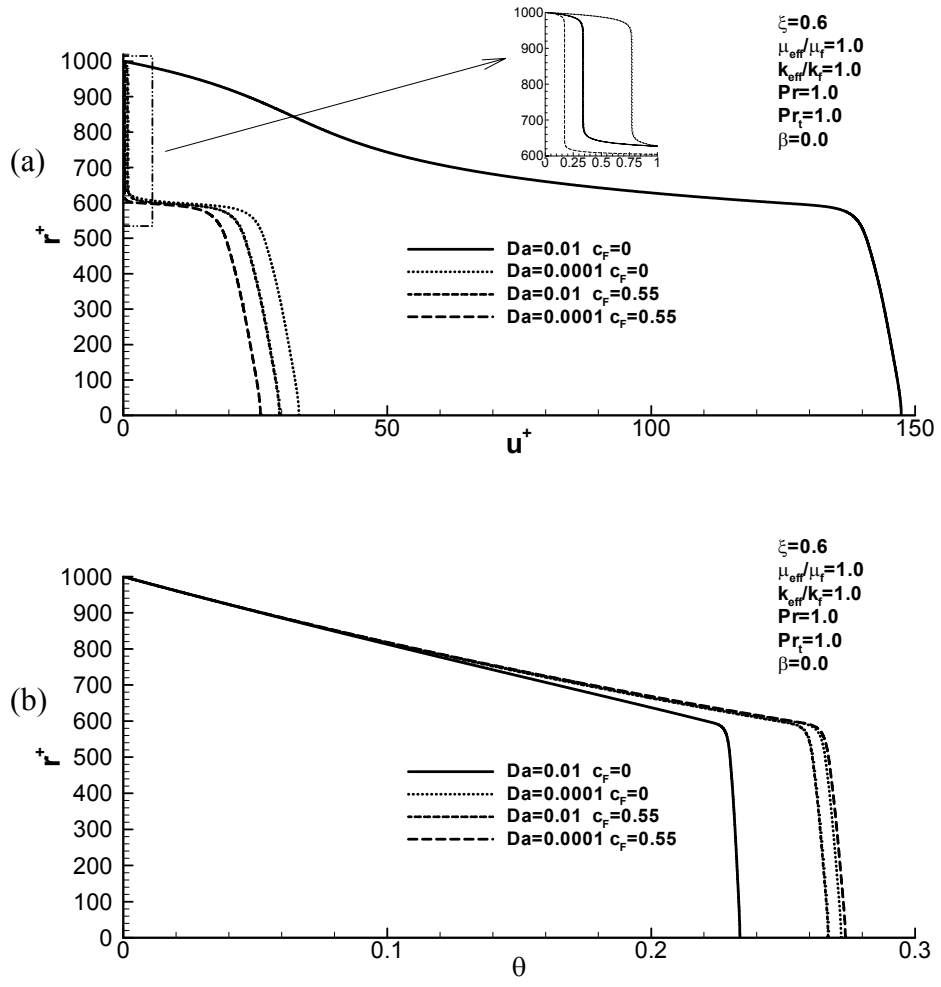

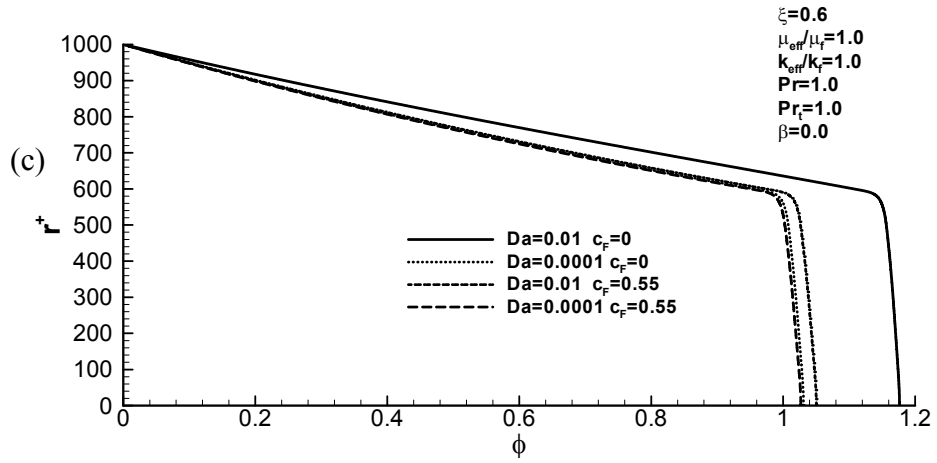

Figure 3.2 Dimensionless velocities (a) and dimensionless temperatures for the isoflux (b) and isothermal (c) wall for different values of the Darcy number and the Forchheimer coefficient assuming turbulent flow in the central portion of the tube

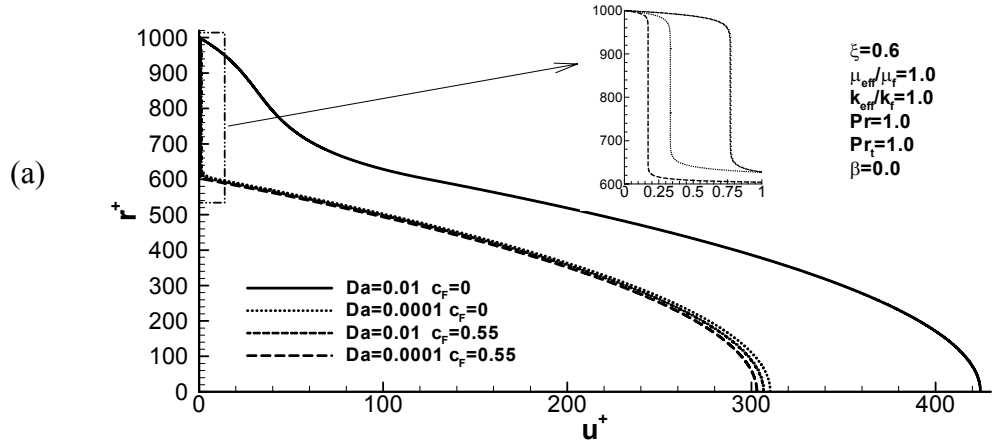

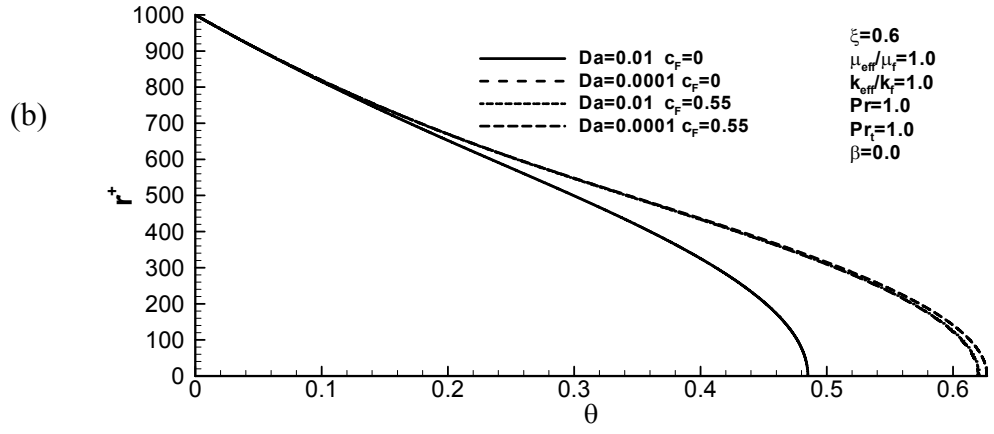

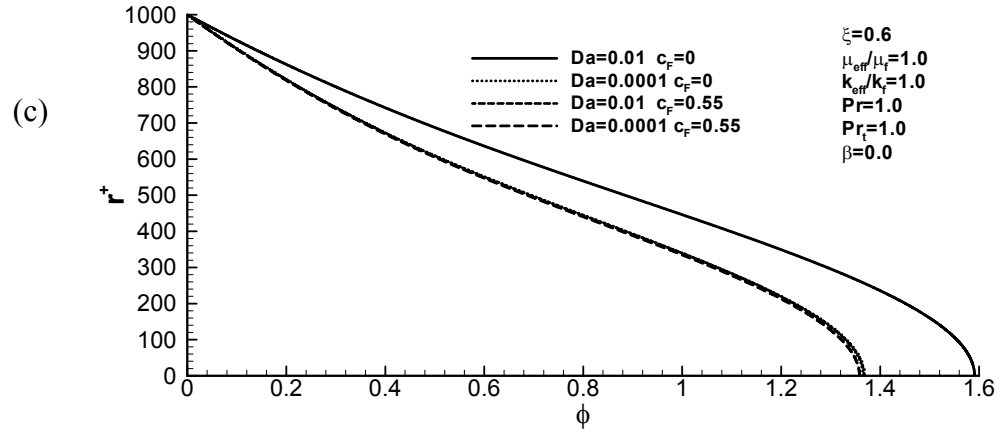

Figure 3.3 Dimensionless velocities (a) and dimensionless temperatures for the isoflux (b) and isothermal (c) wall for different values of the Darcy number and the Forchheimer coefficient assuming laminar flow in the central portion of the tube

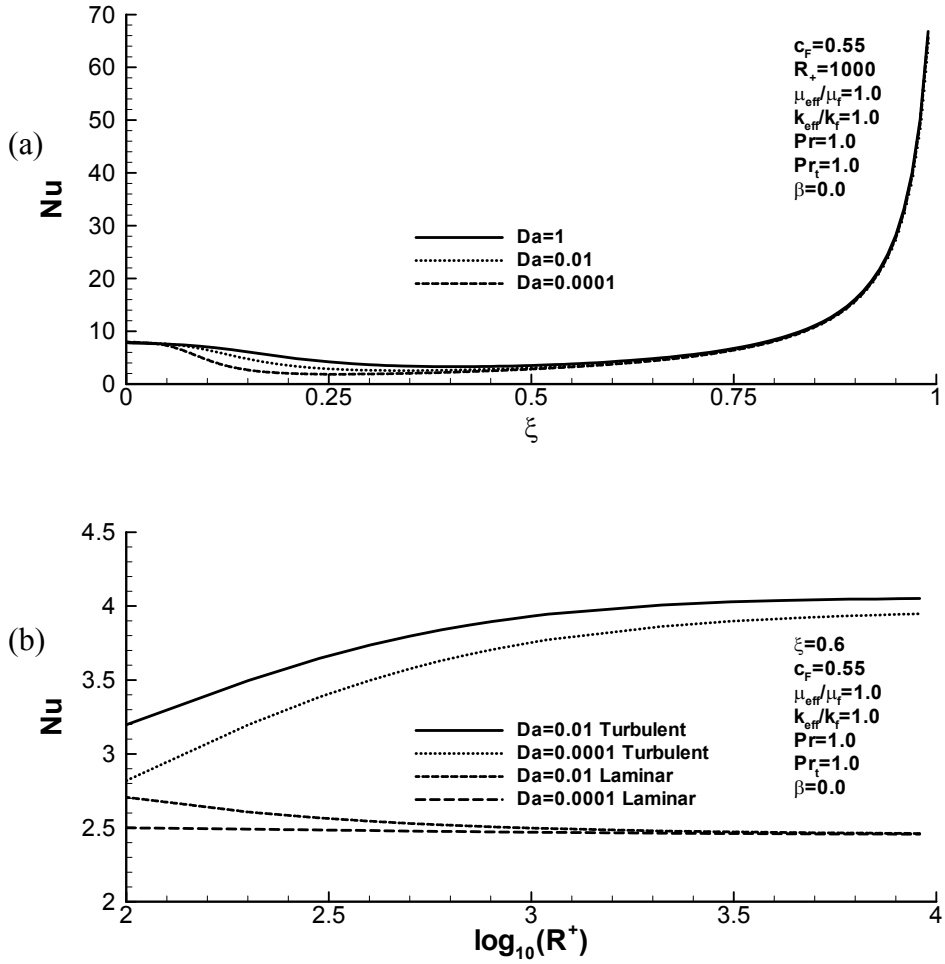

Figure 3.4 Dependence of the Nusselt number on the dimensionless position of the interface (a) and the dimensionless radius of the tube (b) for the case of isoflux wall

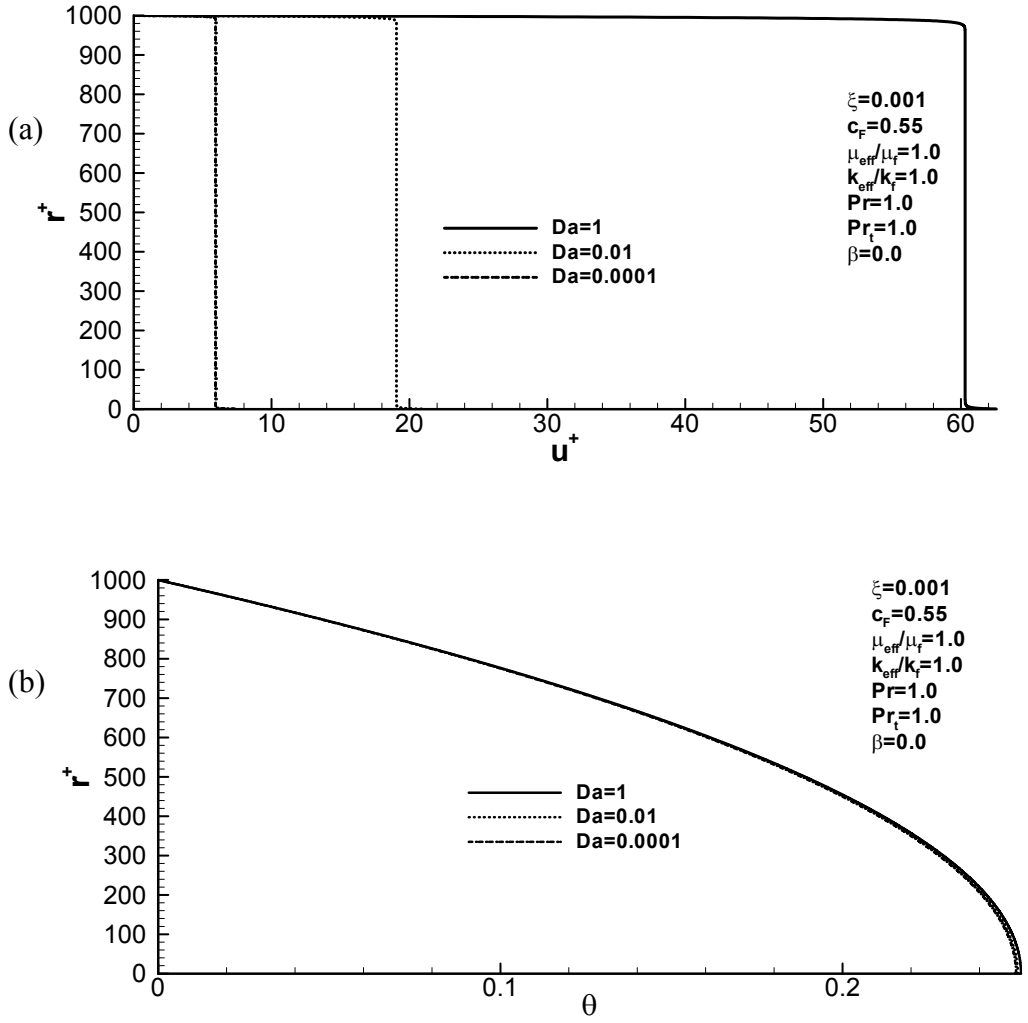

Figure 3.5 Dimensionless velocity (a) and temperature (b) distributions for different values of the Darcy number for the isoflux case when the clear fluid region vanishes ($\xi = 0$)

Figure 3.4(b) shows the effect of the Darcy number and the dimensionless tube radius on the Nusselt number and it also depicts curves computed assuming laminar flow regime in the homogeneous flow region. For the turbulent flow, the Nusselt number increases with R^+, but stays nearly constant for the laminar flow, especially for the small Darcy number case. As expected, the laminar flow assumption heavily underpredicts values of the Nusselt number.

Figures 3.6(a) and 3.6(b) display the change of the Nusselt number with the Darcy number and the Forchheimer coefficient, respectively, for the constant wall heat flux case. The increase of the Darcy number increases the Nusselt number and the increase of the Forchheimer coefficient decreases the Nusselt number, as expected.

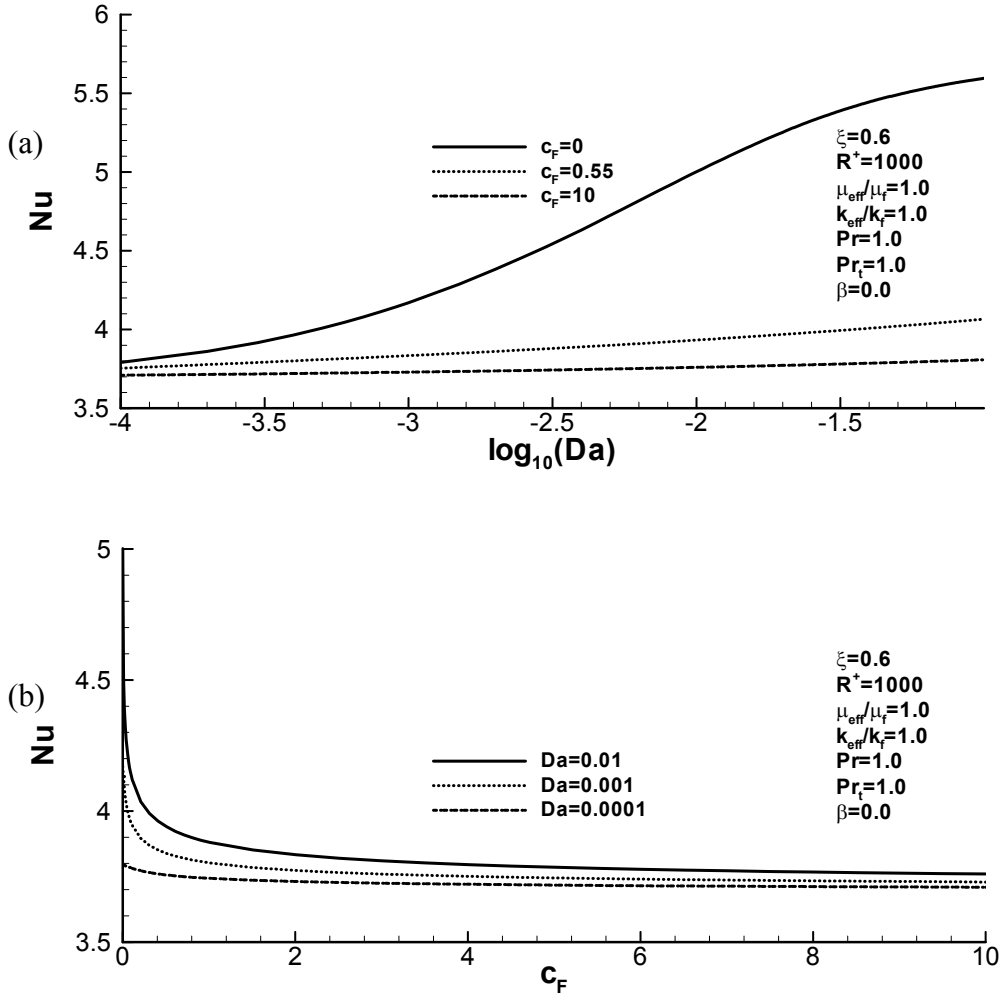

Figure 3.6 Dependence of the Nusselt number on the Darcy number (a) and the Forchheimer coefficient (b) for the case of isoflux wall

For the isotemperature case, the dependence of the Nusselt number on the dimensionless position of the interface, the dimensionless radius of the tube, the Darcy number, and the Forchheimer coefficient are shown in Figures 3.7(a), 3.7(b), 3. 8(a), and 3.8(b), respectively.

The Nusselt number has the same trend as in the isoflux case with the only difference being that the value of the Nusselt number is slightly smaller than that in the isoflux case for the same parameter values.

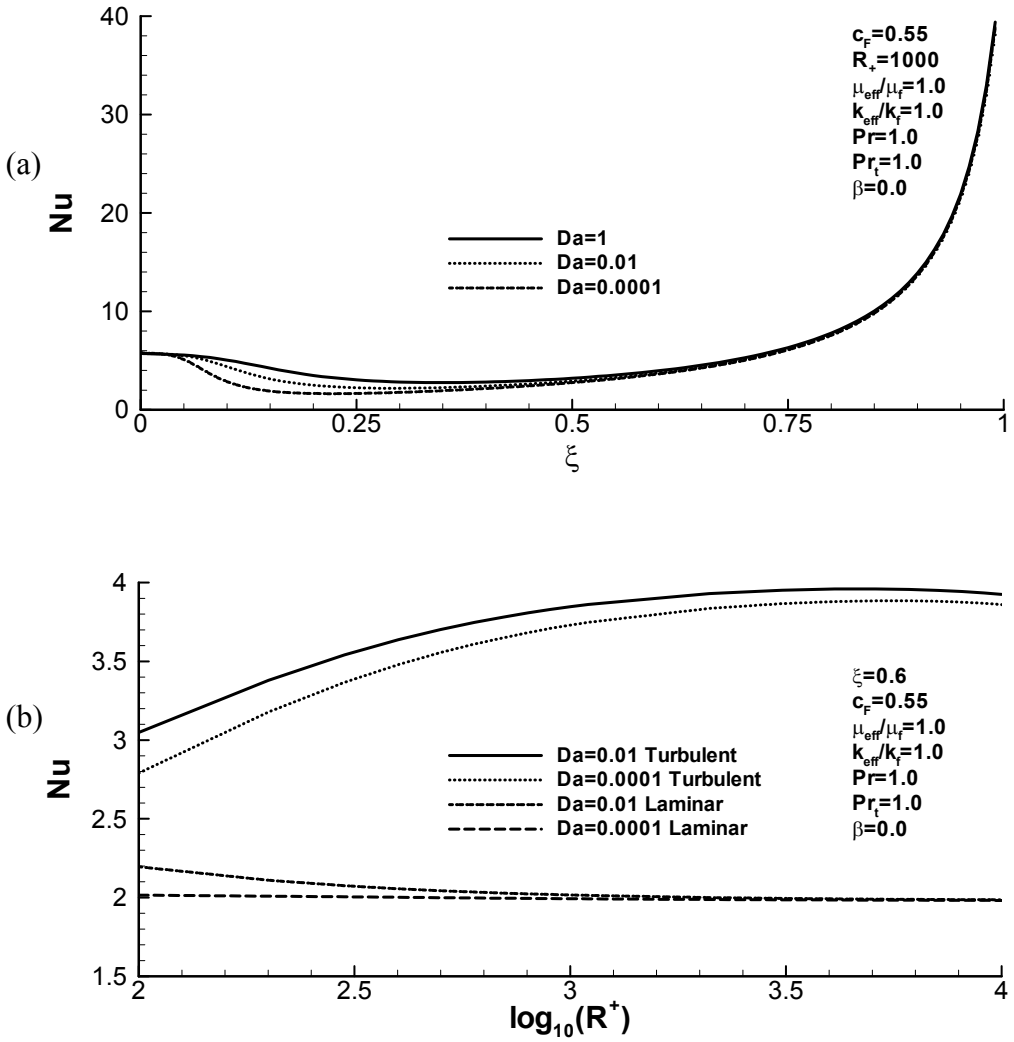

Figure 3.7 Dependence of the Nusselt number on the dimensionless position of the interface (a) and the dimensionless radius of the tube (b) for the case of isothermal wall

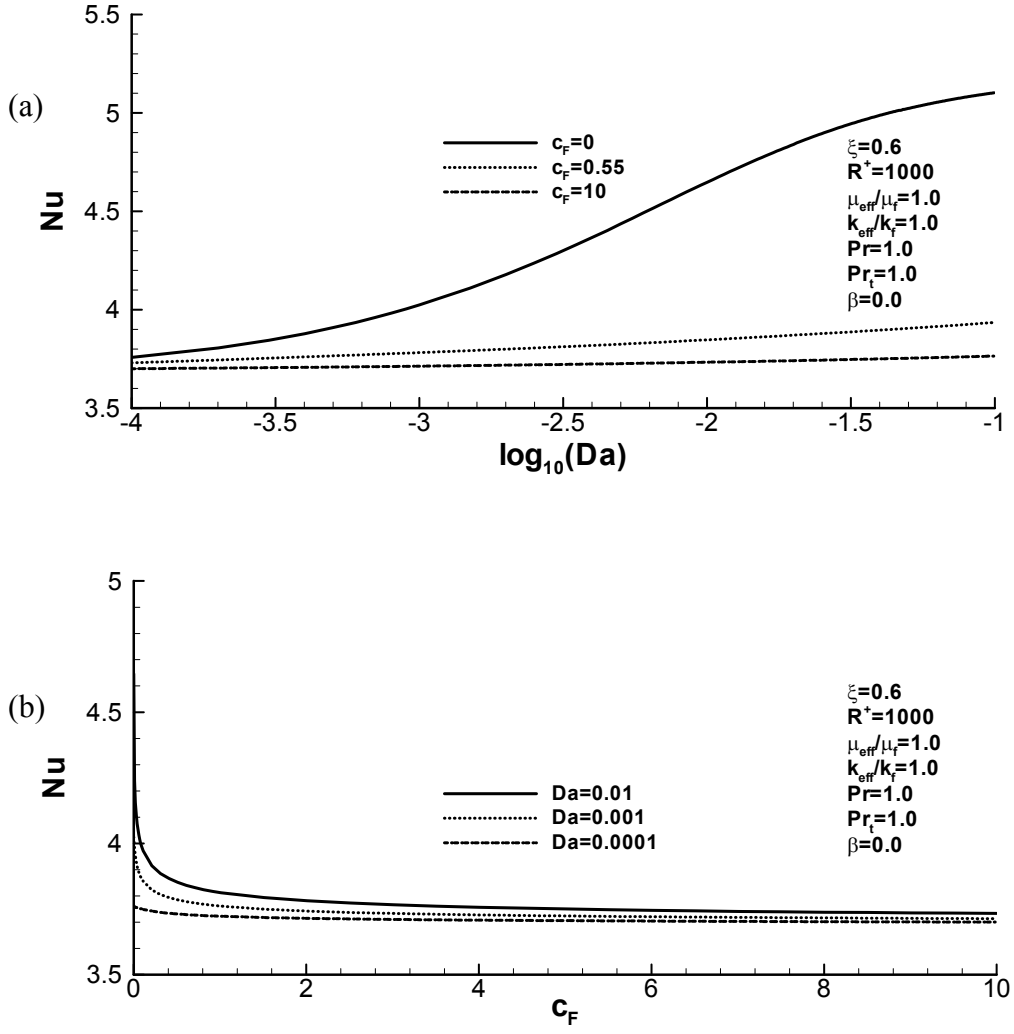

Figure 3.8 Dependence of the Nusselt number on the Darcy number (a) and the Forchheimer coefficient (b) for the case of isothermal wall

Figures 3.9(a) and 3.9(b) display the dependence of the Nusselt number on the Prandtl number and the turbulent Prandtl number, respectively. Computations are performed for a constant wall heat flux and a constant wall temperature. The increase of the Prandtl number increases the Nusselt number, and the increase of the turbulent Prandtl number decreases the Nusselt number. This in agreement with the energy equations for the turbulent flow region, equations (3.17) and (3.28). According to these equations the increase of the Prandtl number and the decrease of the turbulent Prandtl number increases total (molecular plus turbulent)

thermal diffusivity of the fluid, thus enhancing heat transfer. Also, these two figures show that the Nusselt number for the isoflux wall case is a little larger than that for the isothermal wall case, as expected.

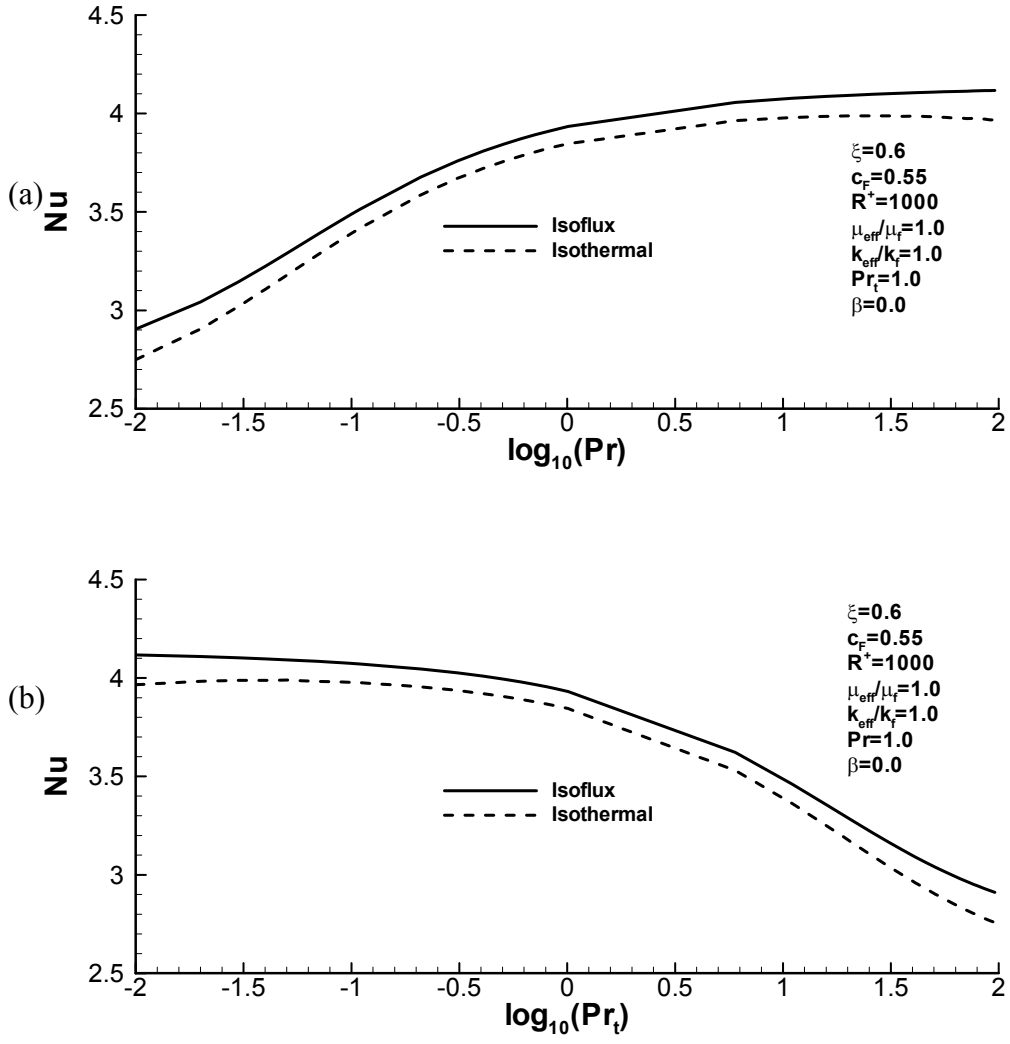

Figure 3.9 Dependence of the Nusselt number on the Prandtl number (a) and the turbulent Prandtl number (b) for a constant wall heat flux and a constant wall temperature

3.7 CONCLUSIONS

The interaction between turbulent flow in the center of a circular tube filled with a homogeneous fluid and laminar flow in the porous layer adjacent to the tube wall is

investigated. The Cebeci-Smith model is utilized to model turbulent flow in the central region of the tube. Two kinds of thermal boundary conditions (isoflux wall and isothermal wall) are investigated. The velocity and temperature profiles are presented for different Darcy numbers and Forchheimer coefficients. The effects of the Darcy number, the Forchheimer coefficient, the dimensionless thickness of the porous layer, and the dimensionless tube radius on the Nusselt number are investigated. The effect of turbulence on the Nusselt number is investigated by comparing turbulent model predictions with predictions of the model that assumes laminar flow in both homogeneous fluid and porous flow domains.

REFERENCES

1. Prescott, PJ; Incropera, FP (1995) The effect of turbulence on solidification of a binary metal alloy with electromagnetic stirring. *ASME Journal of Heat Transfer*, 117: 716-724

2. Wang, H; Takle, ES (1995) Boundary-layer flow and turbulence near porous obstacles. *Boundary Layer Meteorology*, 74: 73-88

3. Kim, SY; Koo, J-M; Kuznetsov, AV (2001) Effect of anisotropy in permeability and effective thermal conductivity on thermal performance of an aluminum foam heat sink. *Numerical Heat Transfer*, A 40: 21-36

4. Prakash, M; Turan, OF; Li, YG; Mahoney, J; Thorpe, GR (2001) Impinging round jet studies in a cylindrical enclosure with and without a porous layer: Part I – Flow visualizations and simulations. *Chemical Engineering Science*, 56: 3855-3878

5. Prakash, M; Turan, OF; Li, YG; Mahoney, J; Thorpe, GR (2001) Impinging round jet studies in a cylindrical enclosure with and without a porous layer: Part II – LDV measurements and simulations. *Chemical Engineering Science*, 56: 3879-3892

6. Pedras, MHJ; de Lemos, MJS (2001) Macroscopic turbulence modeling for incompressible flow through undeformable porous media. *International Journal of Heat and Mass Transfer*, 44: 1081-1093

7. Pedras, MHJ; de Lemos, MJS (2001) Simulation of turbulent flow in porous media using a spatially periodic array and a low Re two-equation closure. *Numerical Heat Transfer*, Part A 39: 35-59

8. Pedras, MHJ; de Lemos, MJS (2000) On the definition of turbulent kinetic energy for flow in porous media. *International Communications in Heat and Mass Transfer*, 27: 211-220

9. Antohe, BV; Lage, JL (1997) A general two-equation macroscopic model for incompressible flow in porous media. *International Journal of Heat and Mass Transfer*, 40: 3013-3024

10. Nakayama, A; Kuwahara, F (1999) A macroscopic turbulence model for flow in a porous medium. *ASME Journal of Fluids Engineering*, 121: 427-433

11. Kuwahara, F; Kameyama, Y; Yamashita, S; Nakayama, A (1998) Numerical modeling of turbulent flow in porous media using a spatially periodic array. *Journal of Porous Media*, 1: 47-55

12. Nield, DA (1997) Turbulence model for flow through porous media – Comments. *International Journal of Heat and Mass Transfer*, 40: 2499-2499

13. Masuoka, T; Takatsu, Y (1996) Turbulence model for flow through porous media. *International Journal of Heat and Mass Transfer*, 39: 2803-2809

14. Poulikakos, D; Kazmierczak, M (1987) Forced convection in a duct partially filled with a porous material. *ASME Journal of Heat Transfer*, 109: 563-662

15. Vafai, K; Thiyagaraja, R (1987) Analysis of flow and heat transfer at the interface region of a porous medium. *International Journal of Heat and Mass Transfer*, 30: 1391-1405

16. Kuznetsov, AV (2000) Analytical studies of forced convection in partly porous configurations, In: *Handbook of Porous Media*, edited by K. Vafai, Marcel Dekker, New York, pp. 269-312

17. Cebeci, T; Smith, AMO (1974) Analysis of Turbulent Boundary Layers, Ser. in *Appl. Math & Mech.*, Vol. XV, Academic Press, New York

18. Wilcox, DC (1994) *Turbulence Modeling for CFD*, DCW Industries, La Canada, CA

19. Nield, DA; Bejan, A (1999) *Convection in Porous Media*, 2nd ed., Springer, New York

20. Ochoa-Tapia, JA; Whitaker, S (1995) Momentum transfer at the boundary between a porous medium and a homogeneous fluid - I. Theoretical development. *International Journal of Heat and Mass Transfer*, 38: 2635-2646

21. Ochoa-Tapia, JA; Whitaker, S (1995) Momentum transfer at the boundary between a porous medium and a homogeneous fluid - II. Comparison with experiment. *International Journal of Heat and Mass Transfer*, 38:2647-2655

22. Kuznetsov, AV (1998) Analytical study of fluid flow and heat transfer during forced convection in a composite channel partly filled with a Brinkman-Forchheimer porous medium. Flow, *Turbulence and Combustion*, 60: 173-192

23. Bear, J (1972) *Dynamics of Fluids in Porous Media*, Elsevier, New York [corrected reprint, Dover, New York, 1988]

24. Bejan, A (1993) *Heat Transfer*, Wiley, New York

PART TWO:

LAMINAR FLOW AND HEAT TRANSFER OF A NON-NEWTONIAN FLUID IN A HELICAL PIPE

4 INVESTIGATION OF A LAMINAR FLOW OF A NON-NEWTONIAN FLUID IN A HELICAL PIPE

ABSTRACT

This chapter presents a numerical study of a fully developed laminar flow of a non-Newtonian fluid in a helical pipe. An orthogonal helical coordinate system is utilized and the Navier-Stokes equations for the non-Newtonian fluid in this coordinate system are derived. The SIMPLE algorithm with a staggered grid is adopted to solve the governing equations. The effects of the pressure gradient, the curvature, and the torsion on the fully developed laminar flow in helical pipes are investigated. The comparison of flow dynamics between Newtonian and non-Newtonian fluids is presented.

Nomenclature

a	pipe radius, m
Dn	Dean number, $\varepsilon^{1/2}\,\mathrm{Re}$
$\mathbf{g}$	gravity vector, m s^{-2}
Gn	Germano number, $(\varepsilon\lambda)\mathrm{Re}$
h	scale factor
m	consistency factor
n	power-law index
Re_F	Reynolds number

r	dimensionless radial coordinate, $\tilde{r}/a$
$\tilde{r}$	radial coordinate, m
$\hat{\mathbf{r}}$	residual vector
R	radius of the coil, defined in Fig. 4.1a
s	dimensionless axial coordinate, $\tilde{s}/a$
$\tilde{s}$	axial coordinate, m
p	pitch, defined in Fig 4.1a
P	dimensionless pressure, $\tilde{P}/\rho U^2$
$\tilde{P}$	pressure, Pa
U	reference velocity, m s^{-1}
$\mathbf{v}$	velocity vector, m s^{-1}
$u_s,\ u_r,\ u_\theta$	dimensionless velocity components, $\frac{\tilde{u}_s}{U}, \frac{\tilde{u}_r}{U}, \frac{\tilde{u}_\theta}{U}$
$\tilde{u}_s,\ \tilde{u}_r,\ \tilde{u}_\theta$	velocity components, m s^{-1}

Greek symbols

ε	dimensionless curvature, κa
θ	angle, defined in Fig. 4.1
κ	curvature, $R/\left(R^2+p^2\right),\ m^{-1}$
λ	the ratio of torsion to curvature, τ/κ

μ_{Newt} dynamic viscosity of a Newtonian fluid, kg m^{-1} s^{-1}

μ effective dynamic viscosity of a non-Newtonian fluid, kg m^{-1} s^{-1}

μ_F reference dynamic viscosity, see Equation (4.22), kg m^{-1} s^{-1}

$\hat{\mu}$ dimensionless effective dynamic viscosity of a non-Newtonian fluid, μ / μ_F

ν kinematic viscosity of a non-Newtonian fluid, m^2 s

ξ angle, defined in Fig. 4.1

ρ fluid density, $kg\ m^{-3}$

τ torsion, $p/\left(R^2 + p^2\right),\ m^{-1}$

$\hat{\tau}$ shear stress

ϕ angle, defined in Equation (4.2)

Subscripts

s axial direction

r radial direction

θ circumferential direction

4.1 INTRODUCTION

When a fluid passes through a curved helically coiled pipe (Figure 4.1a), a secondary flow is induced in a plane perpendicular to the direction of the main flow. It was found that the secondary flow in curved pipes increases the transition Reynolds numbers two to four times

compared to that found in a straight tube and markedly reduces axial dispersion (Truesdell and Adler [1]). The secondary flow helps to achieve better heat and mass transfer, and this is one of the reasons why helically coiled pipes are applied in many branches of industry and the research on the flow dynamics of liquids in helical tubes attracts lots of attention.

The rotating motion of liquids flowing through coiled tubes develops a characteristic swirling action. The frictional resistance of the tube walls and the action of centrifugal force combine to produce this swirling action. Dean [2] indicated that besides the Reynolds number, Re, a new parameter characterizes the magnitude and the shape of the secondary motion, which was later defined as the Dean number $Dn = \varepsilon^{1/2}\,\mathrm{Re}$. Wang [3] used a non-orthogonal coordinate system to solve helical flow problems with small curvature and small torsion. It was found that the major effect of curvature is on the flow rate while the major effect of torsion is on the secondary flow when the Reynolds number is low and the effects of curvature and torsion would diminish as the Reynolds number is increased. It was concluded that both curvature and torsion can produce a first-order effect on the flow. However, Germano [4] indicated that the secondary flow described by Wang is not projected on the normal plane. By extending the Dean equation to a helical pipe flow in an orthogonal coordinate system, he showed that the torsion does not produce the first-order effect in helical pipes of circular cross-section. Germano [5] proposed a third parameter, λ/Re, to describe the effect of torsion on a flow and verified that the effect of torsion on a helical pipe flow is second-order while the effect of the curvature is first-order. Tuttle [6] verified the first-order effect of torsion on the stream tubes and gave some explanation for the previous conclusions that such an effect would be of higher-order. Liu and Maliyah [7] performed comprehensive analyses of the secondary flow viewed both in orthogonal and non-

orthogonal coordinate systems. They concluded that in different coordinate systems (in different reference frames) different patterns of the secondary flow can be observed although the fluid flow itself is independent of the coordinate system. Liu and Maliyah also defined a generalized Dean number, as shown previously, and Germano number, $Gn = (\varepsilon\lambda)\mathrm{Re}$, and proposed another dimensionless parameter, $\gamma = GnDn^{-3/2}$, to analyze the combined effect of the curvature and torsion.

All of the above work is based on either analytical research or experiments. In the analytical research, some high-order terms were neglected so some of the conclusions may be incomplete. With the development of computers, a number of hydrodynamic and thermodynamic investigations have been performed numerically. Yang et al. [8] studied fully developed laminar convective heat transfer in a helical pipe with a finite pitch and found that the secondary flow increases with the Dean number, torsion, and the Prandtl number. Hüttl [9, 10] investigated both laminar and turbulent fully-developed flows in curved and helically coiled pipes. A detailed analysis of the effects of curvature and torsion on the axial velocity was presented and the secondary flow motion was visualized by means of vector plots and contour lines of the stream function in the cross-section of the pipe. The effects of the Reynolds number, the Dean number, and the Germano number were studied and found to be in good agreement with experiments concerning the influence of the curvature and torsion (Hüttl [9]).

However, all of these works studied Newtonian fluids. Many industrial applications deal with non-Newtonian fluids, especially in aseptic processing of foods such as milk, soups, sauces, fruit juices, and other beverages. Sandeep [11] and Sandeep et al. [12] pioneered in modeling flows of non-Newtonian fluids in helical pipes using the Ostwald-de Waele model. However,

since the Cartesian coordinate system was used, the effects of the curvature and torsion on the secondary flow in the plane normal to the main flow could not be clarified. In this chapter the orthogonal coordinate system is adopted for a fully developed laminar flow of a non-Newtonian fluid in a helical pipe and the governing equations in this coordinate system are derived. Since the concentration is made on a fully developed flow in a helical pipe, a coordinate transformation is performed to simplify the general 3D equations, dropping the axial derivatives except for the pressure derivative. The SIMPLE algorithm on a staggered grid is utilized to solve these equations. A comparison between Newtonian and non-Newtonian fluids is performed. The axial velocity is shown by contour lines and the secondary flow is displayed by vector plots to analyze the effects of curvature and torsion on non-Newtonian fluid flow in a helical pipe.

4.2 DERIVATION OF THE GOVERNING EQUATIONS

In this chapter, a steady –state incompressible flow is considered. Germano [4, 5] introduced the orthogonal helical coordinate system shown in Figure 4.1b with the helical coordinate *s* for the axial direction, *r* for the radial direction, and θ for the circumferential direction. The metric for this coordinate system is given by

$$dx \cdot dx = [1 + \kappa r \sin(\theta + \phi)]^2 (ds)^2 + (dr)^2 + r^2 (d\theta)^2 \qquad (4.1)$$

where

$$\phi(s) = -\int_{s_0}^{s} \tau(s')ds' \qquad (4.2)$$

The continuity and momentum equations in the vector form are given by

$$\nabla \cdot \mathbf{v} = 0 \tag{4.3}$$

and

$$\frac{\partial}{\partial t}\rho\mathbf{v} = -\left[\nabla \cdot \rho\mathbf{v}\mathbf{v}\right] - \nabla\widetilde{P} - \left[\nabla \cdot \hat{\tau}\right] + \rho\mathbf{g} \tag{4.4}$$

Assuming constant density, and with the help of Equation (4.3), Equation (4.4) can be rearranged as follows:

$$\rho\frac{D\mathbf{v}}{Dt} = -\nabla\widetilde{P} - \left[\nabla \cdot \hat{\tau}\right] + \rho\mathbf{g} \tag{4.5}$$

If a Newtonian fluid with constant properties is considered and gravity is neglected, Equation (4.5) can be simplified to

$$\rho\frac{D\mathbf{v}}{Dt} = -\nabla\widetilde{P} + \mu_{Newt}\nabla^2\mathbf{v} \tag{4.6}$$

For non-Newtonian fluids, the Ostwald-de Waele model (Bird et al. [13]) (the power law model) is the most popular one. Incorporating this model into the mathematical formulation can be done in two ways. The straightforward method of doing this is to directly use an equation for the shear stress of a non-Newtonian fluid in the momentum equation (Equation (4.5)). The other approach is to use the effective viscosity, which replaces the Newtonian viscosity in the momentum equation. In this study, the latter approach is chosen due to its simplicity in programming. The Navier-Stokes equations for a non-Newtonian fluid can be derived by using the effective viscosity of a non-Newtonian fluid to substitute the Newtonian viscosity in the governing equations:

$$\rho\frac{D\mathbf{v}}{Dt} = -\nabla\widetilde{P} + \nabla \cdot \mu\nabla\mathbf{v} \tag{4.7}$$

which can be expanded as

$$\rho\frac{D\mathbf{v}}{Dt} = -\nabla\widetilde{P} + \mu\nabla^2\mathbf{v} + \nabla\mu\cdot\nabla\mathbf{v} \tag{4.8}$$

Using a vector relation (Synge and Schild [14]), the Laplacian operator of the velocity vector can be recast as

$$\nabla^2\mathbf{v} = \nabla(\nabla\cdot\mathbf{v}) - [\nabla\times[\nabla\times\mathbf{v}]] \tag{4.9}$$

For steady flow, this equation is simplified as

$$(\mathbf{v}\cdot\nabla)\mathbf{v} = -\frac{1}{\rho}\nabla\widetilde{P} + \nu[\nabla(\nabla\cdot\mathbf{v}) - [\nabla\times\nabla\times\mathbf{v}]] + \frac{1}{\rho}\nabla\mu\cdot\nabla\mathbf{v} \tag{4.10}$$

In an orthogonal coordinate system the divergence is expressed as

$$\nabla\cdot\mathbf{v} = \frac{1}{h_1h_2h_3}\left[\frac{\partial(h_2h_3v_1)}{\partial\xi_1} + \frac{\partial(h_3h_1v_2)}{\partial\xi_2} + \frac{\partial(h_1h_2v_3)}{\partial\xi_3}\right], \tag{4.11}$$

where ξ_1, ξ_2, and ξ_3 are the orthogonal coordinates, and h_1, h_2, and h_3 are the scale factors. The components of the gradient are $\frac{1}{h_1}\frac{\partial}{\partial\xi_1}$, $\frac{1}{h_2}\frac{\partial}{\partial\xi_2}$, $\frac{1}{h_3}\frac{\partial}{\partial\xi_3}$. The components of the vector $\nabla\times\nabla\times\mathbf{v}$ are

$$\frac{1}{h_2h_3}\left(\frac{\partial}{\partial\xi_2}\left(\frac{h_3}{h_1h_2}\left(\frac{\partial}{\partial\xi_1}(h_2v_2) - \frac{\partial}{\partial\xi_2}(h_1v_1)\right)\right) - \frac{\partial}{\partial\xi_3}\left(\frac{h_2}{h_1h_3}\left(\frac{\partial}{\partial\xi_3}(h_1v_1) - \frac{\partial}{\partial\xi_1}(h_3v_3)\right)\right)\right) \tag{4.12a}$$

$$\frac{1}{h_1h_3}\left(\frac{\partial}{\partial\xi_3}\left(\frac{h_1}{h_2h_3}\left(\frac{\partial}{\partial\xi_2}(h_3v_3) - \frac{\partial}{\partial\xi_3}(h_2v_2)\right)\right) - \frac{\partial}{\partial\xi_1}\left(\frac{h_3}{h_1h_2}\left(\frac{\partial}{\partial\xi_1}(h_2v_2) - \frac{\partial}{\partial\xi_2}(h_1v_1)\right)\right)\right) \tag{4.12b}$$

$$\frac{1}{h_1h_2}\left(\frac{\partial}{\partial\xi_1}\left(\frac{h_2}{h_1h_3}\left(\frac{\partial}{\partial\xi_3}(h_1v_1) - \frac{\partial}{\partial\xi_1}(h_3v_3)\right)\right) - \frac{\partial}{\partial\xi_2}\left(\frac{h_1}{h_2h_3}\left(\frac{\partial}{\partial\xi_2}(h_3v_3) - \frac{\partial}{\partial\xi_3}(h_2v_2)\right)\right)\right) \tag{4.12c}$$

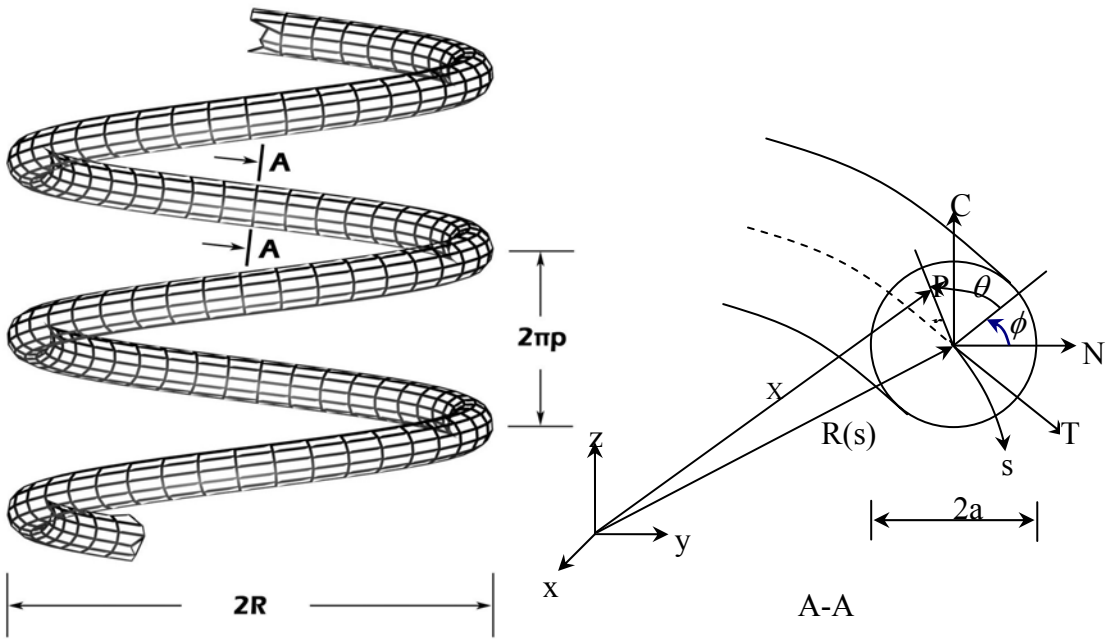

(a) **(b)**

Figure 4.1 Schematic diagram of a helical pipe and the orthogonal helical coordinate system

and the components of the vector $(\mathbf{v}\cdot\nabla)\mathbf{v}$ are

$$Dv_1+\frac{v_2}{h_2h_1}\left(v_1\frac{\partial h_1}{\partial\xi_2}-v_2\frac{\partial h_2}{\partial\xi_1}\right)+\frac{v_3}{h_3h_1}\left(v_1\frac{\partial h_1}{\partial\xi_3}-v_3\frac{\partial h_3}{\partial\xi_1}\right) \qquad (4.13a)$$

$$Dv_2+\frac{v_3}{h_3h_2}\left(v_2\frac{\partial h_2}{\partial\xi_3}-v_3\frac{\partial h_3}{\partial\xi_2}\right)+\frac{v_1}{h_1h_2}\left(v_2\frac{\partial h_2}{\partial\xi_1}-v_1\frac{\partial h_1}{\partial\xi_2}\right) \qquad (4.13b)$$

$$Dv_3+\frac{v_1}{h_1h_3}\left(v_3\frac{\partial h_3}{\partial\xi_1}-v_1\frac{\partial h_1}{\partial\xi_3}\right)+\frac{v_2}{h_2h_3}\left(v_3\frac{\partial h_3}{\partial\xi_2}-v_2\frac{\partial h_2}{\partial\xi_3}\right) \qquad (4.13c)$$

where

$$D = \frac{v_1}{h_1}\frac{\partial}{\partial \xi_1} + \frac{v_2}{h_2}\frac{\partial}{\partial \xi_2} + \frac{v_3}{h_3}\frac{\partial}{\partial \xi_3}. \tag{4.14}$$

Finally, the components of the vector $\nabla\mu \cdot \nabla \mathbf{v}$ are

$$\left[\left(\frac{1}{h_1}\frac{\partial \mu}{\partial \xi_1}\right)\left(\frac{1}{h_1}\frac{\partial v_1}{\partial \xi_1}\right) + \left(\frac{1}{h_2}\frac{\partial \mu}{\partial \xi_2}\right)\left(\frac{1}{h_2}\frac{\partial v_1}{\partial \xi_2}\right) + \left(\frac{1}{h_3}\frac{\partial \mu}{\partial \xi_3}\right)\left(\frac{1}{h_3}\frac{\partial v_1}{\partial \xi_3}\right)\right] \tag{4.15a}$$

$$\left[\left(\frac{1}{h_1}\frac{\partial \mu}{\partial \xi_1}\right)\left(\frac{1}{h_1}\frac{\partial v_2}{\partial \xi_1}\right) + \left(\frac{1}{h_2}\frac{\partial \mu}{\partial \xi_2}\right)\left(\frac{1}{h_2}\frac{\partial v_2}{\partial \xi_2}\right) + \left(\frac{1}{h_3}\frac{\partial \mu}{\partial \xi_3}\right)\left(\frac{1}{h_3}\frac{\partial v_2}{\partial \xi_3}\right)\right] \tag{4.15b}$$

$$\left[\left(\frac{1}{h_1}\frac{\partial \mu}{\partial \xi_1}\right)\left(\frac{1}{h_1}\frac{\partial v_3}{\partial \xi_1}\right) + \left(\frac{1}{h_2}\frac{\partial \mu}{\partial \xi_2}\right)\left(\frac{1}{h_2}\frac{\partial v_3}{\partial \xi_2}\right) + \left(\frac{1}{h_3}\frac{\partial \mu}{\partial \xi_3}\right)\left(\frac{1}{h_3}\frac{\partial v_3}{\partial \xi_3}\right)\right] \tag{4.15c}$$

In the orthogonal helical coordinate system, the scale factors ξ_1, ξ_2, and ξ_3 are expressed as

$$h_s = 1 + \kappa r \sin(\theta + \phi) \qquad h_r = 1 \qquad h_\theta = r \tag{4.16}$$

Thus the dimensionless governing Navier-Stokes equations for a non-Newtonian fluid in the orthogonal helical coordinate system are the continuity equation

$$\frac{\partial(ru_s)}{\partial s} + \frac{\partial(rh_s u_r)}{\partial r} + \frac{\partial(h_s u_\theta)}{\partial \theta} = 0 \tag{4.17}$$

and the momentum equations

$$\begin{aligned}
&\frac{1}{h_s r}\left(\frac{\partial(ru_s u_s)}{\partial s} + \frac{\partial(rh_s u_r u_s)}{\partial r} + \frac{\partial(h_s u_\theta u_s)}{\partial \theta}\right) + \frac{\varepsilon}{h_s} u_s\left(u_r \sin(\theta+\phi) + u_\theta \cos(\theta+\phi)\right) = -\frac{1}{h_s}\frac{\partial p}{\partial s} \\
&\quad + \frac{\hat{\mu}}{\mathrm{Re}_F}\left\{\frac{1}{h_s}\frac{\partial}{\partial s}\left[\frac{1}{h_s r}\left[\frac{\partial(ru_s)}{\partial s} + \frac{\partial(rh_s u_r)}{\partial r} + \frac{\partial(h_s u_\theta)}{\partial \theta}\right]\right] - \right. \\
&\quad \left.\frac{1}{r}\left(\frac{\partial}{\partial r}\left(\frac{r}{h_s}\left(\frac{\partial u_r}{\partial s} - \frac{\partial}{\partial r}(h_s u_s)\right)\right) - \frac{\partial}{\partial \theta}\left(\frac{1}{h_s r}\left(\frac{\partial}{\partial \theta}(h_s u_s) - \frac{\partial}{\partial s}(ru_\theta)\right)\right)\right)\right\} \\
&\quad + \frac{1}{\mathrm{Re}_F}\left[\frac{1}{h_s^{\,2}}\frac{\partial u_s}{\partial s}\frac{\partial \hat{\mu}}{\partial s} + \frac{\partial u_s}{\partial r}\frac{\partial \hat{\mu}}{\partial r} + \frac{1}{r^2}\frac{\partial u_s}{\partial \theta}\frac{\partial \hat{\mu}}{\partial \theta}\right]
\end{aligned} \tag{4.18a}$$

$$\frac{1}{h_s r}\left(\frac{\partial(ru_s u_r)}{\partial s}+\frac{\partial(rh_s u_r u_r)}{\partial r}+\frac{\partial(h_s u_\theta u_r)}{\partial\theta}\right)-\frac{{u_\theta}^2}{r}-\frac{k}{h_s}{u_s}^2\sin(\theta+\phi)=-\frac{\partial p}{\partial r}$$
$$+\frac{\hat{\mu}}{\mathrm{Re}_F}\left\{\frac{\partial}{\partial r}\left[\frac{1}{h_s r}\left[\frac{\partial(ru_s)}{\partial s}+\frac{\partial(rh_s u_r)}{\partial r}+\frac{\partial(h_s u_\theta)}{\partial\theta}\right]\right]-\right.$$
$$\left.\frac{1}{h_s r}\left(\frac{\partial}{\partial\theta}\left(\frac{h_s}{r}\left(\frac{\partial}{\partial r}(ru_\theta)-\frac{\partial u_r}{\partial\theta}\right)\right)-\frac{\partial}{\partial s}\left(\frac{r}{h_s}\left(\frac{\partial u_r}{\partial s}-\frac{\partial}{\partial r}(h_s u_s)\right)\right)\right)\right\} \qquad (4.18b)$$
$$+\frac{1}{\mathrm{Re}_F}\left[\frac{1}{{h_s}^2}\frac{\partial u_r}{\partial s}\frac{\partial\hat{\mu}}{\partial s}+\frac{\partial u_r}{\partial r}\frac{\partial\hat{\mu}}{\partial r}+\frac{1}{r^2}\frac{\partial u_r}{\partial\theta}\frac{\partial\hat{\mu}}{\partial\theta}\right]$$

$$\frac{1}{h_s r}\left(\frac{\partial(ru_s u_\theta)}{\partial s}+\frac{\partial(rh_s u_r u_\theta)}{\partial r}+\frac{\partial(h_s u_\theta u_\theta)}{\partial\theta}\right)-\frac{\varepsilon}{h_s}{u_s}^2\cos(\theta+\phi)+\frac{u_r u_\theta}{r}=-\frac{1}{r}\frac{\partial p}{\partial\theta}$$
$$+\frac{\hat{\mu}}{\mathrm{Re}_F}\left\{\frac{1}{r}\frac{\partial}{\partial\theta}\left[\frac{1}{h_s r}\left[\frac{\partial(ru_s)}{\partial s}+\frac{\partial(rh_s u_r)}{\partial r}+\frac{\partial(h_s u_\theta)}{\partial\theta}\right]\right]-\right.$$
$$\left.\frac{1}{h_s}\left(\frac{\partial}{\partial s}\left(\frac{1}{h_s r}\left(\frac{\partial}{\partial\theta}(h_s u_s)-\frac{\partial}{\partial s}(ru_\theta)\right)\right)-\frac{\partial}{\partial r}\left(\frac{h_s}{r}\left(\frac{\partial}{\partial r}(ru_\theta)-\frac{\partial u_r}{\partial\theta}\right)\right)\right)\right\} \qquad (4.18c)$$
$$+\frac{1}{\mathrm{Re}_F}\left[\frac{1}{{h_s}^2}\frac{\partial u_\theta}{\partial s}\frac{\partial\hat{\mu}}{\partial s}+\frac{\partial u_\theta}{\partial r}\frac{\partial\hat{\mu}}{\partial r}+\frac{1}{r^2}\frac{\partial u_\theta}{\partial\theta}\frac{\partial\hat{\mu}}{\partial\theta}\right]$$

where

$$s=\frac{\tilde{s}}{a},\ r=\frac{\tilde{r}}{a},\ (u_s,u_r,u_\theta)=\left(\frac{\tilde{u}_s}{U},\frac{\tilde{u}_r}{U},\frac{\tilde{u}_\theta}{U}\right),\ P=\frac{\tilde{P}}{\rho U^2},$$
$$\varepsilon=\kappa a,\ \lambda=\frac{\tau}{\kappa},\ \mathrm{Re}_F=\frac{\rho U a}{\mu_F},\ \hat{\mu}=\frac{\mu}{\mu_F},\ U=\frac{1}{\pi}\int_0^{2\pi}\int_0^1 u_s r\,dr\,d\theta \qquad (4.19)$$

where a is the radius of the pipe, U is the bulk velocity defined in Eq. (4.19) and μ_F is a reference viscosity defined in Eq. (4.22).

The following expression for the effective viscosity for a power law fluid is used:

$$\mu=m\left[\frac{1}{2}(\Delta:\Delta)\right]^{\frac{n-1}{2}} \qquad (4.20)$$

where Δ is the rate of deformation tensor and the expression for $(\Delta:\Delta)$ is given by

$$\frac{1}{2}(\Delta:\Delta)=2\left[\left(\frac{\partial}{\partial\tilde{s}}\left(\frac{\tilde{u}_s}{h_s}\right)-\frac{\tau\kappa\tilde{r}\cos(\theta-\tau\tilde{s})}{{h_s}^2}\tilde{u}_s+\frac{\kappa\sin(\theta-\tau\tilde{s})}{h_s}\tilde{u}_r+\frac{\kappa\cos(\theta-\tau\tilde{s})}{h_s}\tilde{u}_\theta\right)^2\right.$$
$$\left.+\left(\frac{\partial\tilde{u}_r}{\partial\tilde{r}}\right)^2+\left(\frac{\partial}{\partial\theta}\left(\frac{\tilde{u}_\theta}{\tilde{r}}\right)+\frac{\tilde{u}_r}{\tilde{r}}\right)^2\right]+\left(h_s\frac{\partial}{\partial\tilde{r}}\left(\frac{\tilde{u}_s}{h_s}\right)+\frac{1}{h_s}\frac{\partial\tilde{u}_r}{\partial\tilde{s}}\right)^2 \qquad (4.21)$$
$$+\left(\frac{h_s}{\tilde{r}}\frac{\partial}{\partial\theta}\left(\frac{\tilde{u}_s}{h_s}\right)+\frac{\tilde{r}}{h_s}\frac{\partial}{\partial\tilde{s}}\left(\frac{\tilde{u}_\theta}{\tilde{r}}\right)\right)^2+\left(\tilde{r}\frac{\partial}{\partial\tilde{r}}\left(\frac{\tilde{u}_\theta}{\tilde{r}}\right)+\frac{1}{\tilde{r}}\frac{\partial\tilde{u}_r}{\partial\theta}\right)^2$$

.

The reference viscosity μ_F is introduced by using

$$\mu_F=m\left[\left(\frac{U}{a}\right)^2\right]^{\frac{n-1}{2}} \qquad (4.22)$$

A fully developed laminar flow is considered so that the dynamic variables, except for the pressure, are independent of *s*, therefore, a simplifying transformation is performed from *s*, *r*, θ to *s*, *r*, ξ:

$$\theta+\phi=\xi\,,\ \frac{\partial}{\partial s}\Rightarrow\frac{\partial}{\partial s}-\varepsilon\lambda\frac{\partial}{\partial\xi}\,,\ \frac{\partial}{\partial\theta}\Rightarrow\frac{\partial}{\partial\xi} \qquad (4.23)$$

The governing equations are then reduced as follows:

$$-\varepsilon\lambda\frac{\partial(ru_s)}{\partial\xi}+\frac{\partial(rh_su_r)}{\partial r}+\frac{\partial(h_su_\theta)}{\partial\xi}=0 \qquad (4.24)$$

$$\frac{1}{h_sr}\left(-\varepsilon\lambda\frac{\partial(ru_su_s)}{\partial\xi}+\frac{\partial(rh_su_ru_s)}{\partial r}+\frac{\partial(h_su_\theta u_s)}{\partial\xi}\right)+\frac{\varepsilon}{h_s}u_s(u_r\sin\xi+u_\theta\cos\xi)=-\frac{1}{h_s}\left(\frac{\partial P}{\partial s}-\varepsilon\lambda\frac{\partial P}{\partial\xi}\right)$$
$$+\frac{\hat{\mu}}{\mathrm{Re}_F}\left\{-\varepsilon\lambda\frac{1}{h_s}\frac{\partial}{\partial\xi}\left[\frac{1}{h_sr}\left[-\varepsilon\lambda\frac{\partial(ru_s)}{\partial\xi}+\frac{\partial(rh_su_r)}{\partial r}+\frac{\partial(h_su_\theta)}{\partial\xi}\right]\right]-\right.$$
$$\left.\frac{1}{r}\left(\frac{\partial}{\partial r}\left(\frac{r}{h_s}\left(-\varepsilon\lambda\frac{\partial u_r}{\partial\xi}-\frac{\partial}{\partial r}(h_su_s)\right)\right)-\frac{\partial}{\partial\xi}\left(\frac{1}{h_sr}\left(\frac{\partial}{\partial\xi}(h_su_s)+\varepsilon\lambda\frac{\partial}{\partial\xi}(ru_\theta)\right)\right)\right)\right\} \qquad (4.25a)$$
$$+\frac{1}{\mathrm{Re}_F}\left[\frac{(\varepsilon\lambda)^2}{{h_s}^2}\frac{\partial u_s}{\partial\xi}\frac{\partial\hat{\mu}}{\partial\xi}+\frac{\partial u_s}{\partial r}\frac{\partial\hat{\mu}}{\partial r}+\frac{1}{r^2}\frac{\partial u_s}{\partial\xi}\frac{\partial\hat{\mu}}{\partial\xi}\right]$$

$$\frac{1}{h_s r}\left(-\varepsilon\lambda\frac{\partial(ru_s u_r)}{\partial\xi}+\frac{\partial(rh_s u_r u_r)}{\partial r}+\frac{\partial(h_s u_\theta u_r)}{\partial\xi}\right)-\frac{u_\theta{}^2}{r}-\frac{\varepsilon}{h_s}u_s{}^2\sin\xi=-\frac{\partial P}{\partial r}$$
$$+\frac{\hat{\mu}}{\mathrm{Re}_F}\left\{\frac{\partial}{\partial r}\left[\frac{1}{h_s r}\left[-\varepsilon\lambda\frac{\partial(ru_s)}{\partial\varsigma}+\frac{\partial(rh_s u_r)}{\partial r}+\frac{\partial(h_s u_\theta)}{\partial\xi}\right]\right]-\right.$$
$$\left.\frac{1}{h_s r}\left(\frac{\partial}{\partial\xi}\left(\frac{h_s}{r}\left(\frac{\partial}{\partial r}(ru_\theta)-\frac{\partial u_r}{\partial\xi}\right)\right)+\varepsilon\lambda\frac{\partial}{\partial\xi}\left(\frac{r}{h_s}\left(-\varepsilon\lambda\frac{\partial u_r}{\partial\xi}-\frac{\partial}{\partial r}(h_s u_s)\right)\right)\right)\right\} \qquad (4.25b)$$
$$+\frac{1}{\mathrm{Re}_F}\left[\frac{(\varepsilon\lambda)^2}{h_s{}^2}\frac{\partial u_r}{\partial\xi}\frac{\partial\hat{\mu}}{\partial\xi}+\frac{\partial u_r}{\partial r}\frac{\partial\hat{\mu}}{\partial r}+\frac{1}{r^2}\frac{\partial u_r}{\partial\xi}\frac{\partial\hat{\mu}}{\partial\xi}\right]$$

$$\frac{1}{h_s r}\left(-\varepsilon\lambda\frac{\partial(ru_s u_\theta)}{\partial\xi}+\frac{\partial(rh_s u_r u_\theta)}{\partial r}+\frac{\partial(h_s u_\theta u_\theta)}{\partial\xi}\right)-\frac{\varepsilon}{h_s}u_s{}^2\cos\xi+\frac{u_r u_\theta}{r}=-\frac{1}{r}\frac{\partial P}{\partial\xi}$$
$$+\frac{\hat{\mu}}{\mathrm{Re}_F}\left\{\frac{1}{r}\frac{\partial}{\partial\xi}\left[\frac{1}{h_s r}\left[-\varepsilon\lambda\frac{\partial(ru_s)}{\partial\xi}+\frac{\partial(rh_s u_r)}{\partial r}+\frac{\partial(h_s u_\theta)}{\partial\xi}\right]\right]-\right.$$
$$\left.\frac{1}{h_s}\left(-\varepsilon\lambda\frac{\partial}{\partial\xi}\left(\frac{1}{h_s r}\left(\frac{\partial}{\partial\xi}(h_s u_s)+\varepsilon\lambda\frac{\partial}{\partial\xi}(ru_\theta)\right)\right)-\frac{\partial}{\partial r}\left(\frac{h_s}{r}\left(\frac{\partial}{\partial r}(ru_\theta)-\frac{\partial}{\partial\xi}(u_r)\right)\right)\right)\right\} \qquad (4.25c)$$
$$+\frac{1}{\mathrm{Re}_F}\left[\frac{(\varepsilon\lambda)^2}{h_s{}^2}\frac{\partial u_\theta}{\partial\xi}\frac{\partial\hat{\mu}}{\partial\xi}+\frac{\partial u_\theta}{\partial r}\frac{\partial\hat{\mu}}{\partial r}+\frac{1}{r^2}\frac{\partial u_\theta}{\partial\xi}\frac{\partial\hat{\mu}}{\partial\xi}\right]$$

4.3 COMPUTATIONAL PROCEDURE

A uniform mesh is generated with an evenly spaced grid in r and θ directions. The SIMPLE algorithm (Patankar [15]) is utilized on a staggered grid arrangement to solve the governing equations (Tao [16]). The control volume based finite-difference method is applied and the second-order accuracy is achieved. The convection-diffusion terms are discretized with the power-law scheme (Patankar [15]).

A one-dimensional parabolic velocity profile is imposed as the initial guess. Computations are terminated when the convergence criterion is met, namely

$$\frac{\left\|\hat{\mathbf{r}}^{(k)}\right\|_\infty}{\left\|\hat{\mathbf{r}}^{(0)}\right\|_\infty}\le 10^{-6} \qquad (4.26)$$

where $\hat{\mathbf{r}}$ is the residual of the pressure correction equation obtained from the continuity equation when using the SIMPLE method. The superscripts (0) and (k) refer to the initial and kth iteration, respectively. A no-slip boundary condition is assumed at the walls of the helical pipe. In this coordinate system, there is a geometrical singularity at the pipe axis (r=0), so boundary values are needed for flow quantities, which are either located directly at the pipe axis or at the opposite sides of the pipe axis (Hüttl [17]).

If an even number of cells in the circumferential direction is used, matching of axial velocities from the opposite sides of the pipe axis can be utilized:

$$u_s(s,-\frac{\Delta r}{2},\theta) = u_s(s,\frac{\Delta r}{2},\theta+\pi) \qquad (4.27)$$

An appropriate matching condition for the circumferential velocity u_θ is

$$u_\theta(s,-\frac{\Delta r}{2},\theta) = -u_\theta(s,\frac{\Delta r}{2},\theta+\pi) \qquad (4.28)$$

The minus sign is due to the fact that the direction of the circumferential velocity at θ is defined opposite of that at $\theta+\pi$. The value of the radial velocity at the pipe axis is determined by a linear interpolation across the axis:

$$u_r(s,r=0,\theta) = \frac{u_r(s,\Delta r,\theta) - u_r(s,\Delta r,\theta+\pi)}{2} \qquad (4.29)$$

The minus sign results from the fact that the coordinate direction changes for the radial velocity when taking the value from the opposite side.

4.4 NUMERICAL RESULTS AND DISCUSSION

The parameter m in Equation (4.20) is the consistency factor and n is the power-law index. There are two special cases: 1) n=1 and 2) n=0. If n=1 it reduces to a Newtonian flow with

$m = \mu$ and if n=0 it represents a perfect plastic flow (Huang et al. [18]). The deviation of n from unity indicates the degree of deviation from the Newtonian behavior. If n is less than unity, the behavior is pseudo-plastic, that is, the fluid has a reduced viscosity when the rate of shear is large. If n is greater than unity, the behavior is dilatant, which means the effective viscosity increases with increasing the rate of shear. In this investigation the behavior of a non-Newtonian fluid with $n=0.8$, which is typical for many food products, is compared with that of a Newtonian fluid ($n=1$). The parameters used in computations are summarized in Table 4.1.

Table 4.1 Parameter values utilized in computations

$\rho\,(kg\ m^{-3})$	a (m)	m	n (non-Newtonian)
10^3	0.0254	0.7	0.8

A FORTRAN code is developed using the above method with a 40×40 grid to compute the flow of a non-Newtonian fluid in a helical pipe and comparisons with the dynamics of a Newtonian fluid are performed. Grid independence of the solution is checked by performing a test computation utilizing a 80×80 grid, and no significant change in the solution is observed. Figure 4.2 shows contour lines of the axial velocities and vector plots of the secondary flow in a pipe cross-section for Newtonian and non-Newtonian fluids in a helical pipe with the dimensionless curvature ε=0.1, the ratio of torsion to curvature λ=0.1, and the dimensionless pressure gradient dP/ds of -30, -100, -300, respectively. From Fig 4.2(a), it can be seen that when the pressure gradient is small, for both Newtonian and non-Newtonian fluids, the parabolic profile of the axial velocity can still be observed and the displacement of the position of the maximum axial velocity from the pipe axis is not significant. Helical pipe deforms the parabolic profile of axial velocity because of the centrifugal force due to the

curvature of the helical pipe. The centrifugal force is proportional to the square of the velocity. When the pressure gradient is not large enough to conquer the viscosity friction (the velocity is small), the centrifugal force is not sufficiently large to drag the maximum of the axial velocity from the pipe axis. Figure 4.2(a) also shows that the mean velocity of a non-Newtonian fluid is greater than that of a Newtonian fluid. The secondary flow is not significant both for Newtonian and non-Newtonian fluid (Figure 4.2(b)).

When the dimensionless pressure gradient is -100 (Figure 4.2(c), (d)), the influence of the helical pipe on the non-Newtonian flow becomes apparent. The maximum of the axial velocity is displaced from the pipe axis to the wall. The vector plots show that the secondary flow in the central region of the pipe cross-section is directed toward the wall and the flow in the peripheral region of the cross-section is directed toward the center. Thus, the secondary flow induces mixing in the fluid. However, for a Newtonian fluid, the deformation of parabolic profile of the axial velocity is still not visible. The secondary flow does not show in the vector plots either. When dP/ds reaches -300, as shown in Figures 4.2(e) and 4.2(f), the parabolic profiles of the axial velocity are more strongly deformed for a non-Newtonian fluid and vector plots also show that the secondary flow for a non-Newtonian fluid is more significant. Under this pressure gradient for the Newtonian flow, the deformation of the parabolic profile becomes apparent and the secondary flow becomes visible. The comparison shows that the distance by which the maximum of the axial velocity is dragged from the pipe axis to the wall for the non-Newtonian fluid is greater than that for the Newtonian fluid and the value of the maximum velocity is also greater.

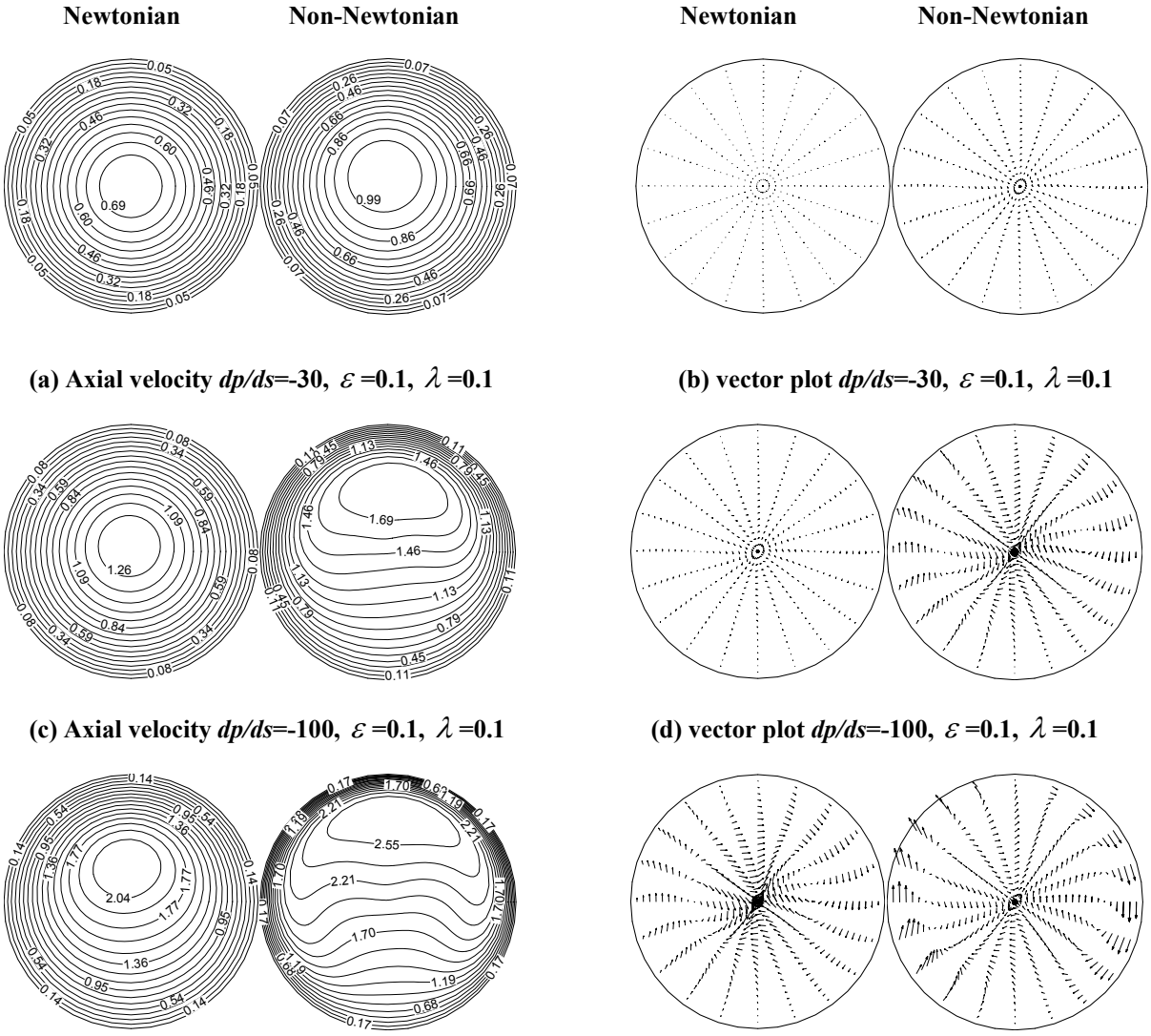

(a) Axial velocity *dp/ds*=-30, ε =0.1, λ =0.1

(b) vector plot *dp/ds*=-30, ε =0.1, λ =0.1

(c) Axial velocity *dp/ds*=-100, ε =0.1, λ =0.1

(d) vector plot *dp/ds*=-100, ε =0.1, λ =0.1

(e) Axial velocity *dp/ds*=-300, ε =0.1, λ =0.1

(f) vector plot *dp/ds*=-300, ε =0.1, λ =0.1

Figure 4.2 Contour lines of the axial velocity and vector plots of the secondary flow in the pipe cross-section for Newtonian and non-Newtonian fluids at different values of the dimensionless pressure gradient: (a, b) *dp/ds*=-30, (c, d) *dp/ds*=-100, (e, f) *dp/ds*=-300 with the same value of curvature ε and the ratio of torsion to curvature λ

One of the most important geometrical parameters of a helical pipe is its curvature. The effect of the dimensionless curvature ε on the Newtonian and non-Newtonian fluid flow for the same pressure gradient, *dP/ds*, is investigated. Figures 4.3 and 4.4 present the contour lines of the axial velocity for the Newtonian and non-Newtonian fluids, respectively, when the pressure gradient *dP/ds* is –300 and the ratio of torsion to curvature λ is fixed at 0.1

while the dimensionless curvature ε equals to 0, 0.05, 0.1, and 0.2, respectively. Both Figures 4.3 and 4.4 show that when the curvature increases, the maximum axial velocity is more and more dragged from the center to the outer wall while the value of the maximum velocity decreases. For the non-Newtonian case, when ε increases from 0 to 0.05, the deformation of the axial velocity distribution is apparent and the maximum of the axial velocity changes significantly (see Figures 4.4(a) and 4.4(b)). However, for the Newtonian fluid, the distribution does not change significantly, as seen from Figures 4.3(a) and 4.3(b). When ε continues to increase (see Figures 4.4(b), 4(c) and 4(d)), the deformation of the axial velocity profile of the non-Newtonian fluid continues and the axial velocity continues to decrease, but the change is not as abrupt as the when ε changes from 0 to 0.05. The changes for the Newtonian flow, nevertheless, are gradual for all examined values of ε (see Figures 4.3(a) to 4.3(d)).

The above results can be more clearly seen in Figures 4.5 and 4.6 that depict the axial velocity profiles for the horizontal and vertical cut view of the pipe for the Newtonian and non-Newtonian fluids. Figure 4.5 shows that the parabolic profile changes to a more and more flat one as the curvature increases. It is easy to see that the mean velocity of the Newtonian fluid flow is less than that of the non-Newtonian one. For the non-Newtonian case, the maximum axial velocity decreases significantly when the pipe changes form a straight one (ε=0) to a helical one with ε=0.05. However, for the Newtonian fluid flow, such an abrupt decrease does not occur. As ε continues to increase, the change of the velocity profile for the Newtonian fluid is slower than for the non-Newtonian fluid. Figure 4.5 also shows two local maxima on the profiles of the axial velocity on the horizontal cut

view of the pipe for the non-Newtonian fluid flow; the Newtonian fluid flow, however, does not exhibit such behavior.

Figure 4.6 presents the axial velocity profiles in the vertical cut view. It shows that as the curvature increases, the position of the maximum velocity gets displaced towards the outer wall while the value of the maximum velocity decreases for both Newtonian and non-Newtonian cases. However, the position of the maximum velocity for the non-Newtonian fluid is dragged towards the wall faster than for the Newtonian fluid. The effect of ε on the helical pipe flow is more apparent for the non-Newtonian than for the Newtonian fluid.

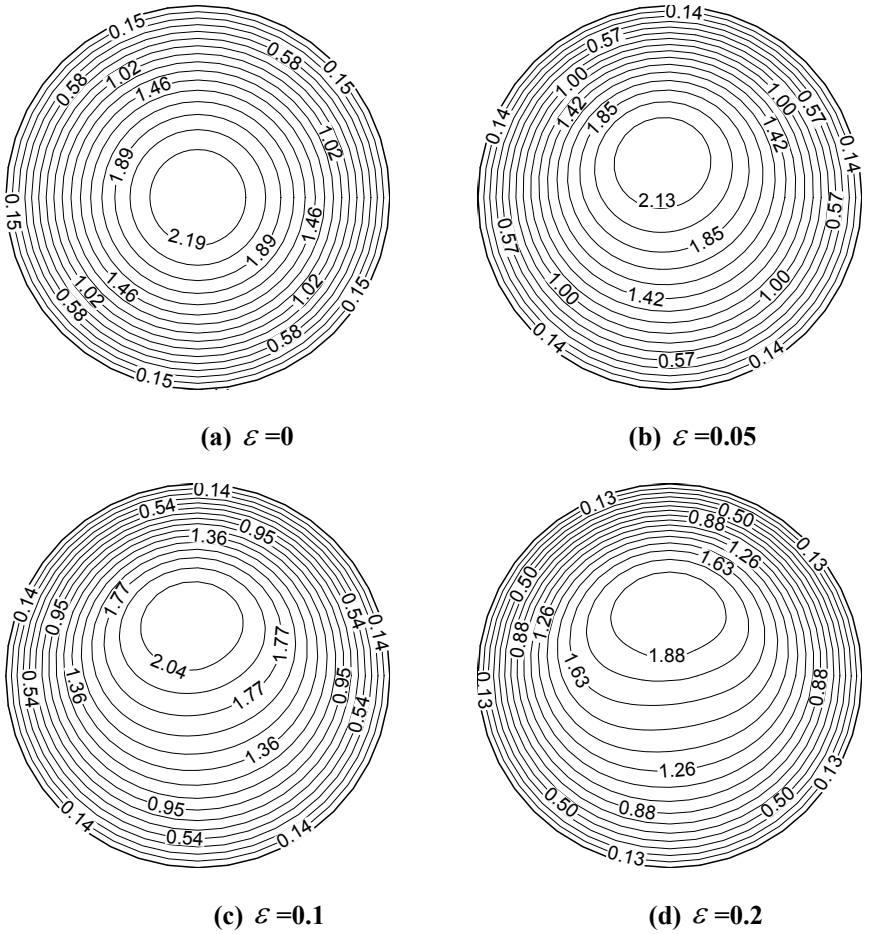

(a) ε =0 **(b) ε =0.05**

(c) ε =0.1 **(d) ε =0.2**

Figure 4.3 Contour lines of the axial velocity for the Newtonian fluid flow for *dp/ds*=-300, λ =0.1 and different values of curvature: (a) ε =0 (b) ε =0.05 (c) ε =0.1 (d) ε =0.2

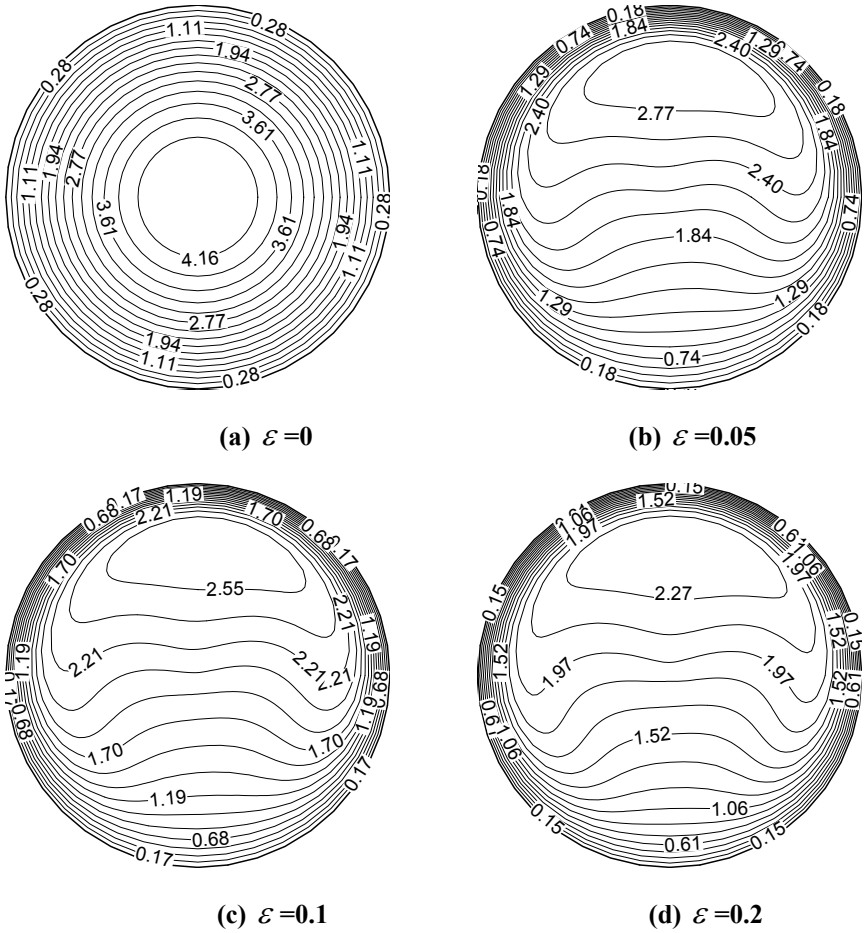

Figure 4.4 Contour lines of the axial velocity for the non-Newtonian fluid flow at *dp/ds*=-300, λ =0.1 and different values of curvature: (a) ε =0 (b) ε =0.05 (c) ε =0.1 (d) ε =0.2

Another important parameter of the helical pipe is torsion. The effect of λ, the ratio of the torsion to curvature, on the dynamics of the Newtonian and non-Newtonian flow is investigated. This parameter was widely used in the previous work to investigate the effect of torsion on the helical pipe flow. Figures 4.7 and 4.8 compare the results for different λ (0.1, 0.5, and 1.0, respectively) when *dP/ds* is fixed at –300 and ε is fixed at 0.1 and depict the contour lines of the axial velocity, vector plots of the secondary flow, and contour lines of the circumferential and radial velocities. From the similarity of contour lines of the axial velocity for the three cases computed with different values of λ in both Figures 4.7 and 4.8, it seems that λ does not have much influence on the axial velocity for both Newtonian and non-

Newtonian flows. The vector plots of the secondary flow, however, exhibit a variation with the change of λ. The effect of λ can be more directly seen from the contour lines of the circumferential velocity. Along the horizontal direction in the cross-section of the pipe, the west wall has a positive circumferential velocity while the east wall has a negative circumferential velocity. The secondary flow, which consists of two vortices, is thus generated. When λ increases, the west vortex becomes stronger and the east vortex becomes weaker. The values of the radial velocity have only a slight difference when λ changes. This phenomenon occurs for both the Newtonian and non-Newtonian fluids but the vector plots of the secondary flow show that the change of the non-Newtonian flow is more apparent than that of the Newtonian flow and the distribution of the circumferential and radial velocities indicate more mixing for the case of a non-Newtonian fluid.

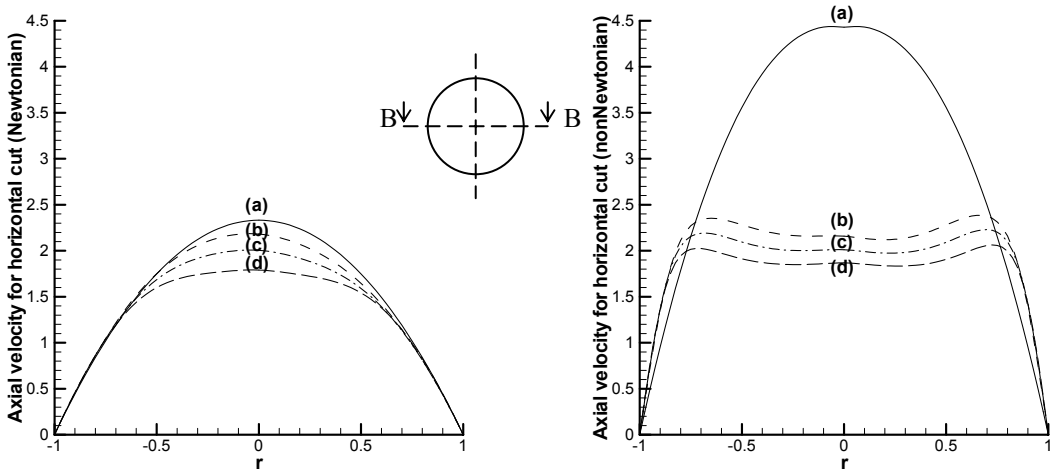

Figure 4.5 Axial velocity profiles in the horizontal cut view of the pipe for the Newtonian and non-Newtonian fluid flow for *dp/ds*=-300, λ =0.1 and different values of curvature: (a) ε =0 (b) ε =0.05 (c) ε =0.1 (d) ε =0.2

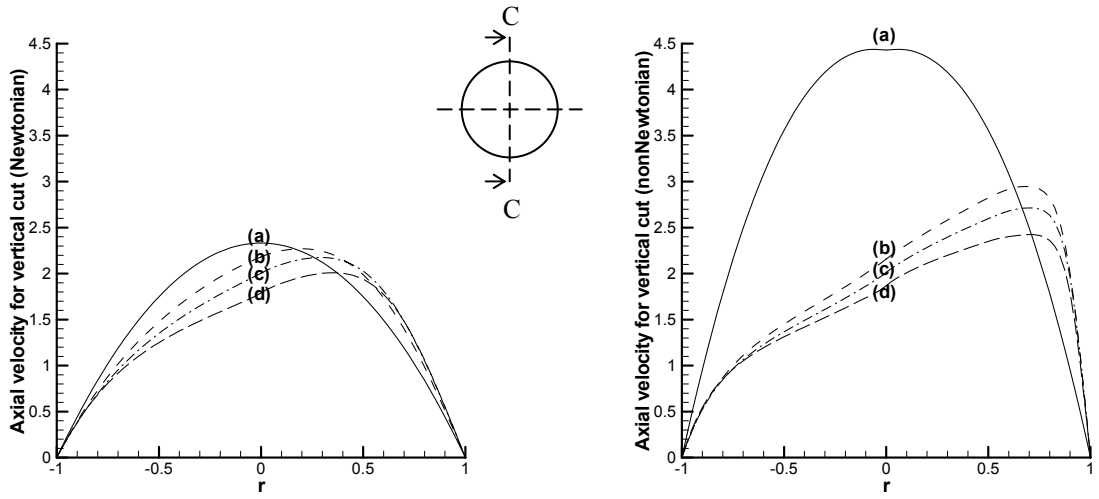

Figure 4.6 Axial velocity profiles in the vertical cut view of the pipe for the Newtonian and non-Newtonian fluids flow for *dp/ds*=-300, λ =0.1 and different values of curvature: (a) ε =0 (b) ε =0.05 (c) ε =0.1 (d) ε =0.2

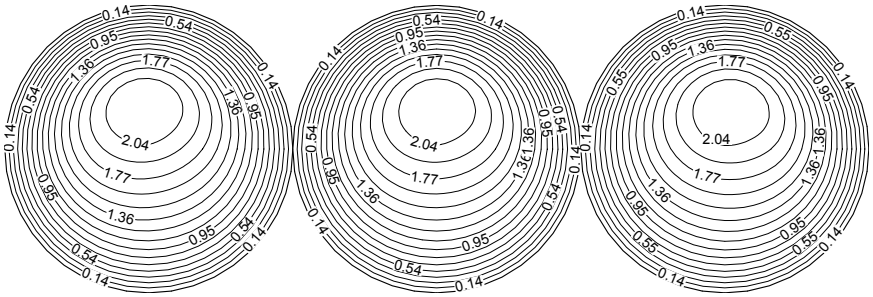

Contour lines of the axial velocity

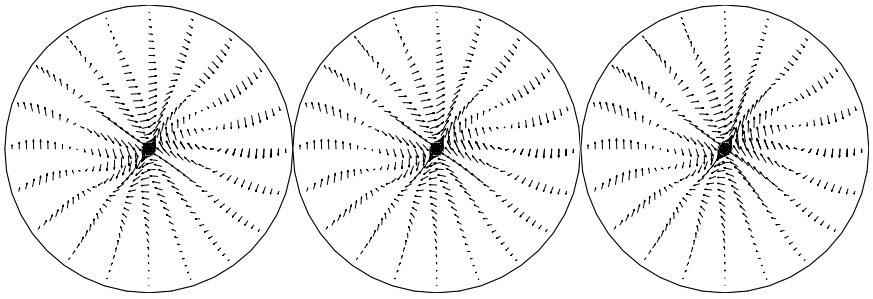

Vector plot of the secondary flow

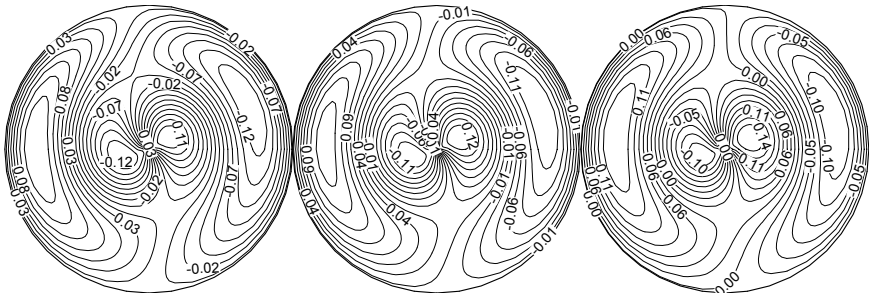

Contour lines of the circumferential velocity

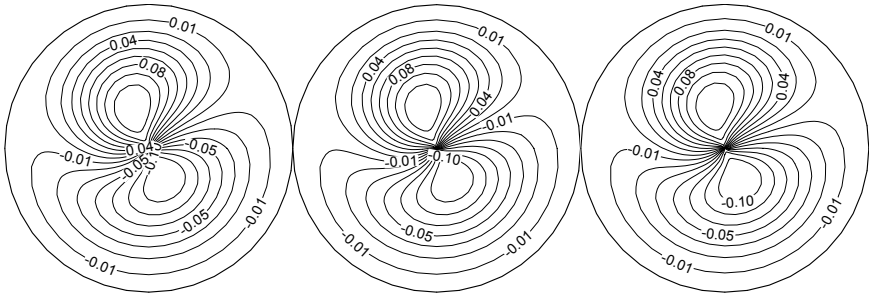

Contour lines of the radial velocity

(a) (b) (c)

Figure 4.7 Velocity components for the Newtonian fluid flow at *dp/ds*=-300, ε =0.1 for different values of the ratio of torsion to curvature: (a) λ =0.1 (b) λ =0.5 (c) λ =1.0

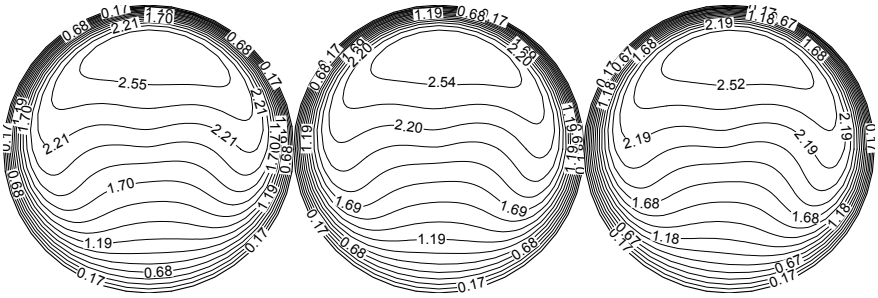

Contour lines of the axial velocity

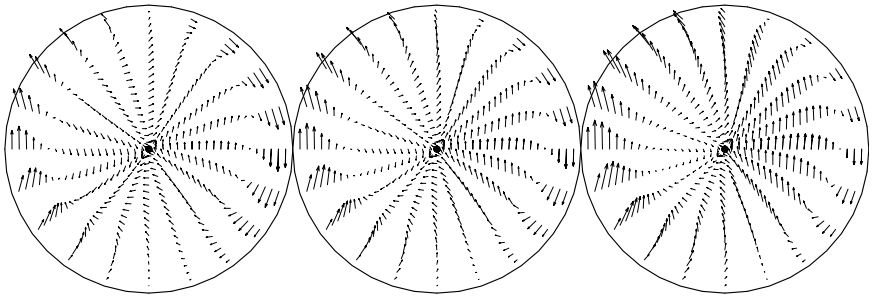

Vector plot of the secondary flow

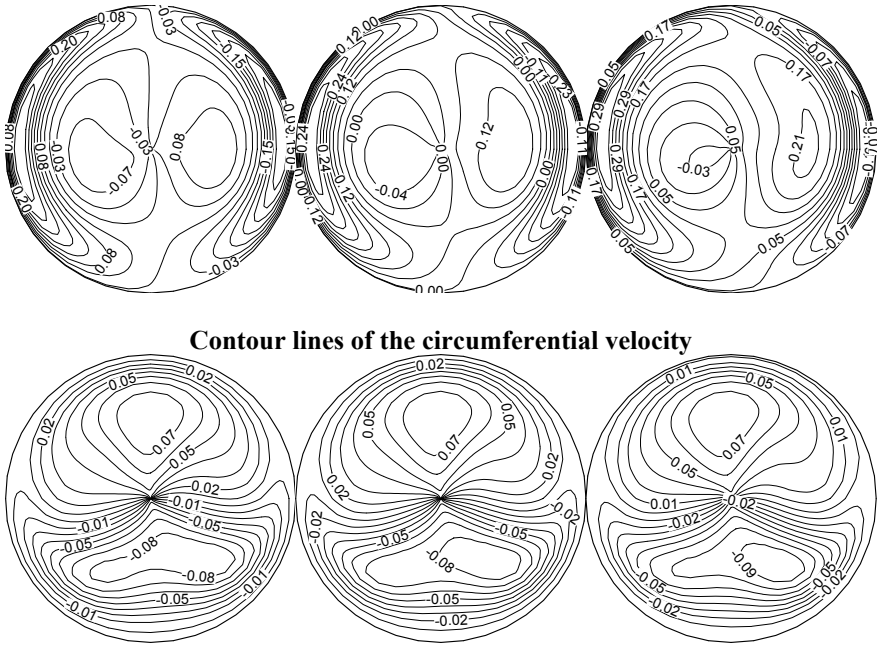

Figure 4.8 Velocity components for the non-Newtonian fluid flow at dp/ds=-300, ε =0.1 for different values of the ratio of torsion to curvature: (a) λ =0.1 (b) λ =0.5 (c) λ =1.0

4.5 CONCLUSIONS

The laminar flow of a non-Newtonian fluid in a helical pipe is modeled using the orthogonal helical coordinate system. Comparisons of the effects of the pressure gradient, curvature, and torsion on the Newtonian and non-Newtonian fluid flows are performed. For the geometrically same helical pipe, increasing the pressure gradient increases the axial velocity and also the distance by which the position of the maximum axial velocity is dragged from the center to the outer wall. These effects are more significant for a non-Newtonian than for a Newtonian fluid. When the pressure gradient is small, the parabolic profile of the axial velocity can still be observed for both non-Newtonian and Newtonian fluids. The study of the effect of curvature on the helical pipe flow is presented by the contour lines and profiles of the axial velocity. It is shown that when the dimensionless curvature increases, the position

of the maximum axial velocity moves farther from the pipe axis to the outer wall and the value of the maximum velocity decreases. The comparison between the behaviors of the Newtonian and non-Newtonian fluids shows that the change for the Newtonian fluid is smoother than that for the non-Newtonian fluid when the dimensionless curvature is changed. Two local maxima that are shown on axial velocity profiles in the horizontal cut view of the pipe for the non-Newtonian fluid cannot be observed for the Newtonian fluid. The position of the maximum axial velocity is more displaced to the outer wall for the non-Newtonian fluid. There is an abrupt change of the dynamics of the non-Newtonian flow between a straight pipe and a helical pipe with small curvature, shown in this chapter as the cases of ε=0 and ε=0.05, but this is not true for the Newtonian flow. The change of λ does not significantly influence the axial velocity but changes the behavior of the secondary flow for both the Newtonian and non-Newtonian flows, however, the effect of λ is more apparent for the non-Newtonian than for the Newtonian flow.

REFERENCES

1. Truesdell L.C. and Adler R.J. (1970) Numerical treatment of fully developed laminar flow in helically coiled tubes. *Aiche Journal*, 16:1010-1014.

2. Dean, W.R. (1927) Note on the motion of fluid in a curved pipe. *Philosophical Magazine*, 4 (7): 208-223.

3. Wang C.Y. (1981) On the low-Reynolds number flow in a helical pipe. *J. Fluid Mech.*, 108: 285-194.

4. Germano M. (1989) The Dean equations extended to a helical pipe flow. *J. Fluid Mech.*, 203: 289-305.

5. Germano M. (1982) On the effect of torsion on a helical pipe flow. *J. Fluid Mech.*, 125: 1-8.

6. Tuttle E.R. (1990) Laminar flow in twisted pipe. *J. Fluid Mech.,* 219: 545-570.

7. Liu, S. and Masliyah, J.H. (1993) Axially invariant laminar flow in helical pipes with a finite pitch. *J. Fluid Mech.*, 251: 315-353.

8. Yang, G., Dong, Z. F. and Ebadian, M. A. (1995) Laminar forced convection in a helicoidal pipe with finite pitch. *Int. J. Heat Mass Transfer*, 38 (5): 853-862.

9. Hüttl, T.J. (1997) Navier Stokes solutions of laminar flows based on orthogonal helical coordinates. *Numerical Methods in Laminar and Turbulent Flow*, 10: 191-202.

10. Hüttl, T.J. (2000) Influence of curvature and torsion on turbulent flow in curved and helically coiled pipes. *Int. J. Heat and Fluid Flow*, 21: 345-353.

11. Sandeep, K.P. (1996) *Computational and experimental studies on the fluid dynamics and heat transfer aspects in conventional and helical holding tubes for aseptic food processing.* PhD Thesis, Pennsylvania State University, State College, Pennsylvania.

12. Sandeep, K.P., Zuritz, C.A. and Puri, V.M. (2000) Modeling non-Newtonian two-phase flow in conventional and helical-holding tubes. *Int. J. Food Science and Technology*, 35: 511-522.

13. Bird, R.B., Stewart, W.E. and Lightfoot, E.N. (2002) *Transport Phenomena*, 2nd ed. -New York: John Wiley and Sons.

14. Synge, J.L. and Schild, A. (1949) *Tensor Calculus*. -Toronto: University of Toronto Press.

15. Patankar, S.V. (1980) *Numerical Heat Transfer and Fluid Flow*. -New York: Hemisphere.

16. Tao, W. (1988) *Numerical Heat Transfer*. Xi'an: Xi'an Jiaotong University Press.

17. Hüttl, T.J. (1999) *Direkte Numerische Simulation turbulenter Strömungen in gekrümmten und tordierten Rohren*. Doktorarbeit, Technische Universität München, Fortschritt-Berichte VDI, Reihe 7, Nr. 364, VDI-Verlag Düsseldorf.

18. Huang, HC, Li, ZH and Usmani, A.S (1999) *Finite element analysis of non-Newtonian flow: theory and software*. - New York: Springer-Verlag.

5 HEAT TRANSFER IN A LAMINAR FLOW OF A NON-NEWTONIAN FLUID IN HELICAL PIPE

ABSTRACT

A numerical investigation of heat transfer in a fully-developed laminar flow of a non-Newtonian fluid in a helical pipe is carried out. The momentum and energy equations are derived in an orthogonal helical coordinate system. The case of a constant wall heat flux is considered. The effects of the Dean number, Germano number, and Prandtl number with a fixed Reynolds number on the hydrodynamics and heat transfer in non-Newtonian fluid flow in helical pipes are investigated.

Nomenclature

a	pipe radius, m
Dn	Dean number
g	gravity, m/s^2
Gn	Germano number
h_1, h_2, h_3	scale factors associated with orthogonal coordinates
h_s, h_r, h_θ	scale factors associated with orthogonal coordinates $\tilde{s}, \tilde{r}, \theta$, defined in Equation (5.14)
k	thermal conductivity, $W\ m^{-1}\ K^{-1}$
m	consistency factor, $Pa\ s^n$
n	power-law index

Nu	Nusselt number
Re_F	Reynlods number
r	dimensionless radial coordinate, $\tilde{r}/a$
$\tilde{r}$	radial coordinate, m
s	dimensionless axial coordinate, $\tilde{s}/a$
$\tilde{s}$	axial coordinate, m
p	pitch, m
P	dimensionless pressure, $\tilde{P}/\rho U^2$
$\tilde{P}$	pressure, Pa
Pr	Prandtl number
$\tilde{t}$	time, s
T	dimensionless temperature, defined in Equation (5.22)
$\tilde{T}$	temperature, K
$\tilde{T}_b$	bulk temperature, defined in Equation (5.22), K
$\tilde{T}_w$	wall temperature, K
U	bulk velocity, defined in Equation (5.22), m/s
v	velocity vector, m/s
u_s, u_r, u_θ	velocity components, m s^{-1}

w, u, v	dimensionless velocity components, $\frac{u_s}{U}, \frac{u_r}{U}, \frac{u_\theta}{U}$

Greek symbols

ε	dimensionless curvature, κa
θ	angle, defined in Fig. 5.1
κ	curvature, m^{-1}
λ	the ratio of torsion to curvature, τ / κ
μ_e	effective dynamic viscosity of non-Newtonian fluid, kg m^{-1} s^{-1}
μ_F	reference dynamic viscosity, defined in Equation (5.25), kg m^{-1} s^{-1}
$\hat{\mu}$	dimensionless effective dynamic viscosity of non-Newtonian fluid, $\frac{\mu_e}{\mu_F}$
ξ	angle, defined in Eq. (5.18)
ξ_1, ξ_2, ξ_3	orthogonal coordinates
ρ	fluid density, $\mathrm{kg\ m}^{-3}$
τ	torsion, m^{-1}
$\hat{\tau}$	shear stress, $\mathrm{N/\ m}^2$
ϕ	angle, defined in Equation (5.2)

Subscripts

s	axial direction
r	radial direction

θ tangential direction

5.1 INTRODUCTION

Helical pipe heat exchangers are extensively used in dairy and food processing as well as in refrigeration and hydrocarbon processing. Helical pipes provide a larger heat exchange surface than straight pipes in a given space with relative simplicity and economy. Also, compared to straight pipes, helical pipes yield higher heat transfer coefficients. As fluid flows within a helical pipe, it experiences a centrifugal force along with the axial pressure gradient. The centrifugal force induces secondary flow, resulting in an increased axial velocity near the pipe outer wall and decreased axial velocity near the pipe inner wall. At the pipe outer wall, the higher velocity decreases the thermal resistance considerably, resulting in a higher heat transfer coefficient (Shah and Joshi [1]).

Jeschke [2] performed the first experimental study on the turbulent flow of air in a curved pipe. His experimental formula was revised by Merkel [3] and the revised formula was referenced as Jeschke's formula in many books. Experimental measurements of fluid flow and heat transfer in helical and curved pipes were later performed by Dravid et al. [4], Balejova et al. [5], Janssen and Hoogendoorn [6], Kalb and Seader [7], and Ausern and Soliman [8].

The first theoretical study of fluid flow in a helical pipe was performed by Dean [9] for the case of fully developed laminar flow. He introduced a new parameter to characterize the magnitude and the shape of the secondary motion, which was later called the Dean number, $Dn = \varepsilon^{1/2}\,\mathrm{Re}$. Wang [10] introduced a non-orthogonal coordinate system to derive Navier-Stokes equations for the helical pipe flow and concluded that both curvature and torsion can

produce a first-order effect on the flow in a helical pipe. Germano [11, 12] suggested an orthogonal coordinate system and showed that the effect of torsion on the secondary flow is of second order. He also introduced another parameter that later was called the Germano number, $Gn = \varepsilon\lambda \,\mathrm{Re}$.

According to Shah and Joshi [1], the enhancement of heat transfer in curved ducts compared to that in straight ducts is most prominent for the laminar flow. For the turbulent flow, curved ducts offer no other significant advantage than space saving. Therefore, the laminar flow in helical pipe attracts most attention. Numerical computations of the laminar flow and heat transfer in helical pipes were reported in Sankariah and Rao [13] utilizing a toroidal coordinate system and in Patankar et al. [14] utilizing a curvilinear cylindrical coordinate system. Liu and Maliyah [15] numerically studied fully developed flows in helical pipes with a finite pitch and summarized the two controlling parameters, the Dean number, *Dn*, and the Germano number, *Gn*. The Dean number is a measure of the ratio of the square root of the product of inertial and centrifugal forces to the viscous forces. The Germano number is a measure of the ratio of the twisting to the viscous forces. Another dimensionless parameter, $\gamma = GnDn^{-3/2}$, was also proposed to analyze the combined effect of the curvature and torsion. The development of the Nusselt number at different Prandtl numbers was presented. Yang et al. [16] investigated the effects of the three parameters on fully developed laminar convective heat transfer in a helical pipe with a finite pitch: the Dean number, torsion, and Prandtl number.

In applications of helical pipes in chemical reactors, food processing, and medical equipment (such as kidney dialysis machines), the fluids flowing in the pipes are often non-Newtonian. However, publications on non-Newtonian flows in helical pipes are very limited. Hsu and

Patankar [17] computed fully developed Nusselt numbers for a power-law fluid. Sandeep et al. [18] modeled flows of non-Newtonian fluids in helical pipes using the Ostwald-de Waele model. However, none of these publications used an orthogonal helical coordinate system, so the effects of the curvature and torsion on the secondary flow in the plane normal to the main flow could not be fully clarified. In this chapter, the orthogonal coordinate system is adopted to investigate a fully developed laminar flow of a non-Newtonian fluid in a helical pipe and governing momentum and energy equations in this coordinate system are derived. The effects of the Dean number, Germano number, and Prandtl number with a fixed Reynolds number on the hydrodynamics and heat transfer in non-Newtonian fluid flow in helical pipes are investigated.

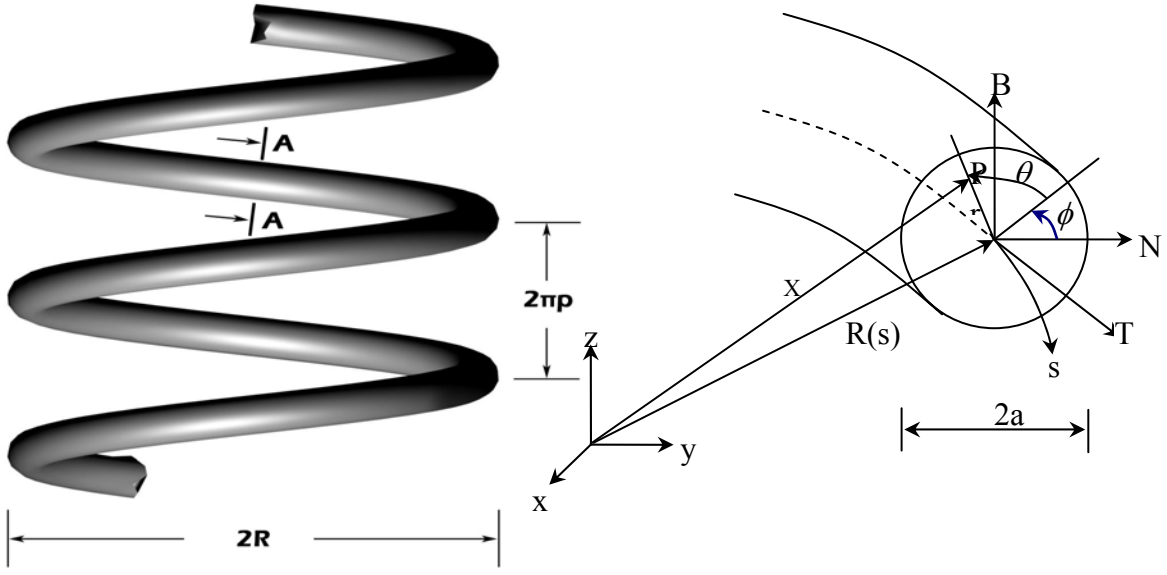

(a) **(b)**

Figure 5.1 Schematic diagram of a helical pipe and the orthogonal helical coordinate system

5.2 THE GOVERNING EQUATIONS

Figure 5.1 depicts the schematic diagram of the helical pipe and the orthogonal helical coordinate system. The geometrical parameters include the pipe diameter, 2*a*, coil diameter, 2*R*, and pitch, *p*. The curvature, κ, and the torsion, τ, are defined as $\kappa = R/(R^2 + p^2)$ and $\tau = p/(R^2 + p^2)$, respectively. Germano [11, 12] introduced this orthogonal helical coordinate system with the helical coordinate $\tilde{s}$ for the axial direction, $\tilde{r}$ for the radial direction, and θ for the circumferential direction. The metric of this coordinate system is given by

$$d\tilde{\mathbf{x}} \cdot d\tilde{\mathbf{x}} = [1 + \kappa\tilde{r}\sin(\theta + \phi)]^2 (d\tilde{s})^2 + (d\tilde{r})^2 + \tilde{r}^2 (d\theta)^2 \qquad (5.1)$$

where

$$\phi(\tilde{s}) = -\int_{\tilde{s}_0}^{\tilde{s}} \tau(\tilde{s}')d\tilde{s}' \qquad (5.2)$$

The continuity and momentum equations in the vector form are

$$\nabla \cdot \mathbf{v} = 0 \qquad (5.3)$$

and

$$\frac{\partial}{\partial \tilde{t}} \rho\mathbf{v} = -[\nabla \cdot \rho\mathbf{v}\mathbf{v}] - \nabla\tilde{P} - [\nabla \cdot \hat{\tau}] + \rho\mathbf{g} \qquad (5.4)$$

With the help of Equation (5.3), Equation (5.4) can be rearranged as

$$\rho \frac{D\mathbf{v}}{D\tilde{t}} = -\nabla\tilde{P} - [\nabla \cdot \hat{\tau}] + \rho\mathbf{g} \qquad (5.5)$$

For non-Newtonian fluids, the Ostwald-de Waele model (Bird et al. [19]) (the power law model) is the most common one. Incorporating this model into the mathematical formulation can be done in two ways. The straightforward method of doing this is to directly use an equation for the shear stress of a non-Newtonian fluid in the momentum equation (Equation

(5.5)). The other approach is to use the effective viscosity, which replaces the Newtonian viscosity in the momentum equation. In this study, the latter approach is chosen due to its simplicity in programming. The Navier-Stokes equations for a non-Newtonian fluid can be derived by using the effective viscosity of a non-Newtonian fluid to substitute the Newtonian viscosity in the governing equations:

$$\rho \frac{D\mathbf{v}}{D\widetilde{t}} = -\nabla \widetilde{P} + \nabla \cdot \mu_e \nabla \mathbf{v} \,. \tag{5.6}$$

A particular expression for the effective viscosity of a power law fluid is given later on by Equation (5.23). Equation (5.6) can be expanded for the steady flow as

$$(\mathrm{v} \cdot \nabla)\mathbf{v} = -\frac{1}{\rho}\nabla \widetilde{P} + \frac{\mu_e}{\rho}\left[\nabla(\nabla \cdot \mathbf{v}) - \left[\nabla \times \nabla \times \mathbf{v}\right]\right] + \frac{1}{\rho}\nabla \mu_e \cdot \nabla \mathrm{v} \tag{5.7}$$

where $\mathbf{v} = (v_1, v_2, v_3)$ is the dimensional fluid velocity vector. In an orthogonal coordinate system the continuity equation is given by

$$\frac{1}{h_1 h_2 h_3}\left[\frac{\partial(h_2 h_3 v_1)}{\partial \xi_1} + \frac{\partial(h_3 h_1 v_2)}{\partial \xi_2} + \frac{\partial(h_1 h_2 v_3)}{\partial \xi_3}\right] = 0\,, \tag{5.8}$$

where ξ_1, ξ_2, and ξ_3 are the orthogonal coordinates, and h_1, h_2, and h_3 are the scale factors.

The momentum equations are derived as (Cheng and Kuznetsov [20]):

$$\begin{aligned}
Dv_1 &+ \frac{v_2}{h_2 h_1}\left(v_1 \frac{\partial h_1}{\partial \xi_2} - v_2 \frac{\partial h_2}{\partial \xi_1}\right) + \frac{v_3}{h_3 h_1}\left(v_1 \frac{\partial h_1}{\partial \xi_3} - v_3 \frac{\partial h_3}{\partial \xi_1}\right) = -\frac{1}{\rho}\frac{1}{h_1}\frac{\partial \widetilde{P}}{\partial \xi_1} \\
&+ \frac{\mu_e}{\rho}\left\{\frac{1}{h_1}\frac{\partial}{\partial \xi_1}\left\{\frac{1}{h_1 h_2 h_3}\left[\frac{\partial(h_2 h_3 v_1)}{\partial \xi_1} + \frac{\partial(h_3 h_1 v_2)}{\partial \xi_2} + \frac{\partial(h_1 h_2 v_3)}{\partial \xi_3}\right]\right\}\right. \\
&\quad \left. - \frac{1}{h_2 h_3}\left(\frac{\partial}{\partial \xi_2}\left(\frac{h_3}{h_1 h_2}\left(\frac{\partial}{\partial \xi_1}(h_2 v_2) - \frac{\partial}{\partial \xi_2}(h_1 v_1)\right)\right) - \frac{\partial}{\partial \xi_3}\left(\frac{h_2}{h_1 h_3}\left(\frac{\partial}{\partial \xi_3}(h_1 v_1) - \frac{\partial}{\partial \xi_1}(h_3 v_3)\right)\right)\right)\right\} \\
&+ \frac{1}{\rho}\frac{1}{h_1 h_2 h_3}\left[\frac{\partial v_1}{\partial \xi_1}\frac{\partial}{\partial \xi_1}\left(\frac{h_2 h_3}{h_1}\mu_e\right) + \frac{\partial v_1}{\partial \xi_2}\frac{\partial}{\partial \xi_2}\left(\frac{h_1 h_3}{h_2}\mu_e\right) + \frac{\partial v_1}{\partial \xi_3}\frac{\partial}{\partial \xi_3}\left(\frac{h_1 h_2}{h_3}\mu_e\right)\right]
\end{aligned} \tag{5.9a}$$

$$
\begin{aligned}
Dv_2 + \frac{v_3}{h_3 h_2}\left(v_2\frac{\partial h_2}{\partial \xi_3} - v_3\frac{\partial h_3}{\partial \xi_2}\right) + \frac{v_1}{h_1 h_2}\left(v_2\frac{\partial h_2}{\partial \xi_1} - v_1\frac{\partial h_1}{\partial \xi_2}\right) &= -\frac{1}{\rho}\frac{1}{h_2}\frac{\partial \widetilde{P}}{\partial \xi_2} \\
+\frac{\mu_e}{\rho}\left\{\frac{1}{h_2}\frac{\partial}{\partial \xi_2}\left\{\frac{1}{h_1 h_2 h_3}\left[\frac{\partial(h_2 h_3 v_1)}{\partial \xi_1} + \frac{\partial(h_3 h_1 v_2)}{\partial \xi_2} + \frac{\partial(h_1 h_2 v_3)}{\partial \xi_3}\right]\right\}\right. & \\
\left. -\frac{1}{h_1 h_3}\left(\frac{\partial}{\partial \xi_3}\left(\frac{h_1}{h_2 h_3}\left(\frac{\partial}{\partial \xi_2}(h_3 v_3) - \frac{\partial}{\partial \xi_3}(h_2 v_2)\right)\right) - \frac{\partial}{\partial \xi_1}\left(\frac{h_3}{h_1 h_2}\left(\frac{\partial}{\partial \xi_1}(h_2 v_2) - \frac{\partial}{\partial \xi_2}(h_1 v_1)\right)\right)\right)\right\} & \\
+\frac{1}{\rho}\frac{1}{h_1 h_2 h_3}\left[\frac{\partial v_2}{\partial \xi_1}\frac{\partial}{\partial \xi_1}\left(\frac{h_2 h_3}{h_1}\mu_e\right) + \frac{\partial v_2}{\partial \xi_2}\frac{\partial}{\partial \xi_2}\left(\frac{h_1 h_3}{h_2}\mu_e\right) + \frac{\partial v_2}{\partial \xi_3}\frac{\partial}{\partial \xi_3}\left(\frac{h_1 h_2}{h_3}\mu_e\right)\right] &
\end{aligned}
\tag{5.9b}
$$

$$
\begin{aligned}
Dv_3 + \frac{v_1}{h_1 h_3}\left(v_3\frac{\partial h_3}{\partial \xi_1} - v_1\frac{\partial h_1}{\partial \xi_3}\right) + \frac{v_2}{h_2 h_3}\left(v_3\frac{\partial h_3}{\partial \xi_2} - v_2\frac{\partial h_2}{\partial \xi_3}\right) &= -\frac{1}{h_3}\frac{1}{\rho}\frac{\partial \widetilde{P}}{\partial \xi_3} \\
+\frac{\mu_e}{\rho}\left\{\frac{1}{h_3}\frac{\partial}{\partial \xi_3}\left\{\frac{1}{h_1 h_2 h_3}\left[\frac{\partial(h_2 h_3 v_1)}{\partial \xi_1} + \frac{\partial(h_3 h_1 v_2)}{\partial \xi_2} + \frac{\partial(h_1 h_2 v_3)}{\partial \xi_3}\right]\right\}\right. & \\
\left. -\frac{1}{h_1 h_2}\left(\frac{\partial}{\partial \xi_1}\left(\frac{h_2}{h_1 h_3}\left(\frac{\partial}{\partial \xi_3}(h_1 v_1) - \frac{\partial}{\partial \xi_1}(h_3 v_3)\right)\right) - \frac{\partial}{\partial \xi_2}\left(\frac{h_1}{h_2 h_3}\left(\frac{\partial}{\partial \xi_2}(h_3 v_3) - \frac{\partial}{\partial \xi_3}(h_2 v_2)\right)\right)\right)\right\} & \\
+\frac{1}{\rho}\frac{1}{h_1 h_2 h_3}\left[\frac{\partial v_3}{\partial \xi_1}\frac{\partial}{\partial \xi_1}\left(\frac{h_2 h_3}{h_1}\mu_e\right) + \frac{\partial v_3}{\partial \xi_2}\frac{\partial}{\partial \xi_2}\left(\frac{h_1 h_3}{h_2}\mu_e\right) + \frac{\partial v_3}{\partial \xi_3}\frac{\partial}{\partial \xi_3}\left(\frac{h_1 h_2}{h_3}\mu_e\right)\right] &
\end{aligned}
\tag{5.9c}
$$

where

$$
D = \frac{v_1}{h_1}\frac{\partial}{\partial \xi_1} + \frac{v_2}{h_2}\frac{\partial}{\partial \xi_2} + \frac{v_3}{h_3}\frac{\partial}{\partial \xi_3} \tag{5.10}
$$

Utilizing the continuity equation, it can be shown that for any variable ϕ , Eq. (5.10) can be recast as

$$
D\phi = \frac{1}{h_1 h_2 h_3}\left(\frac{\partial h_2 h_3 v_1 \phi}{\partial \xi_1} + \frac{\partial h_1 h_3 v_2 \phi}{\partial \xi_2} + \frac{\partial h_1 h_2 v_3 \phi}{\partial \xi_3}\right) \tag{5.11}
$$

Assuming constant thermal conductivity *k*, the energy equation is given by

$$
\rho c_p \frac{D\widetilde{T}}{Dt} = k\nabla^2 \widetilde{T} \tag{5.12}
$$

For steady state flow, this equation can be presented as

$$\rho c_p \frac{1}{h_1 h_2 h_3}\left(\frac{\partial h_2 h_3 v_1 \widetilde{T}}{\partial \xi_1}+\frac{\partial h_1 h_3 v_2 \widetilde{T}}{\partial \xi_2}+\frac{\partial h_1 h_2 v_3 \widetilde{T}}{\partial \xi_3}\right)= \\ k\frac{1}{h_1 h_2 h_3}\left(\frac{\partial}{\partial \xi_1}\left[\frac{h_2 h_3}{h_1}\frac{\partial \widetilde{T}}{\partial \xi_1}\right]+\frac{\partial}{\partial \xi_2}\left[\frac{h_1 h_3}{h_2}\frac{\partial \widetilde{T}}{\partial \xi_2}\right]+\frac{\partial}{\partial \xi_3}\left[\frac{h_1 h_2}{h_3}\frac{\partial \widetilde{T}}{\partial \xi_3}\right]\right) \tag{5.13}$$

In the orthogonal helical coordinate system $(\widetilde{s},\widetilde{r},\theta)$, where tilde indicates a dimensional variable, the scale factors h_s, h_r, and h_θ are expressed as

$$h_s = 1+\kappa\widetilde{r}\sin(\theta+\phi) \qquad h_r = 1 \qquad h_\theta = \widetilde{r} \tag{5.14}$$

Thus, the governing equations for a non-Newtonian fluid in the orthogonal helical coordinate system are the continuity equation

$$\frac{\partial(\widetilde{r}u_s)}{\partial \widetilde{s}}+\frac{\partial(\widetilde{r}h_s u_r)}{\partial \widetilde{r}}+\frac{\partial(h_s u_\theta)}{\partial \theta}=0 \tag{5.15}$$

and the momentum and energy equations

$$\frac{1}{h_s\widetilde{r}}\left(\frac{\partial(\widetilde{r}u_s u_s)}{\partial \widetilde{s}}+\frac{\partial(\widetilde{r}h_s u_r u_s)}{\partial \widetilde{r}}+\frac{\partial(h_s u_\theta u_s)}{\partial \theta}\right)+\frac{k}{h_s}u_s\left(u_r\sin(\theta+\phi)+u_\theta\cos(\theta+\phi)\right)=-\frac{1}{\rho}\frac{1}{h_s}\frac{\partial \widetilde{P}}{\partial \widetilde{s}} \\ +\frac{\mu_e}{\rho}\left\{\frac{1}{h_s}\frac{\partial}{\partial \widetilde{s}}\left[\frac{1}{h_s\widetilde{r}}\left[\frac{\partial(\widetilde{r}u_s)}{\partial \widetilde{s}}+\frac{\partial(\widetilde{r}h_s u_r)}{\partial \widetilde{r}}+\frac{\partial(h_s u_\theta)}{\partial \theta}\right]\right]- \right. \\ \left. \frac{1}{\widetilde{r}}\left(\frac{\partial}{\partial \widetilde{r}}\left(\frac{\widetilde{r}}{h_s}\left(\frac{\partial u_r}{\partial \widetilde{s}}-\frac{\partial}{\partial \widetilde{r}}(h_s u_s)\right)\right)-\frac{\partial}{\partial \theta}\left(\frac{1}{h_s\widetilde{r}}\left(\frac{\partial}{\partial \theta}(h_s u_s)-\frac{\partial}{\partial \widetilde{s}}(\widetilde{r}u_\theta)\right)\right)\right)\right\} \\ +\frac{1}{\rho}\frac{1}{h_s\widetilde{r}}\left[\frac{\partial u_s}{\partial \widetilde{s}}\frac{\partial}{\partial \widetilde{s}}\left(\frac{\widetilde{r}}{h_s}\mu_e\right)+\frac{\partial u_s}{\partial r}\frac{\partial}{\partial r}(h_s\widetilde{r}\mu_e)+\frac{\partial u_s}{\partial \theta}\frac{\partial}{\partial \theta}\left(\frac{h_s}{\widetilde{r}}\mu_e\right)\right] \tag{5.16a}$$

$$\frac{1}{h_s\widetilde{r}}\left(\frac{\partial(\widetilde{r}u_s u_r)}{\partial \widetilde{s}}+\frac{\partial(\widetilde{r}h_s u_r u_r)}{\partial \widetilde{r}}+\frac{\partial(h_s u_\theta u_r)}{\partial \theta}\right)-\frac{{u_\theta}^2}{\widetilde{r}}-\frac{k}{h_s}{u_s}^2\sin(\theta+\phi)=-\frac{1}{\rho}\frac{\partial \widetilde{P}}{\partial \widetilde{r}} \\ +\frac{\mu_e}{\rho}\left\{\frac{\partial}{\partial \widetilde{r}}\left[\frac{1}{h_s\widetilde{r}}\left[\frac{\partial(\widetilde{r}u_s)}{\partial \widetilde{s}}+\frac{\partial(\widetilde{r}h_s u_r)}{\partial \widetilde{r}}+\frac{\partial(h_s u_\theta)}{\partial \theta}\right]\right]- \right. \\ \left. \frac{1}{h_s\widetilde{r}}\left(\frac{\partial}{\partial \theta}\left(\frac{h_s}{\widetilde{r}}\left(\frac{\partial}{\partial \widetilde{r}}(\widetilde{r}u_\theta)-\frac{\partial u_r}{\partial \theta}\right)\right)-\frac{\partial}{\partial \widetilde{s}}\left(\frac{\widetilde{r}}{h_s}\left(\frac{\partial u_r}{\partial \widetilde{s}}-\frac{\partial}{\partial \widetilde{r}}(h_s u_s)\right)\right)\right)\right\} \\ +\frac{1}{\rho}\frac{1}{h_s\widetilde{r}}\left[\frac{\partial u_r}{\partial \widetilde{s}}\frac{\partial}{\partial \widetilde{s}}\left(\frac{\widetilde{r}}{h_s}\mu_e\right)+\frac{\partial u_r}{\partial \widetilde{r}}\frac{\partial}{\partial r}(h_s\widetilde{r}\mu_e)+\frac{\partial u_r}{\partial \theta}\frac{\partial}{\partial \theta}\left(\frac{h_s}{\widetilde{r}}\mu_e\right)\right] \tag{5.16b}$$

$$\frac{1}{h_s\tilde{r}}\left(\frac{\partial(\tilde{r}u_s u_\theta)}{\partial\tilde{s}}+\frac{\partial(\tilde{r}h_s u_r u_\theta)}{\partial r}+\frac{\partial(h_s u_\theta u_\theta)}{\partial\theta}\right)-\frac{k}{h_s}u_s{}^2\cos(\theta+\phi)+\frac{u_r u_\theta}{\tilde{r}}=-\frac{1}{\rho}\frac{1}{\tilde{r}}\frac{\partial\tilde{P}}{\partial\theta}$$
$$+\frac{\mu_e}{\rho}\left\{\frac{1}{\tilde{r}}\frac{\partial}{\partial\theta}\left[\frac{1}{h_s\tilde{r}}\left[\frac{\partial(\tilde{r}u_s)}{\partial\tilde{s}}+\frac{\partial(\tilde{r}h_s u_r)}{\partial\tilde{r}}+\frac{\partial(h_s u_\theta)}{\partial\theta}\right]\right]-\right.$$
$$\left.\frac{1}{h_s}\left(\frac{\partial}{\partial s}\left(\frac{1}{h_s\tilde{r}}\left(\frac{\partial}{\partial\theta}(h_s u_s)-\frac{\partial}{\partial\tilde{s}}(\tilde{r}u_\theta)\right)\right)-\frac{\partial}{\partial\tilde{r}}\left(\frac{h_s}{\tilde{r}}\left(\frac{\partial}{\partial\tilde{r}}(\tilde{r}u_\theta)-\frac{\partial}{\partial\theta}(u_r)\right)\right)\right)\right\} \qquad (5.16c)$$
$$+\frac{1}{\rho}\frac{1}{h_s\tilde{r}}\left[\frac{\partial u_\theta}{\partial\tilde{s}}\frac{\partial}{\partial\tilde{s}}\left(\frac{\tilde{r}}{h_s}\mu_e\right)+\frac{\partial u_\theta}{\partial r}\frac{\partial}{\partial r}(h_s\tilde{r}\mu_e)+\frac{\partial u_\theta}{\partial\theta}\frac{\partial}{\partial\theta}\left(\frac{h_s}{\tilde{r}}\mu_e\right)\right]$$

$$\left(\frac{\partial(\tilde{r}u_s\tilde{T})}{\partial\tilde{s}}+\frac{\partial(\tilde{r}h_s u_r\tilde{T})}{\partial\tilde{r}}+\frac{\partial(h_s u_\theta\tilde{T})}{\partial\theta}\right)= \qquad (5.17)$$
$$\frac{k}{\rho c_p}\left(\frac{\partial}{\partial\tilde{s}}\left[\frac{\tilde{r}}{h_s}\frac{\partial\tilde{T}}{\partial\tilde{s}}\right]+\frac{\partial}{\partial\tilde{r}}\left[h_s\tilde{r}\frac{\partial\tilde{T}}{\partial\tilde{r}}\right]+\frac{\partial}{\partial\theta}\left[\frac{h_s}{\tilde{r}}\frac{\partial\tilde{T}}{\partial\theta}\right]\right)$$

where $u_s, u_r, u_\theta, \tilde{P}$, and $\tilde{T}$ are the dimensional velocity components, pressure, and temperature, respectively. In this study a fully developed laminar flow is considered so that the dynamic variables, except for the pressure, are independent of *s*, therefore, a simplifying transformation is performed from *s*, *r*, θ to *s*, *r*, ξ :

$$\theta+\phi\Rightarrow\xi\,,\ \frac{\partial}{\partial\tilde{s}}\Rightarrow\frac{\partial}{\partial\tilde{s}}-\tau\frac{\partial}{\partial\xi}\,,\ \frac{\partial}{\partial\theta}\Rightarrow\frac{\partial}{\partial\xi} \qquad (5.18)$$

The governing equations are then reduced to the following dimensionless form (the dimensionless parameters are defined in Eq. (5.22)):

$$-\varepsilon\lambda\frac{\partial(rw)}{\partial\xi}+\frac{\partial(rh_s v)}{\partial r}+\frac{\partial(h_s u)}{\partial\xi}=0 \qquad (5.19)$$

$$\frac{1}{h_s r}\left(-\varepsilon\lambda\frac{\partial(rww)}{\partial\xi}+\frac{\partial(rh_s vw)}{\partial r}+\frac{\partial(h_s vw)}{\partial\xi}\right)+\frac{\varepsilon}{h_s}w(v\sin\xi+u\cos\xi)=-\frac{1}{h_s}\left(\frac{\partial P}{\partial s}-\varepsilon\lambda\frac{\partial P}{\partial\xi}\right)$$
$$+\frac{\hat{\mu}}{\mathrm{Re}_F}\left\{-\varepsilon\lambda\frac{1}{h_s}\frac{\partial}{\partial\xi}\left[\frac{1}{h_s r}\left[-\varepsilon\lambda\frac{\partial(rw)}{\partial\xi}+\frac{\partial(rh_s v)}{\partial r}+\frac{\partial(h_s u)}{\partial\xi}\right]\right]-\right. \qquad (5.20a)$$
$$\left.\frac{1}{r}\left(\frac{\partial}{\partial r}\left(\frac{r}{h_s}\left(-\varepsilon\lambda\frac{\partial v}{\partial\xi}-\frac{\partial}{\partial r}(h_s w)\right)\right)-\frac{\partial}{\partial\xi}\left(\frac{1}{h_s r}\left(\frac{\partial}{\partial\xi}(h_s w)+\varepsilon\lambda\frac{\partial}{\partial\xi}(ru)\right)\right)\right)\right\}$$
$$+\frac{1}{\mathrm{Re}_F}\left[\frac{(\varepsilon\lambda)^2}{h_s{}^2}\frac{\partial w}{\partial\xi}\frac{\partial\hat{\mu}}{\partial\xi}+\frac{\partial w}{\partial r}\frac{\partial\hat{\mu}}{\partial r}+\frac{1}{r^2}\frac{\partial w}{\partial\xi}\frac{\partial\hat{\mu}}{\partial\xi}\right]$$

$$\frac{1}{h_s r}\left(-\varepsilon\lambda\frac{\partial(rwv)}{\partial\xi}+\frac{\partial(rh_s vv)}{\partial r}+\frac{\partial(h_s uv)}{\partial\xi}\right)-\frac{{u_\theta}^2}{r}-\frac{\varepsilon}{h_s}w^2\sin\xi=-\frac{\partial P}{\partial r}$$
$$+\frac{\hat{\mu}}{\mathrm{Re}_F}\left\{\frac{\partial}{\partial r}\left[\frac{1}{h_s r}\left[-\varepsilon\lambda\frac{\partial(rw)}{\partial\xi}+\frac{\partial(rh_s v)}{\partial r}+\frac{\partial(h_s u)}{\partial\xi}\right]\right]\right.$$
$$\left.-\frac{1}{h_s r}\left(\frac{\partial}{\partial\xi}\left(\frac{h_s}{r}\left(\frac{\partial}{\partial r}(ru)-\frac{\partial v}{\partial\xi}\right)\right)+\varepsilon\lambda\frac{\partial}{\partial\xi}\left(\frac{r}{h_s}\left(-\varepsilon\lambda\frac{\partial v}{\partial\xi}-\frac{\partial}{\partial r}(h_s w)\right)\right)\right)\right\} \qquad (5.20b)$$
$$+\frac{1}{\mathrm{Re}_F}\left[\frac{(\varepsilon\lambda)^2}{{h_s}^2}\frac{\partial v}{\partial\xi}\frac{\partial\hat{\mu}}{\partial\xi}+\frac{\partial v}{\partial r}\frac{\partial\hat{\mu}}{\partial r}+\frac{1}{r^2}\frac{\partial v}{\partial\xi}\frac{\partial\hat{\mu}}{\partial\xi}\right]$$

$$\frac{1}{h_s r}\left(-\varepsilon\lambda\frac{\partial(rwu)}{\partial\xi}+\frac{\partial(rh_s vu)}{\partial r}+\frac{\partial(h_s uu)}{\partial\xi}\right)-\frac{\varepsilon}{h_s}w^2\cos\xi+\frac{vu}{r}=-\frac{1}{r}\frac{\partial P}{\partial\xi}$$
$$+\frac{\hat{\mu}}{\mathrm{Re}_F}\left\{\frac{1}{r}\frac{\partial}{\partial\xi}\left[\frac{1}{h_s r}\left[-\varepsilon\lambda\frac{\partial(rw)}{\partial\xi}+\frac{\partial(rh_s v)}{\partial r}+\frac{\partial(h_s u)}{\partial\xi}\right]\right]\right.$$
$$\left.-\frac{1}{h_s}\left(-\varepsilon\lambda\frac{\partial}{\partial\xi}\left(\frac{1}{h_s r}\left(\frac{\partial}{\partial\xi}(h_s w)+\varepsilon\lambda\frac{\partial}{\partial\xi}(ru)\right)\right)-\frac{\partial}{\partial r}\left(\frac{h_s}{r}\left(\frac{\partial}{\partial r}(ru)-\frac{\partial v}{\partial\xi}\right)\right)\right)\right\} \qquad (5.20c)$$
$$+\frac{1}{\mathrm{Re}_F}\left[\frac{(\varepsilon\lambda)^2}{{h_s}^2}\frac{\partial u}{\partial\xi}\frac{\partial\hat{\mu}}{\partial\xi}+\frac{\partial u}{\partial r}\frac{\partial\hat{\mu}}{\partial r}+\frac{1}{r^2}\frac{\partial u}{\partial\xi}\frac{\partial\hat{\mu}}{\partial\xi}\right]$$

$$\left(-\varepsilon\lambda\frac{\partial(rwT)}{\partial\xi}+\frac{\partial(rh_s vT)}{\partial r}+\frac{\partial(h_s uT)}{\partial\xi}\right)=ru_s\frac{1}{\mathrm{Re}_F\,\mathrm{Pr}}$$
$$+\frac{1}{\mathrm{Re}_F\,\mathrm{Pr}}\left((\varepsilon\lambda)^2\frac{\partial}{\partial\xi}\left[\frac{r}{h_s}\frac{\partial T}{\partial\xi}\right]+\frac{\partial}{\partial r}\left[h_s r\frac{\partial T}{\partial r}\right]+\frac{\partial}{\partial\xi}\left[\frac{h_s}{r}\frac{\partial T}{\partial\xi}\right]\right) \qquad (5.21)$$

where

$$s=\frac{\tilde{s}}{a},\ r=\frac{\tilde{r}}{a},\ (w,v,u)=\left(\frac{u_s}{U},\frac{u_r}{U},\frac{u_\theta}{U}\right),\ P=\frac{\tilde{P}}{\rho U^2},\varepsilon=\kappa a,\ \lambda=\frac{\tau}{\kappa},\hat{\mu}=\frac{\mu_e}{\mu_F},$$

$$\mathrm{Re}_F=\frac{\rho U a}{\mu_F},\ \mathrm{Pr}=\frac{c_p\mu}{k},Nu=\frac{2a}{k}\frac{q''_w}{(\tilde{T}_w-\tilde{T}_b)},U=\frac{1}{\pi}\int_0^{2\pi}\int_0^1 u_s r dr d\theta,T=\frac{\tilde{T}-\tilde{T}_w}{Nu(\tilde{T}_b-\tilde{T}_w)}, \qquad (5.22)$$

$$\tilde{T}_b=\frac{1}{U\pi}\int_0^{2\pi}\int_0^1 u_s\tilde{T}r dr d\theta$$

where a is the radius of the pipe, U is the bulk velocity defined in Eq. (5.22), and μ_F is a reference viscosity defined in Eq. (5.25).

The following expression for the effective viscosity of a power law fluid is used:

$$\mu_e = m[\frac{1}{2}(\Delta:\Delta)]^{\frac{n-1}{2}} \tag{5.23}$$

where Δ is the rate of deformation tensor and the expression for $(\Delta:\Delta)$ is given by

$$\begin{aligned}\frac{1}{2}(\Delta:\Delta) = 2\Bigg[&\left(\frac{\partial}{\partial\tilde{s}}\left(\frac{u_s}{h_s}\right)-\frac{\tau\kappa\tilde{r}\cos(\theta-\tilde{\omega}s)}{{h_s}^2}u_s+\frac{\kappa\sin(\theta-\tilde{\omega}s)}{h_s}u_r+\frac{\kappa\cos(\theta-\tilde{\omega}s)}{h_s}u_\theta\right)^2\\&+\left(\frac{\partial u_r}{\partial\tilde{r}}\right)^2+\left(\frac{\partial}{\partial\theta}\left(\frac{u_\theta}{\tilde{r}}\right)+\frac{u_r}{\tilde{r}}\right)^2\Bigg]+\left(h_s\frac{\partial}{\partial\tilde{r}}\left(\frac{u_s}{h_s}\right)+\frac{1}{h_s}\frac{\partial u_r}{\partial\tilde{s}}\right)^2\\&+\left(\frac{h_s}{\tilde{r}}\frac{\partial}{\partial\theta}\left(\frac{u_s}{h_s}\right)+\frac{\tilde{r}}{h_s}\frac{\partial}{\partial\tilde{s}}\left(\frac{u_\theta}{\tilde{r}}\right)\right)^2+\left(\tilde{r}\frac{\partial}{\partial\tilde{r}}\left(\frac{u_\theta}{\tilde{r}}\right)+\frac{1}{\tilde{r}}\frac{\partial u_r}{\partial\theta}\right)^2\end{aligned} \tag{5.24}$$

The reference viscosity μ_F is introduced as follows

$$\mu_F = m\left(\frac{U}{a}\right)^{n-1} \tag{5.25}$$

5.3 COMPUTATIONAL PROCEDURE

In the computational domain (the cross-section of the pipe), a uniform mesh is generated with evenly spaced grid in both radial and circumferential directions. The control volume-based finite difference method is applied and the convection-diffusion terms are discretized with the power-law scheme (Patankar [21]). The SIMPLE algorithm (Patankar [21]) is utilized on a staggered grid arrangement to solve equations (5.19)-(5.20).

A one-dimensional parabolic velocity profile is imposed as the initial guess and computations are terminated when the convergence criterion is met. A no-slip boundary condition and constant heat flux are assumed at the walls of the pipe. In this coordinate system, there is a geometrical singularity at the pipe axis (r=0), so boundary values are needed for flow

quantities, which are either located directly at the pipe axis or at the opposite sides of the pipe axis (Hüttl, [22]; Cheng and Kuznetsov [20]).

5.4 NUMERICAL RESULTS AND DISCUSSION

A constant wall heat flux is assumed for this study of the fully-developed laminar non-Newtonian flow in a helical pipe. Because of this thermal boundary condition, the axial temperature gradient is also constant. The parameters used to specify the non-Newtonian fluid, m and n, are 0.7 and 0.8. These parameter values are characteristic for CMC (carboxymethylcellulose), a modified cellulose gum, which is often used in food processing (Sandeep et al. [18]).

Due to the centrifugal force, when the non-Newtonian fluid flows through a helical pipe, the maximum of the axial velocity is shifted towards the outer wall and the parabolic profile is deformed (Fig. 5.2a). The secondary flow is shown in Figures 5.2b and 5.2c by a velocity vector plot and a contour plot of the stream function. The temperature distribution is also deformed and the maximum of the dimensionless temperature is shifted to the outer wall (Fig. 5.2d). The computed values for the Nusselt number show that helical pipes yield higher heat transfer coefficients compared to straight pipes. To test the accuracy of computations of the Nusselt number, the case of a fully-developed Newtonian flow with temperature-independent viscosity in a straight pipe (ε =0) is investigated. Computations yield Nu_{FD}=4.30. This is less than 2% off the exact value for the straight pipe (4.36) given in Bejan [23].

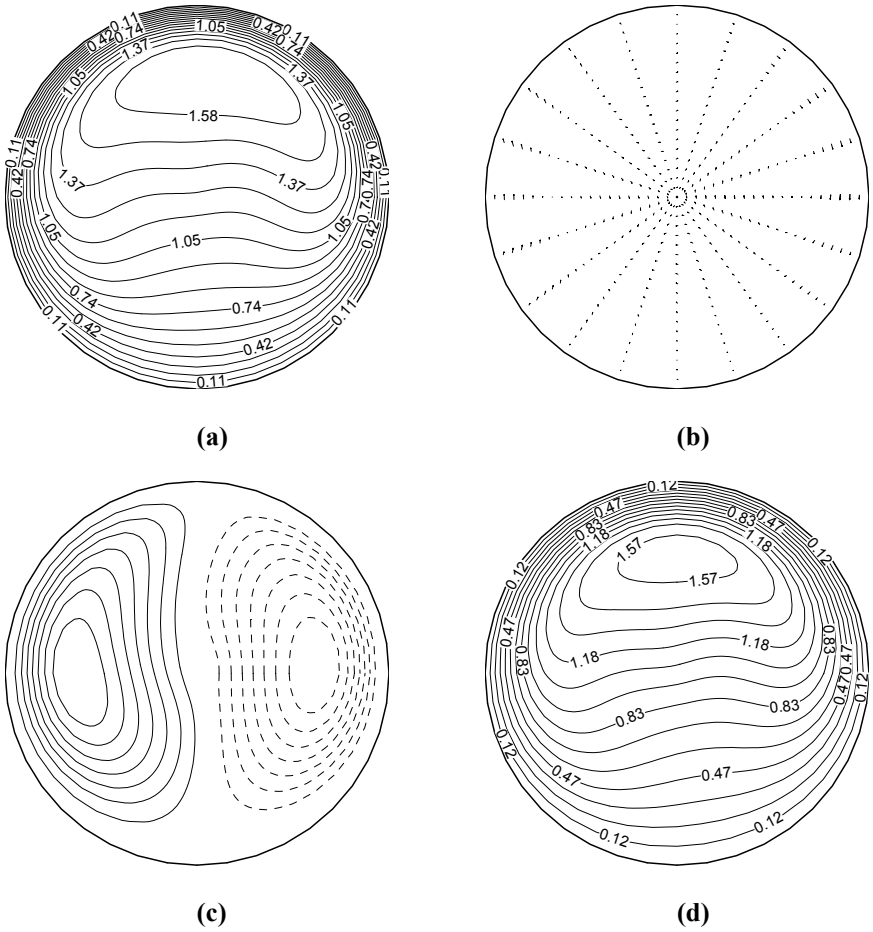

Figure 5.2 Dimensionless velocity and temperature fields in laminar non-Newtonian flow in a helical pipe, Re=1000, ε =0.01, λ =0.1, Pr=1.0 (a) contour lines of the dimensionless axial velocity (b) vector plots of the secondary flow (c) contour lines of the stream function (d) contour lines of the dimensionless temperature.

Figures 5.3, 5.4 and 5.5 display the effect of the Dean number on the dimensionless flow velocity and the dimensionless temperature. Figures 5.3 depicts the contour lines of the axial velocity and the velocity vector plot of the secondary flow for the same values of the Reynolds number, Germano number, and Prandtl number for different values of the dimensionless curvature, ε (so for different Dean numbers). Figure 5.3 shows that when *Dn* increases, the contour lines corresponding to large values of the axial velocity are displaced to the outer wall due to the centrifugal force. The vector plots of the secondary flow show that the effect of ε on the secondary flow is significant. The secondary flow becomes

stronger with an increase in the Dean number. Figure 5.4 shows the effect of the Dean number on the dimensionless temperature distribution. The effect is similar to that on the axial velocity except the maximum value of the dimensionless temperature increases when the Dean number is increased while that of the axial velocity decreases, as shown in the dimensionless axial velocity and temperature profiles in the horizontal and vertical cut views of the pipe (Figure 5.5). Table 5.1 also shows that the Nusselt number increases when the Dean number is increased. From the above comparison, it may be concluded that both heat transfer and fluid flow strongly depend on the dimensionless curvature of the pipe.

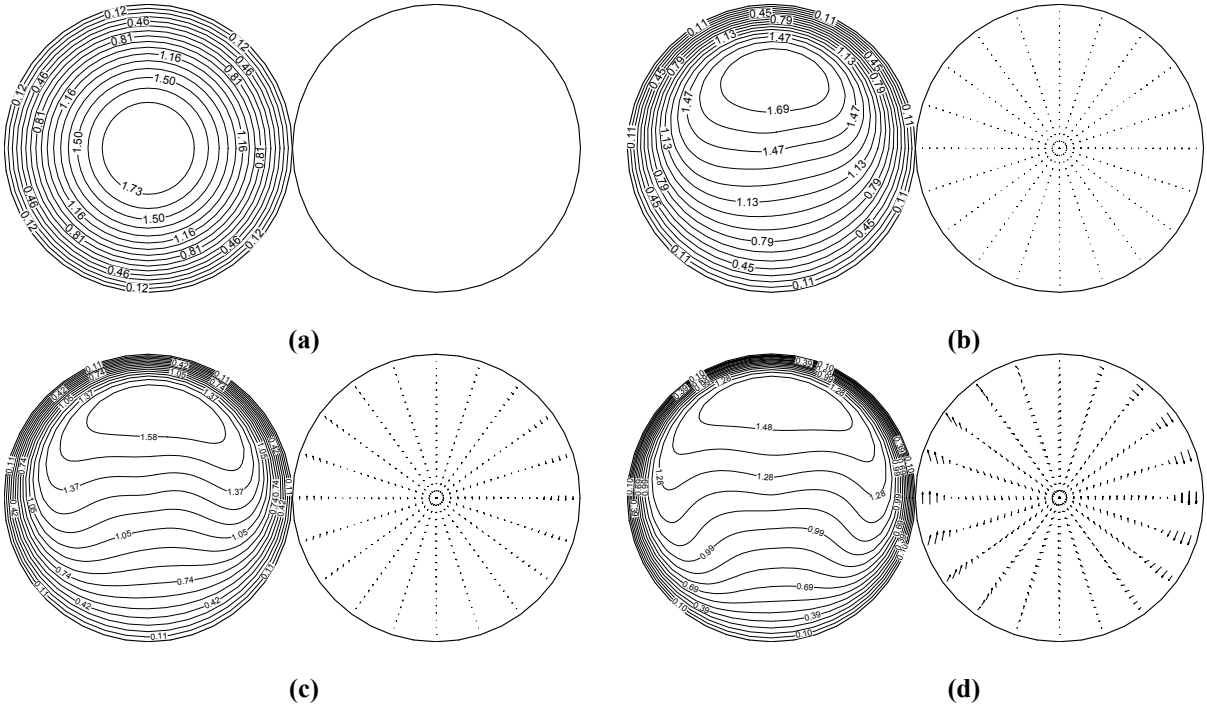

Figure 5.3 Contour lines of the dimensionless axial velocity and vector plots of the secondary flow at *Re*=1000, Gn=0.1, Pr =1.0 for different dimensionless curvatures: (a) ε =0.0, Dn=0.0 (b) ε =0.001, Dn=31.62 (c) ε =0.01, Dn=100.0 (d) ε =0.1, Dn=316.22

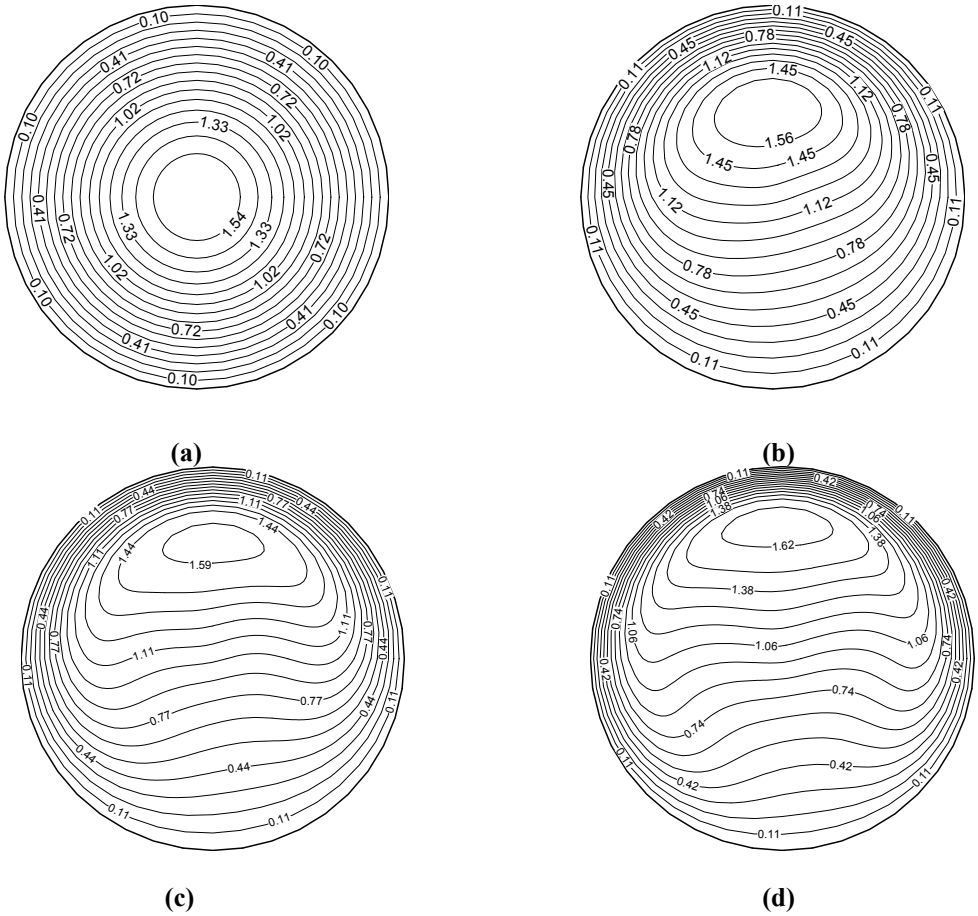

Figure 5.4 Contour lines of the dimensionless temperature at *Re*=1000, Gn=0.1, Pr =1.0 for different dimensionless curvatures: (a) ε =0.0, Dn=0.0 (b) ε =0.001, Dn=31.62 (c) ε =0.01, Dn=100.0 (d) ε =0.1, Dn=316.22

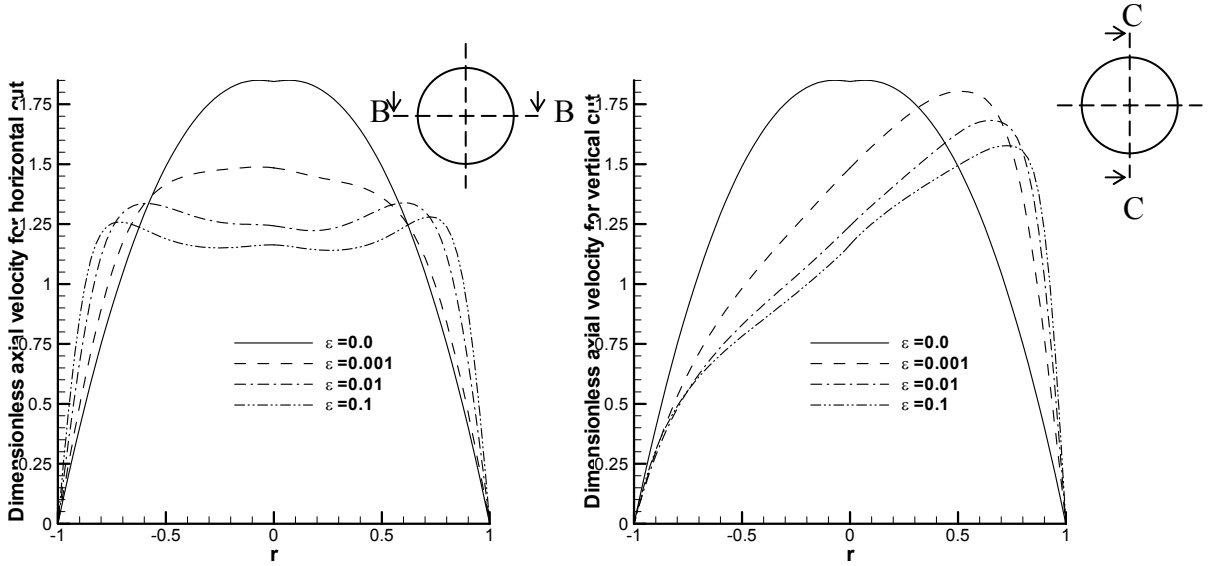

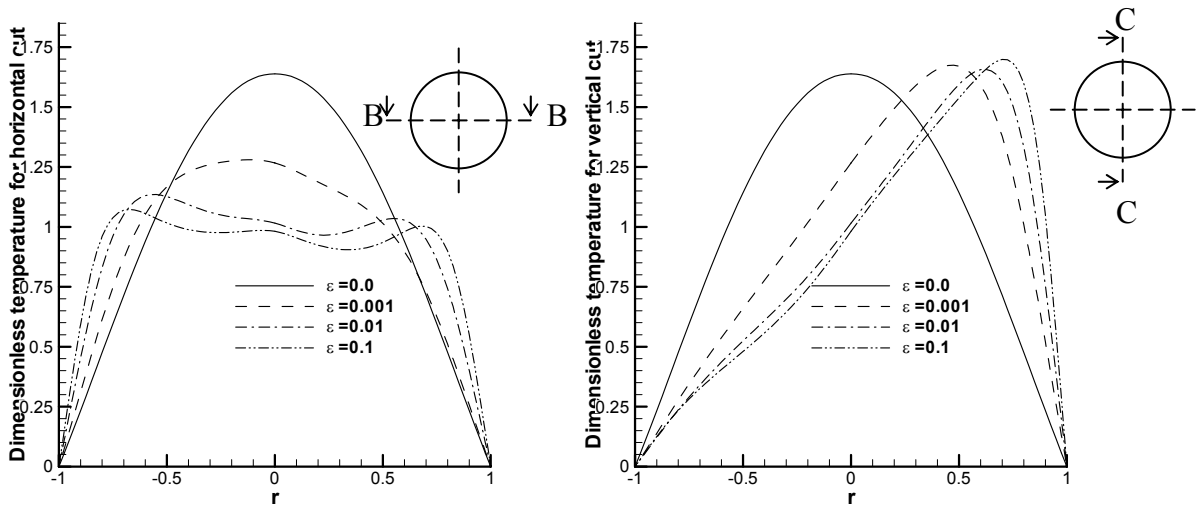

Figure 5.5 Profiles of the dimensionless axial velocity (top) and the dimensionless temperature (bottom) in the horizontal (left) and vertical (right) cut views of the pipe at *Re*=1000, Gn=0.1, Pr =1.0 for different dimensionless curvatures: (a) ε =0.0, Dn=0.0 (b) ε =0.001, Dn=31.62 (c) ε =0.01, Dn=100.0 (d) ε =0.1, Dn=316.22

Table 5.1 Nusselt number for different parameters

ε	λ	Pr	Dn	Gn	Nu
0	0.1	1.0	0.00	0	2.75
0.001	0.1	1.0	31.62	0.1	4.40
0.01	0.01	1.0	100.00	0.1	8.09
0.1	0.001	1.0	316.23	0.1	16.31
0.1	0.1	1.0	316.23	10.0	16.31
0.1	0.5	1.0	316.23	50.0	16.35
0.1	1.0	1.0	316.23	100.0	16.49
0.01	0.1	0.1	100.00	1.0	5.32
0.01	0.1	1.0	100.00	1.0	8.09
0.01	0.1	10	100.00	1.0	13.66

Figures 5.6 and 5.7 display the effect of the ratio of torsion to curvature, λ (which is characterized by the Germano number) when the Reynolds number is fixed, on the dynamics and heat transfer of a non-Newtonian flow in a helical pipe. The contour lines of the dimensionless axial velocity do not exhibit a strong dependence on the Germano number.

The dimensionless temperature distributions in the cross-section of a pipe are also similar for different values of *Gn*. From Table 5.1, it also can be observed that the Germano number does not significantly affect the heat transfer coefficient. However, vector plots of the secondary flow and the contour lines of the stream function in Figure 5.7 exhibit a dependence on the Germano number, a greater value of *Gn* corresponds to a stronger secondary flow. For small values of the Germano number, the symmetric pattern of the secondary flow is only slightly deformed. When λ is increased (the Germano number is increased), the symmetry is destroyed. Therefore, the Germano number influences the secondary flow but not as much as the axial velocity and heat transfer.

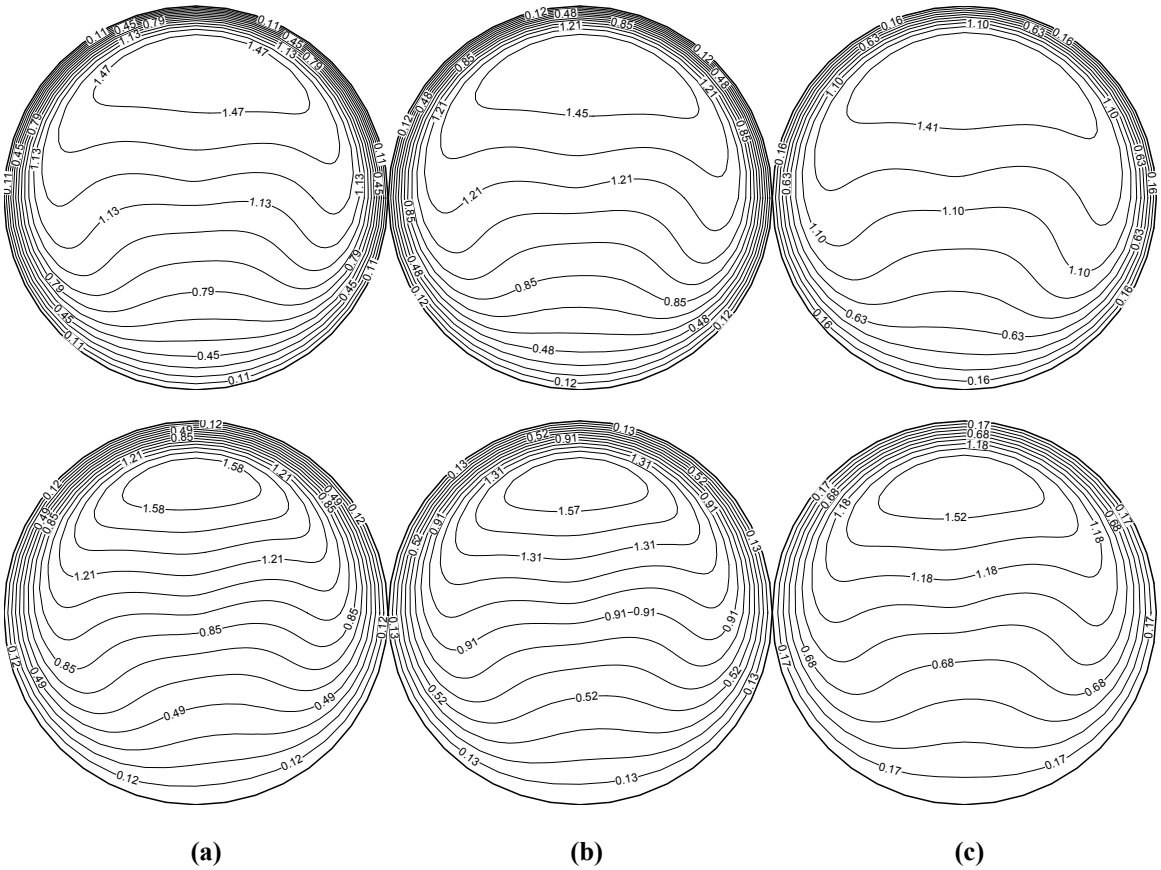

(a) **(b)** **(c)**

Figure 5.6 Contour lines of the dimensionless axial velocity (top) and the dimensionless temperature (bottom) at *Re*=1000, ε =0.1, Dn=316.22, Pr =1.0 for different dimensionless ratio of torsion to curvature: (a) λ =0.1, Gn=10.0 (b) λ =0.5, Gn=50.0 (c) λ =1.0, Gn=100.0

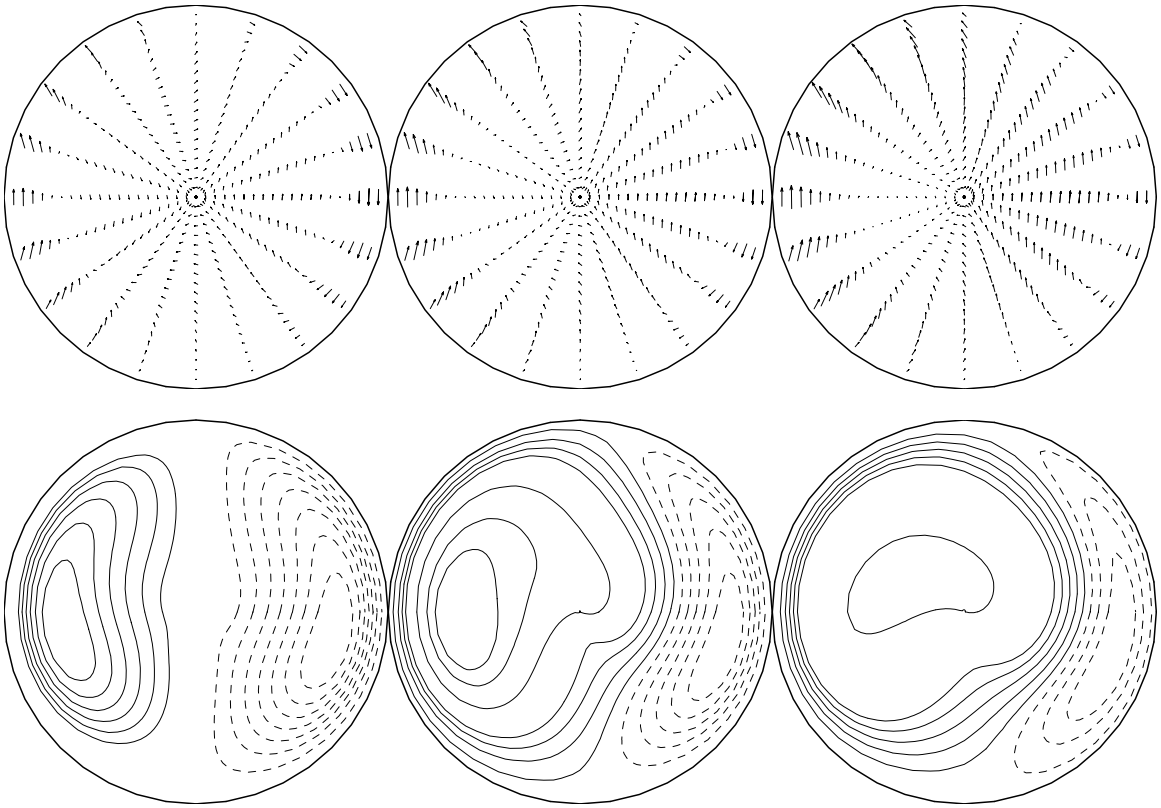

Figure 5.7 Vector plots of the secondary flow (top) and contour lines of the stream function (bottom) for the non-Newtonian fluid flow at *Re*=1000, ε =0.1 for different values of the ratio of torsion to curvature: (a) λ =0.1, Gn=10.0 (b) λ =0.5, Gn=50.0 (c) λ =1.0, Gn=100.0

Since the momentum equations are independent of the energy equation, the axial velocity and the secondary flow do not change with the Prandtl number. Figures 5.8 and 5.9 present the effect of the Prandtl number on the dimensionless temperature. Figure 5.8 shows the contour lines and 3D plots of the dimensionless temperature for three values of the Prandtl number: 0.1, 1.0, and 10. The maximum of the dimensionless temperature gets displaced to the outer wall when the Prandtl number increases. When the Prandtl number increases to as much as 10, two local maxima of the temperature appear (cf. Figures 5.8 and 5.9). The heat transfer coefficient increases with the Prandtl number (Table 5.1), as expected.

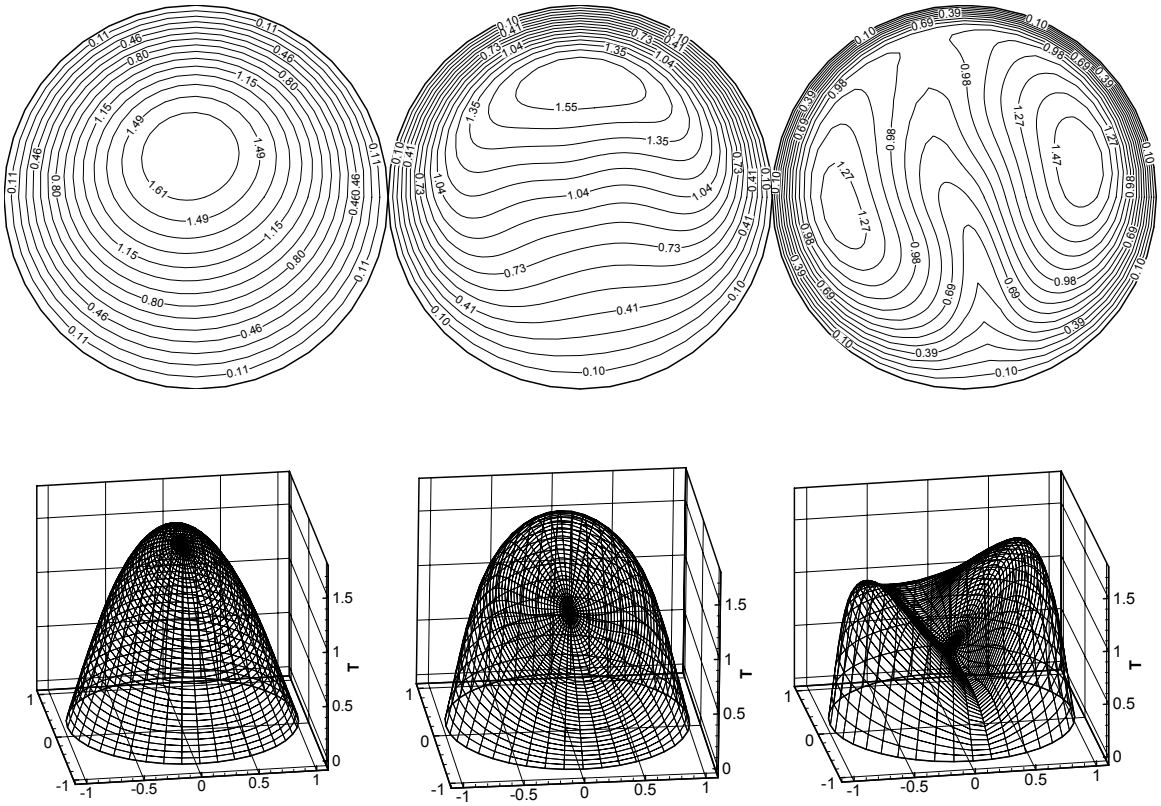

(a) (b) (c)

Figure 5.8 Contour lines (top) and 3D plots (bottom) of the dimensionless temperature at *Re*=1000, ε =0.01, λ =0.1, Dn=100.0, Gn=1.0 for different Prandtl numbers: (a) Pr=0.1 (b) Pr=1.0 (c) Pr=10

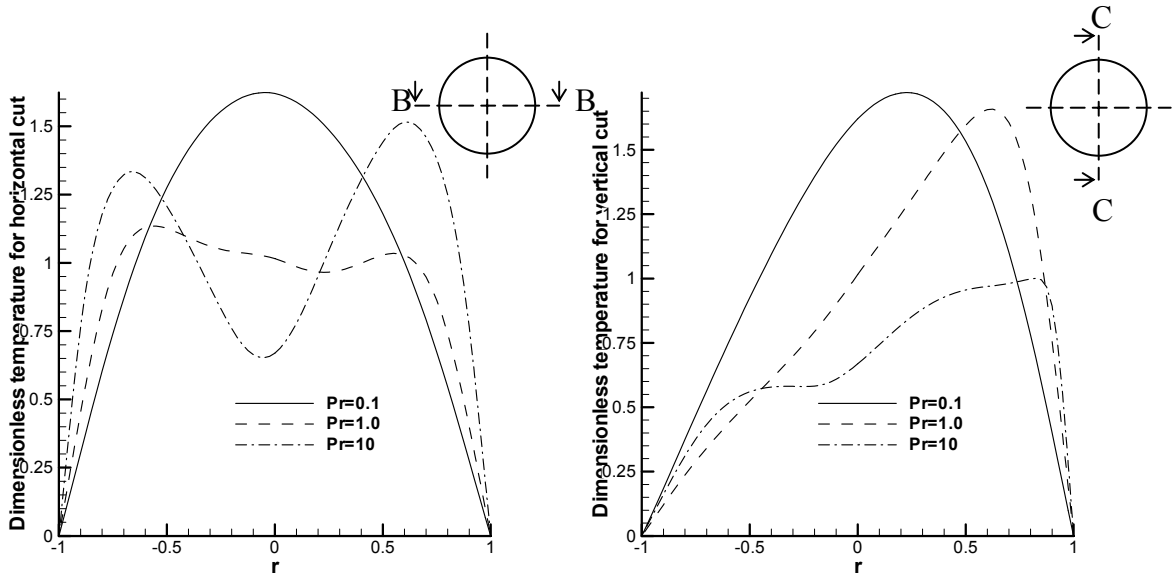

Figure 5.9 Temperature profiles in the horizontal (left) and vertical (right) cut views of the pipe at *Re*=1000, ε =0.01, λ =0, Dn=100.0, Gn=1.0 1for different Prandtl numbers. The curves for different Pr correspond to cases (a)-(c) in Figure 5.8

5.5 CONCLUSIONS

Helical pipes have the advantage of greater heat transfer compared to straight pipes due to heat transfer enhancement by the secondary flow. Heat transfer in the fully developed laminar non-Newtonian flow in a helical pipe is investigated. When the Dean number increases, the contour lines corresponding to large values of the axial velocity are displaced to the outer wall and the value of the maximum axial velocity decreases; the contour lines corresponding to large values of the dimensionless temperature are also displaced to the outer wall but the maximum value of the dimensionless temperature increases. The Nusselt number increases with the Dean number. The secondary flow becomes stronger when the Dean number is increased. The increase of the Germano number does not have any significant effect on the axial velocity and heat transfer but strengthens the secondary flow and destroys the symmetric pattern of the secondary flow. Since temperature-independent viscosity is assumed in this chapter, the Prandtl number does not affect the primary and secondary flow velocity; a greater value of the Prandtl number results in a displacement of the maximum dimensionless temperature to the outer wall and yields higher heat transfer coefficient. When the Prandtl number is large enough, two local maxima of dimensionless temperature appear.

REFERENCES

1. Shah, R.K. and Joshi, S.D. (1987) Convective heat transfer in curved ducts. In *Handbook of Single-phase Convective Heat Transfer*, *Chap. 5*. New York :John Wiley.

2. Jeschke, D. (1925) Wärmeübergang und Druckverlust in Rohrschlagen, *Z. ver. Deut. Ing*. 69, 1526;Z. V.D.I. 24,1.

3. Merkel, F. (1927) Die Grundlagen der Wärmeübertragung. *Steinkopf, Leipzig*. p.51.

4. Dravid, A.N., Smith, K.A., Merrill, E.W. and Brian, P.L.T. (1971) Effect of secondary fluid motion on laminar flow heart transfer in helically coiled tubes. *A.I.Ch.E Journal*, *17*: 1114-1122.

5. Balejova, M., Cakrt, J. and Mik, V.(1977) Heat transfer for laminar flow in curved pipes with uniform wall heat flux. *Acta Technica Csav, 22*: 183-194.

6. Janssen, L.A. and Hoogendoorn, C.J. (1978) Laminar convective heat transfer in helical coiled tubes. *International Journal of Heat and Mass Transfer*, 21: 1197-1206.

7. Kalb, C.E. and Seader, J.D.(1983) Entrance region heat transfer in a uniform wall-temperature helical coil with transition from turbulent to laminar flow. *International Journal of Heat and Mass Transfer*, *26*: 23-32.

8. Austen, D.S. and Soliman, H.M.(1988) Laminar flow and heat transfer in helically coiled tube with substantial pitch. *Experimental Thermal and Fluid Science,* 1: 183-194.

9. Dean, W.R. (1927) Note on the motion of fluid in a curved pipe. *Philosophical Magazine,* 4 (7): 208-223.

10. Wang, C.Y. (1981) On the low-Reynolds number flow in a helical pipe, *J. Fluid Mech.,* 108: 285-194.

11. Germano, M. (1982) On the effect of torsion on a helical pipe flow. *J. Fluid Mech.,* 125: 1-8.

12. Germano, M. (1989) The Dean equations extended to a helical pipe flow. *J. Fluid Mech.,* 203: 289-305.

13. Sankariah, M. and Rao, Y.V.N. (1972) Analysis of steady laminar flow of an incompressible Newtonian fluid through curved pipes of small curvature, *ASME Paper No.72-WA/FE-19*.

14. Patankar, S.V., Pratap, V.S. and Spalding, D.B. (1974) Prediction of laminar flow and heat transfer in helically coiled pipes. *Journal of Fluid Mechanics,* 62 (3): 539-551.

15. Liu, S. & Masliyah, J.H. (1993) Axially invariant laminar flow in helical pipes with a finite pitch. *J. Fluid Mech.,* 251: 315-353.

16. Yang, G., Dong, Z. F. & Ebadian, M. A. (1995) Laminar forced convection in a helicoidal pipe with finite pitch. *Int. J. Heat Mass Transfer,* 38(5): 853-862.

17. Hsu, C.F. and Patankar S.V.(1982) Analysis of laminar non-Newtonian flow and heat transfer in curved tubes. *AICHE J*., 28: 610-616.

18. Sandeep, K. P., Zuritz, C. A. & Puri, V. M. (2000) Modeling non-Newtonian two-phase flow in conventional and helical-holding tubes. *Int. J. food science and Technology,* 35: 511-522.

19. Bird, R. B., Stewart, W. E. & Lightfoot, E. N. (1960) *Transport Phenomena.* New York, NY, USA: John Wiley and Sons.

20. Cheng, L. and Kuzentsov, A.V. (2004) Investigation of a laminar flow of a non-Newtonian fluid in a helical pipe. *International Journal of Applied Mechanics and Engineering* (in press).

21. Patankar, S. V. (1980) *Numerical heat transfer and fluid flow*. New York: Hemisphere.

22. Hüttl, T. J. (1997) Navier Stokes solutions of laminar flows based on orthogonal helical coordinates. *Numerical methods in laminar and turbulent flow,* 10: 191-202.

23. Bejan, A.(1995) *Convection Heat Transfer* (2nd Ed.). New York: Wiley-Interscience.

PART THREE:

LAMINAR FLOW AND HEAT TRANSFER IN A HELICAL PIPE FILLED WITH FLUID SATURATED POROUS MEDIUM

6 INVESTIGATION OF LAMNIAR FLOW IN A HELICAL PIPE FILLED WITH A FLUID SATURATED POROUS MEDIUM

ABSTRACT

Laminar flow in a helical pipe filled with a fluid saturated porous medium is investigated numerically. The analysis is based on a full momentum equation for the flow in porous media that accounts for the Brinkman and Forchheimer extensions of the Darcy law as well as for the flow inertia. Accounting for the flow inertia is shown to be important for predicting secondary flow in a helical pipe. The effects of the Darcy number, the Forchheimer coefficient as well as the curvature and torsion of the helical pipe on the axial flow velocity and secondary flow are investigated numerically.

Nomenclature

a	pipe radius, m
C_F	Forchheimer coefficient
Da	Darcy number, K/a^2
Dn	Dean number, $\varepsilon^{1/2}$ Re
g	gravity, m/s^2
Gn	Germano number, $(\varepsilon\lambda)$Re
h_s	dimensionless scale factor
$\tilde{h}_r$, $\tilde{h}_s$, $\tilde{h}_\theta$	dimensional scale factors
K	permeability, m^2

Re	Reynolds number, $\rho_f Ua/\mu$
r	dimensionless radial coordinate, $\tilde{r}/a$
$\tilde{r}$	radial coordinate, m
$\hat{\mathbf{r}}$	residual vector
s	dimensionless axial coordinate, $\tilde{s}/a$
$\tilde{s}$	axial coordinate, m
p	pitch, m
P	dimensionless pressure, $\tilde{P}/\rho U^2$
$\tilde{P}$	pressure, Pa
U	bulk velocity, defined in Eq. (6.9), m/s
$\tilde{\mathbf{v}}$	velocity vector, m s^{-1}
u_s, u_r, u_θ	dimensionless velocity components, $\frac{\tilde{u}_s}{U}, \frac{\tilde{u}_r}{U}, \frac{\tilde{u}_\theta}{U}$
$\tilde{u}_s, \tilde{u}_r, \tilde{u}_\theta$	velocity components, m s^{-1}

Greek symbols

ε	dimensionless curvature, κa
θ	angle, defined in Fig. 1b
κ	curvature, m^{-1}
λ	the ratio of torsion to curvature, τ/κ
μ	effective dynamic viscosity of the porous medium (assumed to the same as the fluid viscosity), kg m^{-1} s^{-1}
ν	effective kinematic viscosity in a porous medium, m^2 s^{-1}
ξ	angle, defined in Eq. (6.10)

ρ_f	fluid density, $kg\ m^{-3}$
τ	torsion, m^{-1}
φ	porosity
ϕ	angle, defined in Equation (6.3)

Subscripts

s	axial direction
r	radial direction
θ	circumferential direction

6.1 INTRODUCTION

Flow in helical pipes has been a subject of intensive investigation. The major advantage of helical pipe flow is the occurrence of a secondary flow in planes normal to the main flow. Secondary flow increases heat and mass transfer efficiency compared to that in straight pipes. Dean [1] initially studied the flow in loosely coiled pipes and found the secondary flow with two symmetric vortices. Besides the Reynolds number, *Re*, another parameter, the Dean number, *Dn*, was later introduced to characterize the magnitude and the shape of the secondary flow. Germano [2, 3] suggested an orthogonal helical coordinate system and used it to solve a laminar flow problem with a small ratio of torsion to curvature. He concluded that torsion has a second-order effect on the helical pipe flow. The Germano number, *Gn*, was introduced by Liu and Masliyah [4]. The Dean number given by $Dn = \varepsilon^{1/2}\,\mathrm{Re}$ is a measure of the ratio of the square root of the product of inertial and centrifugal forces to the viscous forces. The Germano number given by $Gn = (\varepsilon\lambda)\,\mathrm{Re}$ is a measure of the ratio of the centrifugal forces to the viscous forces (Liu and Masliyah [5]). Liu and Masliyah [4, 5]

performed a comprehensive analysis of fully-developed laminar Newtonian flows in helical pipes of constant circular cross-sections with a finite pitch and found that when the torsion is dominant, the flow in helical pipes approaches that in a straight pipe. When the torsion is small, the developing flow is oscillatory and the flow develops more quickly than in a straight pipe. Numerical studies have been conducted later to examine the effects of torsion and curvature on the fluid flow in helical pipes ([6-11]).

Sandeep [12] extended the analysis of helical pipe flow to non-Newtonian fluids; the numerical research was performed in a Cartesian coordinate system. Cheng and Kuznetsov [13] used an orthogonal helical coordinate system to study the effects of torsion and curvature on non-Newtonian fluid flow in helical pipes and compared the flow dynamics between Newtonian and non-Newtonian fluids.

Nield and Kuznetsov [14] presented a perturbation analysis and obtained an analytical expression for the Nusselt number in a helical pipe filled with a porous medium for the case when flow in a pipe is described by the Darcy law. To the best of the authors' knowledge, nothing has been published before on flows in helical pipes filled with a fluid saturated porous medium. The aim of the present chapter is to fill this gap in the literature. Flow in helical pipes filled with a fluid saturated porous medium is relevant to a number of engineering and biological applications, such as the flow in a helical segment of clotted human coronary artery. This chapter investigates laminar flow in a helical pipe filled with a porous medium. Since the secondary flow in a helical pipe becomes significant at relatively large flow velocity, it is insufficient to describe the drag that the porous medium imposes on a fluid by using just one linear (Darcy) term; at larger filtration velocities the surface drag due to friction becomes comparable with the form drag due to solid obstacles (Nield and

Bejan [15]). Since the form drag due to solid obstacles is proportional to the square of the filtration velocity, to account for this effect an additional quadratic drag term is introduced into the momentum equation, which is called the Forchheimer term. In this chapter, the most general form of a momentum equation for porous media, the Brinkman-Forchheimer-extended Darcy equation with inertia terms, is utilized; this equation is solved numerically in an orthogonal helical coordinate system suggested by Germano [2, 3]. The geometry of a helical pipe is characterized by the curvature and torsion. In this study, the effects of the Darcy number, the Forchheimer coefficient, the curvature and torsion of the helical pipe on the axial flow velocity and secondary flow are investigated numerically. The investigation shows that increasing the Darcy number increases the distortion of the axial velocity profile and enhances the secondary flow. Increasing the Forchheimer coefficient decreases the axial velocity and the secondary flow. The dimensionless curvature of helical pipes affects both the axial velocity distribution and the secondary flow, but the ratio of torsion to curvature produces a noticeable effect only on the secondary flow.

6.2 GOVERNING EQUATIONS

Figure 6.1a shows the schematic diagram of a helical pipe which is characterized by two parameters, the curvature, κ, and the torsion, τ, which are defined as, respectively

$$\kappa = \frac{R}{R^2 + p^2}, \qquad \tau = \frac{p}{R^2 + p^2} \tag{6.1}$$

Figure 6.1(b) displays the orthogonal helical coordinate system introduced by Germano [2, 3] with the helical coordinate *s* for the axial direction, *r* for the radial direction, and θ for the circumferential direction. The metric for this coordinate system is given by

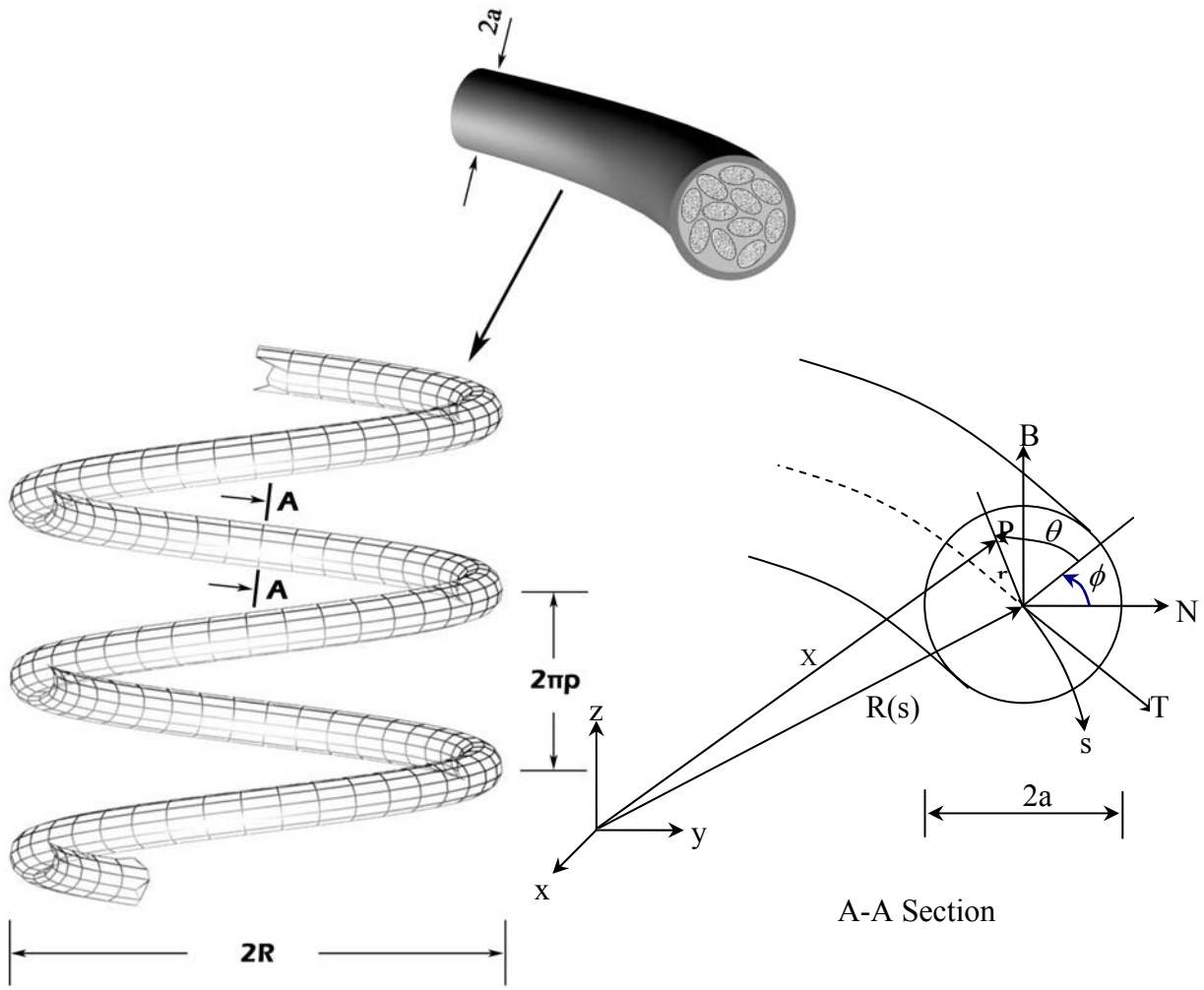

(a) **(b)**

Figure 6.1 Schematic diagram of a helical pipe and the orthogonal helical coordinate system

$$d\mathbf{x}\cdot d\mathbf{x} = [1+\kappa\tilde{r}\sin(\theta+\phi)]^2(d\tilde{s})^2 + (d\tilde{r})^2 + \tilde{r}^2(d\theta)^2 \qquad (6.2)$$

where

$$\phi(\tilde{s}) = -\int_{\tilde{s}_0}^{\tilde{s}} \tau(\tilde{s}')d\tilde{s}' \qquad (6.3)$$

The continuity and momentum equations in the vector form are

$$\nabla\cdot\tilde{\mathbf{v}} = 0 \qquad (6.4)$$

and

$$\frac{\rho_f}{\varphi^2}(\tilde{\mathbf{v}}\cdot\nabla)\tilde{\mathbf{v}} = -\nabla\tilde{P} + \frac{\mu}{\varphi}\nabla^2\tilde{\mathbf{v}} - \frac{\mu}{K}\tilde{\mathbf{v}} - \frac{C_F\rho_f}{K^{1/2}}|\tilde{\mathbf{v}}|\tilde{\mathbf{v}} \qquad (6.5)$$

where K is the permeability of the porous medium, C_F is the Forchheimer coefficient, and φ is the porosity.

Equation (6.5) is a full momentum equation for the steady flow in porous media that accounts for the Brinkman and Forchheimer extensions of the Darcy law as well as for the flow inertia ([15]).

In the orthogonal helical coordinate system, the scale factors are given by

$$\tilde{h}_s = 1+\kappa\tilde{r}\sin(\theta+\phi) \qquad \tilde{h}_r = 1 \qquad \tilde{h}_\theta = \tilde{r} \qquad (6.6)$$

The dimensionless governing equations for the flow in a porous medium written in the orthogonal helical coordinate system are the continuity equation

$$\frac{\partial(ru_s)}{\partial s} + \frac{\partial(rh_s u_r)}{\partial r} + \frac{\partial(h_s u_\theta)}{\partial\theta} = 0 \qquad (6.7)$$

and the momentum equations

$$\frac{1}{\varphi^2}\frac{1}{h_s r}\left(\frac{\partial\left(ru_s u_s\right)}{\partial s}+\frac{\partial\left(rh_s u_r u_s\right)}{\partial r}+\frac{\partial\left(h_s u_\theta u_s\right)}{\partial\theta}\right)+\frac{1}{\varphi^2}\frac{\varepsilon}{h_s}u_s\left(u_r\sin(\theta+\phi)+u_\theta\cos(\theta+\phi)\right)=-\frac{1}{h_s}\frac{\partial P}{\partial s}$$
$$+\frac{1}{\varphi}\frac{1}{\mathrm{Re}}\left\{\frac{1}{h_s}\frac{\partial}{\partial s}\left[\frac{1}{h_s r}\left[\frac{\partial\left(ru_s\right)}{\partial s}+\frac{\partial\left(rh_s u_r\right)}{\partial r}+\frac{\partial\left(h_s u_\theta\right)}{\partial\theta}\right]\right]-\right.$$
$$\left.\frac{1}{r}\left(\frac{\partial}{\partial r}\left(\frac{r}{h_s}\left(\frac{\partial u_r}{\partial s}-\frac{\partial}{\partial r}\left(h_s u_s\right)\right)\right)-\frac{\partial}{\partial\theta}\left(\frac{1}{h_s r}\left(\frac{\partial}{\partial\theta}\left(h_s u_s\right)-\frac{\partial}{\partial\theta}\left(ru_\theta\right)\right)\right)\right)\right\} \qquad (6.8a)$$
$$-\frac{1}{\mathrm{Re}}\frac{1}{Da}u_s-\frac{C_F}{Da^{1/2}}u_s\left(u_s^2+u_r^2+u_\theta^2\right)^{1/2}$$

$$\frac{1}{\varphi^2}\frac{1}{h_s r}\left(\frac{\partial\left(ru_s u_r\right)}{\partial s}+\frac{\partial\left(rh_s u_r u_r\right)}{\partial r}+\frac{\partial\left(h_s u_\theta u_r\right)}{\partial\theta}\right)-\frac{1}{\varphi^2}\frac{{u_\theta}^2}{r}-\frac{1}{\varphi^2}\frac{\varepsilon}{h_s}{u_s}^2\sin\left(\theta+\phi\right)=-\frac{\partial P}{\partial r}$$
$$+\frac{1}{\varphi}\frac{1}{\mathrm{Re}}\left\{\frac{\partial}{\partial r}\left[\frac{1}{h_s r}\left[\frac{\partial\left(ru_s\right)}{\partial s}+\frac{\partial\left(rh_s u_r\right)}{\partial r}+\frac{\partial\left(h_s u_\theta\right)}{\partial\theta}\right]\right]-\right.$$
$$\left.\frac{1}{h_s r}\left(\frac{\partial}{\partial\theta}\left(\frac{h_s}{r}\left(\frac{\partial}{\partial r}\left(ru_\theta\right)-\frac{\partial u_r}{\partial\theta}\right)\right)-\frac{\partial}{\partial s}\left(\frac{r}{h_s}\left(\frac{\partial u_r}{\partial s}-\frac{\partial}{\partial r}\left(h_s u_s\right)\right)\right)\right)\right\} \qquad (6.8b)$$
$$-\frac{1}{\mathrm{Re}}\frac{1}{Da}u_r-\frac{C_F}{Da^{1/2}}u_r\left(u_s^2+u_r^2+u_\theta^2\right)^{1/2}$$

$$\frac{1}{\varphi^2}\frac{1}{h_s r}\left(\frac{\partial\left(ru_s u_\theta\right)}{\partial s}+\frac{\partial\left(rh_s u_r u_\theta\right)}{\partial r}+\frac{\partial\left(h_s u_\theta u_\theta\right)}{\partial\theta}\right)-\frac{1}{\varphi^2}\frac{\varepsilon}{h_s}{u_s}^2\cos\left(\theta+\phi\right)+\frac{1}{\varphi^2}\frac{u_r u_\theta}{r}=-\frac{1}{r}\frac{\partial P}{\partial\theta}$$
$$+\frac{1}{\varphi}\frac{1}{\mathrm{Re}_F}\left\{\frac{1}{r}\frac{\partial}{\partial\theta}\left[\frac{1}{h_s r}\left[\frac{\partial\left(ru_s\right)}{\partial s}+\frac{\partial\left(rh_s u_r\right)}{\partial r}+\frac{\partial\left(h_s u_\theta\right)}{\partial\theta}\right]\right]-\right.$$
$$\left.\frac{1}{h_s}\left(\frac{\partial}{\partial s}\left(\frac{1}{h_s r}\left(\frac{\partial}{\partial\theta}\left(h_s u_s\right)-\frac{\partial}{\partial s}\left(ru_\theta\right)\right)\right)-\frac{\partial}{\partial r}\left(\frac{h_s}{r}\left(\frac{\partial}{\partial r}\left(ru_\theta\right)-\frac{\partial u_r}{\partial\theta}\right)\right)\right)\right\} \qquad (6.8c)$$
$$-\frac{1}{\mathrm{Re}}\frac{1}{Da}u_\theta-\frac{C_F}{Da^{1/2}}u_\theta\left(u_s^2+u_r^2+u_\theta^2\right)^{1/2}$$

where

$$s=\frac{\tilde{s}}{a},\ r=\frac{\tilde{r}}{a},\ \left(u_s,u_r,u_\theta\right)=\left(\frac{\tilde{u}_s}{U},\frac{\tilde{u}_r}{U},\frac{\tilde{u}_\theta}{U}\right),\ P=\frac{\tilde{P}}{\rho_f U^2},\ \varepsilon=\kappa a,\ \lambda=\frac{\tau}{\kappa},$$
$$h_s=1+\varepsilon r\sin(\theta+\phi),\ \mathrm{Re}=\frac{\rho_f U a}{\mu},\ Da=\frac{K}{a^2},\ U=\frac{1}{\pi}\int_0^{2\pi}\int_0^1\tilde{u}_s r\,dr\,d\theta \qquad (6.9)$$

where a is the radius of the pipe, and U is the bulk velocity defined in Eq. (6.9).

A fully developed laminar flow is considered so that the dynamic variables except for the pressure are independent of *s*, therefore, a simplifying transformation is performed from *s*, *r*, θ to *s*, *r*, ξ:

$$\theta + \phi \Rightarrow \xi\,,\ \frac{\partial}{\partial s} \Rightarrow \frac{\partial}{\partial s} - \varepsilon\lambda \frac{\partial}{\partial \xi}\,,\ \frac{\partial}{\partial \theta} \Rightarrow \frac{\partial}{\partial \xi} \tag{6.10}$$

The governing equations are then reduced as:

$$-\varepsilon\lambda \frac{\partial(r u_s)}{\partial \xi} + \frac{\partial(r h_s u_r)}{\partial r} + \frac{\partial(h_s u_\theta)}{\partial \xi} = 0 \tag{6.11}$$

$$\begin{aligned}
&\frac{1}{\varphi^2}\frac{1}{h_s r}\left(-\varepsilon\lambda\frac{\partial(r u_s u_s)}{\partial \xi} + \frac{\partial(r h_s u_r u_s)}{\partial r} + \frac{\partial(h_s u_\theta u_s)}{\partial \xi}\right) + \frac{1}{\varphi^2}\frac{\varepsilon}{h_s} u_s\left(u_r \sin\xi + u_\theta \cos\xi\right) = -\frac{1}{h_s}\left(\frac{\partial P}{\partial s} - \varepsilon\lambda\frac{\partial P}{\partial \xi}\right) \\
&+\frac{1}{\varphi}\frac{1}{\mathrm{Re}}\left\{-\varepsilon\lambda\frac{1}{h_s}\frac{\partial}{\partial \xi}\left[\frac{1}{h_s r}\left[-\varepsilon\lambda\frac{\partial(r u_s)}{\partial \xi} + \frac{\partial(r h_s u_r)}{\partial r} + \frac{\partial(h_s u_\theta)}{\partial \xi}\right]\right] - \right. \\
&\left.\frac{1}{r}\left(\frac{\partial}{\partial r}\left(\frac{r}{h_s}\left(-\varepsilon\lambda\frac{\partial u_r}{\partial \xi} - \frac{\partial}{\partial r}\left(h_s u_s\right)\right)\right) - \frac{\partial}{\partial \xi}\left(\frac{1}{h_s r}\left(\frac{\partial}{\partial \xi}\left(h_s u_s\right) + \varepsilon\lambda\frac{\partial}{\partial \xi}\left(r u_\theta\right)\right)\right)\right)\right\} \\
&-\frac{1}{\mathrm{Re}}\frac{1}{Da} u_s - \frac{C_F}{Da^{1/2}} u_s\left(u_s^2 + u_r^2 + u_\theta^2\right)^{1/2}
\end{aligned} \tag{6.12a}$$

$$\begin{aligned}
&\frac{1}{\varphi^2}\frac{1}{h_s r}\left(-\varepsilon\lambda\frac{\partial(r u_s u_r)}{\partial \xi} + \frac{\partial(r h_s u_r u_r)}{\partial r} + \frac{\partial(h_s u_\theta u_r)}{\partial \xi}\right) - \frac{1}{\varphi^2}\frac{{u_\theta}^2}{r} - \frac{1}{\varphi^2}\frac{\varepsilon}{h_s}{u_s}^2 \sin\xi = -\frac{\partial P}{\partial r} \\
&+\frac{1}{\varphi}\frac{1}{\mathrm{Re}}\left\{\frac{\partial}{\partial r}\left[\frac{1}{h_s r}\left[-\varepsilon\lambda\frac{\partial(r u_s)}{\partial \xi} + \frac{\partial(r h_s u_r)}{\partial r} + \frac{\partial(h_s u_\theta)}{\partial \xi}\right]\right] - \right. \\
&\left.\frac{1}{h_s r}\left(\frac{\partial}{\partial \xi}\left(\frac{h_s}{r}\left(\frac{\partial}{\partial r}\left(r u_\theta\right) - \frac{\partial u_r}{\partial \xi}\right)\right) + \varepsilon\lambda\frac{\partial}{\partial \xi}\left(\frac{r}{h_s}\left(-\varepsilon\lambda\frac{\partial u_r}{\partial \xi} - \frac{\partial}{\partial r}\left(h_s u_s\right)\right)\right)\right)\right\} \\
&-\frac{1}{\mathrm{Re}}\frac{1}{Da} u_r - \frac{C_F}{Da^{1/2}} u_r\left(u_s^2 + u_r^2 + u_\theta^2\right)^{1/2}
\end{aligned} \tag{6.12b}$$

$$\frac{1}{\varphi^2}\frac{1}{h_s r}\left(-\varepsilon\lambda\frac{\partial(ru_s u_\theta)}{\partial\xi}+\frac{\partial(rh_s u_r u_\theta)}{\partial r}+\frac{\partial(h_s u_\theta u_\theta)}{\partial\xi}\right)-\frac{1}{\varphi^2}\frac{\varepsilon}{h_s}u_s{}^2\cos\xi+\frac{1}{\varphi^2}\frac{u_r u_\theta}{r}=-\frac{1}{r}\frac{\partial P}{\partial\xi}$$
$$+\frac{1}{\varphi}\frac{1}{\mathrm{Re}}\left\{\frac{1}{r}\frac{\partial}{\partial\xi}\left[\frac{1}{h_s r}\left[-\varepsilon\lambda\frac{\partial(ru_s)}{\partial\xi}+\frac{\partial(rh_s u_r)}{\partial r}+\frac{\partial(h_s u_\theta)}{\partial\xi}\right]\right]-\right.$$
$$\left.\frac{1}{h_s}\left(-\varepsilon\lambda\frac{\partial}{\partial\xi}\left(\frac{1}{h_s r}\left(\frac{\partial}{\partial\xi}(h_s u_s)+\varepsilon\lambda\frac{\partial}{\partial\xi}(ru_\theta)\right)\right)-\frac{\partial}{\partial r}\left(\frac{h_s}{r}\left(\frac{\partial}{\partial r}(ru_\theta)-\frac{\partial}{\partial\xi}(u_r)\right)\right)\right)\right\} \qquad (6.12c)$$
$$-\frac{1}{\mathrm{Re}}\frac{1}{Da}u_\theta-\frac{C_F}{Da^{1/2}}u_\theta\left(u_s^2+u_r^2+u_\theta^2\right)^{1/2}$$

6.3 COMPUTATIONAL PROCEDURE

The governing equations are discretized based on a control volume method on an evenly spaced 41 by 41 mesh. The convection-diffusion terms are discretized with the power-law scheme (Patankar [16]) and the other terms are approximated with central differences. The SIMPLE algorithm (Patankar [16]) is utilized on a staggered grid arrangement to solve the governing equations.

A one-dimensional parabolic velocity profile is imposed as the initial guess. Computations are terminated when the convergence criterion is met. The following criterion is adopted

$$\frac{\left\|\hat{\mathbf{r}}^{(k)}\right\|_\infty}{\left\|\hat{\mathbf{r}}^{(0)}\right\|_\infty}\le 10^{-6} \qquad (6.13)$$

where $\hat{\mathbf{r}}$ is the residual of the pressure correction equation obtained from the continuity equation when using the SIMPLE method. The superscripts (0) and (k) refer to the initial value and kth iteration, respectively. A no-slip boundary condition is assumed at the walls of the helical pipe. In the coordinate system utilized in this research, there is a numerical singularity at the pipe axis (r=0), so boundary values are needed for flow quantities, which

are either located directly at the pipe axis or at the opposite sides of the pipe axis (Hüttl [8], Cheng and Kuznetsov [13]).

An initial value of the Reynolds number, which is needed to start iterations, is estimated as follows. The flow is driven by a constant pressure gradient $d\widetilde{P}/d\widetilde{s}$ that has to balance the fluid friction in a porous medium. If fluid friction was modeled by only the Darcian resistance, the axial pressure gradient would be estimated as

$$\frac{d\widetilde{P}}{d\widetilde{s}} = -\frac{\mu}{k}\widetilde{u}_S \qquad (6.14)$$

This gives the following equation that relates the dimensionless pressure gradient and the Reynolds number defined in Equation (6.9)

$$\left(\frac{dP}{ds}\right) = -\frac{1}{Da\ \mathrm{Re}} \qquad (6.15)$$

This is used to evaluate only the initial value of Re. During the iteration process, Re is evaluated according to Eq. (6.9) utilizing the value of the mean velocity from the previous iteration.

6.4 RESULTS AND DISCUSSION

This chapter investigates the fully-developed laminar flow in a helical pipe filled with a fluid saturated porous medium driven by a constant pressure gradient. Figure 6.2 displays the axial velocity contours, axial velocity profiles and velocity vector plot of the secondary flow in the plane normal to the main flow at different Darcy numbers. It shows that the axial velocity increases with the Darcy number. This is because a larger Darcy number means larger permeability, which results in larger filtration velocity. The axial velocity profiles show that when the Darcy number is very small, the profile of the axial velocity is almost that of a slug

flow. The effect of the centrifugal force that is usually important in helical pipe flow can not be observed. With an increase of the Darcy number, the distortion of the velocity profile becomes apparent and the maximum axial velocity is displaced towards the outer wall. The effect of the Darcy number on secondary flow is also significant. For small Darcy numbers, the secondary flow can not be seen but when the Darcy number is increased to 5×10^{-2}, the secondary flow becomes very strong. The axial velocity profiles for the horizontal and vertical cut view at different Darcy numbers are plotted in Figure 6.3. It clearly shows the trend of the axial velocity described above when the Darcy number changes.

Axial velocity contour Axial velocity 3D plot Vector plot of secondary flow

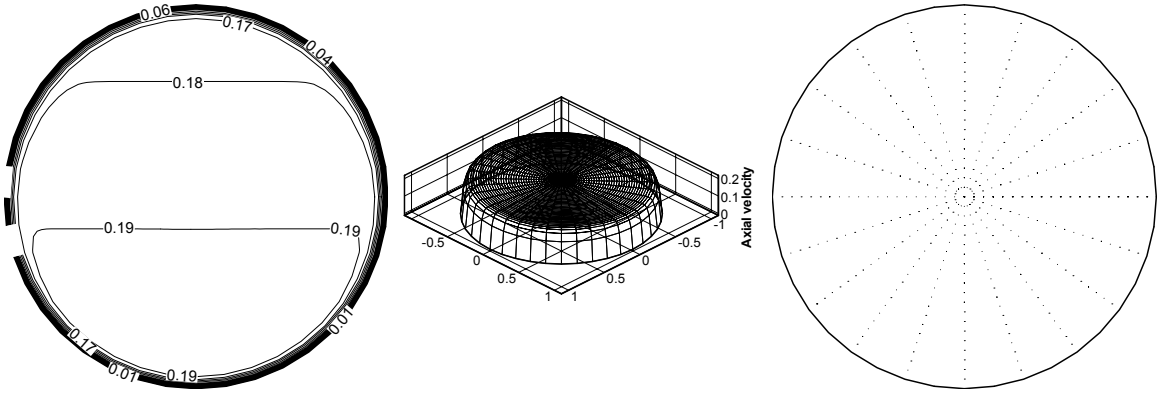

(a) $Da = 5\times10^{-4}$

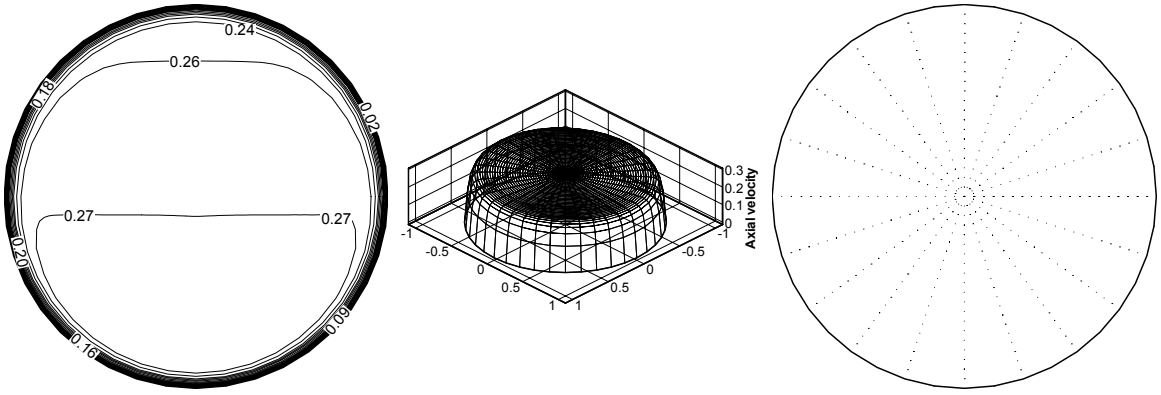

(b) $Da = 1\times10^{-3}$

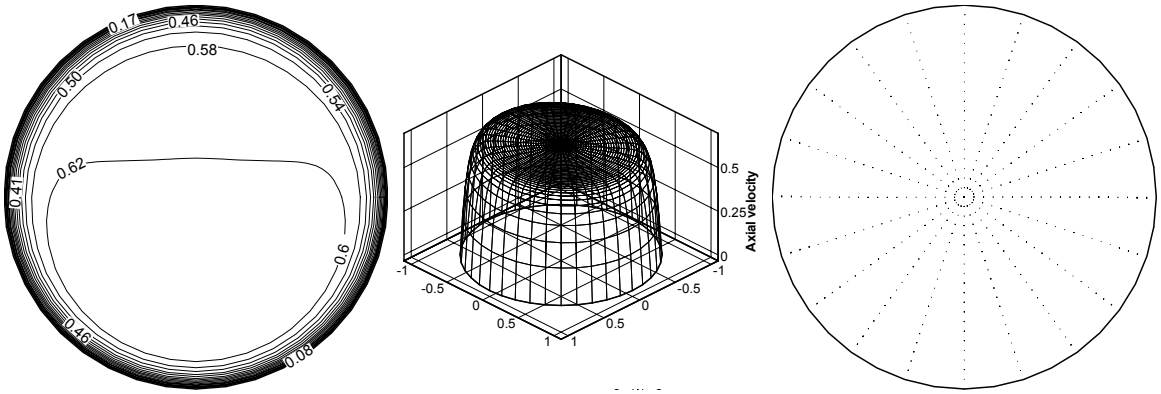

(c) $Da = 5\times10^{-3}$

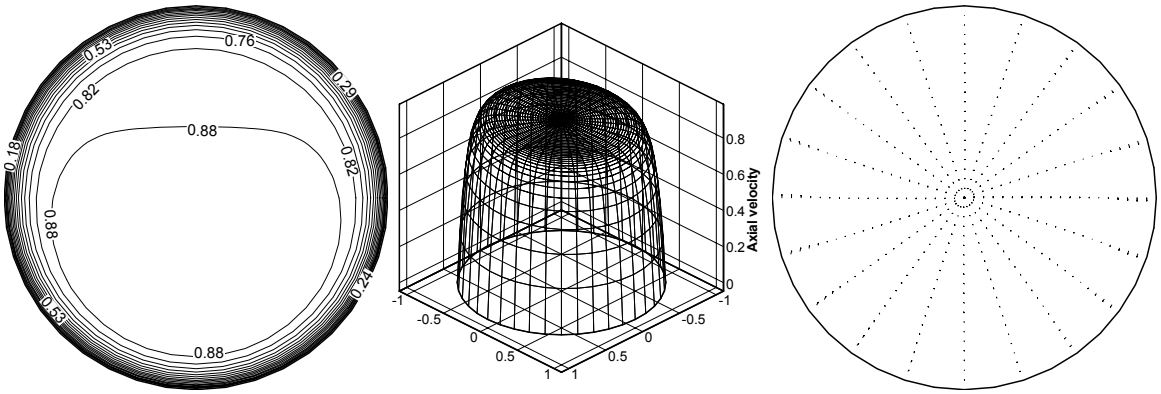

(d) $Da = 1\times10^{-2}$

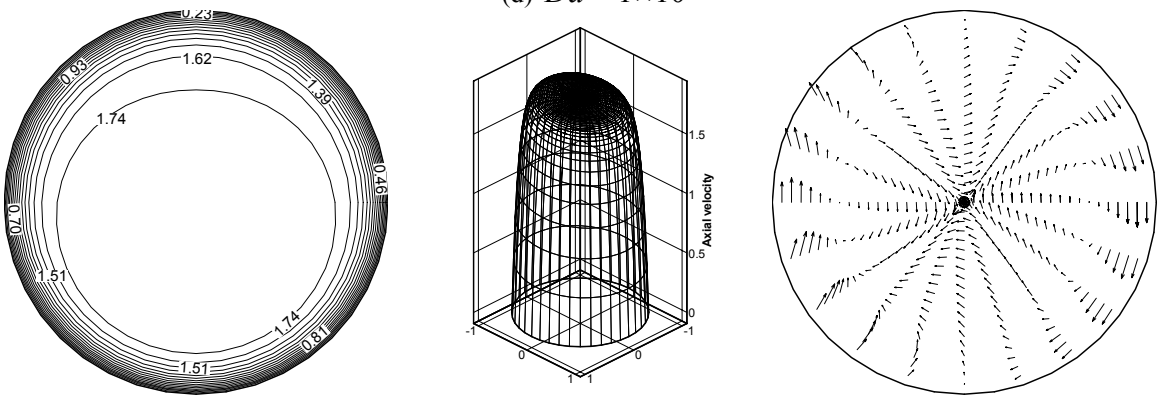

(e) $Da = 5\times10^{-2}$

Figure 6.2 Contour lines and 3D plot of the axial velocity and vector plots of the secondary flow at *dP/ds=-10*, C_F =0.55, φ =0.95, ε =0.1 λ =0.1 for different Darcy numbers: (a) $Da = 5\times10^{-4}$ **(b)** $Da = 1\times10^{-3}$ **(c)** $Da = 5\times10^{-3}$ **(d)** $Da = 1\times10^{-2}$ **(e)** $Da = 5\times10^{-2}$

Figure 6.4 displays the effects of the Forchheimer coefficient, C_F, on the fluid flow in a helical pipe filled with a porous medium. The contour lines and the 3D plots of the axial

velocity show that the distributions of the axial velocity are similar for different values of C_F except that the value of the axial velocity decreases with C_F. A larger Forchheimer coefficient means larger form drag due to solid obstacles in the porous medium, therefore, the axial velocity decreases when C_F increases. The secondary flow is also damped a little for larger Forchheimer coefficients, as shown in the vector plots of the secondary flow. Figure 6.5 shows the profiles of the axial velocity for both the horizontal and vertical cut view of a cross-section normal to the pipe axes. The distortion of the axial velocity profile is observed for all displayed cases. The velocity profiles in the core region of the pipe (outside the boundary layer region) computed for different values of the Forchheimer coefficient are parallel to each other.

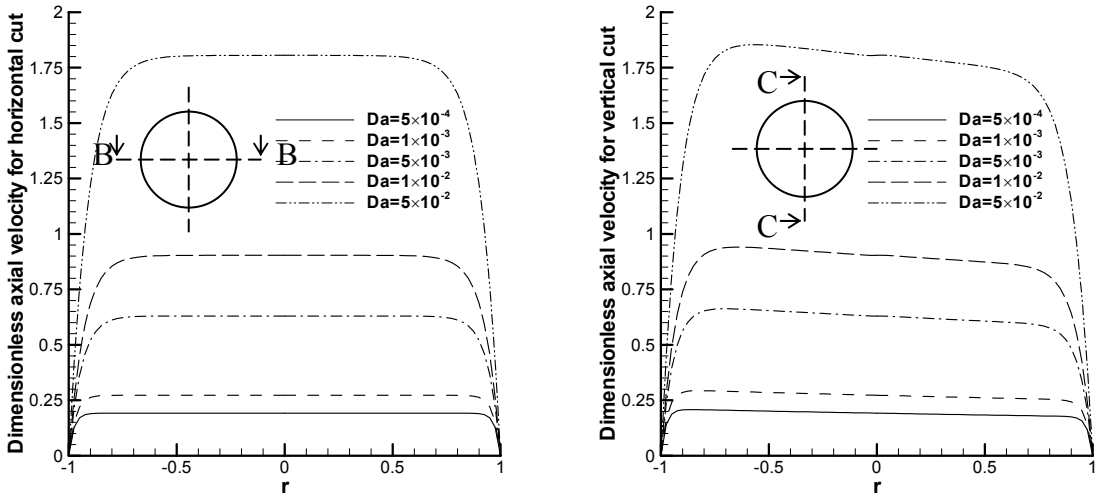

Figure 6.3 Axial velocity profiles in the horizontal (left) and vertical (right) cut view of the pipe at *dP/ds*=-*10*, C_F =0.55, φ =0.95, ε =0.1 λ =0.1 for different Darcy numbers. The curves for different *Da* correspond to the cases (a)-(e) displayed in Figure 6.2

Axial velocity contour Axial velocity 3D plot Vector plot of secondary flow

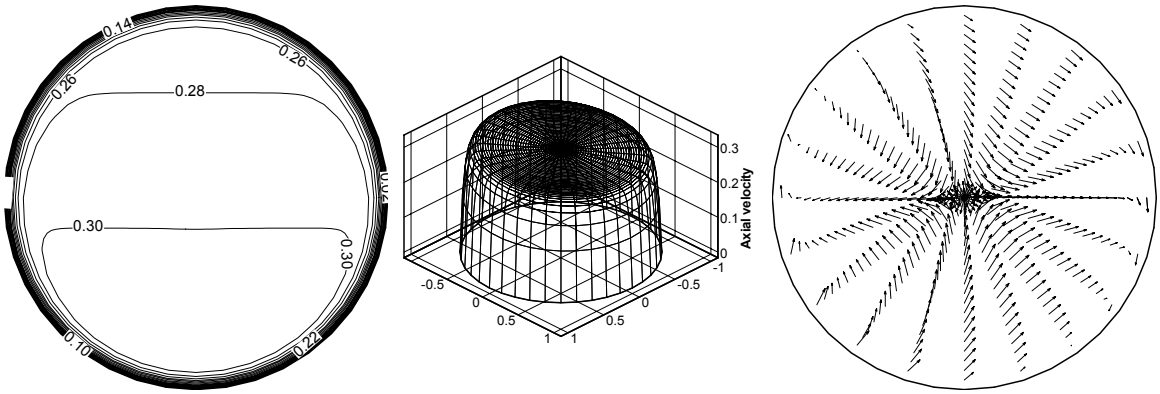

(a) $C_F = 0.0$

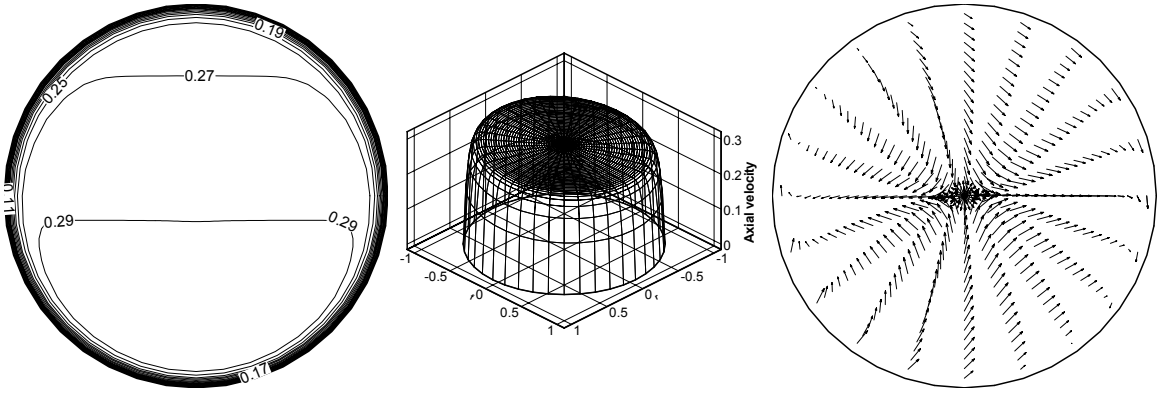

(b) $C_F = 0.25$

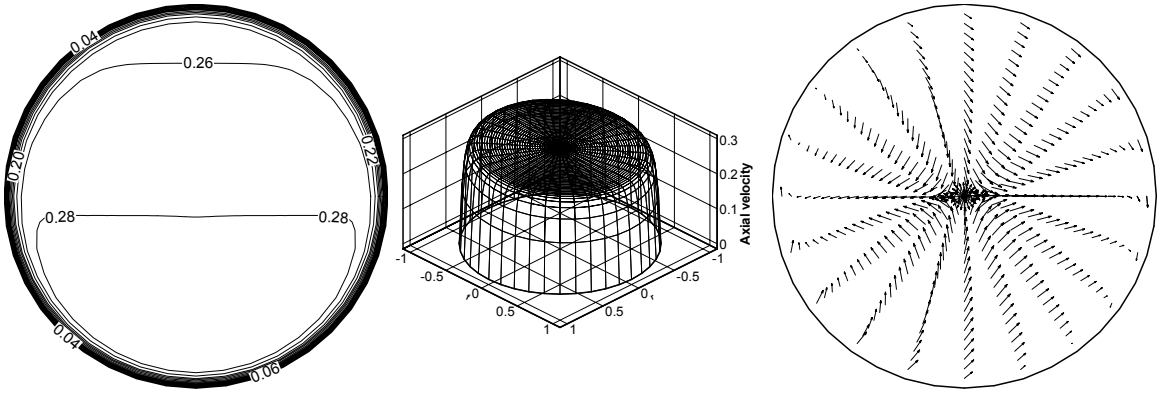

(c) $C_F = 0.50$

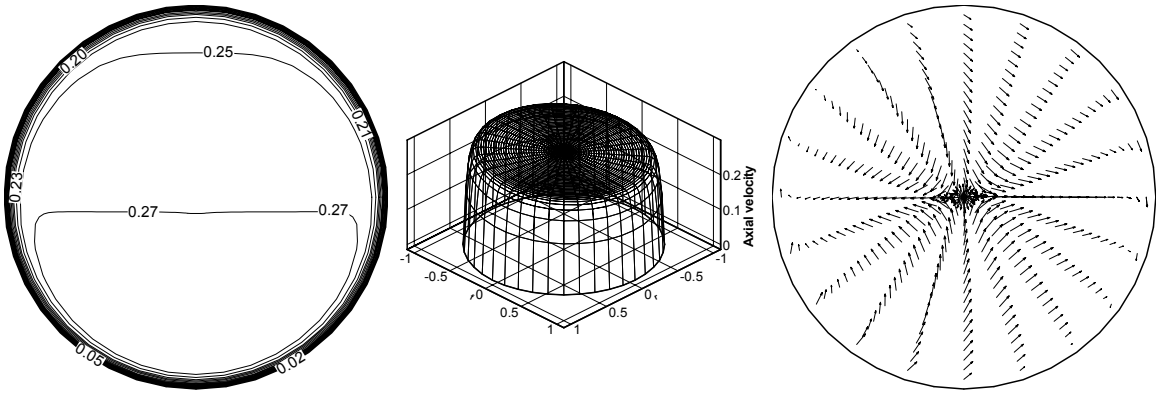

(d) $C_F = 0.75$

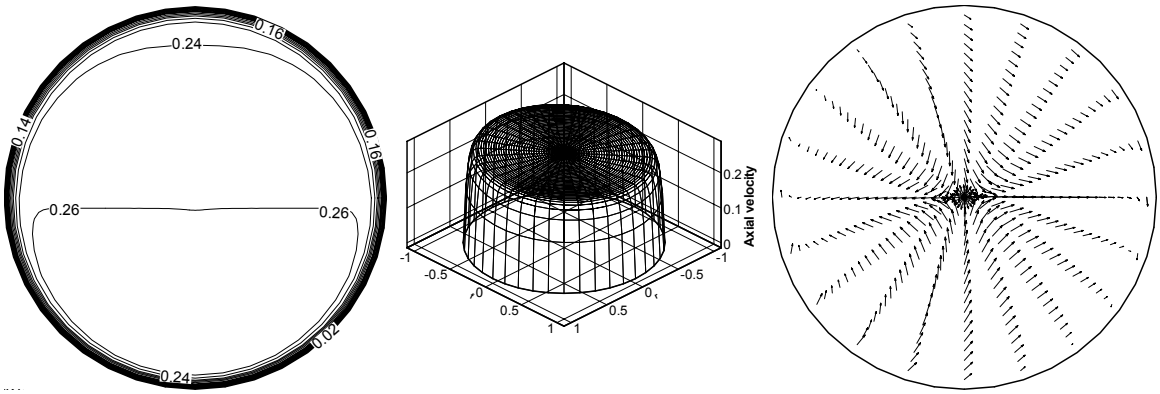

(e) $C_F = 1.0$

Figure 6.4 Contour lines and 3D plots of the axial velocity and vector plots of the secondary flow at *dP/ds=-10*, $Da = 1\times10^{-3}$, φ=0.95, ε=0.1 λ=0.1 for different Forchheimer coefficients: (a) $C_F = 0.0$ **(b)** $C_F = 0.25$ **(c)** $C_F = 0.50$ **(d)** $C_F = 0.75$ **(e)** $C_F = 1.0$

Figures 6.6, 6.7, 6.8 and 6.9 present the effect of the dimensionless curvature, ε, on the distribution of the axial velocity. Both 3D (Figure 6.6) and 2D (Figure 6.7) plots of the axial velocity show that when ε increases, the maximum axial velocity is displaced to the outer wall and the value of the maximum axial velocity increases. Figure 6.8 presents profiles of the axial velocity for the horizontal and vertical cut view. It is interesting that the profiles are quite flat for the horizontal cut view and are relatively independent of ε; the profile for the vertical cut view, however, is inclined to the outer wall and becomes steeper when the dimensionless curvature, ε, increases. The profile of the axial velocity becomes cuneiform for the case of $\varepsilon = 0.8$. The vector plots of the secondary flow displayed in Figure 6.9 show

that the secondary flow is almost invisible for the case of $\varepsilon = 0.1$ but when ε increases the secondary flow becomes much stronger.

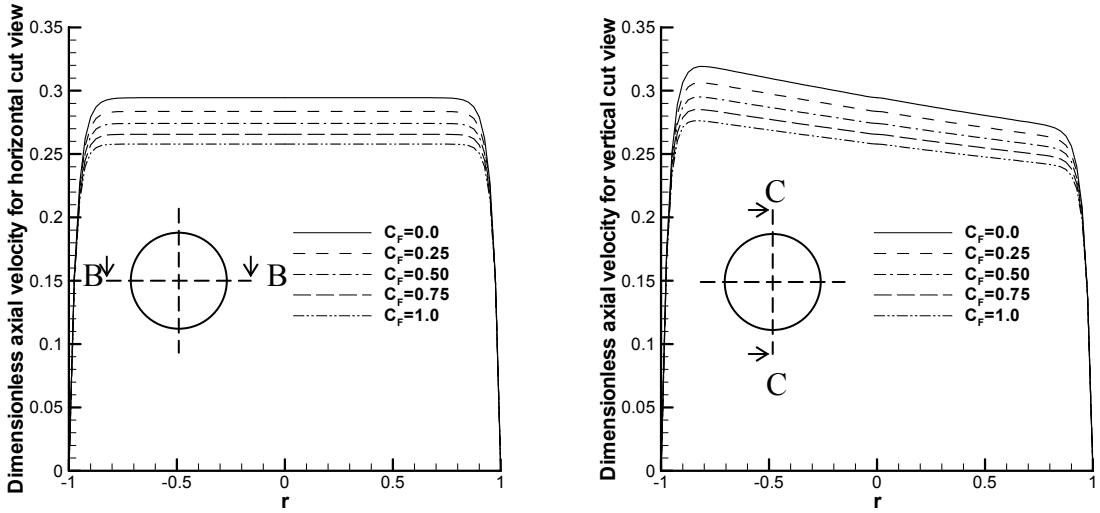

Figure 6.5 Axial velocity profiles in the horizontal (left) and vertical (right) cut view of the pipe at *dP/ds=-10*, $Da = 1 \times 10^{-3}$, φ=0.95, ε=0.1 λ=0.1 for different Forchheimer coefficients. The curves for different C_F correspond to the cases (a)-(e) displayed in Figure 6.4

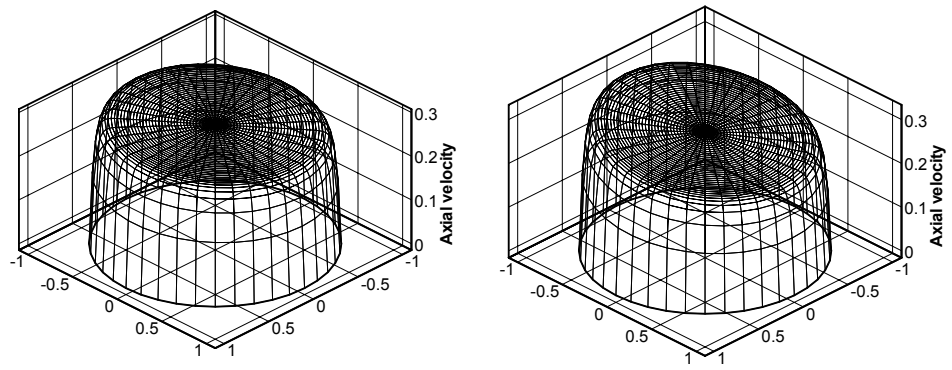

(a) $\varepsilon = 0.1$ (b) $\varepsilon = 0.2$

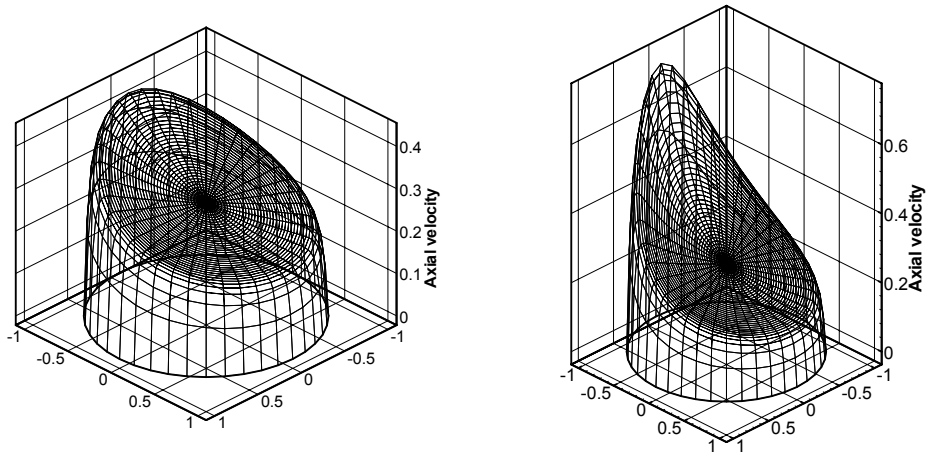

(c) $\varepsilon = 0.5$ (d) $\varepsilon = 0.8$

Figure 6.6 3D plots of the axial velocity at *dP/ds=-10*, $Da = 1 \times 10^{-3}$, C_F =0.55, φ =0.95, λ =0.1 for different dimensionless curvatures: (a) ε =0.1 (b) ε =0.2 (c) ε =0.5 (d) ε =0.8

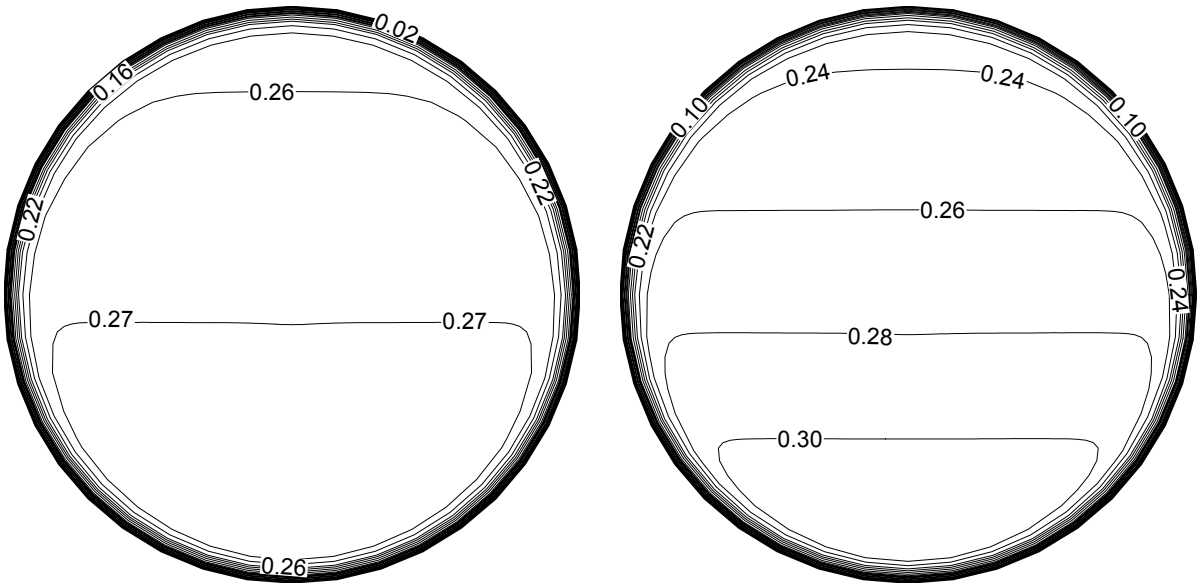

(a) $\varepsilon = 0.1$ (b) $\varepsilon = 0.2$

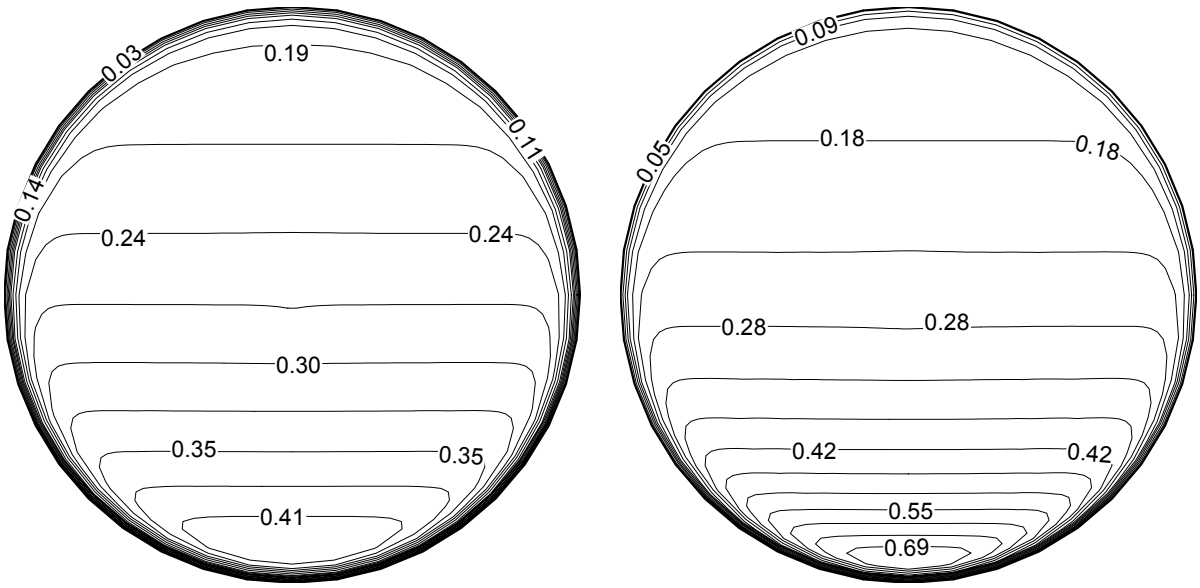

(c) $\varepsilon = 0.5$ (d) $\varepsilon = 0.8$

Figure 6.7 Contour lines of the axial velocity at *dP/ds=-10*, $Da = 1 \times 10^{-3}$, C_F =0.55, φ =0.95, λ =0.1 for different dimensionless curvatures: (a) ε =0.1 (b) ε =0.2 (c) ε =0.5 (d) ε =0.8

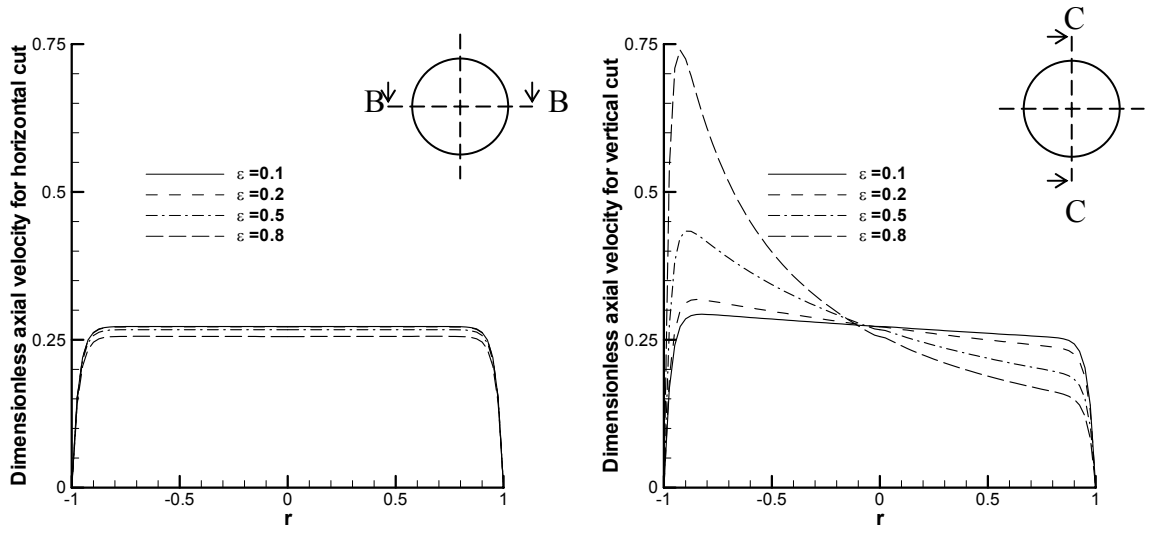

Figure 6.8 Axial velocity profiles in the horizontal (left) and vertical (right) cut view of the pipe at *dP/ds=-10*, $Da = 1 \times 10^{-3}$, C_F =0.55, φ =0.95, λ =0.1 for different dimensionless curvatures. The curves for different ε corresponds to the cases (a)-(d) displayed in Figure 6.6 and 6.7

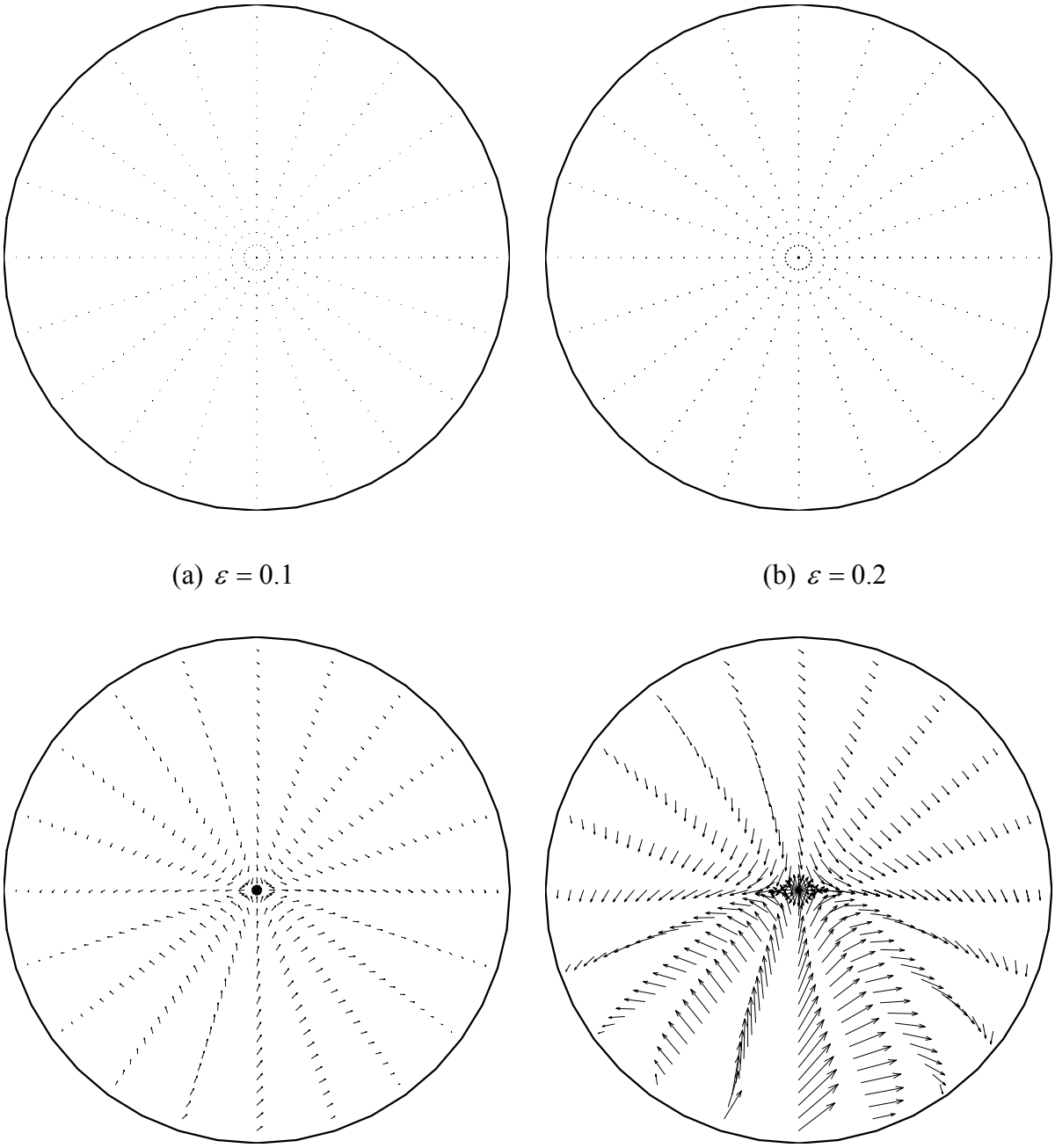

(a) $\varepsilon = 0.1$ (b) $\varepsilon = 0.2$

(c) $\varepsilon = 0.5$ (d) $\varepsilon = 0.8$

Figure 6.9 Vector plots of secondary flow at *dP/ds*=-10, $Da = 1 \times 10^{-3}$, C_F =0.55, φ =0.95, λ =0.1 for different dimensionless curvatures: (a) ε =0.1 (b) ε =0.2 (c) ε =0.5 (d) ε =0.8

Figure 6.10 compares the contour lines of the axial velocity, vector plots of the secondary flow, contour lines of the circumferential velocity and the radial velocity for different ratios

of torsion to curvature, λ, (0.1, 0.5, and 1.0, respectively) when *dP/ds* is fixed at –10, Darcy number *Da* is 1×10^{-3}, Forchheimer coefficient C_F is 0.55, φ is 0.95, and ε is fixed at 0.1. The contour lines of the axial velocity are similar for the three cases computed with different values of λ and the distributions and magnitudes of the axial velocity are almost identical. It seems that λ does not have much influence on the axial velocity. Nevertheless, the vector plots of the secondary flow depend upon λ. When the ratio of torsion to curvature increases, the secondary flow becomes stronger. The contour lines of the circumferential velocity and radial velocity also show that the magnitudes of velocity components in the plane normal to the main flow increase with λ. However, the magnitudes of circumferential and radial velocity are very small compared to that of the axial velocity.

To show the importance of the inertia term for predicting the secondary flow, the Figure 6.11 presents computational results obtained using the full form of the momentum equation (with flow inertia) and the truncated form of the momentum equation (with the inertia term neglected). This figure shows that when the inertia term is accounted for in the momentum equation, the axial velocity is greater and the secondary flow is apparent. When the inertia term is neglected, the secondary flow can not be observed.

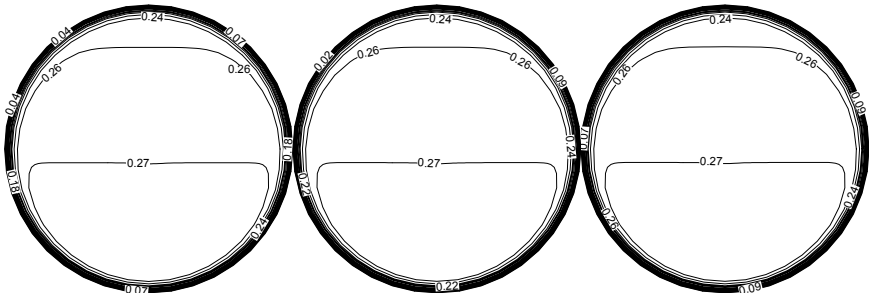

Contour lines of the axial velocity

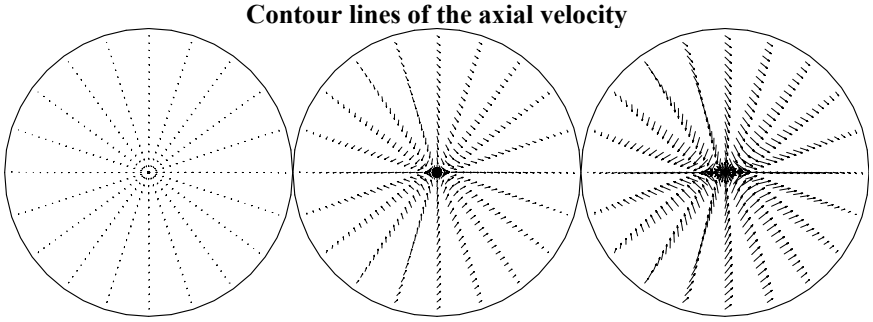

Vector plot of the secondary flow

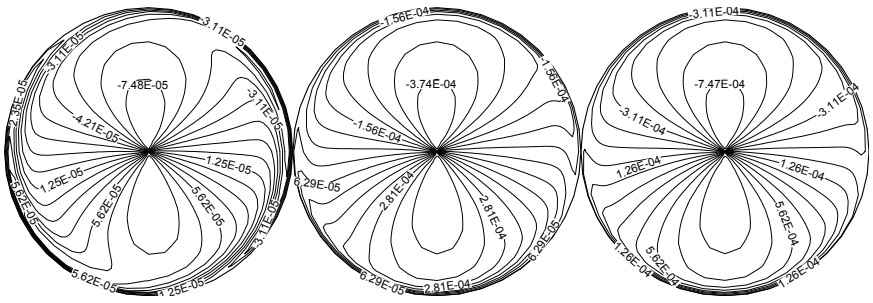

Contour lines of the circumferential velocity

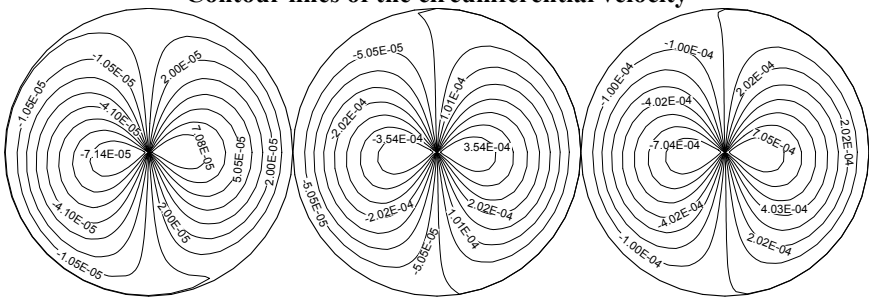

Contour lines of the radial velocity

(a) (b) (c)

Figure 6.10 Velocity components computed at *dP/ds*=-10, $Da = 1 \times 10^{-3}$, C_F =0.55, φ =0.95, ε =0.1 for different values of the ratio of torsion to curvature: (a) λ =0.1 (b) λ =0.5 (c) λ =1.0

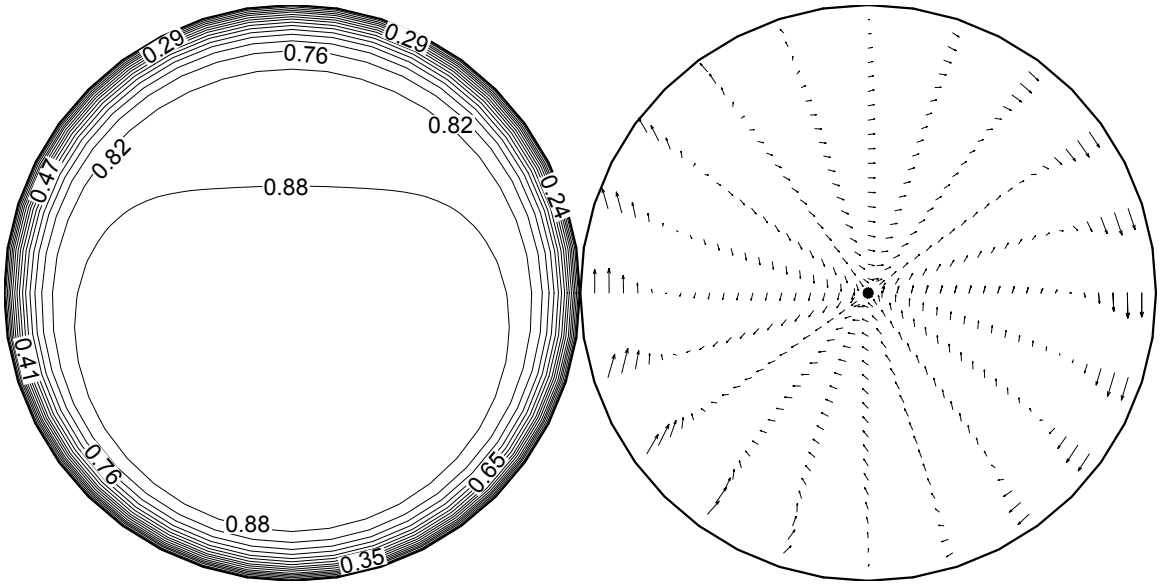

(a) With inertia term

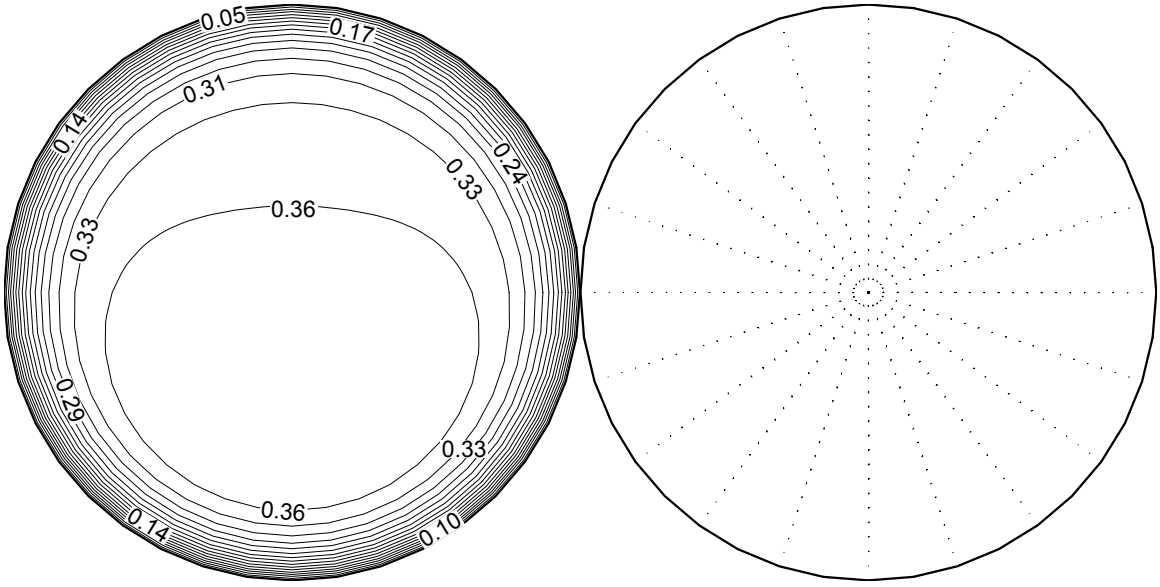

(b) Without inertia term

Figure 6.11 Axial velocity (left) and secondary flow (right) computed for *dP/ds*=-10, $Da = 1 \times 10^{-2}$**,** C_F **=0.55,** φ **=0.95,** ε **=0.1,** λ **=0.1 utilizing (a) the full momentum equation (with the inertia term) (b) truncated form of the momentum equation (without the inertia term)**

6.5 CONCLUSIONS

The laminar flow in a helical pipe filled with a fluid saturated porous medium is investigated. A full momentum equation that accounts for the Brinkman and Forchheimer extensions of the Darcy law and the flow inertia is utilized. The governing equations are projected on an orthogonal helical coordinate system. The objective is to study the effects of the parameters characterizing the porous medium, the Darcy number, *Da*, and the Forchheimer coefficient, C_F, and the geometrical parameters of helical pipes, dimensionless curvature, ε, and the ratio of torsion to curvature, λ. For a given helical pipe, if the Forchheimer coefficient is constant, increasing the Darcy number results in larger axial filtration velocity and the distortion of the axial velocity profile caused by the centrifugal force becomes more apparent. A maximum axial velocity is displaced towards the outer wall. The secondary flow is also intensified with increase in the Darcy number. When *Da* is fixed, the axial velocity decreases and the secondary flow becomes weaker when the Forchheimer coefficient, C_F, increases. In the core region of the helical pipe, the profiles of the axial velocity are represented by straight lines which are parallel to each other for different values of the Forchheimer coefficient. When *Da* and C_F are fixed, investigation shows that the dimensionless curvature, ε, affects both the axial velocity distribution and the secondary flow, but the other dimensionless parameter, the ratio of torsion to curvature, λ, affects only the secondary flow. When ε increases, the flow through the helical pipe is dragged more to the outer wall and the profile of the axial velocity changes from flat to cuneiform. The secondary flow is not visible for small ε, but becomes stronger when ε increases. The larger ratio of torsion to curvature, λ, results in stronger secondary flow but does not significantly affect the distribution of the axial velocity. Computations utilizing the truncated

form of the momentum equation (with the inertia term neglected) show that accounting for the inertia term is crucial for predicting secondary flow in a helical pipe. Thus, in a curved pipe, utilizing the Brinkman-Forchheimer extension of the Darcy law is insufficient to correctly predict the secondary flow. The inertia term must be accounted for as well.

REFERENCES

1. Dean, W.R. (1927) Note on the motion of fluid in a curved pipe, *Philosophical Magazine*, 4: 208-223.

2. Germano, M. (1982) On the effect of torsion on a helical pipe flow, *J. Fluid Mech.,* 125: 1-8.

3. Germano, M. (1989) The Dean equations extended to a helical pipe flow, *J. Fluid Mech.,* 203: 289-305.

4. Liu, S., Masliyah, J.H. (1993) Axially invariant laminar flow in helical pipes with a finite pitch, *J. Fluid Mech.,* 251: 315-353.

5. Liu, S., Masliyah, J.H. (1994) Developing convective heat transfer in helical pipes with finite pitch, *Int. J. Heat and Fluid Flow,* 15: 66-74.

6. Yang, G., Dong, Z. F. and Ebadian, M. A. (1995) Laminar forced convection in a helicoidal pipe with finite pitch, *Int. J. Heat Mass Transfer,* 38: 853-862.

7. Hüttl, T. J. (1997) Navier Stokes solutions of laminar flows based on orthogonal helical coordinates, *Numerical Methods in Laminar and Turbulent Flow,* 10: 191-202.

8. Hüttl, T. J. (2000) Influence of curvature and torsion on turbulent flow in curved and helically coiled pipes, *Int. J. Heat and Fluid Flow,* 21: 345-353.

9. Pharoah, J.G., Litster, S. and Djilali, N. (2003), Mass transfer enhancement in membrane separation –rotating vs. helical modules", CFD 2003, Vancouver, May, pp.28-30.

10. Zheng, B., Lin, C.X. and Ebadian, M.A. (2000) Combined laminar forced convection and thermal radiation in a helical pipe, *Int. J. Heat and Mass Transfer,* 43: 1067-1078.

11. Lin, C.X., Zhang, P. and Ebadian, M.A. (1997) Laminar forced convection in the entrance region of helical pipes, *Int. J. Heat Mass Transfer,* 40: 3293-3304.

12. Sandeep, K. P., Zuritz, C. A. and Puri, V. M. (2000) Modeling non-Newtonian two-phase flow in conventional and helical-holding tubes, *Int. J. Food Science and Technology,* 35: 511-522.

13. Cheng, L. and Kuzentsov, A.V. (2004) Investigation of a laminar flow of a non-Newtonian fluid in a helical pipe. *International Journal of Applied Mechanics and Engineering* (in press).

14. Nield, D. A. and Kuznetsov, A.V. (2004) Forced convection in a helical pipe filled with a saturated medium. *International Journal of Heat and Mass Transfer*, 47: 5175-5180.

15. Nield, D.A. and Bejan, A. (1999) *Convection in Porous Media*, 2nd ed., Springer, New York.

16. Patankar, S. V. (1980) *Numerical Heat Transfer and Fluid Flow*, Hemisphere, New York.

7 HEAT TRANSFER IN A LAMINAR FLOW IN A HELICAL PIPE FILLED WITH A FLUID SATURATED POROUS MEDIUM

ABSTRACT

This chapter presents the first attempt to investigate numerically heat transfer in a helical pipe filled with a fluid saturated porous medium; the analysis is based on the full momentum equation for porous media that accounts for the Brinkman and Forchheimer extensions of the Darcy law as well as for the flow inertia. Numerical computations are performed in an orthogonal helical coordinate system. The effects of the Darcy number, the Forchheimer coefficient as well as the Dean and Germano numbers on the axial flow velocity, secondary flow, temperature distribution, and the Nusselt number are investigated.

Nomenclature

a	pipe radius, m
C_F	Forchheimer coefficient
Da	Darcy number, $\frac{K}{a^2}$
Dn	Dean number, $\varepsilon^{1/2}\,\mathrm{Re}$
Gn	Germano number, $\varepsilon\lambda\,\mathrm{Re}$
h_s	dimensionless scale factor
$\tilde{h}_r$, $\tilde{h}_s$, $\tilde{h}_\theta$	dimensional scale factors
k	thermal conductivity, W m^{-1} K^{-1}

K	permeability, m^2
Nu	Nusselt number, $\frac{2a}{K}\frac{q''_w}{(\tilde{T}_w - \tilde{T}_b)}$
r	dimensionless radial coordinate, $\tilde{r}/a$
$\tilde{r}$	radial coordinate, m
$\hat{\mathbf{r}}$	residual vector
Re	Reynolds number, $\frac{\rho_f U a}{\mu}$
s	dimensionless axial coordinate, $\tilde{s}/a$
$\tilde{s}$	axial coordinate, m
p	pitch, m
P	dimensionless pressure, $\tilde{P}/\rho U^2$
$\tilde{P}$	pressure, Pa
Pr	Prandtl number, $\frac{c_p \mu}{k_m}$
T	dimensionless temperature, defined in Equation (7.10)
$\tilde{T}$	temperature, K
$\tilde{T}_b$	mean temperature, defined in Equation (7.10), K
$\tilde{T}_w$	wall temperature, K
U	reference velocity, ms^{-1}

$\tilde{\mathbf{v}}$ velocity vector, ms^{-1}

u_s, u_r, u_θ dimensionless velocity components, $\frac{\tilde{u}_s}{U}, \frac{\tilde{u}_r}{U}, \frac{\tilde{u}_\theta}{U}$

$\tilde{u}_s, \tilde{u}_r, \tilde{u}_\theta$ velocity components, m s^{-1}

Greek symbols

ε dimensionless curvature, κa

θ angle, defined in Fig. 1b

κ curvature, m^{-1}

λ the ratio of torsion to curvature, τ / κ

μ effective dynamic viscosity of a porous medium, kg m^{-1} s^{-1}

ν effective kinematic viscosity of a porous medium, m^2 s

ξ angle, defined in Fig. 7.1b

ρ_f fluid density, kg m^{-3}

τ torsion, m^{-1}

φ porosity

ϕ angle, defined in Fig. 1a

Subscripts

s axial direction

r radial direction

θ circumferential direction

7.1 INTRODUCTION

The investigation of flows in porous media is motivated by various engineering applications, such as migration of moisture in fibrous insulation, grain storage, transport in contaminated soils, underground disposal of nuclear wastes, transport in drying processes, etc. Nield and Bejan [1] summarized the state-of-art on this topic. Another quickly developing research field related to porous media is concerned with biomedical applications. In a clotted artery, the lesions or "plaques" within the artery wall consist of localized deposits of fat compounds (lipids) surrounded by cells recruited from the blood stream and scar tissue; this acts as a porous medium that may diminish or completely eliminate the blood flow. The coronary arteries surrounding the heart are curved and at least segments of them can be modeled as helical.

Flow in helical pipes is also a subject of intensive investigation. Of primary interest is the secondary flow caused by the centrifugal force in a helical pipe. Numerical studies have been conducted to examine the effects of torsion and curvature on the Newtonian fluid flow in helical pipes utilizing the Dean number, $Dn = \varepsilon^{1/2}\,\mathrm{Re}$, and the Germano number, $Gn = (\varepsilon\lambda)\,\mathrm{Re}$, to characterize the magnitude and the shape of the secondary flow and the effects of the curvature and torsion on helical pipe flow [2-9]. Sandeep [10] extended the analysis of a helical pipe flow to non-Newtonian fluids; the numerical research was performed in a Cartesian coordinate system. Cheng and Kuznetsov [11] used the orthogonal helical coordinate system to study the effects of torsion and curvature on non-Newtonian

fluid flow in helical pipes and compared the flow dynamics between Newtonian and non-Newtonian fluids.

Numerical computations of heat transfer in helical pipes were reported in a number of publications [12-16]. Cheng and Kuznetsov [17] studied heat transfer in a fully-developed laminar flow of a non-Newtonian fluid in a helical pipe with a constant wall heat flux; the effects of the Dean and Germano numbers with a fixed Reynolds number on the hydrodynamics and heat transfer in non-Newtonian fluid flow in helical pipes were investigated. Nield and Kuznetsov [18] presented a perturbation analysis and obtained an analytical expression for the Nusselt number in a helical pipe filled with a porous medium for the case when the flow in a pipe is described by the Darcy law.

In the previous chapter, Cheng and Kuznetsov [19] investigated laminar flow in a helical pipe filled with a porous medium utilizing the Brinkman-Forchheimer-extended Darcy equation with inertia terms. The purpose of this chapter is to perform numerical simulations of heat transfer for a fully developed laminar flow of a Newtonian fluid in a helical pipe filled with a fluid saturated porous medium subjected to a constant wall heat flux. An orthogonal helical coordinate system is utlizied. The effects of the Darcy number, the Forchheimer coefficient, the Dean number, and the Germano number with a fixed Reynolds number on the hydrodynamics and heat transfer in helical pipes are investigated.

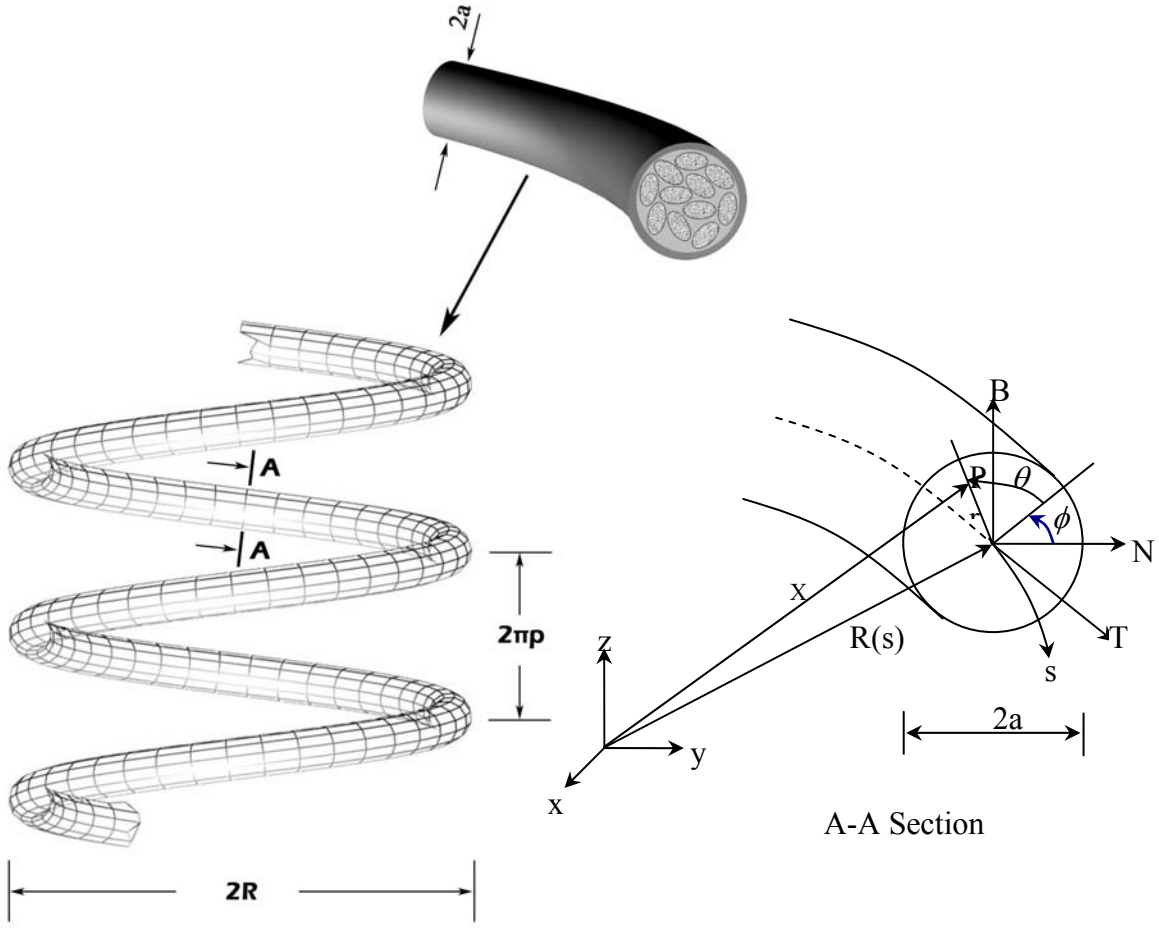

(a) **(b)**

Figure 7.1 Schematic diagram of a helical pipe and the orthogonal helical coordinate system

7.2 GOVERNING EQUATIONS

A helical pipe (Fig. 7.1a) is characterized by two parameters, the curvature, κ, and the torsion, τ, which are defined as, respectively

$$\kappa = \frac{R}{R^2 + p^2}, \qquad \tau = \frac{p}{R^2 + p^2} \tag{7.1}$$

An orthogonal helical coordinate system introduced by Germano [3, 4] is utilized with a helical coordinate *s* for the axial direction, *r* for the radial direction, and θ for the circumferential direction (Figure 7.1b). The continuity and momentum equations in the vector form are

$$\nabla \cdot \tilde{\mathbf{v}} = 0 \tag{7.2}$$

and

$$\frac{\rho_f}{\varphi^2}(\tilde{\mathbf{v}} \cdot \nabla)\tilde{\mathbf{v}} = -\nabla \tilde{P} + \frac{\mu}{\varphi}\nabla^2 \tilde{\mathbf{v}} - \frac{\mu}{K}\tilde{\mathbf{v}} - \frac{C_F \rho_f}{K^{1/2}}|\tilde{\mathbf{v}}|\tilde{\mathbf{v}} \tag{7.3}$$

where *K* is the permeability of the porous medium, C_F is the Forchheimer coefficient, and φ is the porosity.

Equation (7.3) is a full momentum equation for the steady flow in porous media that accounts for the Brinkman and Forchheimer extensions of the Darcy law as well as for the flow inertia [1]. The energy equation (the effect of thermal dispersion is neglected) is given by

$$(\rho c_p)_f \frac{D\tilde{T}}{Dt} = \nabla \cdot \left[k_m \nabla \tilde{T}\right] \tag{7.4}$$

$$k_m = \varphi k_f + (1-\varphi)k_s \tag{7.5}$$

where k_m is the effective thermal conductivity of porous medium and the subscripts '*f*' and '*s*' refer to 'fluid' and 'solid', respectively.

In the orthogonal helical coordinate system, the scale factors are given by

$$\tilde{h}_s = 1 + \kappa \tilde{r}\sin(\theta + \phi) \qquad \tilde{h}_r = 1 \qquad \tilde{h}_\theta = \tilde{r} \tag{7.6}$$

The dimensionless governing equations for the flow in a porous medium written in the orthogonal helical coordinate system are the continuity equation

$$\frac{\partial(ru_s)}{\partial s}+\frac{\partial(rh_s u_r)}{\partial r}+\frac{\partial(h_s u_\theta)}{\partial \theta}=0 \tag{7.7}$$

the momentum equations

$$\begin{aligned}&\frac{1}{\varphi^2}\frac{1}{h_s r}\left(\frac{\partial(ru_s u_s)}{\partial s}+\frac{\partial(rh_s u_r u_s)}{\partial r}+\frac{\partial(h_s u_\theta u_s)}{\partial \theta}\right)+\frac{1}{\varphi^2}\frac{\varepsilon}{h_s}u_s\left(u_r\sin(\theta+\phi)+u_\theta\cos(\theta+\phi)\right)=-\frac{1}{h_s}\frac{\partial P}{\partial s}\\&+\frac{1}{\varphi}\frac{1}{\mathrm{Re}}\left\{\frac{1}{h_s}\frac{\partial}{\partial s}\left[\frac{1}{h_s r}\left[\frac{\partial(ru_s)}{\partial s}+\frac{\partial(rh_s u_r)}{\partial r}+\frac{\partial(h_s u_\theta)}{\partial \theta}\right]\right]-\right.\\&\left.\frac{1}{r}\left(\frac{\partial}{\partial r}\left(\frac{r}{h_s}\left(\frac{\partial u_r}{\partial s}-\frac{\partial}{\partial r}(h_s u_s)\right)\right)-\frac{\partial}{\partial \theta}\left(\frac{1}{h_s r}\left(\frac{\partial}{\partial \theta}(h_s u_s)-\frac{\partial}{\partial \theta}(ru_\theta)\right)\right)\right)\right\}\\&-\frac{1}{\mathrm{Re}}\frac{1}{Da}u_s-\frac{C_F}{Da^{1/2}}u_s\left(u_s^2+u_r^2+u_\theta^2\right)^{1/2}\end{aligned} \tag{7.8a}$$

$$\begin{aligned}&\frac{1}{\varphi^2}\frac{1}{h_s r}\left(\frac{\partial(ru_s u_r)}{\partial s}+\frac{\partial(rh_s u_r u_r)}{\partial r}+\frac{\partial(h_s u_\theta u_r)}{\partial \theta}\right)-\frac{1}{\varphi^2}\frac{u_\theta^{\,2}}{r}-\frac{1}{\varphi^2}\frac{k}{h_s}u_s^{\,2}\sin(\theta+\phi)=-\frac{\partial}{\partial}\\&+\frac{1}{\varphi}\frac{1}{\mathrm{Re}}\left\{\frac{\partial}{\partial r}\left[\frac{1}{h_s r}\left[\frac{\partial(ru_s)}{\partial s}+\frac{\partial(rh_s u_r)}{\partial r}+\frac{\partial(h_s u_\theta)}{\partial \theta}\right]\right]-\right.\\&\left.\frac{1}{h_s r}\left(\frac{\partial}{\partial \theta}\left(\frac{h_s}{r}\left(\frac{\partial}{\partial r}(ru_\theta)-\frac{\partial u_r}{\partial \theta}\right)\right)-\frac{\partial}{\partial s}\left(\frac{r}{h_s}\left(\frac{\partial u_r}{\partial s}-\frac{\partial}{\partial r}(h_s u_s)\right)\right)\right)\right\}\\&-\frac{1}{\mathrm{Re}}\frac{1}{Da}u_r-\frac{C_F}{Da^{1/2}}u_r\left(u_s^2+u_r^2+u_\theta^2\right)^{1/2}\end{aligned} \tag{7.8b}$$

$$\begin{aligned}&\frac{1}{\varphi^2}\frac{1}{h_s r}\left(\frac{\partial(ru_s u_\theta)}{\partial s}+\frac{\partial(rh_s u_r u_\theta)}{\partial r}+\frac{\partial(h_s u_\theta u_\theta)}{\partial \theta}\right)-\frac{1}{\varphi^2}\frac{\varepsilon}{h_s}u_s^{\,2}\cos(\theta+\phi)+\frac{1}{\varphi^2}\frac{u_r u_\theta}{r}=-\frac{1}{r}\\&+\frac{1}{\varphi}\frac{1}{\mathrm{Re}}\left\{\frac{1}{r}\frac{\partial}{\partial \theta}\left[\frac{1}{h_s r}\left[\frac{\partial(ru_s)}{\partial s}+\frac{\partial(rh_s u_r)}{\partial r}+\frac{\partial(h_s u_\theta)}{\partial \theta}\right]\right]-\right.\\&\left.\frac{1}{h_s}\left(\frac{\partial}{\partial s}\left(\frac{1}{h_s r}\left(\frac{\partial}{\partial \theta}(h_s u_s)-\frac{\partial}{\partial s}(ru_\theta)\right)\right)-\frac{\partial}{\partial r}\left(\frac{h_s}{r}\left(\frac{\partial}{\partial r}(ru_\theta)-\frac{\partial u_r}{\partial \theta}\right)\right)\right)\right\}\\&-\frac{1}{\mathrm{Re}}\frac{1}{Da}u_\theta-\frac{C_F}{Da^{1/2}}u_\theta\left(u_s^2+u_r^2+u_\theta^2\right)^{1/2}\end{aligned} \tag{7.8c}$$

and the energy equation

$$\left(\frac{\partial(ru_sT)}{\partial s}+\frac{\partial(rh_su_rT)}{\partial r}+\frac{\partial(h_su_\theta T)}{\partial \xi}\right)=\frac{ru_s}{\mathrm{Re}\,\mathrm{Pr}} + \frac{1}{\mathrm{Re}\,\mathrm{Pr}}\left(\frac{\partial}{\partial s}\left[\frac{r}{h_s}\frac{\partial T}{\partial s}\right]+\frac{\partial}{\partial r}\left[h_s r\frac{\partial T}{\partial r}\right]+\frac{\partial}{\partial \xi}\left[\frac{h_s}{r}\frac{\partial T}{\partial \xi}\right]\right) \tag{7.9}$$

where

$$s=\frac{\tilde{s}}{a},\ r=\frac{\tilde{r}}{a},\ (u_s,u_r,u_\theta)=\left(\frac{\tilde{u}_s}{U},\frac{\tilde{u}_r}{U},\frac{\tilde{u}_\theta}{U}\right),\ P=\frac{\tilde{P}}{\rho_f U^2},\ \varepsilon=\kappa a,\ \lambda=\frac{\tau}{\kappa},$$

$$\mathrm{Re}=\frac{\rho_f U a}{\mu},\ Da=\frac{K}{a^2},\ U=\frac{1}{\pi}\int_0^{2\pi}\int_0^1 u_s r dr d\theta,\ \tilde{T}_b=\frac{1}{U\pi}\int_0^{2\pi}\int_0^1 u_s\tilde{T} r dr d\theta, \tag{7.10}$$

$$\mathrm{Pr}=\frac{c_p\mu}{k_m},\ Nu=\frac{2a}{K}\frac{q''_w}{(\tilde{T}_w-\tilde{T}_b)},\ T=\frac{\tilde{T}-\tilde{T}_w}{Nu(\tilde{T}_b-\tilde{T}_w)}$$

where a is the radius of the pipe and U is the bulk velocity defined in Eq. (7.10).

A fully developed laminar flow is considered so that the dynamic variables except for the pressure are independent of s; therefore, the following simplifying transformation is performed from s, r, θ to s, r, ξ:

$$\theta+\phi=\xi,\ \frac{\partial}{\partial s}\Rightarrow\frac{\partial}{\partial s}-\varepsilon\lambda\frac{\partial}{\partial \xi},\ \frac{\partial}{\partial \theta}\Rightarrow\frac{\partial}{\partial \xi} \tag{7.11}$$

The governing equations are then reduced as:

$$-\varepsilon\lambda\frac{\partial(ru_s)}{\partial \xi}+\frac{\partial(rh_su_r)}{\partial r}+\frac{\partial(h_su_\theta)}{\partial \xi}=0 \tag{7.12}$$

$$\frac{1}{\varphi^2}\frac{1}{h_s r}\left(-\varepsilon\lambda\frac{\partial(ru_s u_s)}{\partial\xi}+\frac{\partial(rh_s u_r u_s)}{\partial r}+\frac{\partial(h_s u_\theta u_s)}{\partial\xi}\right)+\frac{1}{\varphi^2}\frac{\varepsilon}{h_s}u_s\left(u_r\sin\xi+u_\theta\cos\xi\right)=-\frac{1}{h_s}\left(\frac{\partial P}{\partial s}-\varepsilon\lambda\frac{\partial P}{\partial\xi}\right)$$
$$+\frac{1}{\varphi}\frac{1}{\mathrm{Re}}\left\{-\varepsilon\lambda\frac{1}{h_s}\frac{\partial}{\partial\xi}\left[\frac{1}{h_s r}\left[-\varepsilon\lambda\frac{\partial(ru_s)}{\partial\xi}+\frac{\partial(rh_s u_r)}{\partial r}+\frac{\partial(h_s u_\theta)}{\partial\xi}\right]\right]-\right.$$
$$\left.\frac{1}{r}\left(\frac{\partial}{\partial r}\left(\frac{r}{h_s}\left(-\varepsilon\lambda\frac{\partial u_r}{\partial\xi}-\frac{\partial}{\partial r}(h_s u_s)\right)\right)-\frac{\partial}{\partial\xi}\left(\frac{1}{h_s r}\left(\frac{\partial}{\partial\xi}(h_s u_s)+\varepsilon\lambda\frac{\partial}{\partial\xi}(ru_\theta)\right)\right)\right)\right\} \qquad (7.13a)$$
$$-\frac{1}{\mathrm{Re}}\frac{1}{Da}u_s-\frac{C_F}{Da^{1/2}}u_s\left(u_s^2+u_r^2+u_\theta^2\right)^{1/2}$$

$$\frac{1}{\varphi^2}\frac{1}{h_s r}\left(-\varepsilon\lambda\frac{\partial(ru_s u_r)}{\partial\xi}+\frac{\partial(rh_s u_r u_r)}{\partial r}+\frac{\partial(h_s u_\theta u_r)}{\partial\xi}\right)-\frac{1}{\varphi^2}\frac{u_\theta^{\,2}}{r}-\frac{1}{\varphi^2}\frac{\varepsilon}{h_s}u_s^{\,2}\sin\xi=-\frac{\partial}{\partial}$$
$$+\frac{1}{\varphi}\frac{1}{\mathrm{Re}}\left\{\frac{\partial}{\partial r}\left[\frac{1}{h_s r}\left[-\varepsilon\lambda\frac{\partial(ru_s)}{\partial\varsigma}+\frac{\partial(rh_s u_r)}{\partial r}+\frac{\partial(h_s u_\theta)}{\partial\xi}\right]\right]-\right.$$
$$\left.\frac{1}{h_s r}\left(\frac{\partial}{\partial\xi}\left(\frac{h_s}{r}\left(\frac{\partial}{\partial r}(ru_\theta)-\frac{\partial u_r}{\partial\xi}\right)\right)+\varepsilon\lambda\frac{\partial}{\partial\xi}\left(\frac{r}{h_s}\left(-\varepsilon\lambda\frac{\partial u_r}{\partial\xi}-\frac{\partial}{\partial r}(h_s u_s)\right)\right)\right)\right\} \qquad (7.13b)$$
$$-\frac{1}{\mathrm{Re}}\frac{1}{Da}u_r-\frac{C_F}{Da^{1/2}}u_r\left(u_s^2+u_r^2+u_\theta^2\right)^{1/2}$$

$$\frac{1}{\varphi^2}\frac{1}{h_s r}\left(-\varepsilon\lambda\frac{\partial(ru_s u_\theta)}{\partial\xi}+\frac{\partial(rh_s u_r u_\theta)}{\partial r}+\frac{\partial(h_s u_\theta u_\theta)}{\partial\xi}\right)-\frac{1}{\varphi^2}\frac{\varepsilon}{h_s}u_s^{\,2}\cos\xi+\frac{1}{\varphi^2}\frac{u_r u_\theta}{r}=-\frac{1}{r}\frac{\partial}{\partial}$$
$$+\frac{1}{\varphi}\frac{1}{\mathrm{Re}}\left\{\frac{1}{r}\frac{\partial}{\partial\xi}\left[\frac{1}{h_s r}\left[-\varepsilon\lambda\frac{\partial(ru_s)}{\partial\xi}+\frac{\partial(rh_s u_r)}{\partial r}+\frac{\partial(h_s u_\theta)}{\partial\xi}\right]\right]-\right.$$
$$\left.\frac{1}{h_s}\left(-\varepsilon\lambda\frac{\partial}{\partial\xi}\left(\frac{1}{h_s r}\left(\frac{\partial}{\partial\xi}(h_s u_s)+\varepsilon\lambda\frac{\partial}{\partial\xi}(ru_\theta)\right)\right)-\frac{\partial}{\partial r}\left(\frac{h_s}{r}\left(\frac{\partial}{\partial r}(ru_\theta)-\frac{\partial}{\partial\xi}(u_r)\right)\right)\right)\right\} \qquad (7.13c)$$
$$-\frac{1}{\mathrm{Re}}\frac{1}{Da}u_\theta-\frac{C_F}{Da^{1/2}}u_\theta\left(u_s^2+u_r^2+u_\theta^2\right)^{1/2}$$

$$\left(-\varepsilon\lambda\frac{\partial(ru_s T)}{\partial\xi}+\frac{\partial(rh_s u_r T)}{\partial r}+\frac{\partial(h_s u_\theta T)}{\partial\xi}\right)=\frac{ru_s}{\mathrm{Re}\,\mathrm{Pr}}$$
$$+\frac{1}{\mathrm{Re}\,\mathrm{Pr}}\left((\varepsilon\lambda)^2\frac{\partial}{\partial\xi}\left[\frac{r}{h_s}\frac{\partial T}{\partial\xi}\right]+\frac{\partial}{\partial r}\left[h_s r\frac{\partial T}{\partial r}\right]+\frac{\partial}{\partial\xi}\left[\frac{h_s}{r}\frac{\partial T}{\partial\xi}\right]\right) \qquad (7.14)$$

7.3 COMPUTATIONAL PROCEDURE

A control volume-based finite difference method is utilized on an evenly spaced mesh in both radial and circumferential directions. The convection-diffusion terms are discretized with the power-law scheme (Patankar [20]) and the other terms are approximated by central differences. The SIMPLE algorithm (Patankar [20]) is adopted on a staggered grid arrangement to solve the governing equations.

A no-slip boundary condition is assumed at the walls of the helical pipe. To solve the numerical singularity at the pipe axis (r=0), boundary values are needed for flow quantities, which are either located directly at the pipe axis or at the opposite sides of the pipe axis (Hüttl [7]; Cheng and Kuznetsov [11]). An initial value of the Reynolds number, which is needed to start the iterations, is estimated as follows. The flow is driven by a constant pressure gradient dP/ds that has to balance the fluid friction in a porous medium, which implies that approximately (neglecting the Forchheimer resistance) the following equation is satisfied:

$$\left(\frac{dP}{ds}\right) = \frac{1}{Da\ \mathrm{Re}} \qquad (7.15)$$

This is used to evaluate only the initial value of Re. During the iteration process, Re is evaluated according to Eq. (7.10) utilizing the value of the mean velocity from the previous iteration.

A constant wall heat flux is assumed as the boundary condition for the energy equation. Since heat transfer is independent of the flow velocity, the energy equation is solved after the velocity profile has been obtained. The effects of different parameters for the same values of

the Reynolds number on the hydrodynamics and heat transfer in a helical pipe are investigated.

7.4 RESULTS AND DISCUSSION

A constant Reynolds number of 100 is assumed for all cases to compare the effects of the Darcy number, the Forchheimer coefficient, the Dean number, and the Germano number. Values of the Nusselt number for different cases are listed in Table 7.1 to compare the heat transfer efficiency for different parameter values.

Table 7.1 Nusselt number for different parameters

Da	C_F	ε	λ	Dn	Gn	Nu
0.01	0.55	0.1	0.1	31.6	1.0	21.10
0.05	0.55	0.1	0.1	31.6	1.0	12.40
0.1	0.55	0.1	0.1	31.6	1.0	10.19
0.01	0	0.1	0.1	31.6	1.0	6.34
0.01	0.25	0.1	0.1	31.6	1.0	15.34
0.01	0.5	0.1	0.1	31.6	1.0	20.30
0.01	0.55	0.1	0.1	31.6	1.0	21.13
0.01	0.55	0.2	0.05	44.7	1.0	20.88
0.01	0.55	0.5	0.02	70.7	1.0	19.08
0.01	0.55	0.8	0.0125	89.4	1.0	15.21
0.01	0.55	0.1	0.1	31.6	1.0	21.13
0.01	0.55	0.1	0.5	31.6	5.0	21.13
0.01	0.55	0.1	1.0	31.6	10.0	21.13

Figures 7.2 and 7.3 show the effect of the Darcy number on the flow and heat transfer in a helical pipe. Figure 7.2 depicts the axial velocity contours, velocity vector plot of the secondary flow and the dimensionless temperature contours for different Darcy numbers. This figure shows that with the increase of the Darcy number, the axial velocity increases and the secondary flow becomes stronger. This is explained by a larger filtration velocity that can

be attributed to a larger permeability for larger Darcy numbers. However, the dimensionless temperature decreases with the Darcy number, as shown in Fig. 7.2, and the Nusselt number becomes smaller, as shown in Table 7.1. The displacement of the maximum value of the axial velocity to the wall is apparent and can be explained by the effect of the centrifugal force in a helical pipe, but this does not happen for the dimensionless temperature, which remains parabolic for all computed values of the Darcy number. These trends can also be observed from the profile plots of the dimensionless axial velocity and temperature on the horizontal and vertical cut views of the cross section of the pipe (Fig. 7.3).

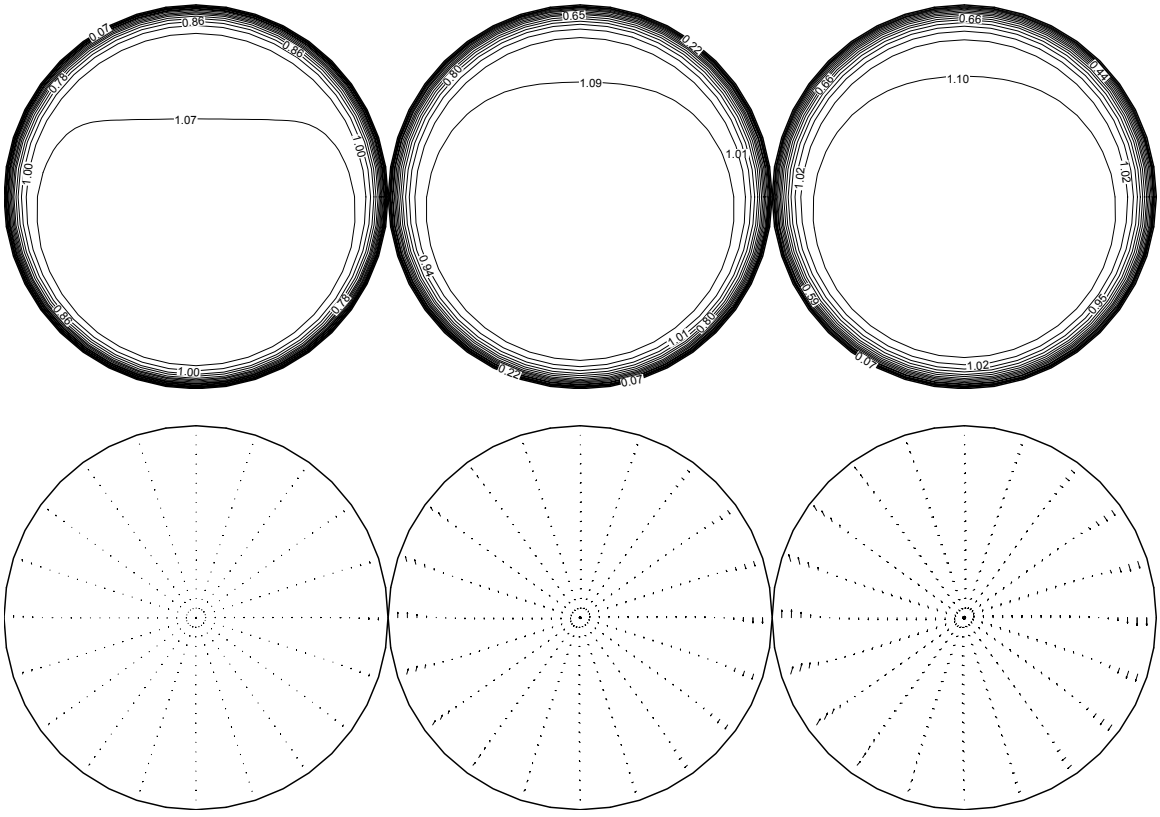

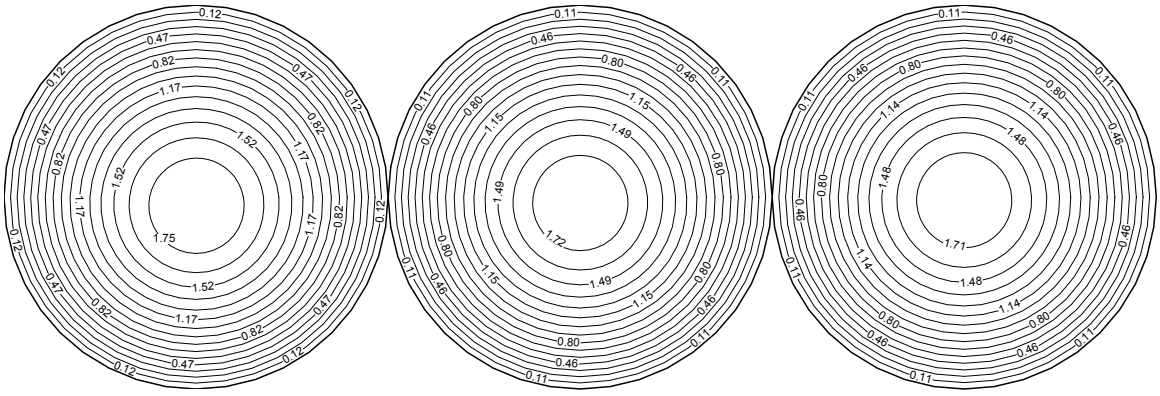

Figure 7.2 Contour lines of the axial velocity (top), vector plots of the secondary flow (middle) and contour lines of the dimensionless temperature (bottom) at *Re=100*, C_F =0.55, φ =0.95, ε =0.1, λ =0.1, *Dn*=31.6, *Gn*=1.0 for different values of the Darcy number: (a) $Da = 10^{-2}$ **(b)** $Da = 5 \times 10^{-2}$ **(c)** $Da = 10^{-1}$

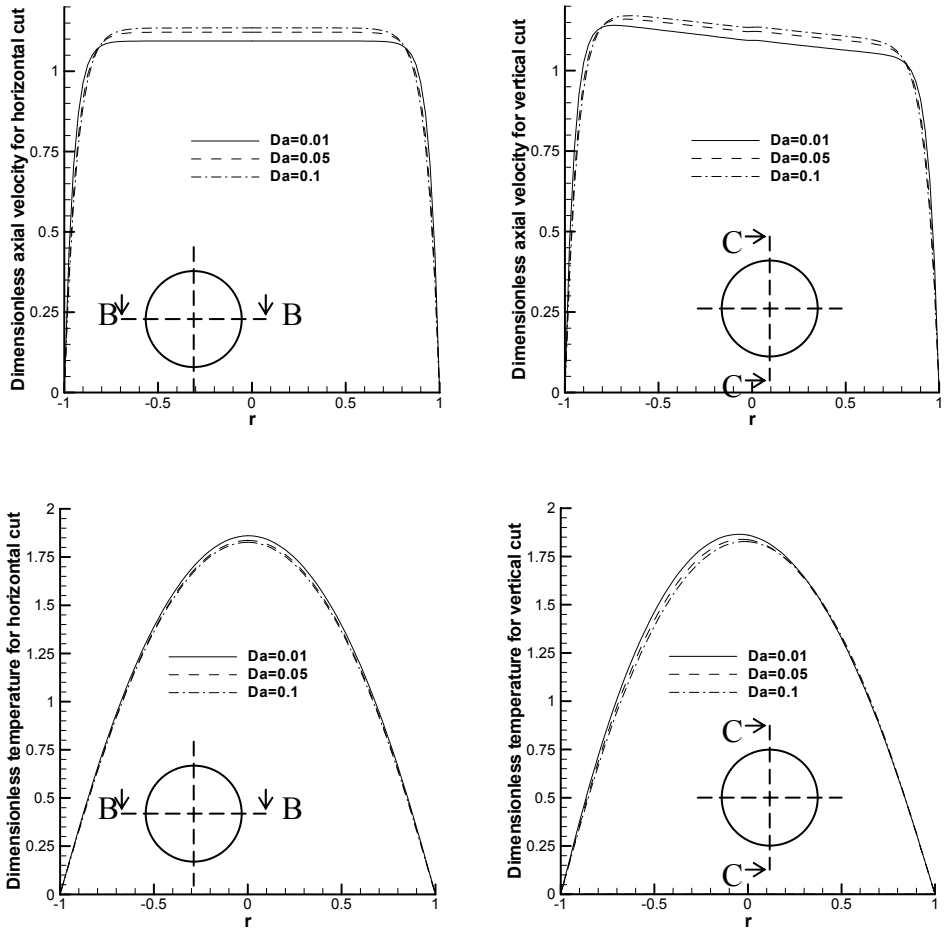

Figure 7.3 Profile plots of the axial velocity (top) and dimensionless temperature (bottom) in the horizontal (left) and vertical (right) cut view of the pipe at *Re=100*, C_F =0.55, φ =0.95, ε =0.1, λ =0.1, *Dn*=31.6, *Gn*=1.0 for different values of the Darcy number. The curves for different *Da* correspond to cases (a)-(c) in Figure 7.2

The effect of the Forchheirmer coefficient, C_F, on the fluid flow and heat transfer in a helical pipe filled with a porous medium is shown in Figures 7.4 and 7.5. The contour lines of the axial velocity show that the value of the maximum axial velocity decreases when C_F is increased and the profile plots of the axial velocity show that increasing C_F results in the displacement of the maximum axial velocity towards the wall. The secondary flow is also damped for larger Forchheimer coefficients (which physically corresponds to larger resistance to the flow by the porous medium), as shown in the vector plots of the secondary flow. The displacement of the maximum value of the dimensionless temperature from the center to the wall becomes smaller with the increase of C_F , however, the value of the maximum increases, opposite to the axial velocity. The Nusselt number also increases, as shown in Table 7.1. When C_F increases from zero (which means that the form drag due to the solid obstacles in the porous medium is totally ignored) to 0.25, the change is much larger than when it increases from 0.25 to 0.5, for both the velocity and the temperature.

The Dean number is a parameter used to characterize the magnitude and the shape of the secondary flow. The effect of the Dean number on the flow and heat transfer is investigated in Figures 7.6, 7.7, and 7.8. Figure 7.6 shows that when *Dn* increases, the contour lines corresponding to large values of the axial velocity are displaced to the outer wall due to the centrifugal force and the value of the maximum axial velocity increases. The secondary flow also becomes stronger. Figure 7.7 shows the contour lines of the dimensionless temperature for the corresponding Dean number. The maximum of the temperature is also displaced to the outer wall with the increase of the Dean number. The profile plots of the axial velocity and temperature in Fig. 7.8 show that the trends are similar except that the profile of the axial velocity is closer to that of a slug flow while the profile of the dimensionless temperature

looks more as a deformed parabolic profile. Table 7.1 shows that the Nusselt number decreases when the Dean number is increased. It can be concluded that the Dean number has significant effect on the axial velocity, secondary flow, and heat transfer.

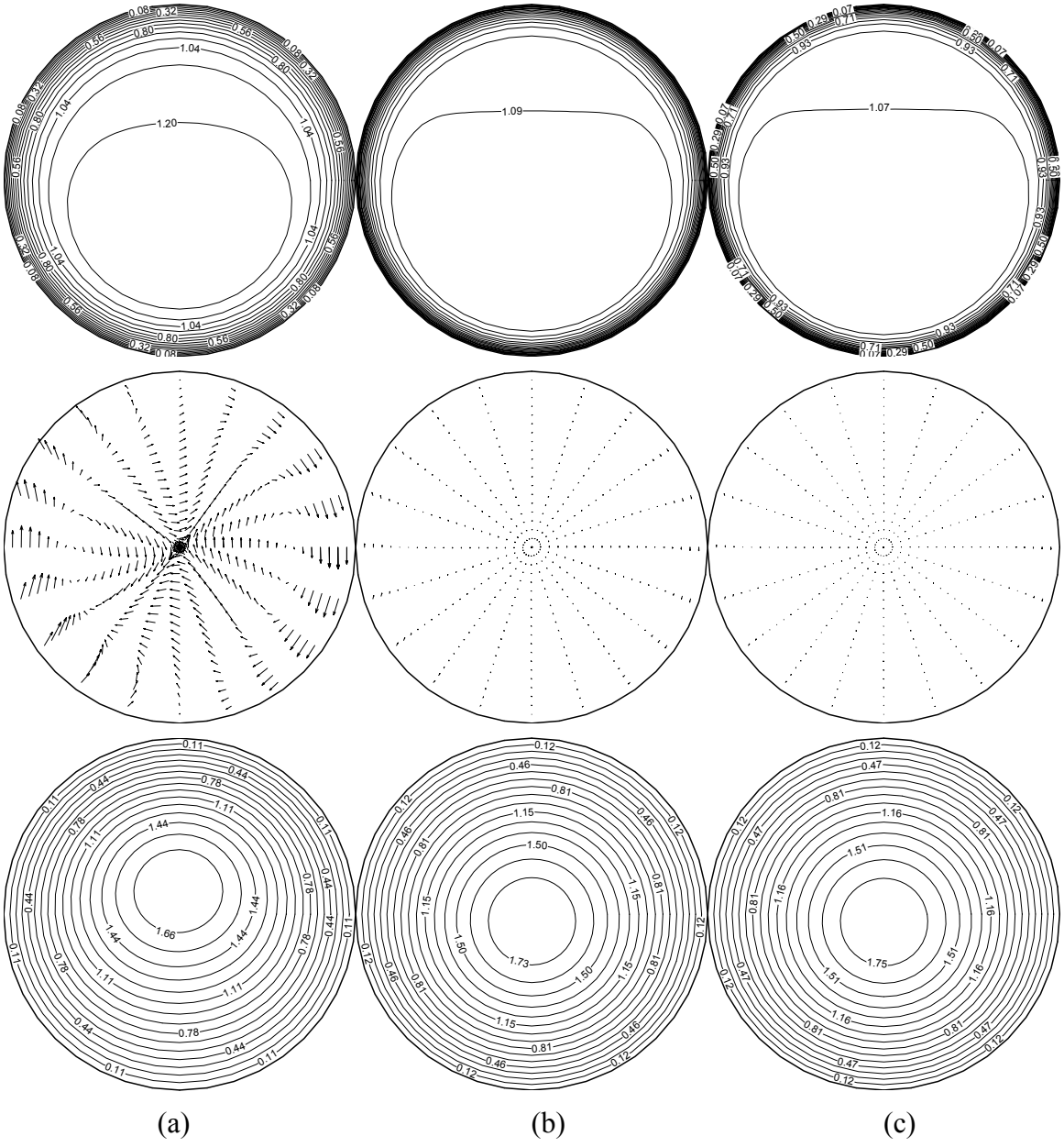

Figure 7.4 Contour lines of the axial velocity (top), vector plots of the secondary flow (middle), and contour lines of the dimensionless temperature (bottom) at *Re=100*, $Da = 10^{-2}$, φ=0.95, ε=0.1, λ=0.1, *Dn*=31.6, *Gn*=1.0 for different values of the Forchheimer coefficient: (a) $C_F = 0.0$ **(b)** $C_F = 0.25$ **(c)** $C_F = 0.50$

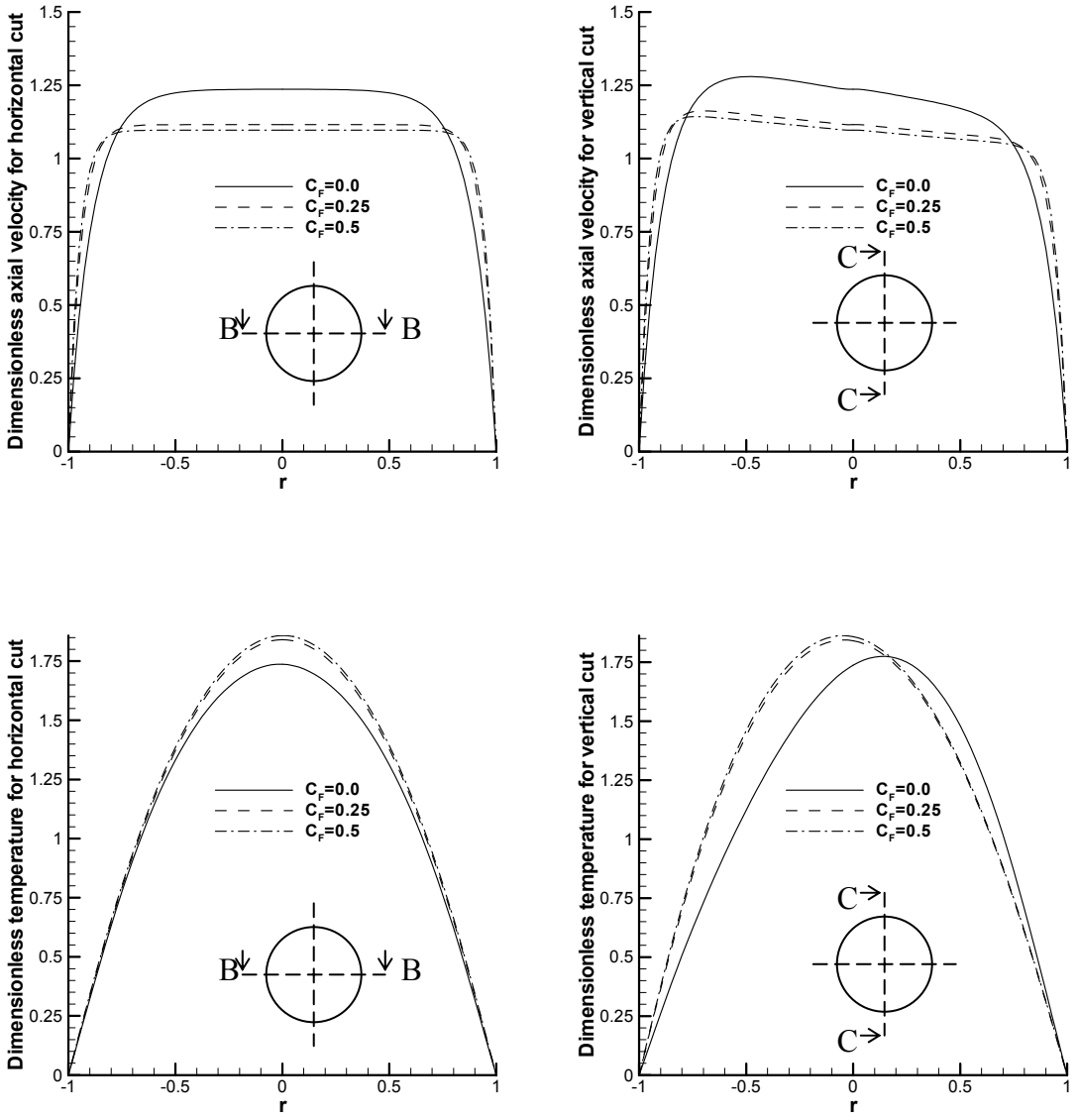

Figure 7.5 Profile plots of the axial velocity (top) and dimensionless temperature (bottom) in the horizontal (left) and vertical (right) cut view of the pipe at *Re=100*, $Da = 10^{-2}$, φ=0.95, $\mathcal{E}$=0.1, λ=0.1, *Dn*=31.6, *Gn*=1.0 for different values of the Forchheimer coefficients. The curves for different C_F correspond to cases (a)-(c) in Figure 7.4

When the Darcy number, the Forchheimer coefficient, and the Dean number are fixed, the distributions of the axial velocity and temperature at the cross-section of a helical pipe do not show any significant sensitivity to the Germano number, which describes the effect of torsion on a flow in a helical pipe (Fig. 7.9). The Nusselt number remains the same, as seen from

Table 7.1. However, the secondary flow does change, as seen from the contour lines of the stream function, which shows that the shape of the swirl is different for different values of the Germano number. It seems that the Germano number only affects the secondary flow but not the axial velocity and heat transfer.

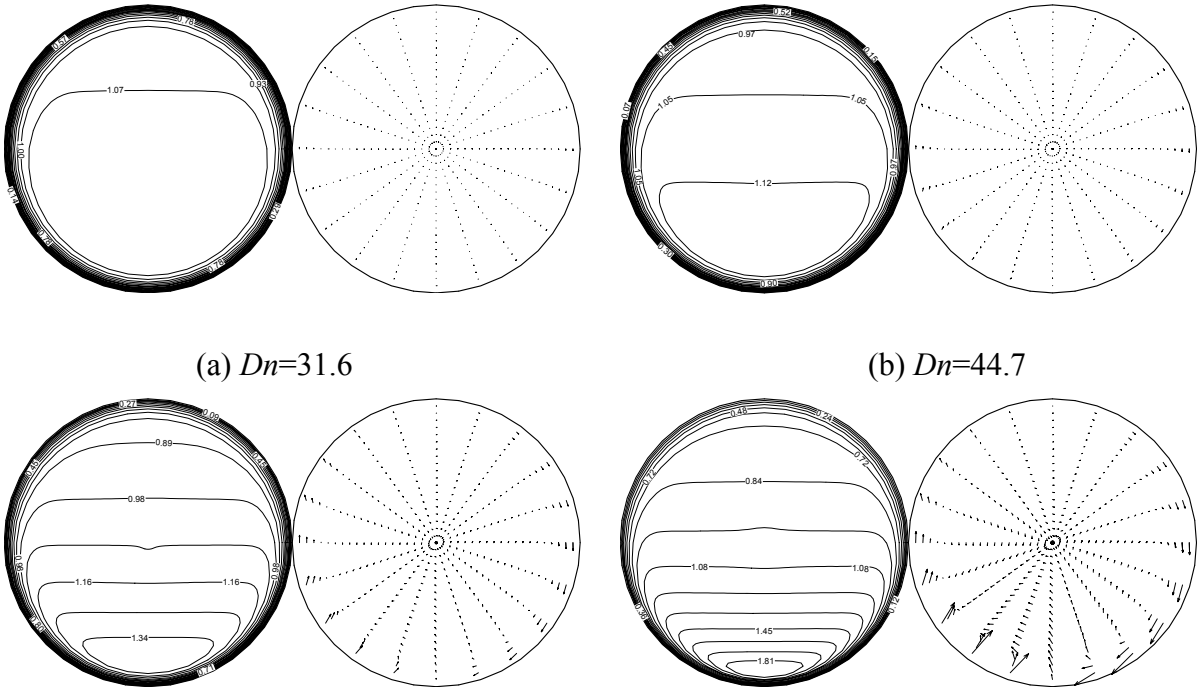

(a) *Dn*=31.6 (b) *Dn*=44.7

(c) *Dn*=70.7 (d) *Dn*=89.4

Figure 7.6 Contour lines of the axial velocity and vector plots of the secondary flow at *Re=100*, $Da = 10^{-2}$, C_F =0.55, φ =0.95, *Gn*=1.0 for different values of the Dean number: (a) ε =0.1, λ =0.1, *Dn*=31.6 (b) ε =0.2, λ =0.05, *Dn*=44.7 (c) ε =0.5, λ =0.02, *Dn*=70.7 (d) ε =0.8, λ =0.0125, *Dn*=89.4

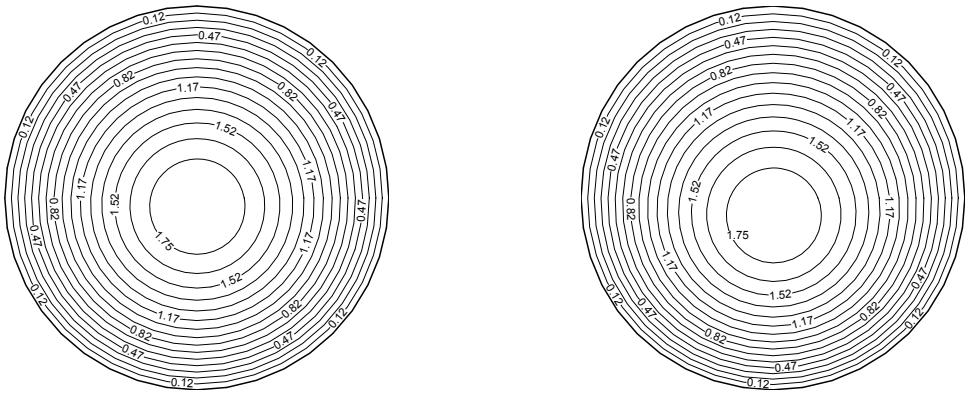

(a) *Dn*=31.6 (b) *Dn*=44.7

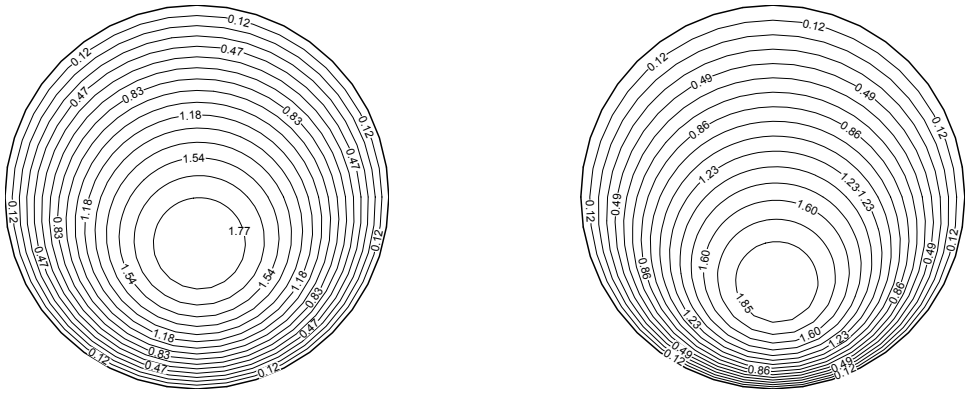

(c) *Dn*=70.7 (d) *Dn*=89.4

Figure 7.7 Contour lines of the dimensionless temperature at *Re*=100, $Da = 10^{-2}$, C_F =0.55, φ =0.95, *Gn*=1.0 for different values of the Dean number: (a) ε =0.1, λ =0.1, *Dn*=31.6 (b) ε =0.2, λ =0.05, *Dn*=44.7 (c) ε =0.5, λ =0.02, *Dn*=70.7 (d) ε =0.8, λ =0.05, *Dn*=89.4

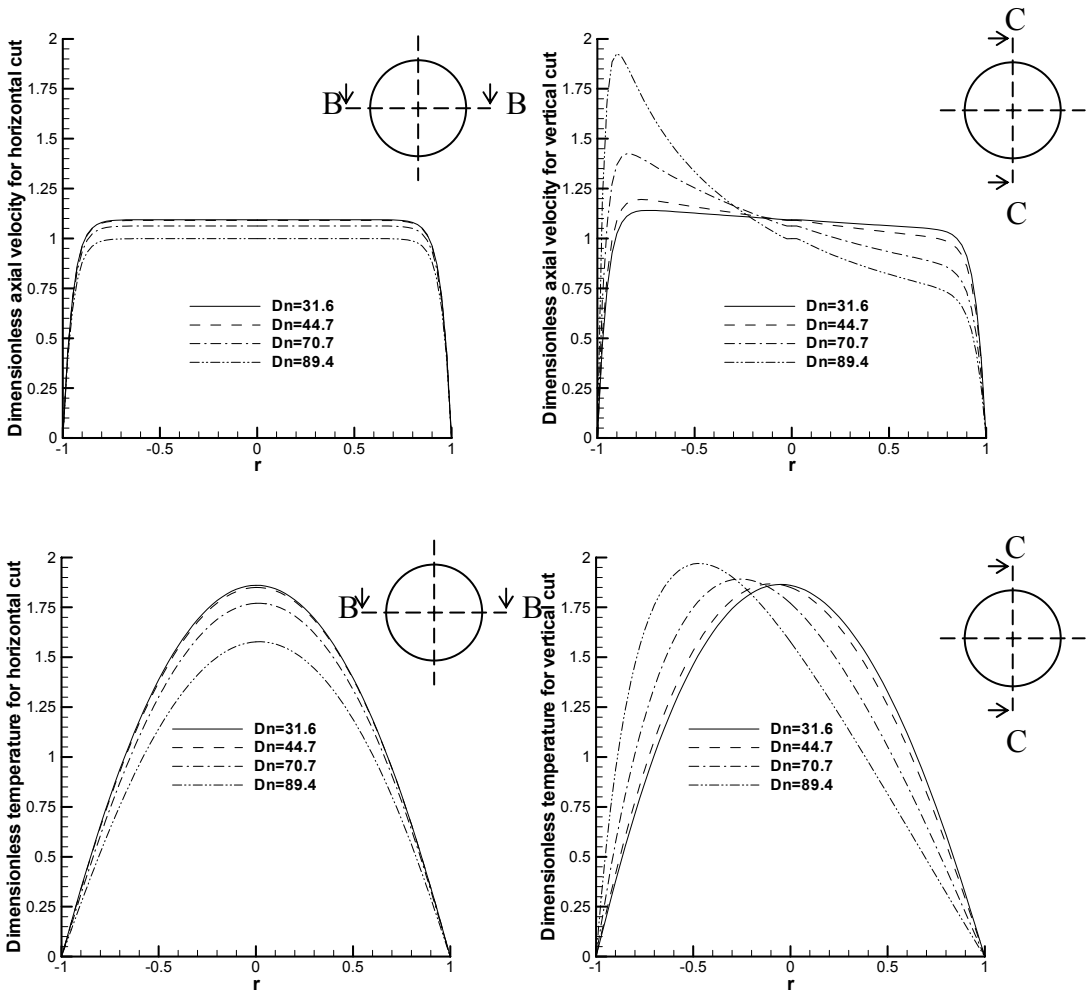

Figure 7.8 Profile plot of the axial velocity (top) and the dimensionless temperature (bottom) in the horizontal (left) and vertical (right) cut view of the pipe at *Re=100*, $Da = 10^{-2}$, C_F =0.55, φ =0.95, *Gn*=1.0 for different values of the Dean numbers. The curves for different *Dn* correspond to cases (a)-(c) in Figure 7.6 and 7.7

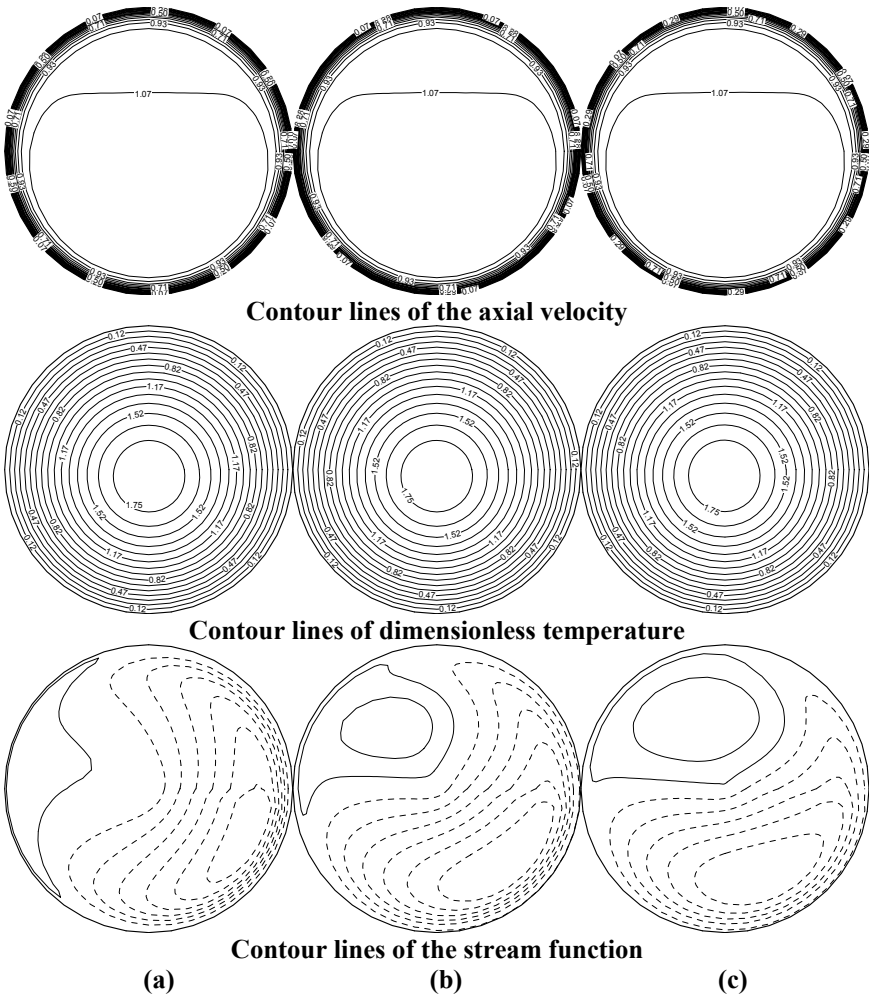

Figure 7.9 Contour lines of the axial velocity, the dimensionless temperature and the stream function at *Re*=100, $Da = 10^{-2}$, C_F =0.55, φ =0.95, ε =0.1, *Dn*=31.6 for different values of the Germano number: (a) λ =0.1, *Gn*=1.0 (b) λ =0.5, *Gn*=5.0 (c) λ =1.0, *Gn*=10.0

7.5 CONCLUSIONS

This chapter studies the laminar flow and heat transfer in a helical pipe filled with a fluid saturated porous medium for a constant wall heat flux. A full momentum equation that accounts for the Brinkman and Forchheimer extensions of the Darcy law and the flow inertia is utilized and derived in an orthogonal helical coordinate system. The effects of the parameters characterizing the porous medium, the Darcy number, *Da*, and the Forchheimer coefficient, C_F, and the parameters characterizing the helical pipe flow, the Dean number,

Dn, and the Germano number, *Gn*, are investigated. Increasing the Darcy number results in a larger axial filtration velocity and a stronger secondary flow but a smaller value of the maximum of the dimensionless temperature and the Nusselt number. When *Da* is fixed and the Forchheimer coefficient, C_F, is increased, the axial velocity decreases and the secondary flow becomes weaker, however, the values of the maximum dimensionless temperature and the Nusselt number increase. The change is especially apparent when C_F changes from zero to a non-zero value. For the same porous medium (i.e., when *Da* and C_F are fixed), when the Dean number increases, the maximum values of the axial velocity and the dimensionless temperature increase and the secondary flow become stronger. The Nusselt number increases with the Dean number. The increase of the Germano number does not have any significant effect on the axial velocity and heat transfer but strengthens the secondary flow.

REFERENCES

1. Nield, D.A., Bejan A.(1999) *Convection in Porous Media*, 2nd ed., Springer, New York.

2. Dean, W.R. (1927) Note on the motion of fluid in a curved pipe, *Philosophical Magazine,* 4: 208-223.

3. Germano, M. (1982) On the effect of torsion on a helical pipe flow, *J. Fluid Mech.,* 125: 1-8.

4. Germano, M. (1989) The Dean equations extended to a helical pipe flow, *J. Fluid Mech.,* 203: 289-305.

5. Liu, S. and Masliyah J.H. (1993) Axially invariant laminar flow in helical pipes with a finite pitch, *J. Fluid Mech.,* 251: 315-353.

6. Liu, S. and Masliyah, J.H. (1994) Developing convective heat transfer in helical pipes with finite pitch, *Int. J. Heat and Fluid Flow,* 15: 66-74.

7. Hüttl, T. J. (1997) Navier Stokes solutions of laminar flows based on orthogonal helical coordinates, *Numerical Methods in Laminar and Turbulent Flow,* 10: 191-202.

8. Hüttl, T. J. (2000) Influence of curvature and torsion on turbulent flow in curved and helically coiled pipes, *Int. J. Heat and Fluid Flow,* 21: 345-353.

9. Pharoah, J.G., Litster, S. and Djilali, N. (2003) Mass transfer enhancement in membrane separation –rotating vs. helical modules", CFD 2003, Vancouver, May, 28-30.

10. Sandeep, K. P., Zuritz, C. A. and Puri, V. M. (2000) Modeling non-Newtonian two-phase flow in conventional and helical-holding tubes, *Int. J. Food Science and Technology,* 35: 511-522.

11. Cheng, L. and Kuzentsov, A.V. (2004) Investigation of a laminar flow of a non-Newtonian fluid in a helical pipe. *International Journal of Applied Mechanics and Engineering* (in press).

12. Sankariah, M. and Rao, Y.V.N. (1972) Analysis of steady laminar flow of an incompressible Newtonian fluid through curved pipes of small curvature, *ASME Paper* No.72-WA/FE-19.

13. Patankar, S.V., Pratap V.S. and Spalding D.B. (1974) Prediction of laminar flow and heat transfer in helically coiled pipes. *Journal of Fluid Mechanics*, 62 (3): 539-551.

14. Yang, G., Dong, Z. F. and Ebadian, M. A. (1995) Laminar forced convection in a helicoidal pipe with finite pitch, *Int. J. Heat Mass Transfer,* 38: 853-862.

15. Lin, C.X., Zhang, P. and Ebadian M.A. (1997) Laminar forced convection in the entrance region of helical pipes, *Int. J. Heat Mass Transfer,* 40: 3293-3304.

16. Zheng, B., Lin, C.X. and Ebadian, M.A. (2000) Combined laminar forced convection and thermal radiation in a helical pipe, *Int. J. Heat and Mass Transfer,* 43: 1067-1078.

17. Cheng, L. and. Kuznetsov, A.V. (2004) Heat transfer in a laminar flow of a non-Newtonian fluid in a helical pipe*, International Journal of Transport Phenomena* (in press).

18. Nield, D. A. and Kuznetsov, A.V. (2004) Forced convection in a helical pipe filled with a saturated medium. *International Journal of Heat and Mass Transfer*, in press.

19. Cheng, L. and Kuznetsov, A.V. (2004) Investigation of laminar flow in a helical pipe filled with a fluid saturated porous medium, *International Journal of Applied Mechanics and Engineering* (in press).

20. Patankar, S. V. (1980) *Numerical Heat Transfer and Fluid Flow*, Hemisphere, New York.

PART FOUR: 3D MODELING OF TWO-PHASE FLOW IN A HELICAL PIPE

8 MATHEMATICAL MODELING OF TWO-PHASE NON-NEWTONIAN FLOW IN A HELICAL PIPE

ABSTRACT

Governing equations for a two-phase 3D helical pipe flow of a non-Newtonian fluid with large particles are derived in an orthogonal helical coordinate system. The Lagrangian approach is utilized to model solid particle trajectories. The interaction between solid particles and the fluid that carries them is accounted for by a source term in the momentum equation for the fluid. The force-coupling method (FCM) is adopted, in which the momentum source term is no longer a Dirac delta function but is spread on a numerical mesh by using a finite-sized envelop with a spherical Gaussian distribution. The influence of inter-particle and particle-wall collisions is also taken into account.

Nomenclature

a	pipe radius, m
a_p	particle radius, m
C_d	drag coefficient, defined in Eq. (19)
D_p	region occupied by a particle
$\mathbf{f}$	source term induced by particles, N m^{-3}
$\mathbf{F}$	force, N
$\mathbf{F}_b$	buoyancy force, N

$\mathbf{F}_d$	drag force, N
$\mathbf{F}_m$	Magnus lift force, N
$\mathbf{F}_{saf}$	Saffiman lift force, N
$\mathbf{g}$	gravity, m s^{-2}
$\mathbf{G}$	force dipole, N m
h_s, h_r, h_θ	scale factors associated with orthogonal coordinates s, r, θ, defined in Equation (3)
I	moment of inertia, kg m^2
$\mathbf{K}$	vorticity vector, s^{-1}
m	consistency factor, Pa s^n
m_f	mass of the fluid in a finite volume, kg
m_p	particle mass, kg
n	power-law index
N	particle number
p	pitch, m
P	pressure, Pa
Pr	Prandtl number
Re_P	particle Reynlods number
r	radial coordinate, m

R	coil radius, m
s	axial coordinate, m
t	time, s
$\mathbf{T}$	torque, N m
$\mathbf{v}$	velocity vector, m s^{-1}
$\mathbf{v}_f$	fluid velocity, m s^{-1}
$\mathbf{v}_p$	particle velocity, m s^{-1}
u_s, u_r, u_θ	velocity components, m s^{-1}

Greek symbols

β	declining angle
ε_p	stiffness parameters for particle-particle interactions, m^3 N^{-1}
ε_w	stiffness parameters for particle-wall interactions, m^3 N^{-1}
θ	angle
κ	curvature, m^{-1}
μ	effective dynamic viscosity of a non-Newtonian fluid, kg m^{-1} s^{-1}
ν	kinematic viscosity, m^2 s^{-1}
$\mathbf{\Omega}$	angular velocity vector, s^{-1}
ρ_f	fluid density, kg m^{-3}

ρ_p particle density, $\mathrm{kg\,m^{-3}}$

τ torsion, $\mathrm{m^{-1}}$

σ length scale for force monopole, m

σ' length scale for force dipole, m

Subscripts

s axial direction

r radial direction

θ tangential direction

Superscripts

P particle to particle

W wall to particle

8.1 INTRODUCTION

Because of space saving and, more importantly, the enhancement of mixing achieved due to the secondary flow, helical pipes are widely used in industry. The centrifugal force increases the axial velocity near the pipe outer wall and decreases that near the pipe inner wall. At the pipe outer wall, the higher velocity decreases the thermal resistance considerably, resulting in a higher heat transfer coefficient between a fluid and pipe wall (Shah and Joshi [1]). Cheng and Kuznetsov [2, 3] numerically investigated heat transfer in a fully-developed laminar flow of a non-Newtonian fluid in a helical pipe with the momentum and energy equations derived in an orthogonal helical coordinate system.

Two-phase flow can be modeled by two approaches, the Eulerian/Eulerican and the Eulerian/Lagrangian. In the Eulerian/Eulerican approach, both the solid phase and carrying fluid are treated as continuum phases. This approach is often used to deal with large concentrations of small particles. In the Eulerian/Lagrangian approach, however, only the carrying fluid is described as a continuum and the continuity and momentum equations for the fluid phase are solved on an Eulerian grid. The particle motion is governed by the second law of Newton. When particles are moving in the fluid, the momentum is exchanged between the particles and the fluid. This effect is described by a source term introduced into the momentum equation for the fluid phase. This approach has advantages in predicting particle trajectories and suits for low concentration of large particles (Shah and Joshi [1]; Liu and Zuritz [2]; Drust [5]). The main practical significance of the results of this part is in predicting the dynamics of large particles in aseptic processing of food, in which information about individual particle trajectories is needed; therefore, the Eulerian/Lagrangian approach is utilized.

To implement this approach, Maxey et al. [6] and Maxey and Patel [7] introduced a forced-coupling method (FCM), the basic idea of which is to model the presence of each particle in the flow by a low-order expansion of finite-valued, force mutlipoles applied as a distributed body force on the flow. Fluid fills the whole domain, including the volume occupied by the particles, and the Navier-Stokes equations with this body force term are solved throughout the domain on a fixed numerical mesh. Based on the fluid flow field, the particle trajectories and velocities are determined. Lomholt and Maxey [8] extended FCM to include higher-order effects by introducing force dipole terms and extended this approach to bounded

domains. To address the collision problem, Glowinski et al. [9] adopted a collision strategy described below, which is based on activating an artificial repelling force at a close range.

Aseptic processing of fruit juices and other homogeneous products has been extensively studied. However, few commercial activities for aseptic processing of foods containing large particles have been approved by the Food and Drug Administration (FDA) due to the lack of information regarding the behavior of large food particles in a flow. This information is the key to determining the residence time distribution (RTD) of particles in the suspension and the heat transfer coefficient between the particles and the fluid, which are the two critical factors in aseptic processing. To ensure that the fastest moving particles get enough thermal treatment and to keep the slower particles from overheating, the residence time distribution must be as narrow as possible. The relative velocity between the solid particles and the fluid has a critical influence on heat transfer as well as on the temperature distribution in the particles. Therefore, the dynamics of the particles and the fluid is the basic information necessary to design a commercially safe and economical aseptic process (Liu and Zuritz [4]; Sandeep et al. [10]).

In aseptic processing, the carrying fluid, such as milk, soup, sauce or fruit juices, is typically non-Newtonian, so the viscosity of the fluid is different at different locations in the pipe, which further complicates the problem. Sandeep et al. [10] made the first attempt to model non-Newtonian two-phase flows in conventional and helical holding pipes. A Cartesian coordinate system was utilized and the low-order effect of back influence of the particles on the fluid flow was investigated. In this dissertation, different from Sandeep et al. [10], an orthogonal helical coordinate system introduced by Germano [11, 12] is utilized. This allows capturing more accurately the secondary flow in the planes normal to the main flow. The

extended FCM method developed by Maxey [6, 7, 8, 13], with a collision strategy, is applied to describe the effect of particles on the flow field. The non-Newtonian fluid is simulated by the Ostwald-de Waele model (Bird et al. [14]). The simulation is based on a fully 3D flow in a helical pipe and the flow field is computed for any moment of time when particles are traveling from the inlet to the outlet of the pipe. In this study, the particles of a spherical shape are considered.

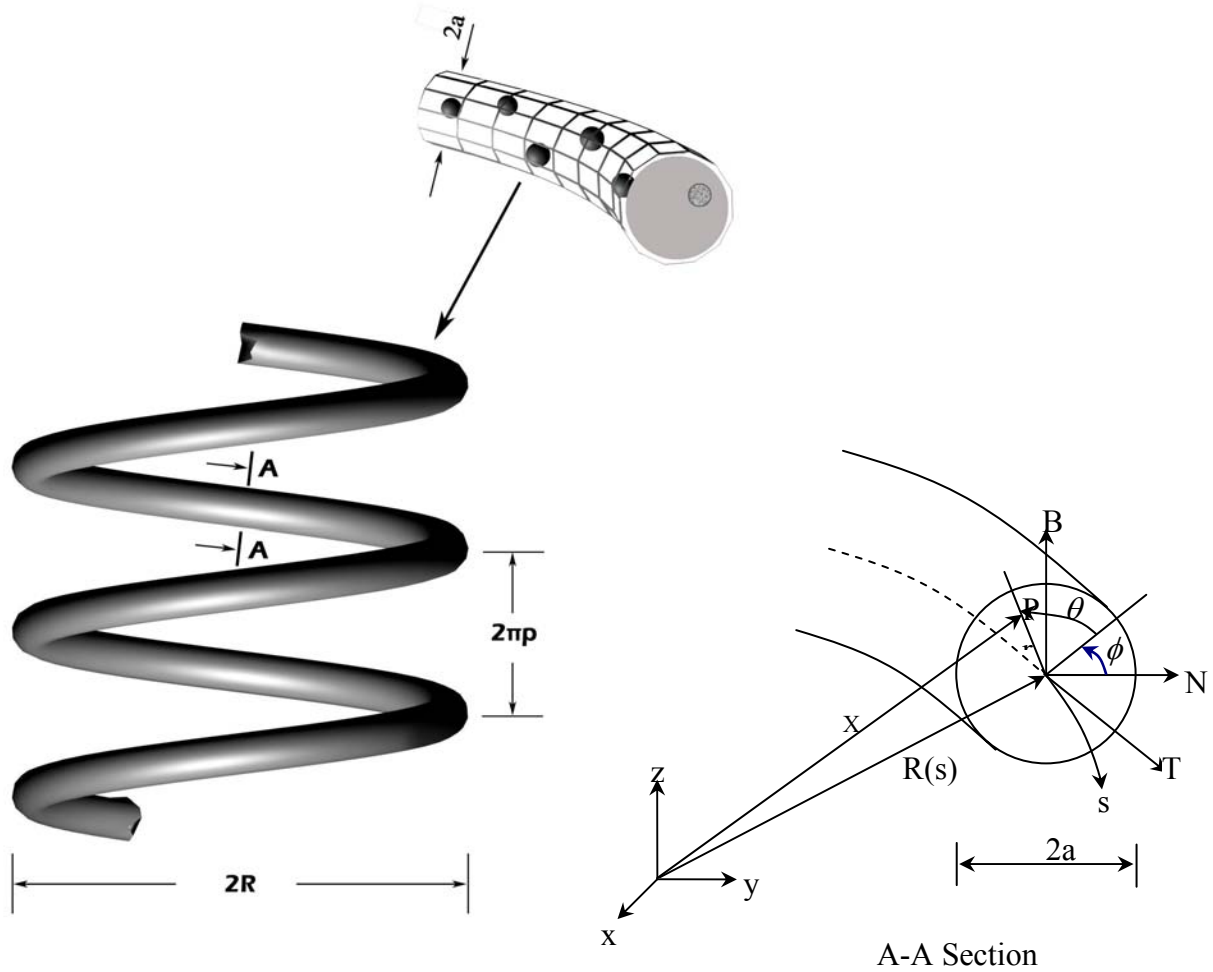

(a) **(b)**

Figure 8.1 Schematic diagram of a two phase flow in a helical pipe and the orthogonal helical coordinate system

8.2 MATHEMATICAL MODELING

8.2.1 EQUATIONS OF MOTION FOR THE FLUID WITH PARTICLES

Figure 8.1(a) depicts a schematic diagram of a helical pipe while Fig. 8.1(b) shows the orthogonal helical coordinate system. The helical pipe can be viewed as a pipe of radius *a* wound around a cylinder of a constant radius, $R-a$. The parameters that characterize the geometry of a helical pipe include the pipe diameter, *2a*, the coil diameter, *2R*, and the pitch, *p*. The curvature κ and the torsion τ are defined as $\kappa = R/(R^2 + p^2)$ and $\tau = p/(R^2 + p^2)$, respectively. The declining angle of the pipe wounding around the cylinder is $\beta = \dfrac{p}{\sqrt{p^2 + R^2}}$.

The governing equations for a non-Newtonian fluid flow in a helical pipe (Cheng and Kuznetsov [2, 3]) that account for gravity as well as the influence of particles on the fluid flow are

$$\nabla \cdot \mathbf{v} = 0 \tag{8.1}$$

$$\rho_f \frac{D\mathbf{v}}{Dt} = -\nabla P + \nabla \cdot \mu \nabla \mathbf{v} + \rho_f \mathbf{g} + \mathbf{f} \tag{8.2}$$

where $\mathbf{f} = (f_s, f_r, f_\theta)$ represents the momentum transfer resulting from all particles, which is given by the sum of the source terms obtained accounting for the contribution of each particle. The derivation of the momentum source term $\mathbf{f}$ is discussed in detail later on.

In the orthogonal helical coordinate system introduced by Germano [11, 12], the scale factors are expressed as

$$h_s = 1 + \kappa r \sin(\theta + \phi) \qquad h_r = 1 \qquad h_\theta = r \tag{8.3}$$

and Eqs. (8.1) and (8.2) become

$$\frac{\partial(ru_s)}{\partial s}+\frac{\partial(rh_s u_r)}{\partial r}+\frac{\partial(h_s u_\theta)}{\partial \theta}=0 \tag{8.4}$$

$$\begin{aligned}
&\frac{\partial u_s}{\partial t}+\frac{1}{h_s r}\left(\frac{\partial(ru_s u_s)}{\partial s}+\frac{\partial(rh_s u_r u_s)}{\partial r}+\frac{\partial(h_s u_\theta u_s)}{\partial \theta}\right)+\frac{\kappa}{h_s}u_s\left(u_r\sin(\theta+\phi)+u_\theta\cos(\theta+\phi)\right)=-\frac{1}{h_s}\frac{1}{\rho}\frac{\partial P}{\partial s}\\
&\quad+\frac{\mu}{\rho}\left\{\frac{1}{h_s}\frac{\partial}{\partial s}\left[\frac{1}{h_s r}\left[\frac{\partial(ru_s)}{\partial s}+\frac{\partial(rh_s u_r)}{\partial r}+\frac{\partial(h_s u_\theta)}{\partial \theta}\right]\right]-\right.\\
&\quad\left.\frac{1}{r}\left(\frac{\partial}{\partial r}\left(\frac{r}{h_s}\left(\frac{\partial u_r}{\partial s}-\frac{\partial}{\partial r}(h_s u_s)\right)\right)-\frac{\partial}{\partial \theta}\left(\frac{1}{h_s r}\left(\frac{\partial}{\partial \theta}(h_s u_s)-\frac{\partial}{\partial s}(ru_\theta)\right)\right)\right)\right\}\\
&\quad+\frac{1}{\rho}\left[\frac{1}{h_s^2}\frac{\partial u_s}{\partial s}\frac{\partial \mu}{\partial s}+\frac{\partial u_s}{\partial r}\frac{\partial \mu}{\partial r}+\frac{1}{r^2}\frac{\partial u_s}{\partial \theta}\frac{\partial \mu}{\partial \theta}\right]\\
&\quad-g\sin\beta+f_s
\end{aligned} \tag{8.5a}$$

$$\begin{aligned}
&\frac{\partial u_r}{\partial t}+\frac{1}{h_s r}\left(\frac{\partial(ru_s u_r)}{\partial s}+\frac{\partial(rh_s u_r u_r)}{\partial r}+\frac{\partial(h_s u_\theta u_r)}{\partial \theta}\right)-\frac{u_\theta^2}{r}-\frac{k}{h_s}u_s^2\sin(\theta+\phi)=-\frac{1}{\rho}\frac{\partial P}{\partial r}\\
&\quad+\frac{\mu}{\rho}\left\{\frac{\partial}{\partial r}\left[\frac{1}{h_s r}\left[\frac{\partial(ru_s)}{\partial s}+\frac{\partial(rh_s u_r)}{\partial r}+\frac{\partial(h_s u_\theta)}{\partial \theta}\right]\right]-\right.\\
&\quad\left.\frac{1}{h_s r}\left(\frac{\partial}{\partial \theta}\left(\frac{h_s}{r}\left(\frac{\partial}{\partial r}(ru_\theta)-\frac{\partial u_r}{\partial \theta}\right)\right)-\frac{\partial}{\partial s}\left(\frac{r}{h_s}\left(\frac{\partial u_r}{\partial s}-\frac{\partial}{\partial r}(h_s u_s)\right)\right)\right)\right\}\\
&\quad+\frac{1}{\rho}\left[\frac{1}{h_s^2}\frac{\partial u_r}{\partial s}\frac{\partial \mu}{\partial s}+\frac{\partial u_r}{\partial r}\frac{\partial \mu}{\partial r}+\frac{1}{r^2}\frac{\partial u_r}{\partial \theta}\frac{\partial \mu}{\partial \theta}\right]\\
&\quad-g\cos\beta\sin(\theta+\phi)+f_r
\end{aligned} \tag{8.5b}$$

$$\begin{aligned}
&\frac{\partial u_\theta}{\partial t}+\frac{1}{h_s r}\left(\frac{\partial(ru_s u_\theta)}{\partial s}+\frac{\partial(rh_s u_r u_\theta)}{\partial r}+\frac{\partial(h_s u_\theta u_\theta)}{\partial \theta}\right)-\frac{\kappa}{h_s}u_s^2\cos(\theta+\phi)+\frac{u_r u_\theta}{r}=-\frac{1}{r}\frac{1}{\rho}\frac{\partial P}{\partial \theta}\\
&\quad+\frac{\mu}{\rho}\left\{\frac{1}{r}\frac{\partial}{\partial \theta}\left[\frac{1}{h_s r}\left[\frac{\partial(ru_s)}{\partial s}+\frac{\partial(rh_s u_r)}{\partial r}+\frac{\partial(h_s u_\theta)}{\partial \theta}\right]\right]-\right.\\
&\quad\left.\frac{1}{h_s}\left(\frac{\partial}{\partial s}\left(\frac{1}{h_s r}\left(\frac{\partial}{\partial \theta}(h_s u_s)-\frac{\partial}{\partial s}(ru_\theta)\right)\right)-\frac{\partial}{\partial r}\left(\frac{h_s}{r}\left(\frac{\partial}{\partial r}(ru_\theta)-\frac{\partial u_r}{\partial \theta}\right)\right)\right)\right\}\\
&\quad+\frac{1}{\rho}\left[\frac{1}{h_s^2}\frac{\partial u_\theta}{\partial s}\frac{\partial \mu}{\partial s}+\frac{\partial u_\theta}{\partial r}\frac{\partial \mu}{\partial r}+\frac{1}{r^2}\frac{\partial u_\theta}{\partial \theta}\frac{\partial \mu}{\partial \theta}\right]\\
&\quad-g\cos\beta\cos(\theta+\phi)+f_\theta
\end{aligned} \tag{8.5c}$$

The following expression for the effective viscosity of a power law fluid is used to evaluate the viscosity of a non-Newtonian fluid:

$$\mu = m[\frac{1}{2}(\Delta:\Delta)]^{\frac{n-1}{2}} \tag{8.6}$$

where Δ is the rate of deformation tensor and the expression for $(\Delta:\Delta)$ is given by

$$\begin{aligned}\frac{1}{2}(\Delta:\Delta) = 2\Bigg[&\left(\frac{\partial}{\partial s}\left(\frac{u_s}{h_s}\right)-\frac{\tau\kappa r\cos(\theta-\tau s)}{{h_s}^2}u_s+\frac{\kappa\sin(\theta-\tau s)}{h_s}u_r+\frac{\kappa\cos(\theta-\tau s)}{h_s}u_\theta\right)^2\\&+\left(\frac{\partial u_r}{\partial r}\right)^2+\left(\frac{\partial}{\partial\theta}\left(\frac{u_\theta}{r}\right)+\frac{u_r}{r}\right)^2\Bigg]+\left(h_s\frac{\partial}{\partial r}\left(\frac{u_s}{h_s}\right)+\frac{1}{h_s}\frac{\partial u_r}{\partial s}\right)^2\\&+\left(\frac{h_s}{r}\frac{\partial}{\partial\theta}\left(\frac{u_s}{h_s}\right)+\frac{r}{h_s}\frac{\partial}{\partial s}\left(\frac{u_\theta}{r}\right)\right)^2+\left(r\frac{\partial}{\partial r}\left(\frac{u_\theta}{r}\right)+\frac{1}{r}\frac{\partial u_r}{\partial\theta}\right)^2\end{aligned} \tag{8.7}$$

8.2.2 MOMENTUM SOURCE TERM INDUCED BY PARTICLES

A force-coupling method (FCM) by Maxey [6, 7, 8, 13] is utilized to simulate the source term incorporated into the momentum equation to account for the presence of the particles. The general principle of FCM is to utilize a localized body force $\mathbf{f}(\mathbf{x},t)$, which is a resultant force of all particles, to represent the effect of the particles on the fluid. The momentum source term is no longer a Dirac delta function but is spread on the numerical mesh by using a finite-sized envelop with a spherical Gaussian distribution. The equations for fluid motion are also solved in the domain occupied by the particles.

The body force generated by *N* spherical particles centered at $\mathbf{Y}^{(n)}(t)$ (*n*=1, 2,…, *N*) is

$$\mathbf{f}(\mathbf{x},t) = \sum_{n=1}^{N}\left[\left(\mathbf{F}^{(n)}\Delta\left(\mathbf{x}-\mathbf{Y}^{(n)}(t)\right)+\mathbf{G}_{ij}^{(n)}\frac{\partial}{\partial x_j}\Delta'\left(\mathbf{x}-\mathbf{Y}^{(n)}(t)\right)\right)/\left(4/3\pi a_p^{(n)}\right)\right] \tag{8.8}$$

where both $\Delta(x)$ and $\Delta'(x)$ are Gaussian functions:

$$\Delta(x) = \left(2\pi\sigma^2\right)^{-3/2}\exp\left(-r^2/2\sigma^2\right) \text{ with } r = |x| \tag{8.9}$$

The first term in the brackets on the right-hand side of Eq. (8.8) refers to a finite force monopole of strength $\mathbf{F}$ and the second term in the brackets on the right-hand side refers to a force dipole $\mathbf{G}_{ij}$. The strength of the force monopole is determined by the sum of the external force $\mathbf{F}^{(n)ext}$ acting on the particles and the inertia of the particle:

$$\mathbf{F}^{(n)} = \mathbf{F}^{(n)ext} - (m_p^{(n)} - m_f)\frac{d\mathbf{v}_p^{(n)}}{dt} \tag{8.10}$$

where $\mathbf{v}_p^{(n)}(t)$ is the particle velocity, which is calculated by averaging the fluid velocity over the region D_p occupied by the particles:

$$\mathbf{v}_p^{(n)}(t) = \int_{D_p} \mathbf{v}(\mathbf{x},t)\Delta\left(\mathbf{x} - \mathbf{Y}^{(n)}(t)\right)d^3\mathbf{x} \tag{8.11}$$

The length scale σ is set in terms of the particle radius, a_p, as

$$\sigma = \frac{a_p}{\sqrt{\pi}} \tag{8.12}$$

The force dipole is introduced to improve the flow representation; it consists of a symmetric part and an anti-symmetric part. The symmetric dipole term is chosen to ensure that the following equation

$$\int_{D_p} \frac{1}{2}\left(\frac{\partial u_i}{\partial x_j} + \frac{\partial u_j}{\partial x_i}\right)\Delta'\left(\mathbf{x} - \mathbf{Y}\right)d^3\mathbf{x} = 0 \tag{8.13}$$

is satisfied. The anti-symmetric part of G_{ij} corresponds to a torque on the flow. The length scale σ' for the second envelop Δ' is set as

$$\sigma' = \frac{a_p}{\left(6\sqrt{\pi}\right)^{1/3}} \tag{8.14}$$

Similarly to the velocity, the angular velocity is calculated as follows

$$\mathbf{\Omega}_p^{(n)} = \frac{1}{2}\int_{D_p} \boldsymbol{\omega}^{(n)}(\mathbf{x},t)\Delta'(\mathbf{x})d^3\mathbf{x} \tag{8.15}$$

The external force $\mathbf{F}^{ext}$ acting on the particles suspended in the fluid consists of the following forces (Liu and Zuritz [4], Sandeep et al. [10]):

(1) Magnus Lift Force

$$\mathbf{F}_m = \pi\rho_f a_p{}^3 \mathbf{\Omega} \times \left(\mathbf{v}_p - \mathbf{v}_f\right) \tag{8.16}$$

where $\mathbf{\Omega}$ is the angular velocity of the particle.

(2) Saffman Lift Force

$$\mathbf{F}_{saf} = 6.46\rho_f a_p{}^2 \left(\frac{\nu}{|\mathbf{K}|}\right)^{1/2} \mathbf{K} \times \left(\mathbf{v}_p - \mathbf{v}_f\right) \tag{8.17}$$

where $\mathbf{K}$ is the vorticity vector, ν is the kinematic viscosity, and a_p is the radius of the particle.

(3) Drag Force

$$\mathbf{F}_d = \frac{1}{2} C_d \rho_f \pi a_p{}^2 \left|\mathbf{v}_f - \mathbf{v}_p\right| \left(\mathbf{v}_f - \mathbf{v}_p\right) \tag{8.18}$$

where the drag coefficient, C_d, is calculated as follows:

$$C_d = \frac{24}{\mathrm{Re}_p}\left[1 + 0.15\,\mathrm{Re}_p{}^{0.687}\right] \tag{8.19}$$

for $1 < \mathrm{Re}_p < 1000$, where the particle Reynolds number is defined as follows

$$\mathrm{Re}_p = \frac{\rho\left(2a_p\right)\left|\mathbf{v}_f - \mathbf{v}_p\right|}{\mu} \tag{8.20}$$

(4) Buoyancy force

The expression to compute the buoyancy force exerted on the particle is given by:

$$F_b = (4/3)\pi a_p^{\,3}(\rho_f - \rho_g)\mathbf{g} \tag{8.21}$$

In the helical coordinate system, the above forces sum up to the following equations for the s, r and θ projections of the total external force on the particles:

$$\begin{aligned}
F_s = {} & \pi\rho_f a_p^{\,3}\frac{1}{r}\left(\Omega_2\left(r\left(u_{\theta p} - u_{\theta f}\right)\right) - \Omega_3\left(u_{rp} - u_{rf}\right)\right) \\
& + 6.46\,\rho_f a^2\left(\frac{\nu}{|\mathbf{K}|}\right)^{1/2}\frac{1}{r}\left(\frac{1}{h_s r}\left(\frac{\partial}{\partial\theta}\left(h_s u_{sf}\right) - \frac{\partial}{\partial s}\left(r u_{\theta f}\right)\right)\left(r\left(u_{\theta p} - u_{\theta f}\right)\right)\right. \\
& \qquad \left. - \frac{1}{h_s}\left(\frac{\partial u_{rf}}{\partial s} - \frac{\partial}{\partial r}\left(h_s u_{sf}\right)\right)\left(u_{rp} - u_{rf}\right)\right) \\
& + \frac{1}{2}C_d\rho_f\pi a^2\left|V_f - V_p\right|h_s\left(u_{sf} - u_{sp}\right) \\
& + \frac{4}{3}\pi a^3\left(\rho_f - \rho_p\right)g\sin\beta
\end{aligned} \tag{8.22a}$$

$$\begin{aligned}
F_r = {} & \pi\rho_f a_p^{\,3}\frac{1}{h_s r}\left(\Omega_3\left(h_s\left(u_{sp} - u_{sf}\right)\right) - \Omega_1\left(u_{\theta p} - u_{\theta f}\right)\right) \\
& + 6.46\,\rho_f a^2\left(\frac{\nu}{|\mathbf{K}|}\right)^{1/2}\frac{1}{h_s r}\left(\frac{1}{h_s}\left(\frac{\partial u_{rf}}{\partial s} - \frac{\partial}{\partial r}\left(h_s u_{sf}\right)\right)\left(h_s\left(u_{sp} - u_{sf}\right)\right)\right. \\
& \qquad \left. - \frac{1}{r}\left(\frac{\partial}{\partial r}\left(r u_{\theta f}\right) - \frac{\partial u_{rf}}{\partial\theta}\right)\left(r\left(u_{\theta p} - u_{\theta f}\right)\right)\right) \\
& + \frac{1}{2}C_d\rho_f\pi a^2\left|V_f - V_p\right|\left(u_{rf} - u_{rp}\right) \\
& + \frac{4}{3}\pi a^3\left(\rho_f - \rho_p\right)g\sin\beta\sin\theta
\end{aligned} \tag{8.22b}$$

$$\begin{aligned}
F_\theta = {} & \pi\rho_f a_p^{\,3}\frac{1}{h_s}\left(\Omega_1\left(u_{rp} - u_{rf}\right) - \Omega_2\left(h_s\left(u_{sp} - u_{sf}\right)\right)\right) \\
& + 6.46\,\rho_f a^2\left(\frac{\nu}{|\mathbf{K}|}\right)^{1/2}\frac{1}{h_s}\left(\frac{1}{r}\left(\frac{\partial}{\partial r}\left(r u_{\theta f}\right) - \frac{\partial u_{rf}}{\partial\theta}\right)\left(u_{rp} - u_{rf}\right)\right. \\
& \qquad \left. - \frac{1}{h_s r}\left(\frac{\partial}{\partial\theta}\left(h_s u_{sf}\right) - \frac{\partial}{\partial s}\left(r u_{\theta f}\right)\right)\left(h_s\left(u_{sp} - u_{sf}\right)\right)\right) \\
& + \frac{1}{2}C_d\rho_f\pi a^2\left|V_f - V_p\right|r\left(u_{\theta f} - u_{\theta p}\right) \\
& + \frac{4}{3}\pi a^3\left(\rho_f - \rho_p\right)g\sin\beta\cos\theta
\end{aligned} \tag{8.22c}$$

where

$$|\mathbf{K}| = \left(\frac{1}{r}\left(\frac{\partial}{\partial r}\left(r u_{\theta f}\right) - \frac{\partial u_{rf}}{\partial\theta}\right)\right)^2 + \left(\frac{1}{h_s r}\left(\frac{\partial}{\partial\theta}\left(h_s u_{sf}\right) - \frac{\partial}{\partial s}\left(r u_{\theta f}\right)\right)\right)^2 + \left(\frac{1}{h_s}\left(\frac{\partial u_{rf}}{\partial s} - \frac{\partial}{\partial r}\left(h_s u_{sf}\right)\right)\right)^2 \tag{8.23}$$

In addition, to prevent particles from overlapping each other domains or penetrating into the wall, an additional inter-particle and particle-wall short-range repulsive force $\mathbf{F}'$ is added to the force $\mathbf{F}$ for each particle, as suggested by Glowinski et al. [9]:

$$\mathbf{F}'^{(n)} = \sum_{\substack{n=1 \\ m\neq n}}^{N} \mathbf{F}^{P(n,m)} + \mathbf{F}^{W(n)} \tag{8.24}$$

The first term on the right-hand side of Eq. (8.24) represents the force exerted on the *n*th particle by the *N-1* other particles and the second term represents that exerted by the pipe wall. The particle-particle force is calculated as follows:

$$\mathbf{F}^{P(n,m)} = \begin{cases} 0, & d^{(n,m)} \geq a_p^{(n)} + a_p^{(m)} + \delta, \\ \dfrac{1}{\varepsilon_P}\left(\mathbf{Y}^{(n)} - \mathbf{Y}^{(m)}\right)\left(a_p{}^{(n)} + a_p{}^{(m)} + \delta - d^{(n,m)}\right)^2, & d^{(n,m)} \leq a_p^{(n)} + a_p^{(m)} + \delta, \end{cases} \tag{8.25}$$

where $d^{(n,m)} = \left|\mathbf{Y}^{(n)} - \mathbf{Y}^{(m)}\right|$ is the distance between the centers of the *n*th and *m*th particles, $a_p^{(n)}$ is the radius of the *n*th particle and ε_P is a small positive stiffness parameter. In Eq. (8.25), δ is the force range, which is the distance between the surfaces of two particles (measured along the line that connects their centers) at which the contact force is activated; δ is set to one mesh size in this study. The particle-wall force is modeled as the force between a particle and the imaginary particle located on the other side of the wall Γ (a mirror image of the particle with respect to the wall) (see Fig. 8.2):

$$\mathbf{F}^{W(n)} = \begin{cases} 0, & d^{(n)'} \geq 2a_p^{(n)} + \delta \\ \dfrac{1}{\varepsilon_W}\left(\mathbf{Y}^{(n)} - \mathbf{Y}^{(n)'}\right)\left(2a_p{}^{(n)} + \delta - d^{(n)'}\right)^2, & d^{(n)'} \leq 2a_p^{(n)} + \delta \end{cases} \tag{8.26}$$

where $d^{(n)'} = \left|\mathbf{Y}^{(n)} - \mathbf{Y}^{(n)'}\right|$ is the distance between the centers of the *n*th particle and the center of its mirror image, $\mathbf{Y}^{(n)'}$ is the position of the imaginary particle, and ε_W is another

stiffness parameter. The stiffness parameters are taken as $\varepsilon_p = 8.15\times10^{-5}$ m^3 N^{-1} and $\varepsilon_w = \varepsilon_p / 2$.

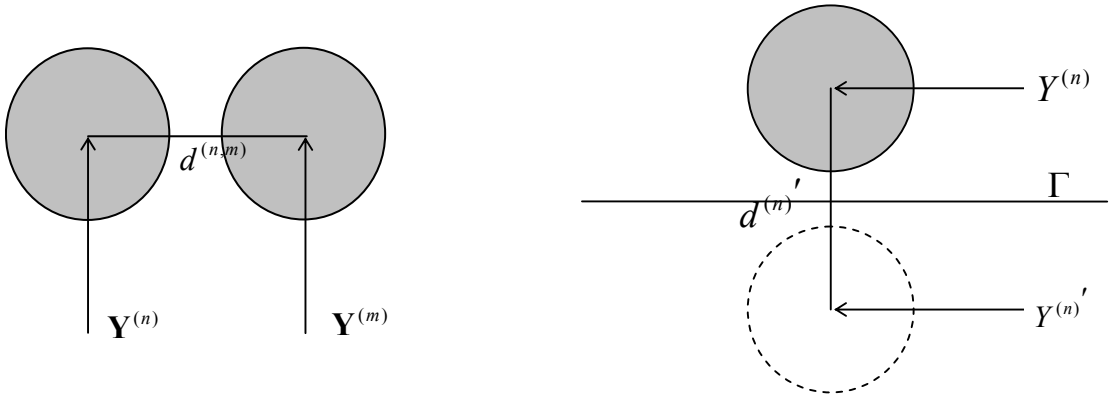

Figure 8.2 Schematic diagram for calculating contact forces of inter-particle and particle-wall collisions

To find the force dipole G_{ij}, the particle torque and angular velocities must be determined from the following equations:

$$I\left(\frac{d\mathbf{\Omega}}{dt}\right) = \Sigma\,\mathbf{T} \tag{8.27}$$

where I is the moment of inertia ($I = 2/5 m_p a_p{}^2$ for a sphere) and $\mathbf{T}$ are the local torques exerted by the viscous fluid on the surface of a particle:

$$\mathbf{T} = \int d\mathbf{T} = \int_A r \times \left(\hat{\tau}\cdot\mathbf{n}\right) dA \tag{8.28}$$

In the (s, r, θ) coordinate system, Eq. (8.28) can be rewritten as

$$T_s = \pi^2 a_p{}^3 \mu\left[\left(r\frac{\partial}{\partial r}\left(\frac{u_\theta}{r}\right)\right) + \frac{1}{r}\left(\frac{1}{r}\frac{\partial u_r}{\partial \theta}\right)\right] \tag{8.29a}$$

$$T_r = \pi^2 a_p{}^3 \mu\left(h_s\left(\frac{h_s}{r}\frac{\partial}{\partial \theta}\left(\frac{u_s}{h_s}\right)\right) + r\left(\frac{r}{h_s}\frac{\partial}{\partial s}\left(\frac{u_\theta}{r}\right)\right)\right) \tag{8.29b}$$

$$T_\theta = \pi^2 a_p{}^3 \mu\left[\frac{1}{h_s{}^2}\frac{\partial u_r}{\partial s} + h_s\frac{\partial}{\partial r}\left(\frac{u_s}{h_s}\right)\right] \tag{8.29c}$$

8.3 COMPUTATIONAL PROCEDURE

To solve a 3D flow problem, three velocity components at the inlet and the pressure at the outlet must be specified. In this chapter, a fully developed velocity profile is specified as the inlet profile of the fluid to the helical pipe. A no-slip boundary condition is specified at the wall of the pipe.

A uniform mesh is generated on an evenly spaced grid in the axial, radial and circumferential directions. An implicit time-integration scheme and the time marching procedure introduced by Patankar and Spalding [15] is adopted to solve the continuity and momentum equations. The SIMPLE algorithm is utilized on a staggered grid and the longitudinal and cross-stream pressure gradients are uncoupled.

The continuity and momentum equations (Eqs. (4) and (5a-c)) for the fluid phase are first solved in the absence of particles. Once the information about the fluid phase motion is obtained, the linear and angular velocities of the particles are determined from Eqs. (11) and (15). The source term defined by Eq. (8), which accounts for the influence of particles on the fluid, is calculated using the force-coupling method. The continuity and momentum equations are then solved again taking the particle source term into account, and the procedure is repeated until convergence.

Computations were performed on a NCSU supercomputer using a single 208 Intel Xeon 3.0 GHz processor. A typical CPU to investigate the process between the moment when the particles are released and the moment when the particles exit the pipe for a $51 \times 21 \times 21$ uniform mesh with a time step of 0.025s is about 360 hours (when the mean flow velocity is 0.5 m/s).

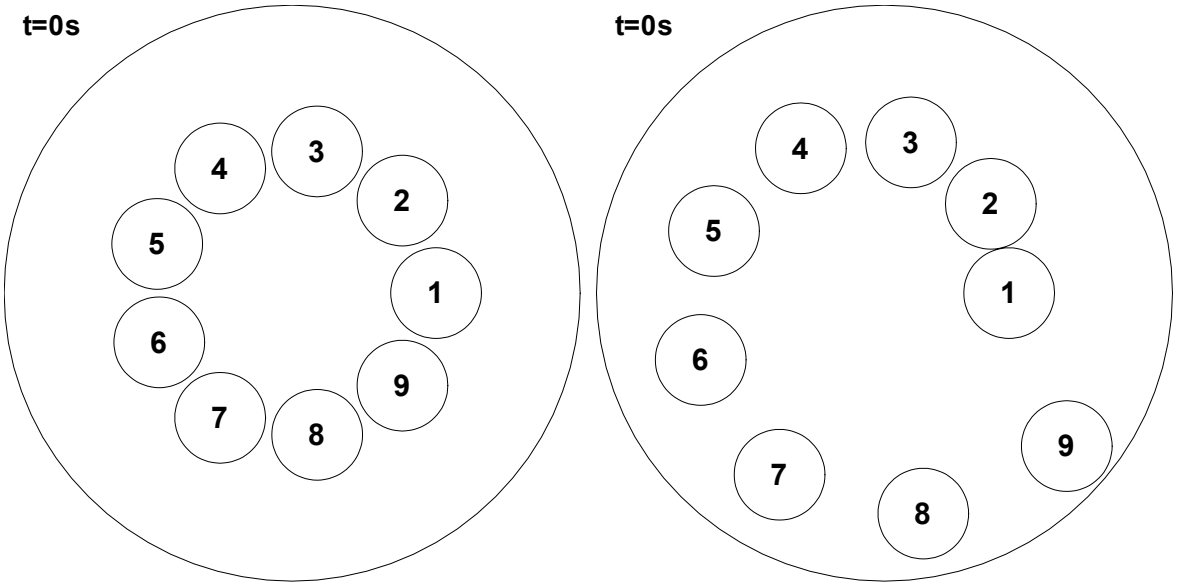

Figure 8.3 Initial positions of particles at the pipe inlet (Case A and Case B)

8.4 RESULTS AND DISCUSSION

In this study, a helical pipe whose length is 1m and whose diameter is 5.08cm, built by coiling the tube around a cylindrical mandrel (whose diameter is 60 cm) is considered; the pitch of the helical pipe is 2 cm. At the inlet, a fully developed parabolic axial velocity profile is imposed, the radial and circumferential velocity components are assumed to be zero. The uniform atmospheric pressure at the outlet of the pipe is specified. The particles are assumed spherical with the diameter of 0.8cm. The density of the particles is assumed the same as that of the fluid. Nine particles are initially introduced at the pipe inlet as fixed obstacles (they initially have zero velocities). The flow in the whole pipe attains steady-state, and then, at t=0s, the particles are suddenly released, and the cluster of 9 particles propagates through the pipe. This makes the flow unsteady, depending on the positions of the particles which are now carried by the fluid. In this study, two cases, A and B, of particle configuration at the inlet are investigated. For Case A, the particles are placed at the inlet

with the same radial position (half of the pipe radius) and the same angle between neighboring particles, as shown in Fig. 8.3(A). For Case B, the particles are placed at the inlet with the same angular interval between them (as in Case A), but at different radial position, as shown in Fig. 8.3(B). The interaction between the particles and the flow field is reciprocal. Both the effect of the particles on the fluid flow and the effects of the flow velocity and different positioning of particles at the inlet of the pipe on particle trajectories and the residence time distribution are investigated.

When there are no particles in the fluid, the maximum of the axial velocity is displaced from the pipe axis to the wall. The secondary flow induces mixing in the fluid. The phenomena of the displacement of the axial velocity and the occurrence of the secondary flow are discussed in detail in Cheng and Kuznetsov [2, 3]. When particles are traveling in the fluid, the impact of the particles on the fluid changes the flow field. First, the case in which the centerline velocity of 1.0m/s and the mean velocity of 0.5m/s (Case A1) is investigated. To show the fluid flow and the trajectories of the particles, the helical pipe is stretched and viewed from an axial cut view. Figure 8.4a shows the contour lines of the fluid axial velocity when the particles have just entered the pipe (t=0.025s). Figure 8.4b shows those when the particles have traveled for 0.3s and are concentrated between cross-sections 2 and 3. Figure 8.4(a) shows that vortices have developed close to the pipe inlet due to the presence of the particles. This is because the particles were introduced to the inlet of the pipe as fixed obstacles, and then suddenly released at t=0. It also shows that the vortices are not symmetric because the pipe is not straight but a helical one. The parabolic distribution of the axial velocity gets deformed as the distance of the cross-section from the inlet increases and the maximum of the axial velocity gets displaced to the outer wall. When the particles are between cross-

sections 2 and 3 (Fig. 8.4(b)), the contour lines of the axial velocity clearly show that the particles create a disturbance in the flow field.

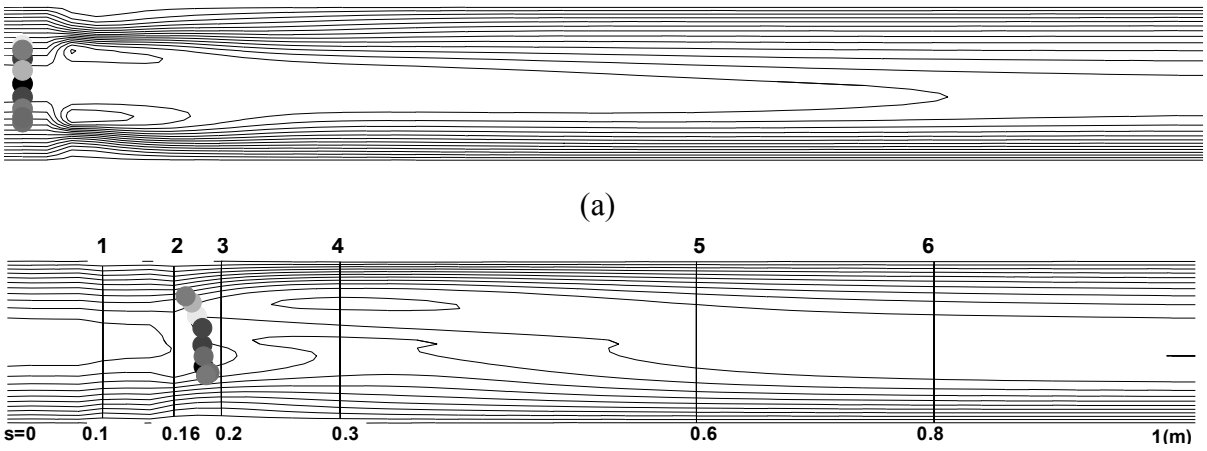

Figure 8.4 Contour lines of the axial velocity of fluid flow in the axial cut view of the pipe at (a) t=0.025s (particles are close to the inlet) and (b) t=0.3s (particles are between cross-sections 2 and 3

To show the influence of the particles on the fluid flow, the axial velocity and the secondary flow for Case A1 in cross-sections 1-6 (the positions of these cross-sections are displayed in Fig. 8.4b) at t=0.3s (at this moment of time, the particles are between cross-sections 2 and 3), are presented in Fig. 8.5. In cross-section 1, since it is close to the inlet, the parabolic profile of the axial velocity is not deformed significantly and the secondary flow is also not strong. The particles have just passed cross-section 2. The vector plot of the secondary flow at cross-section 2 shows that passing of particles through this cross-section increased the strength of the secondary flow and caused an irregular distribution of the axial velocity. The particles most strongly influence the flow in the cross-section in which the particles are passing at a given moment of time. The deformation of the axial velocity distribution and strengthening of the secondary flow are still significant in cross-section 3 but less than those in cross-section 2 because the particles have not yet reached cross-section 3. The effect of the particles on the flow can be observed in cross-section 4 from the contour lines of the axial

velocity but is not apparent in the vector plots of the secondary flow. However, when a cross-section is located too far downstream from the particles (cross-sections 5 and 6), the effect of the particles becomes negligible.

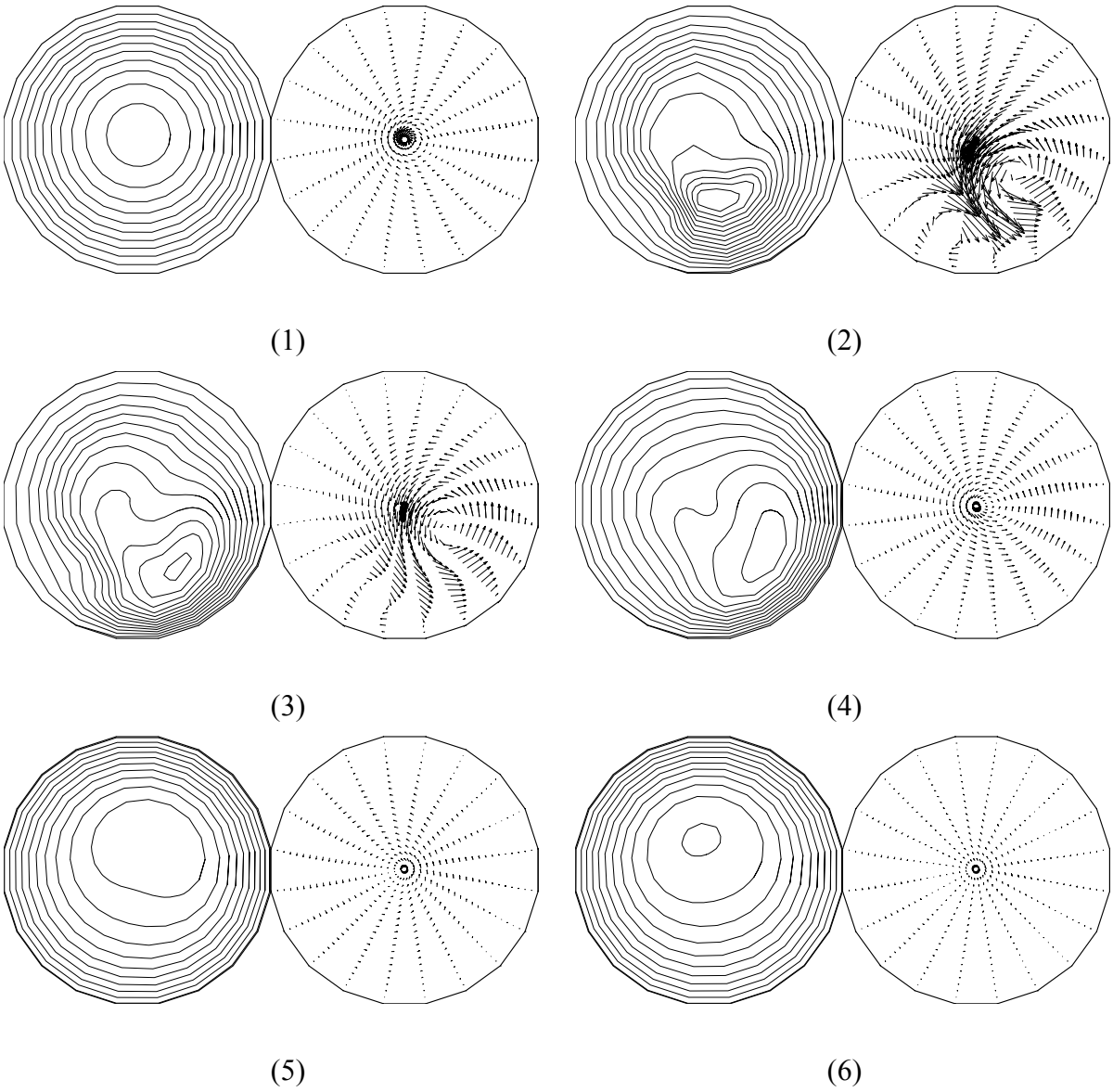

Figure 8.5 Contour lines of the axial velocity (left) and the vector plots of the secondary flow (right) in the cross sections 1-6 at t=0.3s, the positions of these cross-sections are displayed in Fig. 8.4b (Case A1)

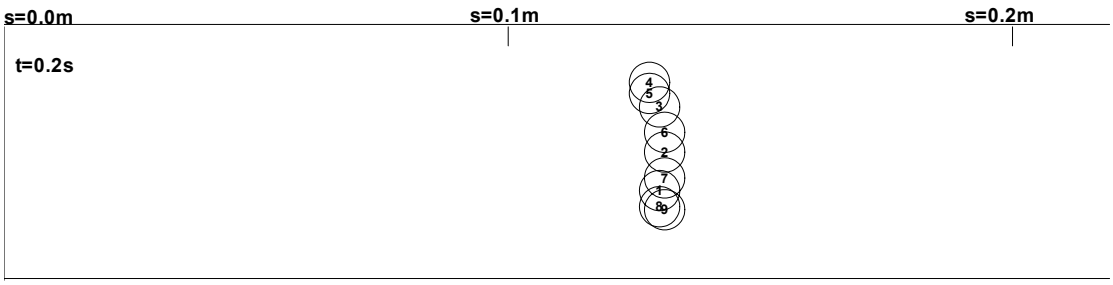
s=0.0m
s=0.1m
s=0.2m
t=0.2s

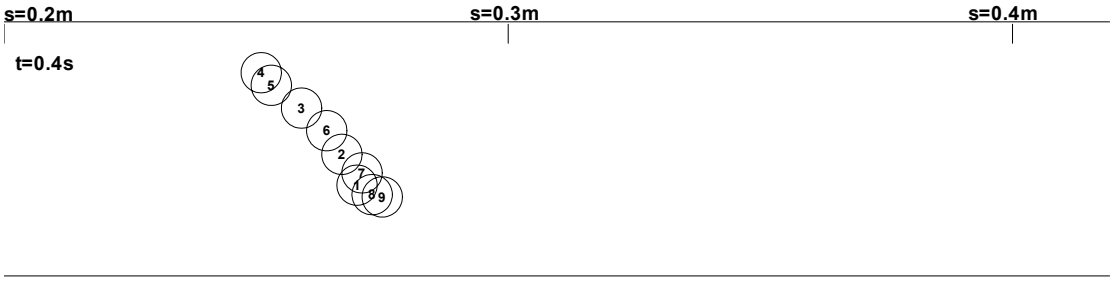
s=0.2m
s=0.3m
s=0.4m
t=0.4s

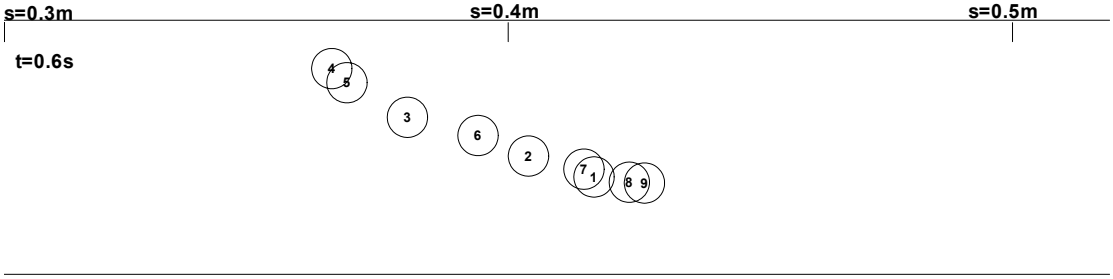
s=0.3m
s=0.4m
s=0.5m
t=0.6s

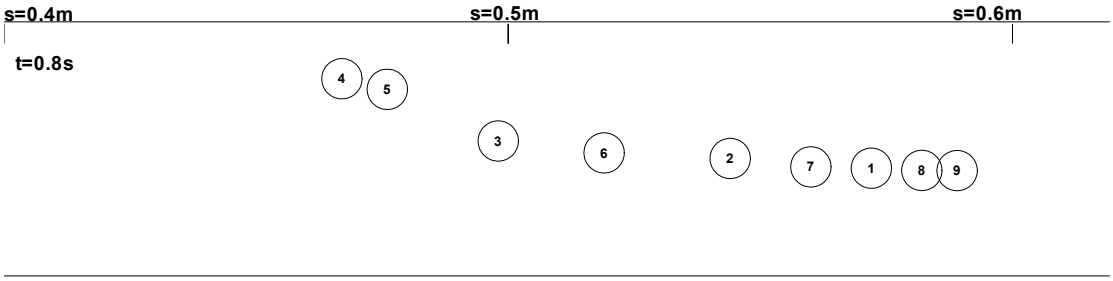
s=0.4m
s=0.5m
s=0.6m
t=0.8s

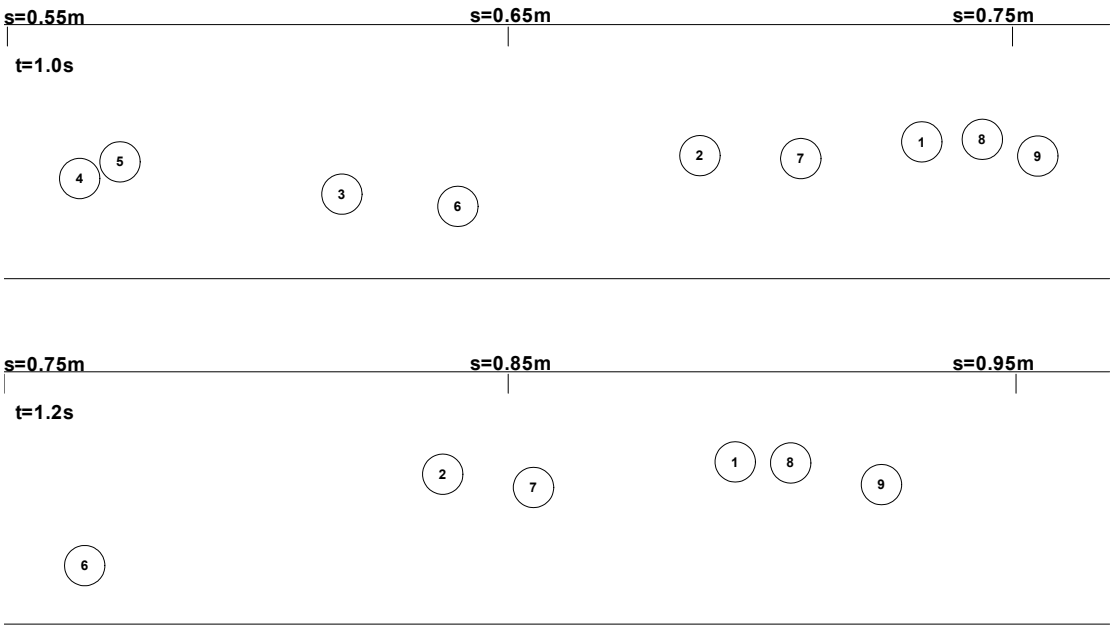

Figure 8.6 Snapshots of the particles at different moments of time (Case A1)

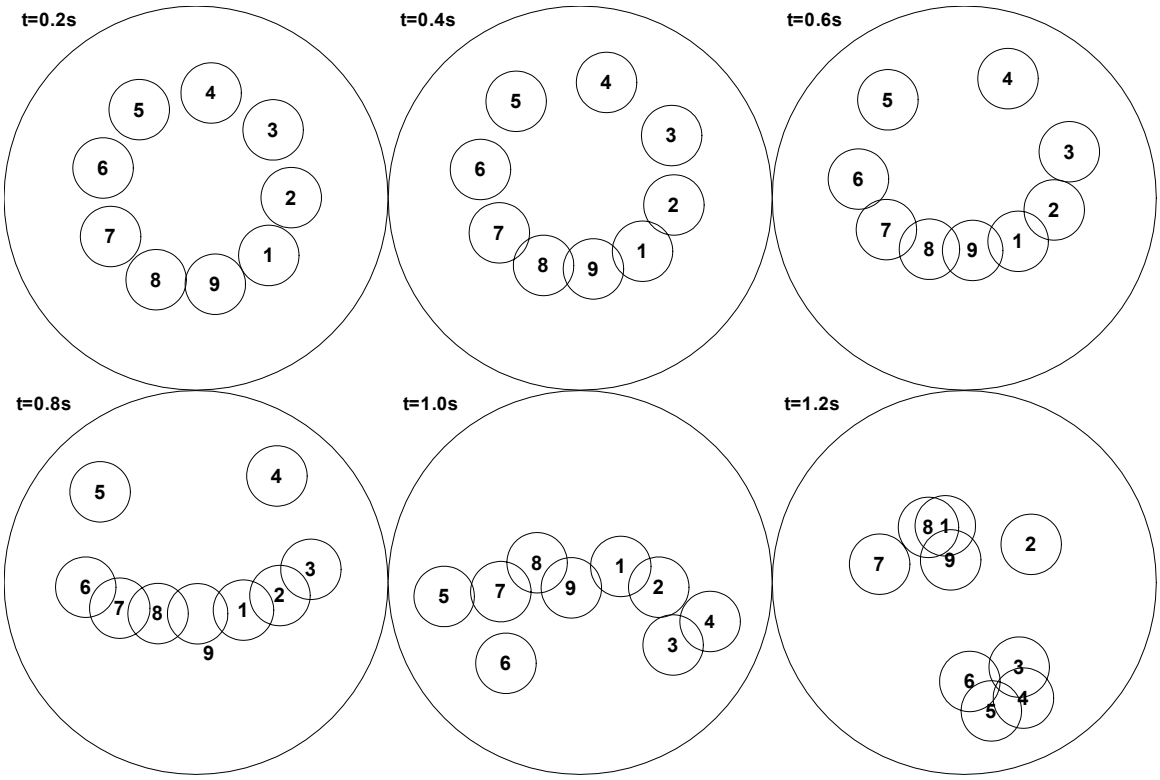

Figure 8.7 Radial positions of the particles at different moments of time (Case A1)

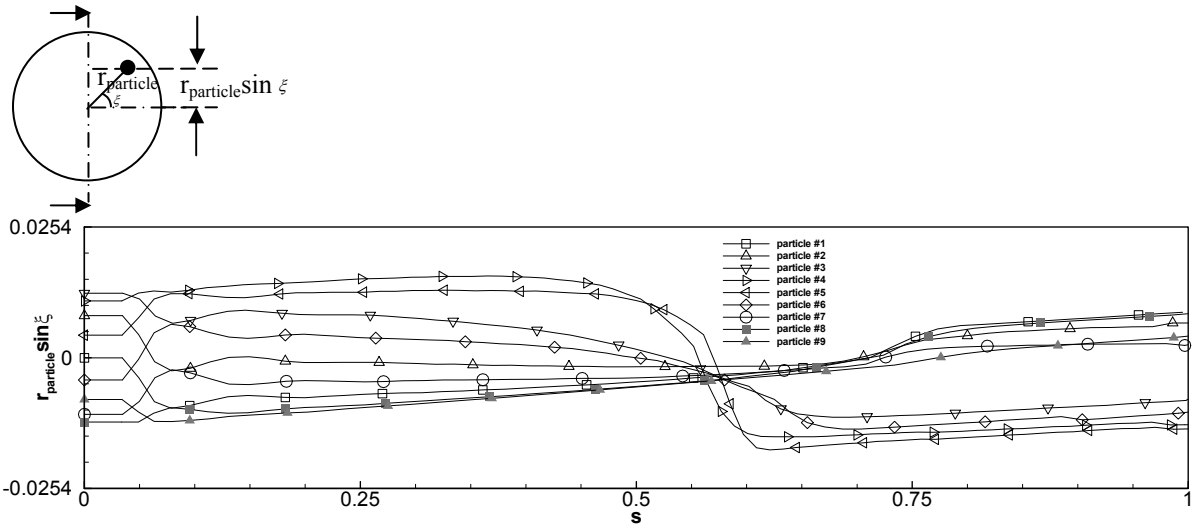

Figure 8.8 Trajectories of the particles viewed in the axial cut view (Case A1)

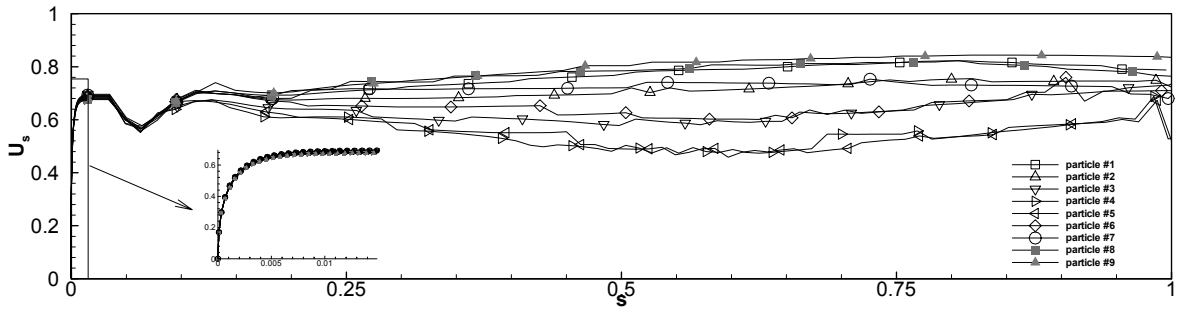

Figure 8.9 Axial velocities of the particles in the pipe versus their axial positions (Case A1)

Figures 8.6 and 8.7 depict the axial and radial positions of the particles at different moments of time for Case A1. In the beginning, the axial velocity profile of the fluid flow remains close to parabolic. Since for this case the particles are initially introduced in the same radial positions at the inlet, once they are released, they enter the pipe parallel to each other and the layout of the particles does not change significantly during the first 0.2s (see Fig. 8.6 and 8.7 for t=0.2s). However, the deformed axial velocity distribution and the secondary flow induced by the helical pipe soon cause the particles to move away from each other. The factors that affect the particle trajectories include the local velocity of the fluid flow, the local viscous drag force, the fluid lift force associated with the shear flow, the particle inertia as

well as particle-particle and particle-wall interactions. Figures 8.8 displays the projections of the particle trajectories on an axial cut view of the pipe while Fig. 8.9 depicts the axial velocities of the particles versus their axial position. Both Figs. 8 and 9 are computed for Case A1. In the beginning, all particles travel parallel to each other with the same axial velocity. At s=0.05m, the particle trajectories start overlapping. At s=0.57m, a "mixing event" occurs. Figure 8.9 shows that once the particles are released, they first accelerate (the inertia of the particles is accounted for) and attain the same axial velocity within a very short time and very short distance from the inlet. The acceleration period of the particles is shown on an enlarged scale in a small separate figure in Fig. 9. The decrease of the axial velocity of the particles, which follows the acceleration period, may be caused by moving the particles to different radial positions. After approximately 0.1s, the secondary flow begins to show visible influence and the particles move to different radial positions which correspond to different axial velocities.

To investigate the effect of the mean flow velocity on the residence time distribution (RTD) of the particles in the pipe, the inlet configuration of Case A, in which 9 particles are introduced at same inlet radial positions, is computed for three more cases with different mean flow velocities (Cases A2, A3 and A4, respectively). The average axial velocity and the residence time of the particles are listed in Table 1. It is shown that the mean, minimum, maximum and standard deviation of the particle residence time (RT_{mean}, RT_{min}, RT_{max}, and RT_{std}, respectively) are significantly affected by the mean flow velocity. As expected, particles travel faster when the mean flow velocity is increased. The increase of a standard deviation means a more scattered residence time distribution of the particles, which shows that the effect of the secondary flow on the particles is more significant when the fluid axial

velocity is small. It can be explained as follows: when the fluid axial velocity increases, the increase of the secondary flow does not keep up with the increase of the axial velocity. This result is in agreement with experimental findings of Tanyel [16].

Table 8.1 Axial velocity and residence time of particles introduced to the inlet of the pipe at same inlet radial positions, computed for different inlet mean flow velocities, $U_{s,f}$

Particle No.	$U_{s,f}$=0.50m/s (A1)		$U_{s,f}$=0.30m/s (A2)		$U_{s,f}$=0.20m/s (A3)		$U_{s,f}$=0.10m/s (A4)	
	$U_{s,p}$(m/s)	RT(s)	$U_{s,p}$(m/s)	RT(s)	$U_{s,p}$(m/s)	RT(s)	$U_{s,p}$(m/s)	RT(s)
1	0.75	1.33	0.50	2.30	0.308	3.25	0.154	6.47
2	0.69	1.46	0.47	2.12	0.283	3.59	0.144	7.04
3	0.63	1.58	0.42	2.39	0.259	3.95	0.131	7.75
4	0.55	1.80	0.37	2.73	0.256	3.58	0.128	7.89
5	0.55	1.83	0.35	2.83	0.260	3.55	0.131	7.04
6	0.65	1.53	0.41	2.49	0.313	3.18	0.155	6.42
7	0.68	1.45	0.47	2.17	0.328	3.01	0.162	6.11
8	0.76	1.33	0.50	2.02	0.327	3.01	0.162	6.06
9	0.77	1.25	0.51	1.97	0.321	3.07	0.160	6.17
RT_{mean}		1.50		2.33		3.35		6.77
RT_{min}		1.83		1.97		3.01		6.06
RT_{max}		1.25		2.83		3.95		7.89
RT_{std}		0.20		0.30		0.33		0.70

To investigate the effect of the inlet radial position of particles on their residence time distribution, Case B, in which the particles are introduced at different inlet radial positions, is computed using the same mean flow velocity as in Case A1. Figure 8.10 displays the snapshots of the particles in the pipe for different moments of time. It can be seen that the particles have already moved away from each other at t=0.2s while for Case A1 all 9 particles still stay together (see Fig. 8.6, t=0.2s). This is because in Case B the particles have different streamwise velocities according to their radial positions. For t=0.2s, the distribution of the particles takes the shape of an inclined “S”. This shape remains when t is increased to

0.4s and even to 0.6s; however, the particles move away from each other even further. When time reaches 0.8s, particle 6 chases up particle 5 and the S-shape is deformed. After this point, the deformed axial velocity distribution and the secondary flow in the helical pipe make the particle distribution even more deformed. This phenomenon can also be observed in Fig. 8.11, which depicts the corresponding radial positions of the particles at different moments of time. At t=0.2, 0.4 and 0.6s, the radial configuration of the 9 particles exhibits only a small deviation from the inlet configuration, but after that the displacements of the particles from their initial positions are significant.

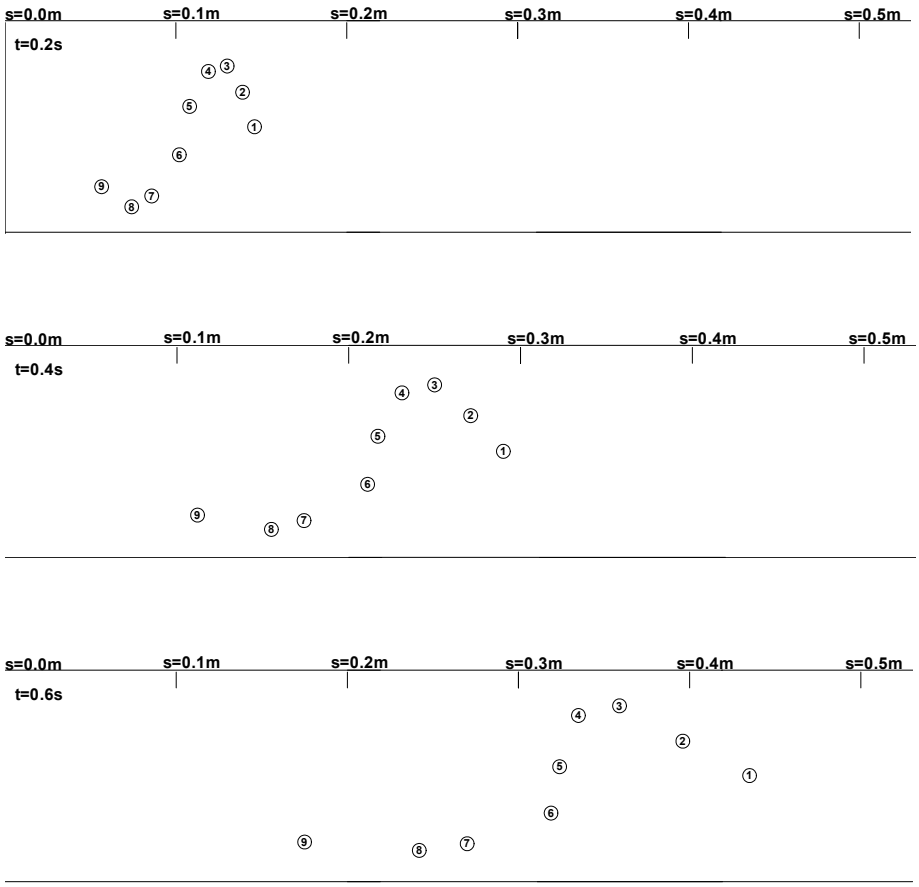

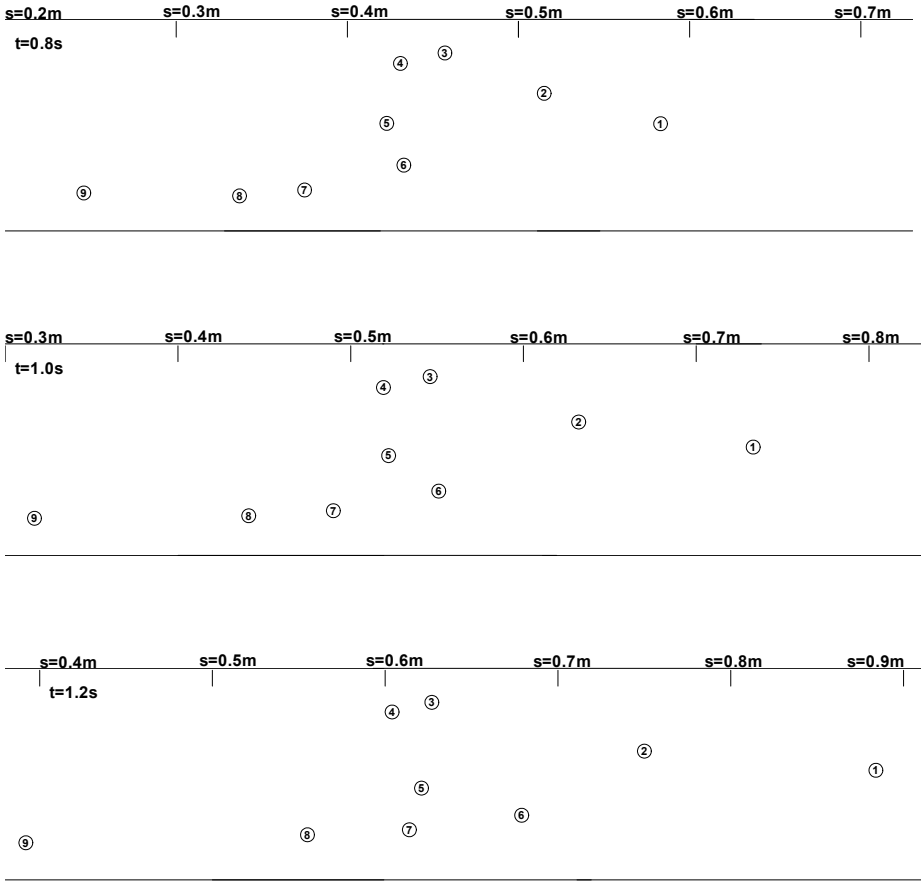

Figure 8.10 Snapshots of the particles at different moments of time (Case B)

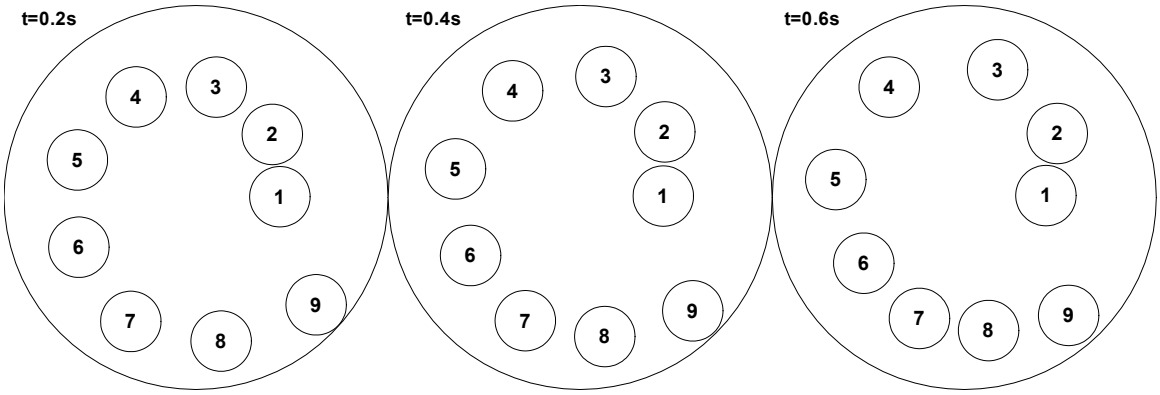

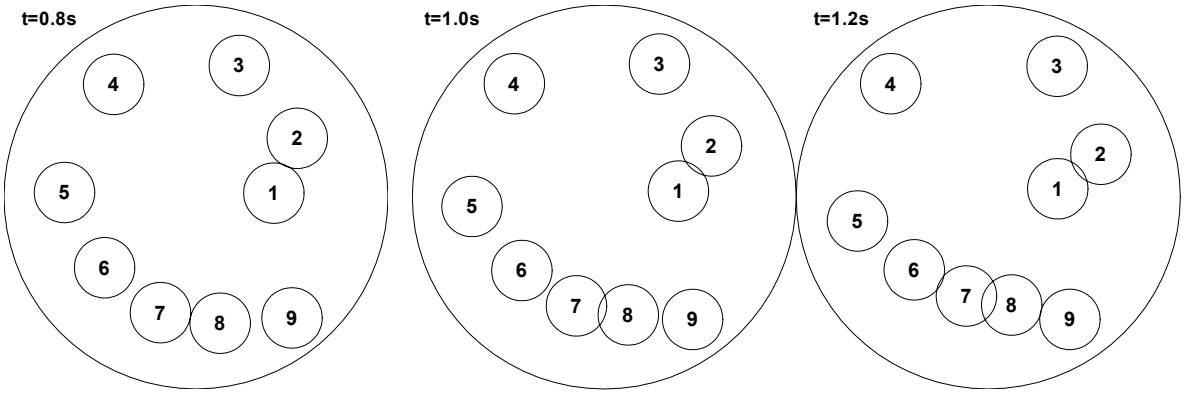

Figure 8.11 Radial positions of the particles at different moments of time (Case B)

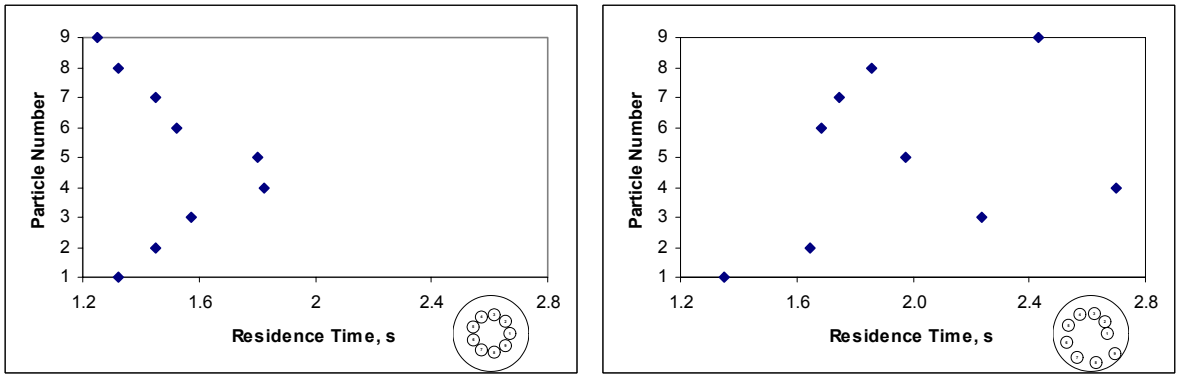

Case A1 Case B

Figure 8.12 Residence time distribution of the particles introduced to the inlet of the pipe with the same mean flow velocity at the same radial position (Case A1) and at different radial positions (Case B)

Table 2 presents the average axial velocities and the residence times of particles for Cases A1 and B. The range of the average velocities of the particles for Case B is much greater than that for Case A, showing that the inlet radial positions of particles significantly impact the residence time of particles in a helical pipe. The range of the residence times of particles for Case B is much greater than that for Case A1. The standard deviation of RTD in this case is 0.43s compared to 0.20s for Case A1, that is, the distribution of the residence time is more scattered, which can also be seen in Fig. 8.12. It is observed in Fig. 8.12 that the range of the residence time of particles is [1.2, 2.0] when the particles enter the pipe at the same radial

position while the range of the residence time is [1.2, 2.8] when the particles enter at different radial positions.

Table 8.2 Axial velocity and residence time of particles introduced to the inlet of the pipe at different inlet radial positions, computed for inlet mean flow velocities, $U_{s,f}$=0.5m/s

Particle No.	Same radial position (Case A1)		Different radial positions (Case B)	
	$U_{s,p}$(m/s)	RT(s)	$U_{s,p}$(m/s)	RT(s)
1	0.75	1.33	0.74	1.35
2	0.69	1.46	0.61	1.64
3	0.63	1.58	0.45	2.23
4	0.55	1.80	0.38	2.70
5	0.55	1.83	0.44	1.98
6	0.65	1.53	0.59	1.68
7	0.68	1.45	0.56	1.75
8	0.76	1.33	0.53	1.86
9	0.77	1.25	0.41	2.43
RT_{mean}		1.50		2.70
RT_{min}		1.83		1.35
RT_{max}		1.25		1.96
RT_{std}		0.20		0.43

8.5 CONCLUSIONS

A flow model is developed to simulate a two-phase 3D flow of a non-Newtonian fluid in a helical pipe with large particles. The governing equations for the fluid flow in an orthogonal helical coordinate system are derived. The forces acting on the particles are analyzed. The influence of the particles on the fluid is described by adding a source term to the momentum equation for the fluid flow. The source term is computed utilizing the force-coupling method. The particle-particle and particle-wall interactions are taken into account. It is shown that the particles have a significant effect on the flow field, including the axial velocity distribution

and the strength of the secondary flow. The trajectories and velocities of the particles are predicted. The residence time distribution (RTD) of particles is analyzed. It is shown that when the fluid axial velocity decreases, the mean residence time, minimum residence time, maximum residence time and standard deviation of the residence time increase. When the particles are initially placed at different radial positions at the inlet of the pipe, the distribution of the residence time is more scattered than that for the case of the same inlet radial positions.

REFERENCES

1. Shah, R.K. and Joshi, S.D. (1987) Convective heat transfer in curved ducts. *Handbook of Single-phase Convective Heat Transfer*, *Chap. 5*. New York :John Wiley.
2. Cheng, L., Kuzentsov, A.V. (2004) Investigation of a laminar flow of a non-Newtonian fluid in a helical pipe. *International Journal of Applied Mechanics and Engineering (in press)*.
3. Cheng, L. and. Kuznetsov, A.V. (2004) Heat transfer in a laminar flow of a non-Newtonian fluid in a helical pipe. *International Journal of Transport Phenomena (in press)*.
4. Liu, Y. and Zuritz, C.A. (1995) Mathematical modeling of solid-liquid two phase tube flow: an application to aseptic processing. *Journal of Food Process Engineering*, 18: 135-163.
5. Durst, F., Milojevic, D, and Schonung, B. (1984) Eulerian and Lagrangian predictions of particulate two-phase flows: a numerical study. *Applied Mathematical Modeling*, 8: 101-115.
6. Maxey, M.R., Patel, B.K., Chang, E.J., and Wang, P. (1997) Simulation of dispersed turbulent multiphase flow, *Fluid Dyn. Res.*, 20: 143-156.

7. Maxey, M.R., Patel, B.K (2001) Localized force representations for particles sedimenting in Stokes flow, *Int. J. Multiphase Flow*, 27: 1603-1626.

8. Lomholt, S., Maxey, M.R. (2003) Force-coupling method for particulate two-phase flow: Stokes flow, *Journal of Computational Physics*, 184: 381-405.

9. Glowinski, R., Pan, T.-W., Hesla, T. I. and Joseph, D.D. (1999) A distributed Lagrange multiplier/fictitious domain method for particulate flows, *Int. J. Multiphase Flow*, 25: 755-794.

10. Sandeep, K. P., Zuritz, C. A. & Puri, V. M. (2000) Modeling non-Newtonian two-phase flow in conventional and helical-holding tubes. *Int. J. food science and Technology,* 35: 511-522.

11. Germano, M. (1982). On the effect of torsion on a helical pipe flow. *J. Fluid Mech.,* 125: 1-8.

12. Germano, M. (1989). The Dean equations extended to a helical pipe flow. *J. Fluid Mech.,* 203: 289-305.

13. Liu, D., Maxey, M. and Karniadakis, G.E. (2002) A fast method for particulate microflows. *Journal of Microelectromechanical Systems*, 11 (6): 691-702.

14. Bird R.B., Stewart W.E. and Lightfoot, E.N. (2002) *Transport Phenomena*, 2nd ed. - New York: John Wiley and Sons.

15. Patankar, S.V. and Spalding, D.B. (1972) A calculation procedure for heat, mass and momentum transfer in three-dimensional parabolic flows. *Journal of Heat and Mass Transfer*, 15: 1787-1806.

16. Tanyel, Z. (2004) Residence time distribution of multiphase particles in four configurations of holding tubes. *Master Thesis, North Carolina State University, Raleigh, NC*.

9 CONCLUSIONS

This dissertation investigates the interaction of turbulent flow in a homogeneous fluid region with flow in a porous region in a composite porous/fluid domain; laminar flow and heat transfer of a non-Newtonian fluid in a helical pipe; the modeling of the laminar flow and heat transfer in a helical pipe filled with fluid saturated porous medium; two-phase (non-Newtonian fluid and solid particles) flow in a helical pipe. Mathematical modeling and numerical results are presented.

9.1 REMARKS ON TURBULENCE EFFECTS ON COMPOSITE POROUS/FLUID DOMAIN

Forced convection heat transfer in composite porous/fluid domains draws lots of attention due to a wide variety of its engineering applications. If permeability of the porous medium is sufficiently small, even if the flow in the clear fluid region is turbulent, the flow in the porous region may still remain laminar. However, previous work addressed only the laminar flow case in both homogeneous fluid and porous regions of the domain. In this dissertation, an interaction between turbulent flow in the center of a circular tube filled with a homogeneous fluid and laminar flow in the porous layer adjacent to the tube wall is investigated.

The flow in the porous region of the channel is governed by the Brinkma-Forchheimer-extended Darcy equation and the flow in the central region of the tube is governed by a two-layer algebraic turbulence model suggested by Cebeci and Smith. The effects of turbulence in the central region on velocity and temperature distributions as well as on the Nusselt number

are presented for both constant wall temperature and constant heat flux cases in a channel (Chapter 2) and a tube (Chapter3).

9.2 REMARKS ON NON-NEWTONIAN LAMINAR FLOW IN A HELICAL PIPE

Secondary flow occurs in the flow in a helical pipe. It increases heat and mass transfer efficiency compared to that in straight pipes. To investigate the helical pipe flow applied in dairy and food processing industry, non-Newtonian fluid model is adopted and the derivation of the momentum and energy equations in an orthogonal coordinate system is presented. Comparisons of the effects of the pressure gradient, curvature, and torsion on the Newtonian and non-Newtonian fluid flows are performed. These effects are more significant for a non-Newtonian fluid studied in this dissertation than for a Newtonian fluid.

When investigating the heat transfer problem, a constant wall heat flux and a fixed Reynolds number are assumed for this study of the fully-developed laminar non-Newtonian flow in a helical pipe. The effect of two controlling parameters, the Dean number, *De*, and the Germano number, *Gn*, are investigated. The development of the Nusselt number at different Prandtl numbers is also presented. It is found that helical pipes do have the advantage of greater heat transfer compared to straight pipes. The Nusselt number increases and the secondary flow becomes stronger with increase of the Dean number. The increase of the Germano number does not have any significant effect on the axial velocity and heat transfer but strengthens the secondary flow. Since temperature-independent viscosity is assumed, the Prandtl number affects heat transfer but not the primary and secondary flow velocities.

9.3 Remarks on Laminar Flow in a Helical Pipe Filled with Porous Medium

The original motivation of this topic comes from biomedical applications. In a clotted artery, the lesions or "plaques" within the artery wall consist of localized deposits of fat compounds (lipids) surrounded by cells recruited from the blood stream and scar tissue; this acts as a porous medium that may diminish or completely eliminate the blood flow. The coronary arteries surrounding the heart are curved and at least segments of them can be modeled as helical. Nothing has been published before on flows in helical pipes filled with a fluid saturated porous medium. The aim of the present chapter is to fill this gap in the literature.

The analysis is based on the full momentum equation for porous media that accounts for the Brinkman and Forchheimer extensions of the Darcy law as well as for the flow inertia. This equation is derived in an orthogonal helical coordinate system. The effects of the Darcy number, the Forchheimer coefficient as well as the Dean and Germano numbers on the axial flow velocity, secondary flow, temperature distribution, and the Nusselt number are investigated.

9.4 Remarks on 3D Modeling of Two-Phase Flow in a Helical Pipe

A 3D two-phase flow model is set up for large particles carried by a non-Newtonian fluid in a helical pipe. The governing equations of the fluid flow in an orthogonal coordinate system are derived. The forces acting on the particles are analyzed. The influence of the particles on the fluid is described by adding a source term to the momentum equation for the fluid flow. The source term is modeled by the Force-Coupling method developed by Maxey. The particle-particle and particle-wall interactions are taken into account. It is shown that the

particles have a significant effect on the flow field, including the axial velocity distribution and the secondary flow strength. The trajectories and velocities of the particles are predicted. The residence time and the residence time distribution (RTD) of the particles are analyzed. The residence time distribution (RTD) of particles is analyzed. It is shown that when the fluid axial velocity decreases, fewer particles fall into the central interval and the residence time distribution becomes more scattered.

Appendix A: Derivation of the external forces acting on a particle in a helical orthogonal coordinate system

Particles suspended in a viscous fluid are subjected to the following forces:

(1) Magnus Lift Force

The Magnus lift force is the one that causes the curving of a spinning sphere. This force acts in a direction perpendicular to the direction of motion of the particle. The Magnus lift force $\mathbf{F}_{rk}$ is calculated by

$$\mathbf{F}_{rk} = \pi\rho_f a_p{}^3 \boldsymbol{\Omega} \times \left(\mathbf{v}_p - \mathbf{v}_f\right) \tag{A.1}$$

where $\boldsymbol{\Omega}$ is the angular velocity of the particle. In the above expression, the difference in velocities $\mathbf{v}_p - \mathbf{v}_f$ is called the slip velocity or relative velocity ($\mathbf{v}_{rel}$). The vector product $\boldsymbol{\Omega} \times \mathbf{v}_{rel}$ in an orthogonal coordinate system (e_1, e_2, e_3) is determined as follows:

$$\boldsymbol{\Omega} \times \mathbf{v}_{rel} = \frac{1}{h_1 h_2 h_3} \begin{pmatrix} h_1 e_1 & h_2 e_2 & h_3 e_3 \\ \Omega_1 & \Omega_2 & \Omega_3 \\ h_1 V_{rel1} & h_2 V_{rel2} & h_3 V_{rel3} \end{pmatrix} \tag{A.2}$$

Substituting Equation (A.2) into (A.1) results in the following expressions for the projections of the Magnus lift force, respectively:

$$F_{sk1} = \pi\rho_f a_p{}^3 \frac{1}{h_2 h_3} \left(\Omega_2 \left(h_3 V_{rel3}\right) - \Omega_3 \left(h_2 V_{rel2}\right)\right) \tag{A.3a}$$

$$F_{sk2} = \pi\rho_f a_p{}^3 \frac{1}{h_1 h_3} \left(\Omega_3 \left(h_1 V_{rel1}\right) - \Omega_1 \left(h_3 V_{rel3}\right)\right) \tag{A.3b}$$

$$F_{sk3} = \pi\rho_f a_p{}^3 \frac{1}{h_1 h_2} \left(\Omega_1 \left(h_2 V_{rel2}\right) - \Omega_2 \left(h_1 V_{rel1}\right)\right) \tag{A.3c}$$

(2) Saffman Lift Force

In vector notation, the Saffman lift force on a particle is given by:

$$\mathbf{F}_s = 6.46\rho_f a_p{}^2\left(\frac{\nu}{|\mathbf{K}|}\right)^{1/2}\mathbf{K}\times\left(\mathbf{v}_p-\mathbf{v}_f\right) \tag{A.4}$$

where $\mathbf{K}$ is the curl of the fluid velocity, ν is the kinematic viscosity, and a is the radius of the particle. The expression for $\mathbf{K}$ in the above equation can been obtained as follows:

$$\begin{aligned}\mathbf{K} &= \nabla\times\mathbf{v}_f = \frac{1}{h_1h_2h_3}\begin{pmatrix} h_1e_1 & h_2e_2 & h_3e_3 \\ \dfrac{\partial}{\partial\xi_1} & \dfrac{\partial}{\partial\xi_2} & \dfrac{\partial}{\partial\xi_3} \\ h_1V_{f1} & h_2V_{f2} & h_3V_{f3}\end{pmatrix} \\ &= \frac{1}{h_2h_3}\left(\frac{\partial}{\partial\xi_2}\left(h_3V_{f3}\right)-\frac{\partial}{\partial\xi_3}\left(h_2V_{f2}\right)\right)\quad e_1 \\ &+ \frac{1}{h_1h_3}\left(\frac{\partial}{\partial\xi_3}\left(h_1V_{f1}\right)-\frac{\partial}{\partial\xi_1}\left(h_3V_{f3}\right)\right)\quad e_2 \\ &+ \frac{1}{h_1h_2}\left(\frac{\partial}{\partial\xi_1}\left(h_2V_{f2}\right)-\frac{\partial}{\partial\xi_2}\left(h_1V_{f1}\right)\right)\quad e_3\end{aligned} \tag{A.5}$$

The vector product in Equation (A.4) can be evaluated as follows:

$$\begin{aligned}\mathbf{K}\times\left(\mathbf{v}_p-\mathbf{v}_f\right) &= \mathbf{K}\times\mathbf{v}_{rel} = \frac{1}{h_1h_2h_3}\begin{pmatrix} h_1e_1 & h_2e_2 & h_3e_3 \\ K_1 & K_2 & K_3 \\ h_1V_{rel1} & h_2V_{rel2} & h_3V_{rel3}\end{pmatrix} \\ &= \frac{1}{h_2h_3}\left(K_2\left(h_3V_{rel3}\right)-K_3\left(h_2V_{rel2}\right)\right)\quad e_1 \\ &+ \frac{1}{h_1h_3}\left(K_3\left(h_1V_{rel1}\right)-K_1\left(h_3V_{rel3}\right)\right)\quad e_2 \\ &+ \frac{1}{h_1h_2}\left(K_1\left(h_2V_{rel2}\right)-K_2\left(h_1V_{rel1}\right)\right)\quad e_3\end{aligned} \tag{A.6}$$

where

$$|\mathbf{K}| = \left(\frac{1}{h_2h_3}\left(\frac{\partial}{\partial\xi_2}\left(h_3V_{f3}\right)-\frac{\partial}{\partial\xi_3}\left(h_2V_{f2}\right)\right)\right)+\left(\frac{1}{h_1h_3}\left(\frac{\partial}{\partial\xi_3}\left(h_1V_{f1}\right)-\frac{\partial}{\partial\xi_1}\left(h_3V_{f3}\right)\right)\right)^2+\left(\frac{1}{h_1h_2}\left(\frac{\partial}{\partial\xi_1}\left(h_2V_{f2}\right)-\frac{\partial}{\partial\xi_2}\left(h_1V_{f1}\right)\right)\right)^2 \tag{A.7}$$

Thus, the scalar forms of the Saffman lift force in the (e_1, e_2, e_3) coordinates are, respectively

$$F_{s1} = 6.46\rho_f {a_p}^2 \left(\frac{\nu}{|K|}\right)^{1/2} \frac{1}{h_2 h_3}\left(\frac{1}{h_1 h_3}\left(\frac{\partial}{\partial \xi_3}\left(h_1 V_{f1}\right) - \frac{\partial}{\partial \xi_1}\left(h_3 V_{f3}\right)\right)\left(h_3 V_{rel3}\right)\right.$$
$$\left. - \frac{1}{h_1 h_2}\left(\frac{\partial}{\partial \xi_1}\left(h_2 V_{f2}\right) - \frac{\partial}{\partial \xi_2}\left(h_1 V_{f1}\right)\right)\left(h_2 V_{rel2}\right)\right) \qquad \textit{(A.8a)}$$

$$F_{s2} = 6.46\rho_f {a_p}^2 \left(\frac{\nu}{|K|}\right)^{1/2} \frac{1}{h_1 h_3}\left(\frac{1}{h_1 h_2}\left(\frac{\partial}{\partial \xi_1}\left(h_2 V_{f2}\right) - \frac{\partial}{\partial \xi_2}\left(h_1 V_{f1}\right)\right)\left(h_1 V_{rel1}\right)\right.$$
$$\left. - \frac{1}{h_2 h_3}\left(\frac{\partial}{\partial \xi_2}\left(h_3 V_{f3}\right) - \frac{\partial}{\partial \xi_3}\left(h_2 V_{f2}\right)\right)\left(h_3 V_{rel3}\right)\right) \qquad \textit{(A.8b)}$$

$$F_{s3} = 6.46\rho_f {a_p}^2 \left(\frac{\nu}{|K|}\right)^{1/2} \frac{1}{h_1 h_2}\left(\frac{1}{h_2 h_3}\left(\frac{\partial}{\partial \xi_2}\left(h_3 V_{f3}\right) - \frac{\partial}{\partial \xi_3}\left(h_2 V_{f2}\right)\right)\left(h_2 V_{rel2}\right)\right.$$
$$\left. - \frac{1}{h_1 h_3}\left(\frac{\partial}{\partial \xi_3}\left(h_1 V_{f1}\right) - \frac{\partial}{\partial \xi_1}\left(h_3 V_{f3}\right)\right)\left(h_1 V_{rel1}\right)\right) \qquad \textit{(A.8c)}$$

(3) Drag Force

The expression for the drag on a particle in a viscous fluid is given by:

$$\mathbf{F}_d = \frac{1}{2} C_d \rho_f \pi {a_p}^2 \left|\mathbf{v}_f - \mathbf{v}_p\right|\left(\mathbf{v}_f - \mathbf{v}_p\right) \qquad \textit{(A.9)}$$

where the drag coefficient, C_d is obtained from the following equation:

$$C_d = \frac{24}{\mathrm{Re}_p}\left[1 + 0.15\,\mathrm{Re}_p^{\,0.687}\right] \qquad \textit{(A.10)}$$

for $1 < \mathrm{Re}_p < 1000$ and the particle Reynolds number is defined by

$$\mathrm{Re}_p = \frac{\rho\left(2a_p\right)\left|\mathbf{v}_f - \mathbf{v}_p\right|}{\mu} \qquad \textit{(A.11)}$$

(4) Buoyancy force

The expression to compute the buoyancy force exerted on the particle is given by:

$$F_b = (4/3)\pi a_p^{\,3}(\rho_f - \rho_g)\mathbf{g} \tag{A.12}$$

Substituting the helical orthogonal coordinate system with

ξ_i	s	r	θ
h_i	$1+\kappa r\sin(\theta+\phi)$	1	r
v_i	u_s	u_r	u_θ

into the three forces and setting $h_s = h_1$ result as follows:

$$\begin{aligned}
F_s = {} & \pi\rho_f a_p^{\,3}\frac{1}{r}\left(\Omega_2\left(r\left(u_{\theta p}-u_{\theta f}\right)\right)-\Omega_3\left(u_{rp}-u_{rf}\right)\right) \\
& + 6.46\,\rho_f a^2\left(\frac{\nu}{|K|}\right)^{1/2}\frac{1}{r}\left(\frac{1}{h_s r}\left(\frac{\partial}{\partial\theta}\left(h_s u_{sf}\right)-\frac{\partial}{\partial s}\left(ru_{\theta f}\right)\right)\left(r\left(u_{\theta p}-u_{\theta f}\right)\right)\right. \\
& \qquad \left. -\frac{1}{h_s}\left(\frac{\partial u_{rf}}{\partial s}-\frac{\partial}{\partial r}\left(h_s u_{sf}\right)\right)\left(u_{rp}-u_{rf}\right)\right) \\
& + \frac{1}{2}C_d\rho_f\pi a^2\left|V_f - V_p\right|h_s\left(u_{sf}-u_{sp}\right) \\
& + \frac{4}{3}\pi a^3\left(\rho_f-\rho_p\right)g\sin\beta
\end{aligned} \tag{A.13a}$$

$$\begin{aligned}
F_r = {} & \pi\rho_f a_p^{\,3}\frac{1}{h_s r}\left(\Omega_3\left(h_s\left(u_{sp}-u_{sf}\right)\right)-\Omega_1\left(u_{\theta p}-u_{\theta f}\right)\right) \\
& + 6.46\,\rho_f a^2\left(\frac{\nu}{|K|}\right)^{1/2}\frac{1}{h_s r}\left(\frac{1}{h_s}\left(\frac{\partial u_{rf}}{\partial s}-\frac{\partial}{\partial r}\left(h_s u_{sf}\right)\right)\left(h_s\left(u_{sp}-u_{sf}\right)\right)\right. \\
& \qquad \left. -\frac{1}{r}\left(\frac{\partial}{\partial r}\left(ru_{\theta f}\right)-\frac{\partial u_{rf}}{\partial\theta}\right)\left(r\left(u_{\theta p}-u_{\theta f}\right)\right)\right) \\
& + \frac{1}{2}C_d\rho_f\pi a^2\left|V_f - V_p\right|\left(u_{rf}-u_{rp}\right) \\
& + \frac{4}{3}\pi a^3\left(\rho_f-\rho_p\right)g\sin\beta\sin\theta
\end{aligned} \tag{A.13b}$$

$$\begin{aligned}
F_\theta = {} & \pi\rho_f a_p^{\,3}\frac{1}{h_s}\left(\Omega_1\left(u_{rp}-u_{rf}\right)-\Omega_2\left(h_s\left(u_{sp}-u_{sf}\right)\right)\right) \\
& + 6.46\,\rho_f a^2\left(\frac{\nu}{|K|}\right)^{1/2}\frac{1}{h_s}\left(\frac{1}{r}\left(\frac{\partial}{\partial r}\left(ru_{\theta f}\right)-\frac{\partial u_{rf}}{\partial\theta}\right)\left(u_{rp}-u_{rf}\right)\right. \\
& \qquad \left. -\frac{1}{h_s r}\left(\frac{\partial}{\partial\theta}\left(h_s u_{sf}\right)-\frac{\partial}{\partial s}\left(ru_{\theta f}\right)\right)\left(h_s\left(u_{sp}-u_{sf}\right)\right)\right) \\
& + \frac{1}{2}C_d\rho_f\pi a^2\left|V_f - V_p\right|r\left(u_{\theta f}-u_{\theta p}\right) \\
& + \frac{4}{3}\pi a^3\left(\rho_f-\rho_p\right)g\sin\beta\cos\theta
\end{aligned} \tag{A.13c}$$

where

$$|K| = \left(\frac{1}{r}\left(\frac{\partial}{\partial r}\left(ru_{\theta f}\right)-\frac{\partial u_{rf}}{\partial\theta}\right)\right)^2 + \left(\frac{1}{h_s r}\left(\frac{\partial}{\partial\theta}\left(h_s u_{sf}\right)-\frac{\partial}{\partial s}\left(ru_{\theta f}\right)\right)\right)^2 + \left(\frac{1}{h_s}\left(\frac{\partial u_{rf}}{\partial s}-\frac{\partial}{\partial r}\left(h_s u_{sf}\right)\right)\right)^2 \tag{A.14}$$

Appendix B: Derivation of the Torque Experienced by a particle in a helical orthogonal coordinate system

The equation that is used to calculate the torque experienced by particles suspended in a viscous fluid is:

$$\mathbf{T} = \int d\mathbf{T} = \int_A r \times (\tau \cdot \mathbf{n}) dA \tag{B.1}$$

where

$$\begin{aligned}(\tau \cdot n) = &\left[e_1\left(e_1\tau_{e_1e_1} + e_2\tau_{e_1e_2} + e_3\tau_{e_1e_3}\right) + e_2\left(e_1\tau_{e_2e_1} + e_2\tau_{e_2e_2} + e_3\tau_{e_2e_3}\right)\right.\\ &\left. + e_3\left(e_1\tau_{e_3e_1} + e_2\tau_{e_3e_2} + e_3\tau_{e_3e_3}\right)\right]\cdot\left(e_1 n_{e_1} + e_2 n_{e_2} + e_3 n_{e_3}\right)\\ &= e_1\left(n_{e_1}\tau_{e_1e_1} + n_{e_2}\tau_{e_2e_1} + n_{e_3}\tau_{e_3e_1}\right)\\ &+ e_2\left(n_{e_1}\tau_{e_1e_2} + n_{e_2}\tau_{e_2e_2} + n_{e_3}\tau_{e_3e_2}\right)\\ &+ e_3\left(n_{e_1}\tau_{e_1e_3} + n_{e_2}\tau_{e_2e_3} + n_{e_3}\tau_{e_3e_3}\right)\end{aligned} \tag{B.2}$$

and

$$\begin{aligned}d\mathbf{T} &= \frac{1}{h_1h_2h_3}\begin{pmatrix} h_1e_1 & h_2e_2 & h_3e_3 \\ r_1 & r_2 & r_3 \\ h_1(\tau\cdot n)_1 & h_2(\tau\cdot n)_2 & h_3(\tau\cdot n)_3 \end{pmatrix}\\ &= \frac{1}{h_2h_3}\left(r_2h_3\left(n_{e_1}\tau_{e_1e_3} + n_{e_2}\tau_{e_2e_3} + n_{e_3}\tau_{e_3e_3}\right) - r_3h_2\left(n_{e_1}\tau_{e_1e_2} + n_{e_2}\tau_{e_2e_2} + n_{e_3}\tau_{e_3e_2}\right)\right)\ e_1\\ &+ \frac{1}{h_1h_3}\left(r_3h_1\left(n_{e_1}\tau_{e_1e_1} + n_{e_2}\tau_{e_2e_1} + n_{e_3}\tau_{e_3e_1}\right) - r_1h_3\left(n_{e_1}\tau_{e_1e_3} + n_{e_2}\tau_{e_2e_3} + n_{e_3}\tau_{e_3e_3}\right)\right)\ e_2\\ &+ \frac{1}{h_1h_2}\left(r_1h_2\left(n_{e_1}\tau_{e_1e_2} + n_{e_2}\tau_{e_2e_2} + n_{e_3}\tau_{e_3e_2}\right) - r_2h_1\left(n_{e_1}\tau_{e_1e_1} + n_{e_2}\tau_{e_2e_1} + n_{e_3}\tau_{e_3e_1}\right)\right)\ e_3\end{aligned} \tag{B.3}$$

Thus

$$dT_{e_1} = \frac{1}{h_2h_3}\left(r_2h_3\left(n_{e_1}\tau_{e_1e_3} + n_{e_2}\tau_{e_2e_3} + n_{e_3}\tau_{e_3e_3}\right) - r_3h_2\left(n_{e_1}\tau_{e_1e_2} + n_{e_2}\tau_{e_2e_2} + n_{e_3}\tau_{e_3e_2}\right)\right) \tag{B.4}$$

Since normal shear stresses have no contribution toward the torque, the above equation reduces to the following form:

$$dT_{e_1} = \frac{1}{h_2 h_3}\left(r_2 h_3\left(n_{e_1}\tau_{e_1e_3} + n_{e_2}\tau_{e_2e_3}\right) - r_3 h_2\left(n_{e_1}\tau_{e_1e_2} + n_{e_3}\tau_{e_3e_2}\right)\right) \qquad (B.5)$$

It is also noted that the shear stresses in the e_1 direction do not contribute toward the e_1 component of the torque and that $\tau_{e_2e_3}$ and $\tau_{e_3e_2}$ must have opposite signs in order to produce a torque in the same direction. Thus, the above equation reduces to:

$$dT_{e_1} = \frac{1}{h_2 h_3}\left(r_2 h_3\left(n_{e_2}\tau_{e_2e_3}\right) + r_3 h_2\left(n_{e_3}\tau_{e_2e_3}\right)\right) \qquad (B.6)$$

substituting with helical coordinate system results in:

$$\begin{aligned} dT_s &= \frac{1}{r}\left(r r_r\left(n_r\tau_{r\theta}\right) + r_\theta\left(n_\theta\tau_{r\theta}\right)\right) \\ &= r_r n_r \mu\left(r\frac{\partial}{\partial r}\left(\frac{u_\theta}{r}\right) + \frac{1}{r}\frac{\partial u_r}{\partial\theta}\right) + \frac{1}{r} r_\theta n_\theta \mu\left(r\frac{\partial}{\partial r}\left(\frac{u_\theta}{r}\right) + \frac{1}{r}\frac{\partial u_r}{\partial\theta}\right) \end{aligned} \qquad (B.7)$$

with

$$\tau_{ss} = 2\mu\left(\frac{\partial}{\partial s}\left(\frac{u_s}{h_s}\right) - \frac{\tau\kappa r\cos(\theta - \tau s)}{h_s^{\,2}}u_s + \frac{\kappa\sin(\theta - \tau s)}{h_s}u_r + \frac{\kappa\cos(\theta - \tau s)}{h_s}u_\theta\right),$$

$$\tau_{rr} = \frac{2}{\mathrm{Re}}\left(\frac{\partial u_r}{\partial r}\right), \tau_{\theta\theta} = 2\mu\left(\frac{\partial}{\partial\theta}\left(\frac{u_\theta}{r}\right) + \frac{u_r}{r}\right), \tau_{sr} = \tau_{rs} = \mu\left(h_s\frac{\partial}{\partial r}\left(\frac{u_s}{h_s}\right) + \frac{1}{h_s}\frac{\partial u_r}{\partial s}\right), \qquad (B.8)$$

$$\tau_{s\theta} = \tau_{\theta s} = \mu\left(\frac{h_s}{r}\frac{\partial}{\partial\theta}\left(\frac{u_s}{h_s}\right) + \frac{r}{h_s}\frac{\partial}{\partial s}\left(\frac{u_\theta}{r}\right)\right), \tau_{r\theta} = \tau_{\theta r} = \mu\left(r\frac{\partial}{\partial r}\left(\frac{u_\theta}{r}\right) + \frac{1}{r}\frac{\partial u_r}{\partial\theta}\right)$$

Since $\partial u_\theta / \partial r$ is parallel to r_θ and $\partial u_r / \partial\theta$ is parallel to r_r, they do not contribute toward the torque and hence are dropped, thereby reducing the above equation to the following form:

$$dT_s = r_r n_r \mu\left(r\frac{\partial}{\partial r}\left(\frac{u_\theta}{r}\right)\right) + \frac{1}{r} r_\theta n_\theta \mu\left(\frac{1}{r}\frac{\partial u_r}{\partial \theta}\right) \qquad (B.9)$$

In the above equation, the term $r_r n_r$ and $r_\theta n_\theta$ can be written in the following form:

$$r_r n_r = (r \cdot n) - r_s n_s - r_\theta n_\theta,\ r_\theta n_\theta = (r \cdot n) - r_s n_s - r_r n_r \qquad (B.10)$$

Then

$$dT_s = ((r \cdot n) - r_s n_s - r_\theta n_\theta)\mu\left(r\frac{\partial}{\partial r}\left(\frac{u_\theta}{r}\right)\right) + \frac{1}{r}((r \cdot n) - r_s n_s - r_r n_r)\mu\left(\frac{1}{r}\frac{\partial u_r}{\partial \theta}\right) \qquad (B.11)$$

It is noted that the lever arm r_s cannot contribute toward the torque in the s-direction and that the velocity which has the same direction as the lever arm, cannot contribute toward the torque. Thus, the above expression reduces to the following form:

$$dT_s = a_p \mu\left[\left(r\frac{\partial}{\partial r}\left(\frac{u_\theta}{r}\right)\right) + \frac{1}{r}\left(\frac{1}{r}\frac{\partial u_r}{\partial \theta}\right)\right] \qquad (B.12)$$

In obtaining this equation it is noted that the scalar product $(r \cdot \mathbf{n})$ is equal to the radius of the particle a_p.

In order to convert the above expression for the torque on an infinitesimal area on the surface of the particle to the total torque experienced by the particle, the above expression was integrated over the entire surface of the particle. In spherical coordinates, the lever arm, $r_{particle}$, varies as $r_{particle} = a_p \sin\theta$. It is also noted that the shear stress at the center of the particle is a constant and hence the s-component of the torque on the particle is given by:

$$
\begin{aligned}
T_s &= \int_A r_{partilce}\mu\left[\left(r\frac{\partial}{\partial r}\left(\frac{u_\theta}{r}\right)\right)+\frac{1}{r}\left(\frac{1}{r}\frac{\partial u_r}{\partial\theta}\right)\right]dA \\
&= \int_0^{2\pi}\int_0^{\pi} a_p \sin\theta\mu\left[\left(r\frac{\partial}{\partial r}\left(\frac{u_\theta}{r}\right)\right)+\frac{1}{r}\left(\frac{1}{r}\frac{\partial u_r}{\partial\theta}\right)\right]{a_p}^2 \sin\theta d\theta d\phi \\
&= 2\pi {a_p}^3\mu\left[\left(r\frac{\partial}{\partial r}\left(\frac{u_\theta}{r}\right)\right)+\frac{1}{r}\left(\frac{1}{r}\frac{\partial u_r}{\partial\theta}\right)\right]\int_0^{\pi}\sin^2 \\
&= \pi^2 {a_p}^3\mu\left[\left(r\frac{\partial}{\partial r}\left(\frac{u_\theta}{r}\right)\right)+\frac{1}{r}\left(\frac{1}{r}\frac{\partial u_r}{\partial\theta}\right)\right]
\end{aligned}
\qquad (B.13)
$$

Repeating the same procedure, the other two components of torque are obtained as:

$$
\begin{aligned}
dT_r &= \frac{1}{h_s r}\left(r_\theta h_s\left(n_r\tau_{rs}+n_\theta\tau_{\theta s}\right)-r_s r\left(n_s\tau_{s\theta}+n_r\tau_{r\theta}\right)\right) \\
&= \frac{1}{h_s r}\left(r_\theta h_s\left(n_\theta\tau_{\theta s}\right)+r_s r\left(n_s\tau_{\theta s}\right)\right) \\
&= \frac{1}{h_s r}\left(r_\theta h_s\left(n_\theta\mu\left(\frac{h_s}{r}\frac{\partial}{\partial\theta}\left(\frac{u_s}{h_s}\right)+\frac{r}{h_s}\frac{\partial}{\partial s}\left(\frac{u_\theta}{r}\right)\right)\right)+r_s r\left(n_s\mu\left(\frac{h_s}{r}\frac{\partial}{\partial\theta}\left(\frac{u_s}{h_s}\right)+\frac{r}{h_s}\frac{\partial}{\partial s}\left(\frac{u_\theta}{r}\right)\right)\right)\right) \\
&= \frac{1}{h_s r}\left(r_\theta h_s\left(n_\theta\mu\left(\frac{h_s}{r}\frac{\partial}{\partial\theta}\left(\frac{u_s}{h_s}\right)\right)\right)+r_s r\left(n_s\mu\left(\frac{r}{h_s}\frac{\partial}{\partial s}\left(\frac{u_\theta}{r}\right)\right)\right)\right) \\
&= \frac{1}{h_s r}\left[\left((r\cdot n)-r_s n_s-r_r n_r\right)h_s\left(\mu\left(\frac{h_s}{r}\frac{\partial}{\partial\theta}\left(\frac{u_s}{h_s}\right)\right)\right)+\right. \\
&\qquad \left.\left((r\cdot n)-r_\theta n_\theta-r_r n_r\right)r\left(\mu\left(\frac{r}{h_s}\frac{\partial}{\partial s}\left(\frac{u_\theta}{r}\right)\right)\right)\right] \\
&= a_p\mu\frac{1}{h_s r}\left(h_s\left(\frac{h_s}{r}\frac{\partial}{\partial\theta}\left(\frac{u_s}{h_s}\right)\right)+r\left(\frac{r}{h_s}\frac{\partial}{\partial s}\left(\frac{u_\theta}{r}\right)\right)\right)
\end{aligned}
\qquad (B.14)
$$

$$
\begin{aligned}
dT_\theta &= \frac{1}{h_s}\left(r_s\left(n_s\tau_{sr}+n_r\tau_{rr}+n_\theta\tau_{\theta r}\right)-r_r h_s\left(n_s\tau_{ss}+n_r\tau_{rs}+n_\theta\tau_{\theta s}\right)\right) \\
&= \frac{1}{h_s}\left(r_s\left(n_s\tau_{sr}+n_\theta\tau_{\theta r}\right)-r_r h_s\left(n_r\tau_{rs}+n_\theta\tau_{\theta s}\right)\right) \\
&= \frac{1}{h_s}\left(r_s\left(n_s\tau_{sr}\right)+r_r h_s\left(n_r\tau_{sr}\right)\right) \\
&= \frac{1}{h_s}\left[r_s n_s\mu\left(h_s\frac{\partial}{\partial r}\left(\frac{u_s}{h_s}\right)+\frac{1}{h_s}\frac{\partial u_r}{\partial s}\right)+r_r h_s n_r\mu\left(h_s\frac{\partial}{\partial r}\left(\frac{u_s}{h_s}\right)+\frac{1}{h_s}\frac{\partial u_r}{\partial s}\right)\right] \\
&= \frac{1}{h_s}\left[r_s n_s\mu\left(\frac{1}{h_s}\frac{\partial u_r}{\partial s}\right)+r_r h_s n_r\mu\left(h_s\frac{\partial}{\partial r}\left(\frac{u_s}{h_s}\right)\right)\right] \\
&= a_p\mu\left[\frac{1}{{h_s}^2}\frac{\partial u_r}{\partial s}+h_s\frac{\partial}{\partial r}\left(\frac{u_s}{h_s}\right)\right]
\end{aligned}
\qquad (B.15)
$$

and

$$T_r = \pi^2 {a_p}^3 \mu \left(h_s \left(\frac{h_s}{r} \frac{\partial}{\partial \theta} \left(\frac{u_s}{h_s} \right) \right) + r \left(\frac{r}{h_s} \frac{\partial}{\partial s} \left(\frac{u_\theta}{r} \right) \right) \right) \tag{B.16}$$

$$T_\theta = \pi^2 {a_p}^3 \mu \left[\frac{1}{{h_s}^2} \frac{\partial u_r}{\partial s} + h_s \frac{\partial}{\partial r} \left(\frac{u_s}{h_s} \right) \right] \tag{B.17}$$

The angular dynamics equation for the particles is as follows:

$$I \left(\frac{d\boldsymbol{\Omega}}{dt} \right) = \Sigma \, \mathbf{T} \tag{B.18}$$

where I is the moment of inertia ($I = 2/5 m_p {a_p}^2$ for a sphere) and $\mathbf{T}$ are the local torques exerted by the viscous fluid on the surface of a particle.

Substituting the expression for the torque into the angular momentum equation results in:

$$\frac{d\Omega_s}{dt} = \frac{15}{\rho_p {a_p}^2} \mu \left[\frac{\pi}{8} \left(\left(r \frac{\partial}{\partial r} \left(\frac{u_\theta}{r} \right) \right) + \frac{1}{r} \left(\frac{1}{r} \frac{\partial u_r}{\partial \theta} \right) \right) \right] \tag{B.19a}$$

$$\frac{d\Omega_r}{dt} = \frac{15}{\rho_p {a_p}^2} \mu \left[\frac{\pi}{8} \left(\frac{h_s h_s}{r} \frac{\partial}{\partial \theta} \left(\frac{u_s}{h_s} \right) + \frac{rr}{h_s} \frac{\partial}{\partial s} \left(\frac{u_\theta}{r} \right) \right) \right] \tag{B.19b}$$

$$\frac{d\Omega_\theta}{dt} = \frac{15}{\rho_p {a_p}^2} \mu \left[\frac{\pi}{8} \left(\frac{1}{{h_s}^2} \frac{\partial u_r}{\partial s} + h_s \frac{\partial}{\partial r} \left(\frac{u_s}{h_s} \right) \right) \right] \tag{B.19c}$$